

An Analytical Model of a Radially Magnetised Longitudinal-Flux Permanent Magnet Air-cored Linear Oscillatory Machine

by

Dickson Kanungwe Chembe



*Dissertation presented for the degree of Doctor of Philosophy
in the Faculty of Engineering at Stellenbosch University*

Dr. J. M. Strauss and Prof. P. J. Randewijk

December 2019

Declaration

By submitting this dissertation electronically, I declare that the entirety of the work contained therein is my own, original work, that I am the sole author thereof (save to the extent explicitly otherwise stated), that reproduction and publication thereof by Stellenbosch University will not infringe any third party rights and that I have not previously in its entirety or in part submitted it for obtaining any qualification.

Date: December 2019
.....

Copyright © 2019 Stellenbosch University
All rights reserved.

Abstract

An Analytical Model of a Radially Magnetised Longitudinal-Flux Permanent Magnet Air-cored Linear Oscillatory Machine

D. K. Chembe

*Department of Electrical and Electronic Engineering,
University of Stellenbosch,
Private Bag X1, Matieland 7602, South Africa.*

Dissertation: PhD-Eng (E & E)

December 2019

The research presented in this dissertation is focused on the pre-optimisation-design stages of the design optimisation of air-cored radially magnetised longitudinal flux permanent magnet (LFPM) linear oscillatory machines. Electrical linear machine design optimisation involves the determination of the magnetic field, the output force and the inductance as the pre-optimisation parameters. Once the pre-optimisation parameters are solved, the design moves into the optimisation design stage and finally the experimental testing stage. The pre-optimisation stage can be achieved by employing either the finite element method (FEM) or the analytical model method. The pre-optimisation stage is as critical as the optimisation design stage for the final design of the machine to be accurate. While FEM is accurate, the determination of the pre-optimisation design parameters is time consuming and in addition, the commercial packages are expensive. This dissertation therefore focuses on the development of an analytical model to accurately simulate the pre-optimisation design parameters of an air-cored radially magnetised longitudinal flux permanent magnet linear oscillatory machine.

The developed analytical model takes into consideration the finite permeability and finite thickness of the yoke materials. This has not been not been done for this kind of machine according to literature. This allows for the capability to monitor the flux concentration in the yokes to determine the saturation levels. The development of the analytical model is approached by firstly developing a model that assumes the machine to be infinitely long, while taking the machine yokes to have a finite permeability and thickness. The model is then extended to model the actual finite length of the machine and its end effects. Again the yokes are considered to have the finite permeability and thickness. The analytical model has the advantage of being much faster than FEM and can be adopted as a cheaper option for the pre-optimisation design stage.

The topology of the linear oscillatory machine for which the analytical model has been developed has an air-cored tubular structure machine with surface mounted radially magnetised permanent magnets and with longitudinal flux pattern. The machine is single-phase and is intended to operate at resonant frequency (with free-piston Stirling engines as the prime mover).

The analytical model for the presumably infinitely long machine as well as the analytical model for the finite (actual) length of the machine have been validated by the commercial finite element method package MagNet by infolytica inc.. The results for the analytical models correlate well with the results obtained from the FEM package. This indicates that the analytical model can be adopted in the pre-optimisation design stage as a design tool.

Uittreksel

'n Analitiese Model van 'n Radiaalgemagnetiseerde Longitudinale Vloed Permanente Magneet Lugkern Lineêre Ossillerende Masjien

D. K. Chembe

*Departement Elektriese en Elektroniese Ingenieurswese,
Universiteit van Stellenbosch,
Privaatsak X1, Matieland 7602, Suid Afrika.*

Proefskrif: PhD (E & E)

Desember 2019

Die navorsing wat in hierdie proefskrif aangebied word fokus op die vooroptimeringsstadiums van die ontwerpsoptimering van lugkern radiaalgemagnetiseerde longitudinale vloed permanente magneet (LVPM) lineêre ossillerende masjiene. Lineêre elektriese masjien ontwerpsoptimering behels die bepaling van die magnetiese veld, die uittrekkrag en die induktansie as die vooroptimeringsparameters. As die vooroptimeringsparameters bepaal eers is, beweeg die ontwerp aan na die optimeringsontwerpstadium en uiteindelik na die eksperimentele toetsstadium. Die vooroptimeringsstadium kan bereik word deur die aanwending van of die eindige element metode (EEM) of die analitiese model metode. Die vooroptimeringsstadium is net so krities as die optimeringsstadium vir die finale ontwerp van die masjien om akkuraat te wees. Terwyl EEM akkuraat is, is die bepaling van die vooroptimeringsontwerpsparameters tydrowend en daarmee saam is kommersiële pakette duur. In hierdie proefskrif word daarom gefokus op die ontwikkeling van 'n analitiese model om die vooroptimeringsontwerpsparameters van 'n lugkern radiaalgemagnetiseerde longitudinale vloed permanente magneet lineêre ossillerende masjien topologie.

Die ontwikkelde analitiese model neem die eindige permeabiliteit en eindige dikte van die jukmateriaal in ag. Volgens die literatuur vir hierdie tipe masjien is dit nie voorheen gedoen nie. Dit maak die vermoë moontlik om die vloedkonsentrasie in die jukke te monitor om die versadigingsvlakke te bepaal. Die ontwikkeling van die analitiese model is benader deur eers 'n model te ontwikkel wat die masjien benader as oneindig lank, terwyl die jukke geneem word met eindige permeabiliteit en dikte. Die model is dan uitgebrei om die werklike eindige lengte van die masjien en die eindeffekte te modelleer. Die jukke is weereens geneem met eindige permeabiliteit en dikte. Die analitiese model

het die voordeel om baie vinniger te wees as EEM en kan aangepas word as 'n goedkoper opsie vir die vooroptimeringsontwerpstadium.

Die topologie van die lineêre ossillerende masjien waarvoor die analitiese model ontwikkel is, het 'n lugkern tubulêre struktuur met oppervlaktgemonteerde radiaal gemagnetiseerde permanente magnete en 'n longitudinale vloedpatroon. Die masjien is enkelfase en werk teen 'n resonante frekwensie (met vrysuier Stirling enjins as aanlegger).

Die akkuraatheid van die analitiese model vir die veronderstelde oneindige lengte masjien sowel as die eindige (werklike) lengte masjien is bevestig deur die kommersiële eindige element metode pakket Magnet deur Infolytica Inc.. Die resultate van die analitiese model korreleer goed met die resultate wat van die EEM pakket verkry is. Dit dui daarop dat die analitiese model gebruik kan word in die vooroptimeringsontwerpstadium as 'n ontwerpsinstrument.

Acknowledgments

I wish to acknowledge and thank:

- My wife Anna, for her love, support and wonderful encouragements. Sharing life with her is the best thing that happened to my life,
- My children and my blessings; Kunda, Eunice and Ian, for their support and presence during the project. Their smiles and desire to spend time with me encouraged me to soldier on,
- The Almighty God and His son - Jesus the Christ, for nothing exists without your Word and blessings,
- Dr. J. M. Strauss, my supervisor, for his coming up with the project and handing me the responsibility to execute it, together, with his full support and immeasurable encouragement,
- Prof. P. J. Randewijk, my co-supervisor, for his guidance and especially with python programming and latex,
- Dr. D. Ralaivasaona and Dr. A. Chama, for their guidance in mathematical modeling,
- Africa for Innovation, Mobility, Exchange, Globalization and Quality (AFIMEGQ) for the Scholarship,
- The Copperbelt University (Zambia) for the support and logistics provided during the study period,
- My Mother, who always called when I was low and encouraged me to keep moving forward,
- My father (late), who could have been very proud of his son. Thank you for sharing your life with me for eleven years from my birth,
- My research mates, Stiaan, Pushman, Lilian, Bola, Neneva and others, your support and friendship will forever be cherished,
- My relatives and friends, whom not much communication has been maintained during the research period, their patience is enough support,

List of Publications

Part of the work:

[1] D. K. Chembe, J. M. Strauss and P. J. Randewijk., " Development of an analytical model for a moving coil tubular permanent magnet linear oscillatory machine" *24th Southern African Universities Power Engineering Conference (SAUPEC)*, Vereeniging, Johannesburg, South Africa, Jan. 2016

[2] D. K. Chembe and J. M. Strauss., "Armature reaction magnetic field prediction for a moving-coil tubular permanent magnet linear oscillatory machine" *25th Southern African Universities Power Engineering Conference (SAUPEC)*, Stellenbosch, South Africa, Jan. 2017.

[3] D. K. Chembe, J. M. Strauss and P. J. Randewijk., " Analytical Model Development for a Moving-coil Tubular Linear Oscillating Permanent Magnet Generator" *IEEE Transactions on Magnetics* , Submitted for consideration.

Dedications

To **Anna**

My beautiful and wonderful wife, who has shared her life with me and always supported me in this research, our journey together is extraordinary and blessed because you are my soul mate. I love you always.

To **Kunda, Eunice and Ian**

My children, whom I owe years of play time, you are the biggest blessing I ever received in my life.
I love you all.

Contents

Declaration	i
Abstract	ii
Uittreksel	iv
Acknowledgments	vi
List of Publications	vii
Dedications	viii
Contents	ix
List of Figures	xv
List of Tables	xviii
Nomenclature	xviii
1 Introduction	1
1.1 Brief history of Stirling engines as prime movers	1
1.2 Brief review of Free-piston Stirling engines and their application	2
1.3 Linear machines, history and applications	7
1.3.1 Brief History of linear machines	7
1.3.2 Principal of operation of linear machines	8
1.3.3 Classification of linear machines	8
1.3.4 Types of linear oscillatory generators or machines	9
1.4 Analysis of linear permanent magnet machines and oscillatory generators .	14
1.5 Dissertation Problem Statement	16
1.5.1 Research approach	17
1.5.2 Scope of this research	18
1.6 Dissertation Overview	18
2 Prediction of the flux density with PMs as the only field source	20
2.1 Introduction	20
2.2 Open Circuit field distribution	20

2.2.1	Assumptions for the O.C analysis	21
2.2.2	Magnetic characteristics of materials	22
2.3	Governing equations for the O.C analysis	23
2.3.1	Adoption of the magnetic vector potential	23
2.4	General Solutions to Magnetic Field - O.C analysis	26
2.4.1	General Solution to the Laplace equation for O.C analysis	26
2.4.2	General solution to the Poisson equation for the O.C analysis	30
2.4.3	General solutions to the magnetic vector potential for all subdomains for O.C analysis	35
2.5	General solution to the PM magnetic flux density	35
2.5.1	Radial magnetic flux density general solutions for all subdomains in O.C analysis	36
2.5.2	Axial magnetic flux density general solutions for all subdomains	37
2.6	Boundary Conditions for the O.C. analysis	37
2.7	Implementation of boundary conditions to solve for the magnetic vector potential and the magnetic flux density in the O.C analysis	39
2.7.1	Internal bore radius boundary of subdomain I	40
2.7.2	Boundary between subdomain I and II - O.C. analysis	40
2.7.3	Boundary between subdomain II and III - O.C. analysis	40
2.7.4	Boundary between subdomain III and IV - O.C. analysis	40
2.7.5	Boundary between subdomain IV and V - O.C. analysis	41
2.7.6	Outer radius boundary of subdomain V - O.C. analysis	41
2.7.7	Solving the ten simultaneous equations - O.C. analysis	41
2.8	Final solutions to the magnetic vector potential and the magnetic flux densities (O.C. analysis)	44
2.8.1	Solutions to the magnetic vector potential- O.C. analysis	44
2.8.2	Solution to the radial magnetic flux densities - O.C. analysis	44
2.8.3	Solution to the axial magnetic flux densities - O.C. analysis	44
2.8.4	Solution to the total magnetic flux - O.C. analysis	44
2.9	Validation of the model (PM field only) with finite element method (FEM)	45
2.9.1	Radial PM Flux density distribution - with PM field only	45
2.9.2	Axial PM Flux density distribution - with PM field only	46
2.9.3	Flux density distribution in the yokes and saturation monitoring	46
2.9.4	Contour plot comparison - with PM field only	49
2.10	Summary and conclusion - with PM field only	51
3	Prediction of the armature reaction (AR) field	54
3.1	Introduction	54
3.2	Governing equations - AR analysis	54

3.2.1	Assumptions for the AR analysis	56
3.2.2	Representation of the Laplace and the Poisson equations in cylindrical coordinate system	56
3.3	General solution to the Laplace equation - AR analysis	56
3.4	General solution to the Poisson equation - AR analysis	57
3.4.1	Solution to the current density	57
3.4.2	Inserting the solution to the current density into the Poisson equation	59
3.5	General solutions to the magnetic vector potential for all the subdomains for the AR analysis	60
3.6	General solution to the AR magnetic flux density	60
3.6.1	Radial magnetic flux density general solutions for all subdomains in AR analysis	61
3.6.2	General solution for the axial magnetic flux density in all subdomains	61
3.7	Implementation of boundary conditions for the AR analysis	62
3.7.1	Internal bore radius boundary of subdomain I' - AR analysis	62
3.7.2	Boundary between subdomain I' and II' - AR analysis	63
3.7.3	Boundary between subdomain II' and III' - AR analysis	63
3.7.4	Boundary between subdomain III' and IV' - AR analysis	63
3.7.5	Boundary between subdomain IV' and V' - AR analysis	63
3.7.6	Outer radius boundary of subdomain V' - AR analysis	64
3.7.7	Solving the ten simultaneous equations - AR analysis	64
3.8	AR Final solutions to the magnetic vector potential and the magnetic flux densities	66
3.8.1	Solutions to the magnetic vector potential - AR analysis	66
3.8.2	Solutions to the radial magnetic flux densities	66
3.8.3	Solutions to the axial flux densities	66
3.8.4	The total magnetic flux density for the armature reaction	66
3.9	Inductance calculation	67
3.9.1	Flux linkage due to the armature reaction	67
3.9.2	Self-inductance calculation	68
3.10	Comparison of the armature reaction model with finite element method (FEM)	68
3.10.1	AR - Radial flux density distribution	68
3.10.2	AR - Axial flux density distribution	68
3.10.3	AR - Contour plot comparison	69
3.11	Summary and conclusion for the AR analysis	69
4	Prediction of Force and EMF	71
4.1	Introduction	71

4.2	Force Prediction formulations	73
4.2.1	Assumptions for the formulation of global quantities	73
4.2.2	Thrust Force predictions	74
4.2.3	Total force	75
4.3	Flux linkage and EMF calculations	76
4.4	Validation of the analytically derived global quantities by FEM	77
4.4.1	Flux linkage and EMF comparison between FEM and analytical	77
4.4.2	Thrust force comparison between FEM and analytical	78
4.5	Summary and conclusion	78
5	Discrete PM series analytical model	80
5.1	Introduction	80
5.2	Challenges to obtain a finite machine length analytical model and alternative approach	81
5.3	Alternative analytical model approximating the magnetic flux density distribution of a finite length machine	83
5.3.1	Assumptions	84
5.3.2	General solution to the Laplace Equation (PM -finite-length)	85
5.3.3	General solution to the Poisson equation (PM - finite-length)	85
5.3.4	General solutions to the magnetic vector potential for all the sub-domains (PM field only)	87
5.3.5	General solution to the magnetic flux density	88
5.3.6	Implementation of boundary conditions	88
5.3.7	Solving the ten simultaneous equations by matrix method	90
5.3.8	Validation of the Model with FEM	92
5.4	Summary and conclusion	98
6	Discrete AR series analytical model	100
6.1	Introduction	100
6.2	Armature reaction and inductance formulation	101
6.2.1	Assumptions	101
6.2.2	Laplace and Poisson equations in cylindrical coordinates	101
6.2.3	General solutions to Laplace and Poisson equations	101
6.2.4	General solution to the magnetic vector potential for finite length armature reaction	103
6.2.5	General solution to the magnetic flux density in the radial direction	104
6.2.6	General solution to the magnetic flux density in the axial direction	105
6.2.7	Boundary conditions	105
6.2.8	Solving the ten equations simultaneously for AR analysis	108

6.2.9	Final Solutions to the magnetic vector potential and the magnetic flux densities	110
6.2.10	Determination of inductance	110
6.2.11	Validation of the armature reaction field with finite element software, MagNet by infolytica inc..	111
6.3	Global quantities - finite length	116
6.3.1	Force prediction	116
6.3.2	Assumptions (Finite length model)	116
6.3.3	Flux linkage and EMF prediction	117
6.3.4	Comparison with FEM	118
6.4	Summary and conclusion	121
7	Conclusions and recommendations	124
7.1	Introduction	124
7.2	Conclusions	124
7.2.1	Analytical model developed for an infinitely long machine	124
7.2.2	Analytical model developed for a finite length machine	125
7.3	Dissertation contribution made to this work	126
7.4	Recommendations to be considered for future work	126
	Appendices	128
A	Magnetisation vector determination for various magnet arrangements	130
A.1	Magnetisation vector for four pole double sided machine with two configurations	130
A.1.1	One central complete magnet length and two half length size magnets on each side	130
A.1.2	Two full magnet arrangement for a four pole machine double sided .	132
B	Simplified analytical model -open circuit only	134
B.1	Magnetic field distribution due to permanent magnets (coil switched off) .	134
B.1.1	Assumptions for the simplified model	134
B.1.2	Solving the simultaneous equations for the simplified model	137
B.1.3	Comparison with finite element model	139
B.1.4	Comparison of the radial magnetic flux density from the simplified model with FEM	139
B.1.5	Comparison of the axial magnetic flux density from the simplified model to FEM	139
C	Bessel Functions	142
C.1	Brief Introduction to Bessel functions	142

<i>CONTENTS</i>	xiv
C.1.1 Bessel function of the first kind	142
C.1.2 Bessel functions of the second kind	143
C.1.3 Modified Bessel functions	144
List of References	145

List of Figures

1.1	Three main types of Stirling Engines, H - Heater, R - Regenerator, C - Cooler, 1 - Expansion space, 2 - Compression space. Redrawn from [4]	3
1.2	Free-piston Stirling engine configuration [5; 6]	3
1.3	Linear alternator hermetically sealed in a free-piston Stirling engine configuration [5; 6]	4
1.4	Illustration of the dish/Stirling solar system [12]	6
1.5	Revolution of linear machines from rotary to linear [25]	7
1.6	Moving Iron LOG redrawn from [34]	11
1.7	A cross section of a tubular moving-magnet LOM	11
1.8	Moving Coil linear alternator proposed by Beale [7]	13
1.9	Quarter View of Moving-Coil linear alternator with double sided PMs	13
	(a) Quarter assembled view.	13
	(b) Exploded view.	13
1.10	Moving-Coil linear machine with double air-gaps	14
2.1	Half-cut cylindrical moving coil linear oscillatory generator	21
2.2	quarter section of the LOG illustrating the subdomains	22
2.3	Radial component of magnetic flux along the axial coordinate	31
2.4	Gaussian surface and a closed path constructed between two media [79]	38
2.5	Left: Dirichlet Boundary Conditions; Right: Neumann Boundary Conditions [80]	39
2.6	Radial flux density distribution due to PMs	46
2.7	Axial flux density distribution due to PMs	47
2.8	B-H Curve of Cold Rolled 1010 Steel [Infolytica MagNet]	48
2.9	Axial and radial flux density of the inner yoke (unsaturated case)	48
2.10	Axial and radial flux density of the inner yoke (saturated case)	49
2.11	Axial and radial flux density of the outer yoke (unsaturated case)	50
2.12	Axial and radial flux density of the outer yoke (saturated case)	50
2.13	Contour plot obtained from FEM	51
2.14	Field line plot and contour plot obtained from the analytical model	51
3.1	Armature reaction subdomain representation	55
3.2	Domain representation for armature reaction field distribution	58
3.3	Radial flux density distribution due to AR	69
3.4	Radial flux density distribution due to AR	70

3.5	Contour plot obtained from FEM	70
3.6	Field line plot and contour plot obtained from the analytical model	71
4.1	Linear machine to illustrate displacement of the coil	75
4.2	Flux linkage with armature position	77
4.3	Induced voltage obtained against time	78
4.4	Thrust force with displacement	79
5.1	Illustration of a finite length machine with end effects	81
5.2	Discrete linear machines in infinite series	83
5.3	An axisymmetrical structure of the LOG with infinitely long iron yokes and with finite permeability (series PM-array). Below the machine is the magnetisation vector for radial magnetisation	84
5.4	An illustration of the MagNet set-up of the simulation and a solution mesh	93
	(a) LOG FEM Simulation setup	93
	(b) Solution mesh	93
5.5	Radial flux densities obtained analytically and compared to a finite length FEM model	93
5.6	Full spectrum radial flux density plot compared to a finite length FEM model	94
5.7	Analytically obtained axial flux density compared to a finite length FEM model	95
5.8	Full spectrum of axial flux density plot compared to a finite length FEM model	95
5.9	Contour plot of the FEM model	96
5.10	The magnetic field lines and a contour plot as obtained from the analytical model	97
5.11	Analytically determined magnetic field lines and contour plot considering an axial length of $2\tau_p$	97
5.12	Analytically determined magnetic field lines and contour plot considering an axial length of $2\tau_p$ with half PMs at axial edges of the machine	98
6.1	The LOG with PMs removed and only showing the discrete finite length armatures in series separated by τ_l . Also shown is a current density vector formulation	102
6.2	An illustration of MagNet set-up for the armature reaction field	112
6.3	Radial flux density compared to a finite length FEM model	112
6.4	Radial flux density compared to a finite length FEM model with full analytical model axial length analysis	113
6.5	Axial flux density compared to a finite length FEM model	114
6.6	Axial flux density compared to a finite length FEM model considering the full analytical spectrum	114
6.7	Contour plot obtained from the finite-element solution	115

6.8	Analytically determined magnetic field lines and contour plot considering the machine length plus extra mm on the axial edges for the armature reaction fields prediction	115
6.9	Analytically determined magnetic field lines and contour plot considering an axial length of $2\tau_{lp}$ for the armature reaction fields prediction	116
6.10	Flux linkage in relation with the armature displacement	119
6.11	Flux linkage in relation with time	120
6.12	Simulated and analytically obtained voltages	121
6.13	Thrust force against translational position	122
6.14	Thrust force against time	122
A.1	Four pole double sided PM linear machine with one complete central magnet and two half length magnets	130
A.2	Four pole double sided PM linear machine with two full length magnets	132
B.1	LOG with infinite PM series and infinitely long and permeable iron yokes	135
B.2	Analytically Radial flux density plot compared to a finite length FEM model	139
B.3	Full spectrum radial flux density plot compared to a finite length FEM model	140
B.4	Axial flux density plot compared to a finite length FEM model	140
B.5	Full spectrum of axial flux density plot compared to a finite length FEM model	141

List of Tables

2.1	Machine dimensions	46
-----	------------------------------	----

Nomenclature

Constants

$$\mu_0 = 4\pi \times 10^{-7} \text{ Wb/(A.m)}$$

μ_o Magnetic permeability of free space [H/m] or Wb/(A.m)

Acronyms

2-D Two Dimensional

AC Alternating Current

PM Permanent Magnet

AR Armature Reaction

LFPM Longitudinal Flux Permanent Magnet

LFAPM Longitudinal Flux Air-cored Permanent Magnet

LA Linear Alternator

LOG Linear Oscillatory Generator

LOM Linear Oscillatory Machine

SE Stirling Engine

FPSE Free-Piston Stirling Engine

FE Finite Element

FEA Finite Element Analysis

FEM Finite Element Method

NdFeB Neodymium Iron Boron

EMF Electromotive Force

Variables and machine dimensions

A_{cond} Conductor cross section area [mm²]

A_{slot} Slot cross section area [mm²]

τ_m	Magnet pole length
τ_p	Magnet pole pitch
τ_w	Winding pole length
τ_{wp}	Winding pole pitch
l_{ms}	Space between the magnet poles
l_{ws}	Space between the winding poles
h_{ics}	Inner yoke thickness
h_{ipm}	Inner PM thickness
h_{coil}	Winding thickness
h_{opm}	Outer PM thickness
h_{ocs}	Outer yoke thickness
iR_s	Inner bore radius
iR_r	Outer radius of the Inner yoke
iR_m	Outer radius of the Inner PMs
iR_{coil}	Inner radius of the windings
oR_{coil}	Outer radius of the windings
oR_m	Inner radius of the outer PMs
oR_s	Inner radius of the outer yoke
R_o	Outer most radius of the outer yoke

Electromagnetics

A	Magnetic vector potential	[Wb/m]
B	Magnetic flux density	[T]
H	Magnetic field intensity	[A/m]
J	Current density	[A/mm ²]
M	Magnetisation Vector	[A/m]
λ	Flux linkage	

μ	Permeability	
μ_r	Relative recoil permeance	[]
B_{rem}	Permanent magnet remanence	[T]

Bessel functions

I_0	Modified Bessel function of the first kind of zero order
I_1	Modified Bessel function of the first kind of the first order
K_0	Modified Bessel function of the second kind of zero order
K_1	Modified Bessel function of the second kind of the first order
L_0	Modified Struve function of zero order
L_1	Modified Struve function of the first order

Chapter 1

Introduction

1.1 Brief history of Stirling engines as prime movers

The original name of the Stirling engine was the "Economiser Hot-Air Engine" and was patented by a 25 year old inventor and minister of the Church of Scotland, Rev. Robert Stirling in September, 1816. Although there had been many other engines in the line of hot-air engines, Rev. Stirling's engine stood out due to its much higher efficiency in comparison to other machines invented by his counterparts in the nineteenth century. According to Hargreaves, had it not been for the Stirling engine's high efficiency, it could not have survived into the twentieth century. During the early twentieth century, Stirling type hot-air engines were manufactured for application in water pumping, powering of domestic as well as farm machines of smaller sizes. These machines were manufactured by Heinrich in Germany, Rider Ericsson Engine company in the United States of America and W. H. Bailey, A.E.H Robinson, Gardner and Sons Limited in England amongst others [1].

In early 1900, hot-air engines gained popularity alongside steam engines, but the invention of internal combustion engines by 1930 made a huge impact on the use of steam engines and hot-air engines. Most steam engines were replaced and hot-air engines were almost eliminated from usage. A paradigm shift on hot-air engines occurred due to the research work of H. De Brey between 1930 and 1938 under the Philips Company. The research revealed that higher efficiencies could be obtained by replacing air with helium or hydrogen as working fluids for the hot-air engines. In 1954, the Philips company then renamed the hot-air engine to Stirling engine in honour of the original inventor [1].

Despite the success obtained on the working fluid of the Stirling engine, displacer balancing still remained a challenge. An engineer by the name of R. J. Meijer succeeded in solving the balancing challenge and demonstrated his knowledge by building the first 'Rhombic drive'. His work facilitated clues for designing single cylinder well balanced engines by 1953. A wave of interest in Stirling engines emerged, as somewhere in 1958, General Motors Corporation of Detroit proposed to collaborate under licence with Philips to develop Stirling engines for underwater power, space vessels and surface vessel propulsion. The collaboration agreement lasted for thirteen (13) years, after which it was revoked and Ford Motors Company replaced General motors on the licence in 1971. Ford Motor company made substantial investments (\$180m) to realise their goal because of their

huge interest in developing Stirling engines for automotive application. Unfortunately, seven years later, experiments for the implementation of Stirling engines for automotive applications were not successful. Experimental records and tests done by Ford Motors are scarce [2].

A Stirling engine can then be described as an external combustion mechanical device which principally employs a closed regenerative thermodynamic cycle, within which the flow of the working fluid undergoes volume expansion and compression at varying levels of temperature. The device can be applied in refrigerating engines, heat pumps, pressure engines, and most importantly as per focus of this research, prime movers for generators [2].

There exists three main configurations of Stirling engines, namely the Alpha, Gamma and Beta types of engines. Among the three, the Beta exhibits better efficiency which has been attributed to having less dead space. The Beta type is suitable for linear generator applications. As can be seen from the diagram, the displacer piston is located at the hot end, while the power piston is located at the cold end. Both pistons are held up in a single cylinder. The Gamma type on the other hand has two cylinders within which there is the displacer piston in the hot end cylinder and the power piston in the cold cylinder. Because of connection pipes (dead space), this configuration has lower efficiency. The Alpha type also has two cylinders in both of which there are power pistons with an addition of a displacer mounted onto a power piston in one cylinder [3]. In Figure 1.1, the smaller piston (blue in colour) is the power piston and the larger piston is the displacer piston [4]. In structural construction of Stirling engines, the displacer is much lighter as compared to the power piston which is heavy [5].

1.2 Brief review of Free-piston Stirling engines and their application

While General Motors and Philips were experimenting and testing Stirling engines, a professor in mechanical engineering named William Beale, from the university of Ohio, invented the free-piston Stirling engine (FPSE). By the time of his invention, late 1950s, the University of Ohio could not take up the opportunity presented to them to commercialise the project. This prompted professor Beale to register his own company for the sole purpose of commercialising the production of free-piston Stirling engines. Professor Beale's company was registered under the name 'SunPower Incorporation'. According to Walker [2], "*A free-piston Stirling engine is a machine in which the motion of the reciprocating elements to accomplish the thermodynamic cycle are affected by the fluidic forces and by the dynamic, fluidic interactions of the components*". The free-piston Stirling engines champions over the traditional Stirling engine as highlighted below. First of all,

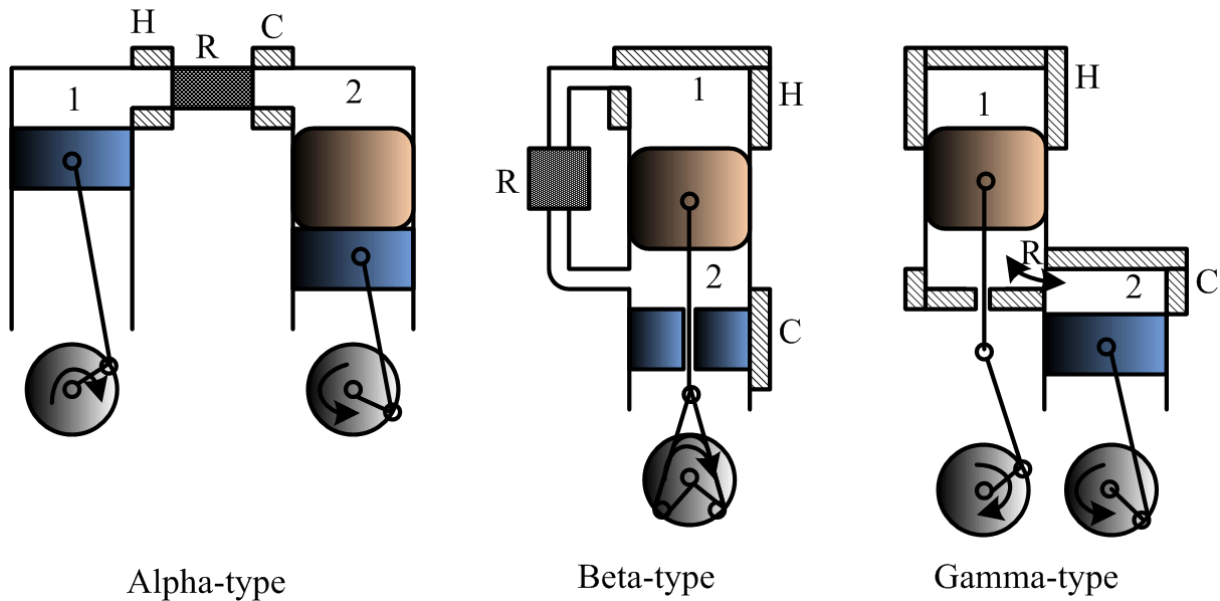


Figure 1.1: Three main types of Stirling Engines, H - Heater, R - Regenerator, C - Cooler, 1 - Expansion space, 2 - Compression space. Redrawn from [4]

free-piston Stirling engines have no crank mechanisms or rotating parts (Figure 1.2); secondly, dry running of pistons is possible in free-piston Stirling engines giving them longer maintenance free periods which is a huge advantage. Besides that, further advantages in terms of efficiency and configurations plus control methods are explained by Beale [6].

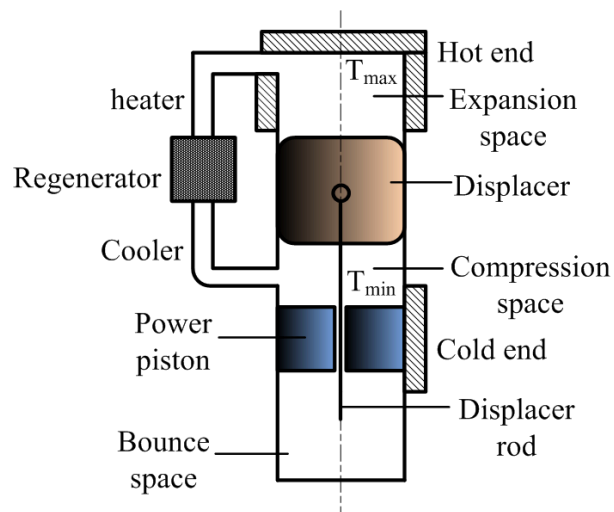


Figure 1.2: Free-piston Stirling engine configuration [5; 6]

The other advantage of the free-piston Stirling engine is the ability to be hermetically sealed. Through hermetic sealing, a linear alternator (LA) can be enclosed within the free-piston Stirling engine from which power can be extracted. The linear alternator and the FPSE sealed together make a robust power generator that could be used for power

generation in rural areas or areas far from the power grid. The free-piston Stirling linear alternator is illustrated in Figure 1.3.

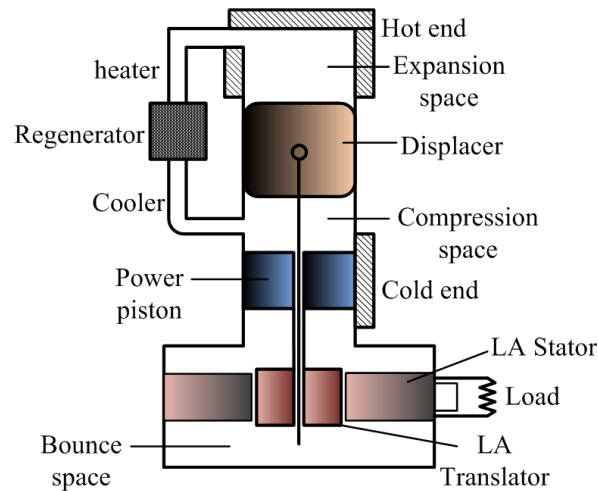


Figure 1.3: Linear alternator hermetically sealed in a free-piston Stirling engine configuration [5; 6]

The candidacy of the linear alternator hermetically sealed with the FPSE, cannot be more emphasized as the machine operates for longer periods of time without any leakages of the working fluid and almost maintenance free [7]. Taylor [8] further highlights free-piston Stirling engines as having higher mechanical efficiency measure of about 99% for a 1 kW output engine than the crank type Stirling engine with about 88% mechanical efficiency. Most notable advantages of the free-piston Stirling engines in comparison to crank type Stirling engines are:

- higher thermal efficiency,
- multiple-fuel sources (solar, bio-gas, bio-mass, etc),
- self-starting if well designed,
- no liquid lubricant required,
- hermetically sealed and
- quiet operation [8].

Even with all the advantages highlighted above, the free-piston Stirling engine cannot be claimed to be without challenges. Load matching, loading devices to operate at frequencies of 50 or 60Hz and shorter stroke lengths, centring, starting, heater heads are the most common problems experienced by designers in building free-piston Stirling engines [9].

Because of the machine being an external combustion engine, it makes it a huge candidate for rural power generation by employing heat sources such as solar, biomass, or biogas and etc. Beale investigated the application of the FPSE with a linear alternator for power generation employing solar concentrated radiation and claimed an overall efficiency, with addition of losses from the collector and absorber, of about 20% with an estimated range of 10 kW electrical power output per cylinder as feasible [7; 9]. Some hypothetical cost estimates were weaved together by Beale [10] on the dish solar free-piston Stirling installation in comparison to diesel generators of that time. The costs for the dish/Stirling solar system were estimated at \$ 600 kW/peak which would due to longer maintenance free periods, life cycle and out-of-pockets costs outweigh the diesel generator in the long run. A 60 Hz 5 kW dish/free-piston Stirling engine with a linear alternator solar system was proposed for commercialisation after a successful validation of a 4 kW dish/free-piston Stirling-alternator solar system by Cummins Power Generation (CPG) between 1989 and 1990. Despite challenges with the heat pipe receiver sustained during the validation process, the 5 kW dish/Stirling solar system commenced with the redesigning of the heat pipe to overcome the earlier experienced problem of overheating. The proposed plans were to supply 10 000 units of 5 kW dish/Stirling solar systems worldwide per year [11]. From 1990 to 1995, several experiments were conducted by Cummins Power generation in conjunction with the Ministry of Energy (MOE) of the United States of America (USA), however the commercialisation objective set in 1990 could not be realised. By 1993 about five 5.2 kW dish/Stirling solar systems were regularly being modernised as experiments continued being conducted. In addition, several 7 kW systems were being adopted for experiments and study according to Stine and Diver [12]; Bean and Diver [13]. Further developmental elaboration of dish/Stirling solar systems can be accessed in [12].

Figure 1.4 shows components of a Dish/Stirling solar system. Concentrators reflect light photons onto the receiver, which through heat pipes directs the heat onto the heating head of the free-piston Stirling engine. The thermal energy is converted into mechanical energy in the Stirling engine, whereas the mechanical energy is finally converted into electrical power by the alternator (inbuilt alternator with the Free-piston Stirling engine).

Biomass in form of rice husks were proposed as a heat source for heating up the free-piston Stirling engine incorporated with a 4 kW linear generator design by Wood *et al* [14]. The design was employed to target the largest producers of rice - the Indian and the Chinese customers for rural electrification. For a similar purpose as the design by Wood *et al*, a 3 KW linear alternator was investigated by Berchowitz [15]. A 40 W/kg specific power as well as 18 % overall peak efficiency was expected for a complete alternator and burner. Due to their large populations, China and India were target for industrial implementation of Stirling engines in various sectors [16]. The free-piston Stirling engine in application with biomass, could produce a kilo-watt hour electricity from 10 kilograms

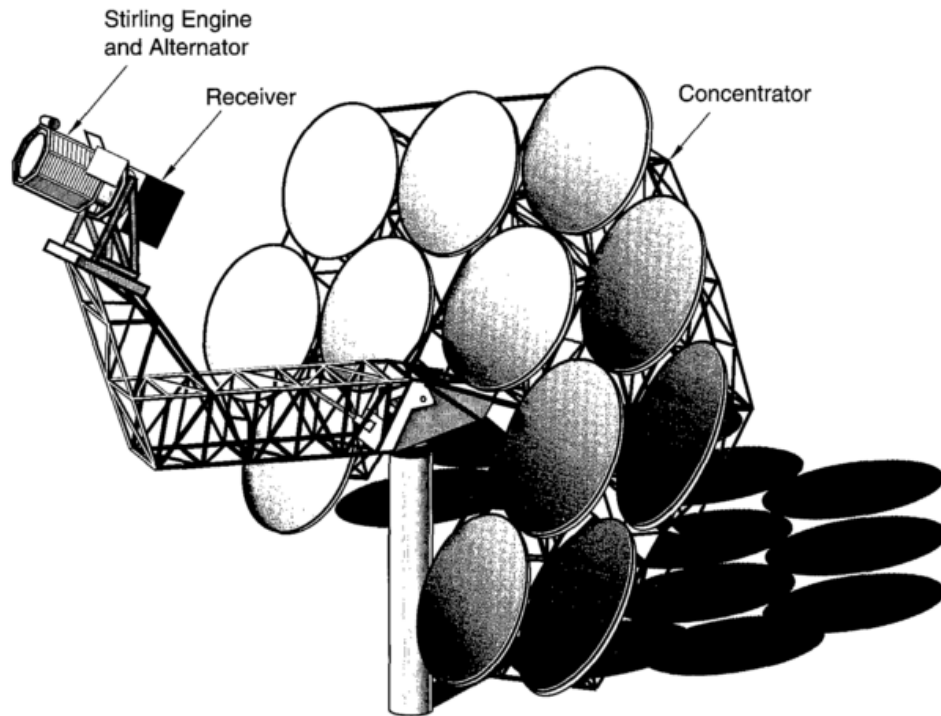


Figure 1.4: Illustration of the dish/Stirling solar system [12]

(kg) of ordinary biomass, whereas with 6 kg of coal as the biomass, could produce as much electricity [17; 18]. SunPower Incorporation, Beale's company, with partners have produced micro-scale biomass systems called Biowatt for co-generation, that is heat and electricity production [19; 20].

Space applications of free-piston Stirling engines have been undertaken by SunPower Incorporation by request and funding from the American Space Agency - National Aeronautics and Space Administration (NASA). The most accomplished SunPower products that have been adopted by NASA are the Cryocoolers. Cryocoolers are small scale free-piston Stirling engine linear cooling devices capable of cooling an environment to cryogenic temperature levels (less than -150°C). Cryocoolers gained recognition in the 1990s when established test results were validated [21]. Cryocoolers have since been adopted for cooling important components for NASA projects, as refrigerators on the International Space Station (ISS) and many applications related to cooling in various industrial applications. M77 Cryocooler; a 4 W, 77 K cooler, installed on the Reuven Ramaty High energy Solar Spectroscopic Imager (RHessi) NASA solar orbiter, exemplifies the satisfactory application of Cryocoolers [22; 23]. A 35 W free-piston Stirling engine converter heated up by plutonium-238 and intended for replacing batteries is yet another project that was funded by NASA and could reach efficiencies of 50% of Carnot with 90 W/kg specific power. The plutonium powered converters could be adopted for space exploration projects replacing the lithium-ion batteries due to their low energy density [24].

1.3 Linear machines, history and applications

1.3.1 Brief History of linear machines

The history of linear machines dates back to the Wheatstone in 1841, but could not be fully developed due to the tradition of machine development being rotary. Therefore, it took a while for engineers to actively engage in researching the linear machines. It was not until the 1940s to 1950s that active research was reborn on linear machines. Initially, the primitive understanding was the cutting, unrolling and rolling of any existing rotating machine to reconfigure it into a linear counterpart [25].

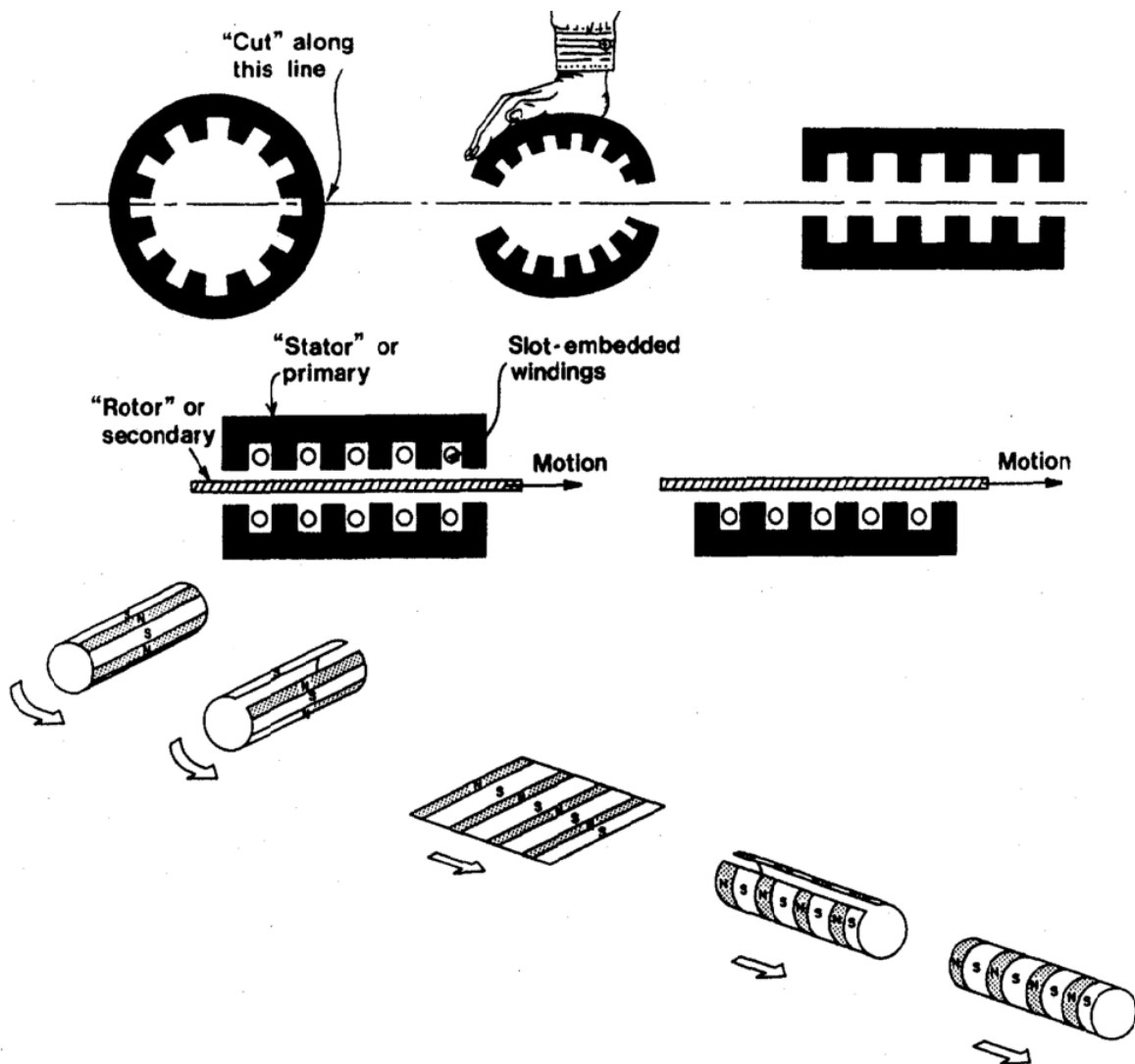


Figure 1.5: Revolution of linear machines from rotary to linear [25]

From such an exercise, linear machines could be developed as cylindrical/tubular and as planar/flat linear machines. From induction to synchronous linear motor counterparts have been developed and in operation since the 1970s. A reasonable amount of time

passed before engineers could realise that topology modification could inspire new types of linear machines. This discovery led to more design modifications and performance analysis of linear machines [26].

Notable achievements in the implementation of electric linear motors were spearheaded by a German engineer named Kemper. His work focused on the technology of magnetic levitation to propel a vehicle incorporating a linear motor in 1937. Later on, a high thrust linear induction machine was developed by Electropult from the United States of America (USA), which aided in the rapid takeoffs of aircraft from aircraft carriers. Between 1955 and 1965, various designs and prototypes of linear machines emerged from an engineer named Laithwaite from the United Kingdom (UK). From the 1970s and 1980s, people movers operating with long stroke linear machines and magnetically levitated machines (MAGLEVS) became prominent at large international airports in Romania, USA, UK, Japan, Germany and Canada [25].

1.3.2 Principal of operation of linear machines

The electromotive force in linear machines is generated by the basic law of electromagnetic induction formulated by Faraday and published around the 1831. According to Faraday, a voltage is induced into a coil by any variation of its flux linkage with time. The linear machines convert electrical energy into direct linear motion which may be progressive or oscillatory. A force developed by flux interaction with the coil produces linear motion. Linear machines operate as actuators or generators much in the same way as their counterpart the rotary machines. When connected to oscillatory prime movers, linear generators can convert mechanical energy to electrical energy.

1.3.3 Classification of linear machines

Linear machines can be categorised as either **progressive linear machines** or **oscillatory linear machines**. Despite the machines operating in linear motion, linear progressive machines operate at a non-periodic motion with variable frequency and voltage. Hence these machines can have a longer stroke length from above 50 mm to kilometres. On the contrary, linear oscillatory machines or generators (LOM/LOG), (the focus of this research) operate in a periodic motion. LOM operate at resonant (fixed) frequency (mechanical eigenfrequency equals the electrical frequency) and voltage. For this reason, LOMs are short stroke translator displacement machines (less than 30 mm). Since LOGs are driven by prime movers, a free-piston Stirling engine in this case, the operating voltage's phase sequence reverses when the prime mover reverses its oscillatory motion. Consequently, LOGs are single phase machines. Progressive linear machines on the contrary are distinguished by being polyphase (three-phase) machines [25; 27]. Examples of

types of progressive linear machines are:

Linear Induction Machines (LIMs) - Linear induction machines operate much in the same way as rotary induction machines but only in linear motion. These machines can be in flat or tubular topologies and also can be single or double sided machine. Jansen *et al* highlights various types of topologies for LIMs for high speed technologies [28],

Linear Synchronous Machines (LSMs) - Linear synchronous machines are designed from the same principle of cutting and flattening or rolling conventional rotary machines. These machines operate in the same way as rotary machines in linear motion and are mostly brushless alternating current (AC) machines. In mover technologies, tracks are built with PMs and the mover seats on three-phase AC windings. The synchronous linear motors are renamed PM-LSMs. Danielsson - Leijon [29] and other authors [30; 31] have studied these machines and they can be referenced for further study of PM-LSMs,

Linear Switched Reluctance Machines (LSRM) - principal of operation is the same as rotary machines. Garcia-Amoros *et al* [32], Baoming *et al* [33] present some interesting work on LSRMs,

Linear Direct Current (DC) Brush or Brushless Machines - Boldea [34] can be referenced for more details on such machines.

1.3.4 Types of linear oscillatory generators or machines

Linear oscillatory machines or generators are driven by prime movers at resonant frequency and at a fixed voltage. Commonly known prime movers are direct wave energy engines exhibiting longer stroke lengths, single piston engines that are linear internal combustion engines (ICE) and Free-piston Stirling engines (FPSE) which is the adopted prime mover for this study. Most hybrid vehicles have adopted the single piston linear internal combustion engines as prime movers [27]. Three types of linear oscillatory machines exist, each with an arsenal of advantages over the other but with some drawbacks in comparison to one another. Each type of machine is briefly discussed to highlight the topological distinctions and similarities in their operation and design. These machines can be further categorised as:

Transverse Flux (TF) or Longitudinal Flux (LF) - Transverse flux machines run the flux perpendicular to the line of motion of the translator; longitudinal flux machines run the flux in the direction of movement of the translator. Since the focus of this research is on a longitudinal flux linear machine, the transverse flux will not be further discussed. However, Schutte and Strauss [35], Joubert *et al* [36]

extensively studied the optimisation design of this type of machine. Longitudinal flux is the focus of this study and has also been studied by [37; 38] among others.

Flat or Tubular - as depicted in Fig. 1.5, a flat linear machine is obtained by simply cutting a rotary machine on both sides and flattening it. On the same diagram, if the flat linear machine is rolled over a tubular machine is obtained. Flat linear machines have poor volume usage as flux leakage and flux fringing is increased due to many edges. On the other hand, tubular machine topologies better utilises the volume and in addition to that, may also transmit heat better than flat linear machines

Slotless or Slotted - Slotless machines refers to machines in which the windings are not placed within the stator core slots. Windings may also be mounted onto an iron core and will be deemed slotless. In a case where the windings are not attached to any core, then the term *core-less* or *air-cored* is preferred. Slotted windings or commonly referred to as iron-cored windings are placed in stator slots and this enhances the flux density thereby increasing the force density. Attraction forces or cogging forces between the stator teeth and the translator is predominant in iron-cored or slotted machines whereas, these cogging forces are practically zero in air-cored windings.

Air-cored or Iron-cored - as mentioned above, a slotless machine with a core-less winding is an air-cored machine. Air-cored machines exhibit a higher air-gap, hence a slightly lower flux density is obtained in the air-gap as compared to iron-cored machines. Besides that, the reduced flux density leads to lower inductance in air-cored machines which increases the power factor.

Single-sided or double-sided - as illustrated in Fig. 1.5, the double sided has an increased air-gap flux density due to the increased number of magnetic poles.

1.3.4.1 Moving-iron

The moving-iron machine is configured in such a way that both the PMs and the coils are fixed to the stator of the machine while the mover - translator is only composed of iron, hence the name. The translator has a larger mover mass that promotes low frequency oscillations [39]. Besides that, the large inductance in these configurations complicates the control and operation of these machines because the large inductance lowers the power factor at the same time slowing the current response rendering the machine exposed to possible demagnetisation of the PMs [25; 40]. Moving-iron linear machines also exhibit high levels of cogging forces [40]. Schutte and Strauss [35] conducted a design optimisation of a transverse flux moving-iron machine. Due to low flux densities in such machines, the results by Schutte and Strauss of the power-to-weight ratio were not as expected. The

moving-iron is not under the scope of this research and therefore will not be further discussed in the following chapters.

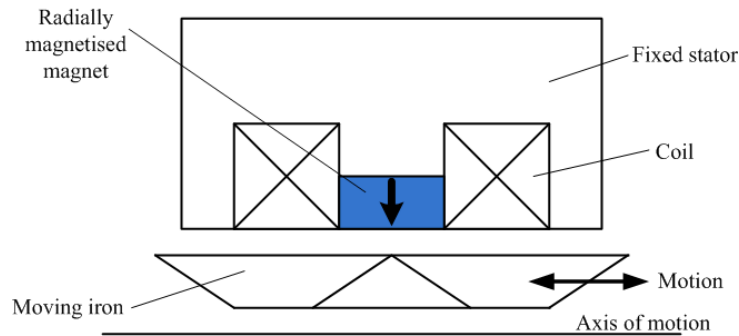


Figure 1.6: Moving Iron LOG redrawn from [34]

Figure 1.6 highlights the topological design of a moving-iron LOG.

1.3.4.2 Moving-PM

The moving PM machine is configured such that the translator, moving part of a linear machine, is composed of the PM in either axial or radial magnetisation. Other permanent magnet arrangements are Halbach array and Quasi-Halbach array magnetisation. The moving-magnet can also be designed with a slotted stator or a slotless stator, while the topologies can be designed in a tubular structure or a flat structure [40; 27]. Moving magnet machines exhibit a high force density and hence the adoption in compressor applications and refrigeration applications [41]. For slotted moving magnet machines, cogging forces are present especially if the slots are large [40]. An illustration of a PM mover adopted from [42] is shown in Figure 1.7.

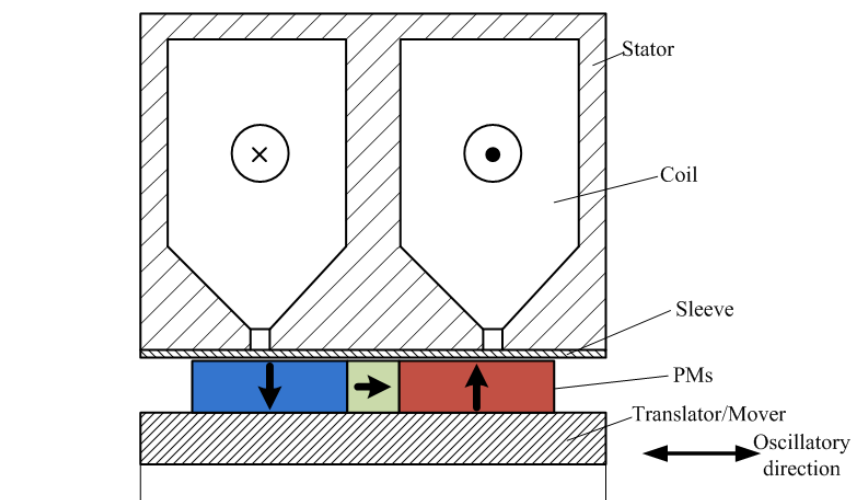


Figure 1.7: A cross section of a tubular moving-magnet LOM

The moving magnet may risk or suffer from its permanent magnets being demagnetised because of the increased temperatures caused by high frequency oscillations or vibrations [34]. The moving magnet translator may be heavier due to the magnetic core on which the magnets are attached thereby requiring a more expensive mechanical spring and lower operating frequency of about 50 Hz to 60 Hz. Flexure bearings are usually installed on the axial edges of moving permanent magnet machines to improve the resonance operation [40]. Several authors have considered the PM-mover topology in their works. Particular attention can be paid to Vermaak and Kamper [43; 44] whose generator, designed on the PM-mover principal, for direct drive wave converters, was prototyped successfully. Other authors [45; 42; 46; 47; 48; 36] and more have analysed the moving magnet machine for various applications. The PM-mover will not be analysed further as it is not part of the scope of this research.

1.3.4.3 Moving-Coil

The moving-coil machine has a distinctive structure from the previous two types of LOGs mentioned in that, it has the lowest translator mass. The reduced translator mass enhances high frequency oscillations and high force density can be achieved. Besides that, the spring cost is highly lessened by the smaller mover mass as demonstrated by the relationship of the mass and spring constant in (1.1),

$$2\pi f_m = \sqrt{\frac{K}{M}} \quad (1.1)$$

where f_m is the resonant frequency, K is the spring constant and M is the mass of the translator. The moving-coil is so called because only the coils oscillate in between the slotless stator where the permanent magnets are fixed. The coils are usually air - cored thereby leading to being fragile. The coil fragility explains why epoxy resins are mostly moulded onto the coils to reduce the fragility and strengthen the coil structure. For bigger machines (kW), a non magnetic core maybe attached to the coils for stability. The machine being air -cored also exhibits low levels of inductance and larger power factors. However, the coils do experience direct electromagnetic force. These types of machines are disadvantaged by having a flexible cable for tapping or supplying power to the coils. Nevertheless, these machines have practically no cogging forces [40; 27]. The moving-coil machine was proposed by Beale in some of his works in [7] as shown in Figure 1.8.

The moving-coil LOM(G) may be designed having shorter coil lengths in relation to PM lengths [49]. This could reduce the copper losses but still have an increased cost on the PMs. In this research, the topology considered has longer coil length in relation to PM length. The cost of the PMs is thus reduced. This configuration has been modified slightly from the configuration proposed by Strauss [50] in which he considered three pairs of magnet poles matched in length to the coils.

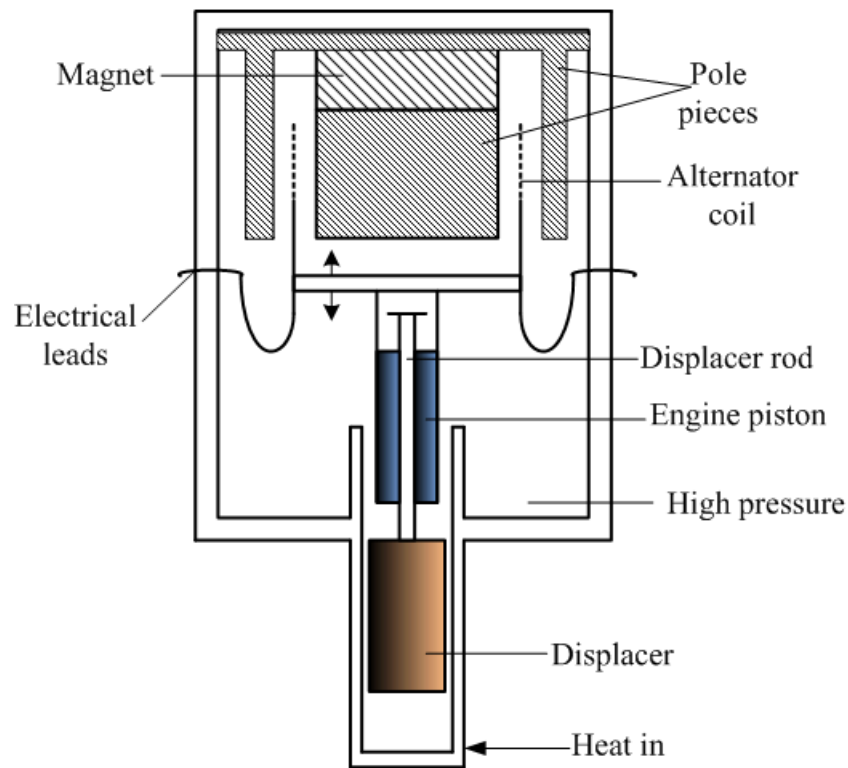
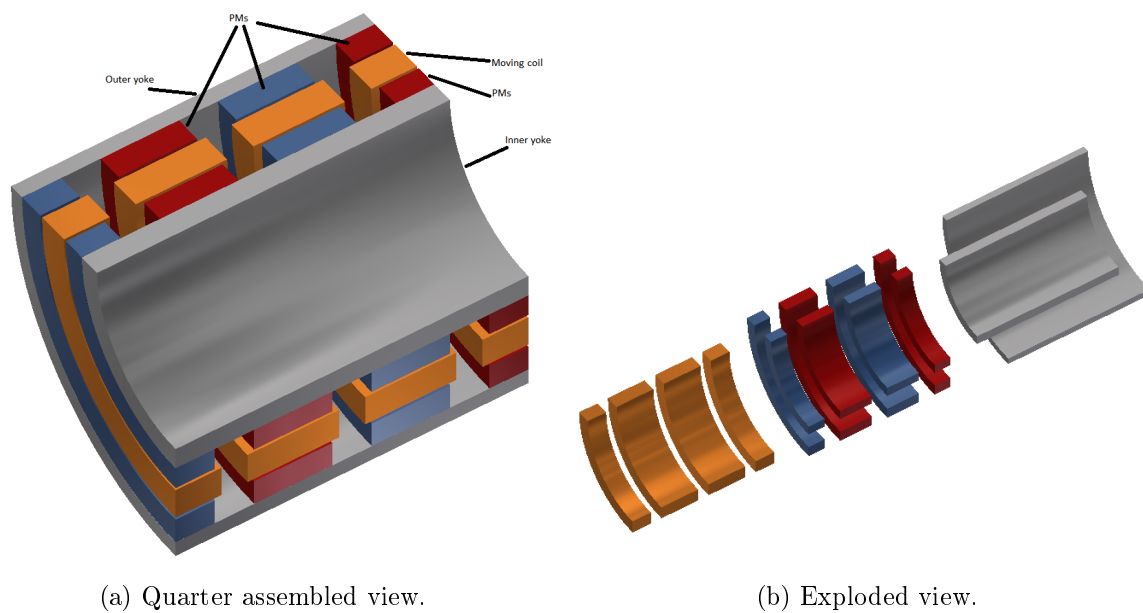


Figure 1.8: Moving Coil linear alternator proposed by Beale [7]



(a) Quarter assembled view.

(b) Exploded view.

Figure 1.9: Quarter View of Moving-Coil linear alternator with double sided PMs

The moving coil has been studied, of late, by various researchers for various applications. Xu *et al* [51] analysed the performance of the moving-coil tubular PM oscillating machine in free-piston internal combustion engines which had advantages in cooling implementation and had no PM demagnetisation risk as in the PM-Moving machines. Xu *et al* argues against the conclusions reached by Wang *et al* in their comparisons of LOMs for active vehicle suspension [39] by indicating that the moving-coil may still be a candi-

date for such applications. Coil-moving machines may be designed in single coil topology preferably called homo-polar coils mostly for small devices of lower forces such as micro-speakers employed in mobile phones, laptops, mp3 players and similar devices. whereas for larger forces, moving coil machines may be multi-coil.

1.4 Analysis of linear permanent magnet machines and oscillatory generators

Electrical linear machines have been analysed analytically and numerically through various methods and techniques. The critical aspect of any analysis of such machines is the determination of the magnetic field distribution in the air-gap. The field distribution once determined leads to the calculation of the global quantities (flux linkage, electromotive force and force) for the performance analysis of the linear machine. Numerical methods are not discussed in this dissertation but referenced to in the explanation of the benefits of employing analytical methods in the initial stages of designing a linear machine. It should also be noted that the study is limited to permanent magnet excitation of the machine.

The adoption of the analysis of a longitudinal flux air-cored linear permanent magnet oscillatory generator comes from the work of Strauss [50] in which he considered a suitable type of linear oscillatory machine for direct piston displacement control of free-piston Stirling engines. With the advantage of the longitudinal flux air-cored machine having low inductance to enhance the current control as compared to iron-cored machines, Strauss considered this machine type a candidate for integrating into the direct piston control study. Besides that, the moving coil boasts with the lightest mover in comparison to the iron-mover and the magnet-mover thereby having increased frequency oscillations and high force density.

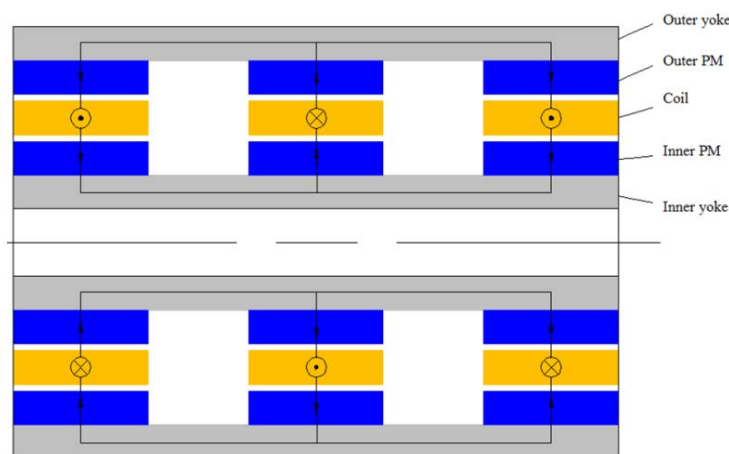


Figure 1.10: Moving-Coil linear machine with double air-gaps

Fig. 1.10 show the topology structure as Strauss proposed. The machine yoke thicknesses in this type of machine topology are different. The inner yokes are thicker than the outer yokes because there is more flux concentration in the inner yokes. This calls for care in optimisation and also in the analysis of the machine as yoke thickness becomes a critical aspect which should not be neglected. Whereas Strauss [50] adopted this machine topology, an analytical analysis of the machine was not conducted. As mentioned before, the prediction of the magnetic flux distribution in the machine is a key factor in the initial optimisation design stages of a machine [52; 53; 54]. Therefore analytical models become tools capable of providing the engineer with predictive electrical machine performance indicators much quicker than numerical tools such as finite element (FEM) method packages. The advantage of analytical methods over FEM packages is the lack of mesh dependence. The accuracy of FEM packages highly depends on the quality of the mesh provided in the simulations. The finer the mesh the more accurate the results are obtained which in turn increases the simulation time during optimisation procedures. The possibility of adopting analytical models into real-time control systems to monitor electrical machine performance indicators in real-time makes analytical models very attractive.

Various analytical approaches have been employed in the development of analytical models. The most commonly employed method is the Magnetic Equivalent Circuit (MEC) method. Similar to electrical equivalent resistive circuits, a reluctance path circuit in which the equivalent reluctance is determined is what defines the MEC method. Once the equivalent reluctance is determined, the air-gap flux density is then calculated. Some works by Bianchi *et al* [55] and Polinder *et al* [56] employed the Magnetic Equivalent Circuit (MEC) method. In the analysis of an Halbach permanent magnet-mover machine, similarly Wang *et al* [57] considered the MEC method. The MEC method despite its speed and accuracy and even consideration of saturation, is highly geometry dependent. Inaccuracy may result because of the changes of geometrical parameters and also the changes in the geometry itself. With increased complexity of the flux paths in a machine, MEC struggles to produce accurate results. Improvements have been proposed by various authors, noticeably by Xu and Chang [51] but geometry changes still affect the accuracy of the solutions. Another analytical approach is Conformal Mapping (CM) where analytic functions are considered conformal as long as they have nonzero derivatives. Conformal mapping dates as back as 1851 from Riemann mapping theorem, in which any complex structure can be mathematically transformed from one domain to another domain. Gysen *et al* [58] adopts the Swartz-Christoffel mapping (SC-CM) to determine the air-gap flux density. The method is also employed by Connel *et al* [59], Krop *et al* [60] and Zarko *et al* in [61] for magnetic field analysis of electrical machines. Depending on the type of electrical machine, this method has been mostly utilised with rotary machines and may be complex depending on the shapes to be mapped. Another analytical method is the subdomain method or the Resolution of Maxwell's equation incorporating separation

of variables. This method is based on finding the solution of the Laplace and Poisson equation utilising the Fourier expansion techniques. The subdomain method is fast and accurate and it is the method adopted in this work.

Several authors have approached their works by employing the subdomain method. Wang *et al* [62; 63] analysed single-sided axial, radial and Halbach array magnetised tubular linear machines where only the PM domains and air-gap domains were considered for finding the solution to the Laplace and Poisson equations. In the analysis done by Wang *et al*, the iron yokes are assumed as infinitely permeable and infinitely thick. Some alterations are made to the work of Wang *et al* by accounting for the magnetic saturation effects through the derivation of a correction factor for the Laplace and Poisson equations by Chen *et al* [42]. Chen *et al* incorporates the Magnetic equivalent circuit together with the subdomain method to determine the correction factor. Similar to Chen *et al*, Ouagued *et al* in [64] combines the magnetic equivalent circuit or reluctance networks and the Fourier expansion subdomain method to determine the cogging force for an iron-cored linear PM machine. Other works such as by Amara *et al* in [65; 66] considered slotting effects and the model considered solving the Maxwell's equations for the PM, slots and air-gap domains only. Iron yokes were assumed infinitely permeable and infinitely thick. Without any shift in the approach of the analytical development, Gysen *et al* [52] and Tiegna *et al* [67] adopts the same assumption of infinite permeability in the machine iron yokes in their work. Tiegna *et al* highlights the lack of yoke saturation monitoring by many works. A double PM layered machine similar to the linear machine for the work of this dissertation is proposed by Yan *et al* [68; 49] with PM arranged in a Halbach array, with short coil length. However, Yan *et al* too considers the iron yokes with infinite permeability and thickness. Wang and Howe [69] analysed a radially magnetised iron-cored tubular machine with a slotted stator but differs from the analytical model in this dissertation in that the yoke permeability was taken as infinitely permeable and infinitely thick.

1.5 Dissertation Problem Statement

This research is in the area of design optimisation of a linear oscillatory type of electrical machine for free-piston Stirling engine applications. Various types of linear oscillatory machines have been designed and optimised for free-piston Stirling engines in the past. Most of these machines have been iron-cored machines. The question is raised as to how an air-cored linear oscillatory machine would perform in free-piston Stirling engine applications. To accurately simulate the linear oscillating machine, an analytical model has to be established due to the advantage of shorter simulation time than finite element method (FEM) packages. The possibility of making the analytical model part of a real-

time control system also encourages the choice of employing it. In addition, the lack of dependence of analytical models on the mesh density, which FEM relies on, shortens the optimisation time making analytical models faster. The analytical model focuses on a tubular structure with surface mounted radially magnetised permanent magnets, air-cored and slot-less linear oscillatory machine.

Similar analytical models have been established by various authors, nevertheless, most of the authors considered the machine stator yokes to be infinitely permeable and infinitely thick. This approach deprives the designer of the means and ways to monitor saturation levels in the stator yokes. There is little attention by researchers in considering the yoke thickness to be finite together with a finite permeability for the stator yokes. Therefore, the analytical model development in this research considers the stator yokes to have a finite permeability and a finite thickness for easier monitoring of the flux saturation levels in the stator yokes. Yet another observation is that most analytical models in literature have assumed the length of the machine to be infinitely long. This assumption ensures that end effects such as fringing of fields are neglected and provides for easier harmonic expansion of Fourier series in the analysis. In this research, the approach focuses on how a model can be developed considering the actual finite length of the machine and also considering a finite permeability of the iron yokes. There is so far little to no literature and emphasis in employing this method to linear tubular oscillating machines. Kumar *et al* [70] demonstrated this approach on a brushless PM direct current (DC) motor. A similar approach is seen in works of Randewijk *et al* [71] for a radial flux air-cored PM machine. It must be observed that both these mentioned machines are rotating machines. Tsai *et al* [72] show some similarities to this work where as the consideration of the governing equations differs.

1.5.1 Research approach

The following research steps are identified as follows:

- Establishment of an analytical model to accurately simulate the air-cored longitudinal flux permanent magnet linear oscillating machine by firstly assuming **infinite length** of the machine while the iron yokes are given a finite permeability to enable monitoring of saturation in them. Since the total flux in the air-gap is the summation of the magnetic flux produced by the permanent magnets and the armature reaction field, the model has to predict the magnetic field distribution due to the permanent magnets and due to the armature reaction. The model is further expanded to determine the global quantities such as the flux linkage, the back electromotive force and the force,
- Establishment of a comparative analysis between the analytical model (assumed

infinitely long) established and a finite element package (FEM) MagNet by Infolytica Inc.,

- Establishment of an analytical model to accurately simulate a **finite length** linear oscillatory machine to be able to capture the actual machine magnetic field distribution behaviour,
- Establishment of a comparative analysis between the analytical model (actual finite length) established and a finite element package (FEM)-MagNet by Infolytica Inc..

These steps are addressed in the following chapters as highlighted in 1.6

1.5.2 Scope of this research

This research is focused on a single-phase longitudinal flux air-cored linear permanent magnet oscillatory machine with surface mounted radially magnetised permanent magnets. Linear oscillatory generators are single phase machines driven by prime movers. In this research, the linear oscillatory machine is considered for application with a free-piston Stirling engines as a prime mover for the purpose of power generation. The analytical model developed considers radial magnetisation only but can easily be modified to incorporate Halbach array permanent magnet set-up. Due to the complexity of the test set-up for the high frequency oscillatory machines, only a virtual prototype is considered for this research.

1.6 Dissertation Overview

The remaining sections of this dissertation are arranged in the following manner:

Chapter 2: An analytical model for the prediction of the magnetic field distribution behaviour created when the magnetic fields are generated by the permanent magnets as the only source of the magnetic field. The chapter demonstrates the process of the model development through the application of harmonic expansions of the Maxwell's equation and the separation of variables to obtain solutions for the Laplace and Poisson equations,

Chapter 3: The analytical model is further developed to consider the field distribution behaviour that is created by the coils of the machine mostly referred to as the armature reaction. In this chapter, the magnetisation influence of the permanent magnets is ignored and only the magnetic field generated by allowing a current to flow through the conductors of the coils is considered. A similar approach is taken as in the previous chapter,

Chapter 4: The analytical model is further enhanced to include the solutions of the global quantities of the linear oscillating generator. These include the flux linkage, the electromotive force and the force of the linear oscillating generator,

Chapter 5: The expansion of the analytical model to consider the finite length of the machine and the effects of fringing is investigated in this chapter. Various approaches to taking the finite length are considered and an analytical model is developed,

Chapter 6: The expansion of the analytical model in terms of the armature reaction is considered in this chapter for a finite length analytical model,

Chapter 7: Research conclusions as well as recommendations are placed in this chapter.

Appendix A: Magnetisation vector calculations for various PM arrangements,

Appendix B: Simplified analytical model for a finite length PM linear machine,

Appendix C: Introduction to Bessel functions.

Chapter 2

Prediction of the flux density with PMs as the only field source

2.1 Introduction

In this chapter the procedure of the development of an analytical model for the prediction of the flux densities with the PMs as the only field source (Usually referred to as open circuit analysis) is demonstrated. In this prediction, it is taken that the magnetic field source are only the permanent magnets and the coils are not present in the machine for this analysis. This step ensures that only the influence of the permanent magnets is captured and therefore the flux distribution can be predicted. The method adopted in this work is the Resolution of Maxwell's equations (Subdomain method) and separation of variables, a method widely employed for its speed, accuracy and for initial machine design optimisation stages. Employing the sub-domain method indicates that the linear oscillating machine is sub-divided into domains based on magnetic characteristics of each domain. The magnetic vector potential is then adopted to determine the solution of two dimensional partial differential equations. The introduction and explanation of a selected number of analytical methods have been explained in 1.4. The analytical analysis is for a tubular structured linear oscillatory generator with radially magnetised magnets and taking the permeability of the machine iron yokes to be finite so as to monitor saturation levels.

2.2 Open Circuit field distribution

Due to the tubular structure of the PM linear oscillating machine (LOM) [63], a cylindrical coordinate system is more appropriate to adopt for the determination of the solutions to the Laplace and the Poisson equations. This study develops a model for radially magnetised LOM(G), but with an addition of an axial component of the magnetisation vector, the model can easily accommodate Halbach-array configured linear machines. A half-cut representation of the LOG topology is displayed in Figure 2.1.

In order to analyse the PM field distribution of figure 2.1, the LOG machine is sub-divided into subdomains. Due to the axisymmetric topology of linear machine, a quarter section of the full model of the machine is sufficient for the formulation of the analytical

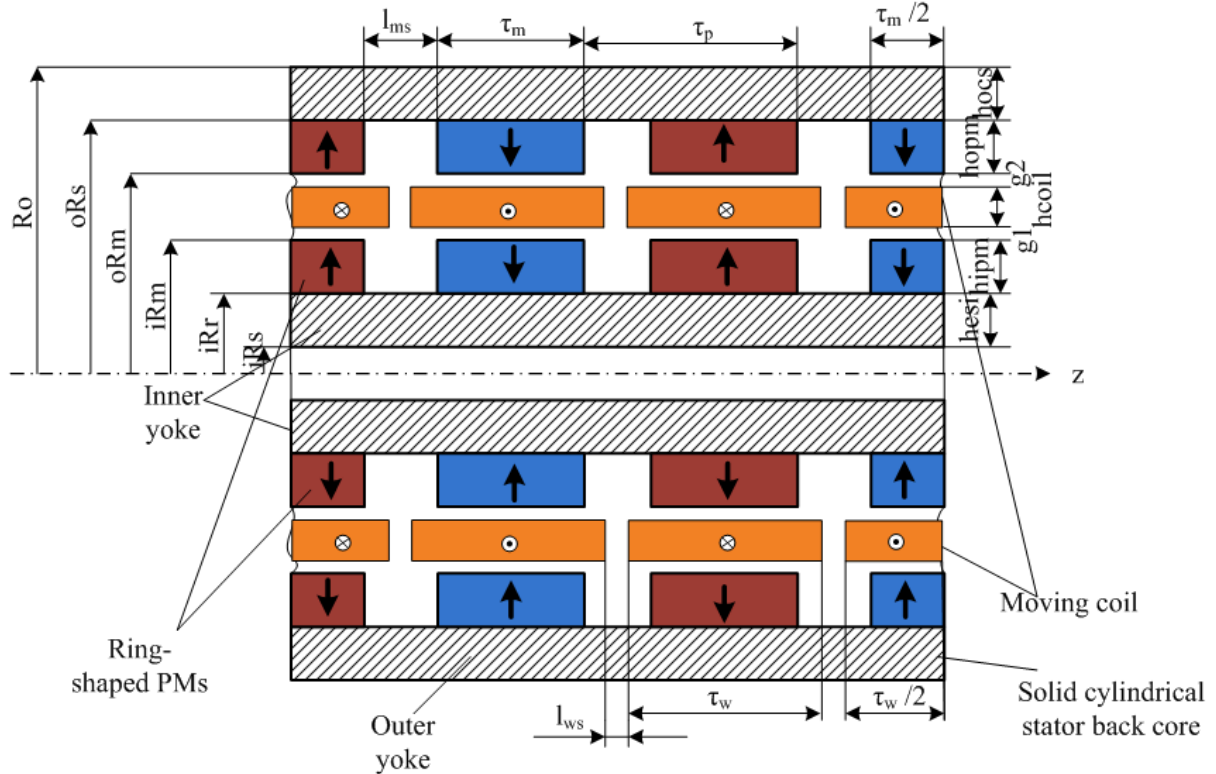


Figure 2.1: Half-cut cylindrical moving coil linear oscillatory generator

model. Besides that, the linear oscillatory machine in this research, qualifies to be analysed fully in 2-D. Each subdomain can then be represented by an expression to specify the magnetic vector potential at all points as explained by Wang *et al* [62]. The vector potentials for each separate domains are chosen such that Laplace and Poisson equations are satisfied. At the intersections of these subdomains are boundary conditions that govern the the behaviour of the magnetic field.

2.2.1 Assumptions for the O.C analysis

A number of assumptions are put in place for simplification of the formulation of the analytical model as follows:

1. The relative permeability of the permanent magnet is assumed unity ($\mu_r = 1$), which is a good assumption when using NdFeB magnets, as their relative recoil permeability is close to 1,
2. Axial length of the machine is considered infinite so that the field distribution is axisymmetric and periodic in the z-direction,
3. The effects of Eddy currents are not considered in both the permanent magnets and the coils,

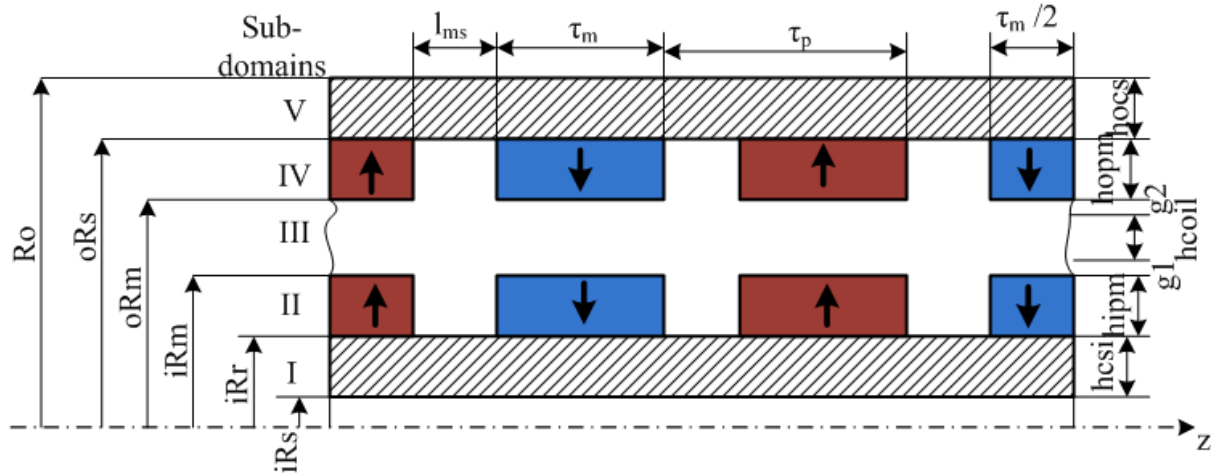


Figure 2.2: quarter section of the LOG illustrating the subdomains

4. The armature is slot-less and the stator cores are assumed to have a relative permeability of 1000 to allow for the main magnetic saturation in the machine cores to be monitored,
5. The iron yokes are assumed with a finite permeability and finite thickness so as to monitor the saturation of the yokes.

Figure 2.2 illustrates the subdomains as assigned for a quarter section of the linear oscillatory machine

2.2.2 Magnetic characteristics of materials

The magnetic field analysis focuses on two categories of subdomains: subdomains with no permanent magnets and subdomains with permanent magnets. The magnetic flux density \mathbf{B} for the subdomains I, III , and V is given by

$$\mathbf{B} = \mu_0 \mathbf{H}, \quad (2.1a)$$

whereas in the PM regions of the subdomains II and IV , \mathbf{B} is given by

$$\mathbf{B} = \mu_0 \mu_r \mathbf{H} + \mu_0 \mathbf{M}. \quad (2.1b)$$

where μ_0 , μ_r , \mathbf{H} and \mathbf{M} represents the permeability of free space, the recoil relative permeability, the magnetic field intensity and the magnetisation vector, respectively. From equation (2.1b) \mathbf{M} is the magnetisation vector in cylindrical coordinates and is calculated by

$$\mathbf{M} = M_r \mathbf{e}_r + M_z \mathbf{e}_z \quad (2.2)$$

where M_r and M_z express the components of \mathbf{M} in the r and z directions. Since the machine being analysed has only radially magnetised permanent magnets, the magnetisation

vector considers the vector in the radial direction as

$$\mathbf{M} = M_r \mathbf{e}_r . \quad (2.3)$$

The magnetisation vector is determined through the Fourier series expansion and is demonstrated later.

2.3 Governing equations for the O.C analysis

The electromagnetic field is generated by a continuous distribution of current and charge within a defined space and time and linked by current density \mathbf{J} and charge density ρ . This explains the link of the field to the Maxwell's equations

$$\nabla \times \mathbf{E} + \frac{\partial \mathbf{B}}{\partial t} = 0 , \quad (2.4a)$$

$$\nabla \times \mathbf{H} = \mathbf{J}_e + \frac{\partial \mathbf{D}}{\partial t} . \quad (2.4b)$$

Equations (2.4a) and (2.4b) are the last two of Maxwell's equations in point form for time varying fields. The two equations represent Faraday's law and Ampere's law in point form, respectively. In the equation (2.4); \mathbf{E} is the electric field intensity, \mathbf{B} is the magnetic flux density, \mathbf{H} is the magnetic field intensity and \mathbf{D} is the electric flux density. For non-time-varying fields, Maxwell's equations are presented as

$$\nabla \cdot \mathbf{D} = \rho_v , \quad (2.5a)$$

$$\nabla \cdot \mathbf{B} = 0 . \quad (2.5b)$$

Equations (2.5a) and (2.5b) are the first two equations of Maxwell's four equations. The equations can be applicable to steady magnetic fields as well as static fields. The equation (2.5) are the order of Gauss's laws on the conservation of electric flux (2.5a) and magnetic flux (2.5b). In the equation (2.5), ρ_v is the free charge density [73; 74]. The four Maxwell's equations are the governing equations for the formulation of the analytical model as is demonstrated in the further sections of this chapter.

2.3.1 Adoption of the magnetic vector potential

solving for the magnetic fields can be conducted through the employment of Maxwell's equation with difficulty. Therefore, the magnetic vector magnetic potential \mathbf{A} or scalar potential ψ provides a more approachable method to obtain the magnetic fields. The magnetic vector potential \mathbf{A} can be employed in both regions where the current density \mathbf{J} may be zero and where the current density is not equal to zero [75]. Hence the adoption of

the magnetic vector potential to determine the fields. The formulation of the equations for the magnetic vector potential \mathbf{A} is outlined below. Considering the divergence theorem

$$\nabla \cdot \mathbf{B} = 0 , \quad (2.6)$$

and also considering that the divergence of the curl of any vector field is zero,

$$\mathbf{B} = \nabla \times \mathbf{A} , \quad (2.7)$$

where \mathbf{A} is the magnetic vector potential. The relationship between the magnetic flux density and the magnetic vector potential as demonstrated in equation (2.7) is very critical in determining the fields. It is for this reason that the focus is to initially solve for the magnetic vector potential and then employ equation (2.7) to obtain the magnetic flux density. The vector fields \mathbf{B} and \mathbf{H} are related through the permeability μ (in henry's/metre) as

$$\mathbf{B} = \mu \mathbf{H} \quad (2.8)$$

and also knowing that,

$$\nabla \times \mathbf{H} = \mathbf{J} . \quad (2.9)$$

Taking \mathbf{H} from equation (2.8) inserting into equation (2.9) yields

$$\nabla \times \mathbf{B} = \mu \mathbf{J} . \quad (2.10)$$

Taking equation (2.7) into equation (2.10) obtains

$$\nabla \times (\nabla \times \mathbf{A}) = \mu \mathbf{J} . \quad (2.11)$$

Equation (2.11), is the suitable equation for solving an axisymmetric topology which is under study in this dissertation. Equation (2.11) is a what is called a Poisson equation. When the current density is zero ($\mathbf{J} = 0$), then the equation becomes a Laplace equation

$$\nabla \times (\nabla \times \mathbf{A}) = 0 . \quad (2.12)$$

Equation (2.12) can be applied to subdomains that do not have a field generating source. Examples of such subdomains would be the iron yokes and the air-gaps. For the current analytical model represented on Figure 2.2, the Laplace equation would define subdomains I, III, V . For the PM regions II, IV , a combination of equation (2.1) and Maxwell's equation yields

$$\nabla \times \mathbf{B} = \mu_0 \mu_r \mathbf{J} + \mu_0 \nabla \times \mathbf{M} . \quad (2.13)$$

To complete the derivation of the equation for the PM regions, equation (2.7) is inserted into the left side of equation (2.13) to produce

$$\nabla \times (\nabla \times \mathbf{A}) = -\mu_0 \nabla \times \mathbf{M} . \quad (2.14)$$

Since the machine being analysed is an axisymmetric cylindrical linear oscillatory machine, it is appropriate to adopt the cylindrical coordinate system to express the Laplace equation (2.12) and Poisson equation (2.14). The magnetic vector potential has only the ϕ component (A_ϕ) because of the axisymmetrical nature of the tubular linear machine under study. Therefore, partial differential equations of the Laplace and Poisson equations derived are expressed as

$$\frac{\partial^2 A_\phi}{\partial z^2} + \frac{\partial^2 A_\phi}{\partial r^2} + \frac{1}{r} \frac{\partial A_\phi}{\partial r} - \frac{1}{r^2} A_\phi = 0 \quad (2.15)$$

and

$$\frac{\partial^2 A_\phi}{\partial z^2} + \frac{\partial^2 A_\phi}{\partial r^2} + \frac{1}{r} \frac{\partial A_\phi}{\partial r} - \frac{1}{r^2} A_\phi = -\mu_0 \nabla \times \mathbf{M} \quad (2.16)$$

The expressions of (2.15) and (2.16) can further be presented according to the subdomains (I, II, III, IV, V), as shown in Figure 2.2, that they represent which is defined as:

The subdomains I, III and V , which are the lower yoke, the air-gap and the upper yoke respectively, are represented by the Laplace equations

$$\frac{\partial^2 A_{\phi I}}{\partial z^2} + \frac{\partial^2 A_{\phi I}}{\partial r^2} + \frac{1}{r} \frac{\partial A_{\phi I}}{\partial r} - \frac{1}{r^2} A_{\phi I} = 0 , \quad (2.17a)$$

$$\frac{\partial^2 A_{\phi III}}{\partial z^2} + \frac{\partial^2 A_{\phi III}}{\partial r^2} + \frac{1}{r} \frac{\partial A_{\phi III}}{\partial r} - \frac{1}{r^2} A_{\phi III} = 0 , \quad (2.17b)$$

$$\frac{\partial^2 A_{\phi V}}{\partial z^2} + \frac{\partial^2 A_{\phi V}}{\partial r^2} + \frac{1}{r} \frac{\partial A_{\phi V}}{\partial r} - \frac{1}{r^2} A_{\phi V} = 0 . \quad (2.17c)$$

And the subdomains II, IV consisting of lower PMs and upper PMs are expressed by the Poisson equations

$$\frac{\partial^2 A_{\phi II}}{\partial z^2} + \frac{\partial^2 A_{\phi II}}{\partial r^2} + \frac{1}{r} \frac{\partial A_{\phi II}}{\partial r} - \frac{1}{r^2} A_{\phi II} = -\mu_0 \nabla \times \mathbf{M} , \quad (2.18a)$$

$$\frac{\partial^2 A_{\phi IV}}{\partial z^2} + \frac{\partial^2 A_{\phi IV}}{\partial r^2} + \frac{1}{r} \frac{\partial A_{\phi IV}}{\partial r} - \frac{1}{r^2} A_{\phi IV} = -\mu_0 \nabla \times \mathbf{M} . \quad (2.18b)$$

As mentioned earlier, the keen interest is to solve for the magnetic vector potential A which can be utilised to solve for the magnetic flux density B through $\mathbf{B} = \nabla \times \mathbf{A}$. General solution for equations (2.17) and (2.18) are solved in the following section.

2.4 General Solutions to Magnetic Field - O.C analysis

2.4.1 General Solution to the Laplace equation for O.C analysis

Since the Laplace and Poisson equations are two dimensional, it is simpler to separate the two variables r and z and directly find solutions. Separate solutions obtained for each variable can be recombined by employing the superposition principal. To achieve this, separation of variables method [74, Chapter 4] is applied to the equations (2.17a) - (2.17c). The Laplace equation is rewritten in the form of (2.19) to demonstrate the separation procedure,

$$\frac{\partial^2 A_{\phi^i}}{\partial z^2} + \frac{\partial^2 A_{\phi^i}}{\partial r^2} + \frac{1}{r} \frac{\partial A_{\phi^i}}{\partial r} - \frac{1}{r^2} A_{\phi^i} = 0 \quad (2.19)$$

where i represents subdomains I, III , and V , i.e. the lower stator yoke, the air-gap and the upper stator yoke. The magnetic vector potential A_{ϕ} is assumed as

$$A_{\phi}(r, z) = R(r) Z(z) , \quad (2.20)$$

where A_{ϕ} is a function of r and z . Substituting equation (2.20) into the partial differential equation (2.19) and the partial derivative results into an ordinary differential equation

$$R(r) \frac{d^2 Z(z)}{dz^2} + \frac{Z(z)}{1} \frac{d^2 R(r)}{dr^2} + \frac{Z(z)}{r} \frac{dR(r)}{dr} - \frac{R(r)Z(z)}{r^2} = 0 . \quad (2.21)$$

Dividing equation(2.21) by $R(r) Z(z)$ yields

$$\frac{1}{Z(z)} \frac{d^2 Z(z)}{dz^2} + \frac{1}{R(r)} \frac{d^2 R(r)}{dr^2} + \frac{1}{R(r)} \frac{dR(r)}{dr} - \frac{1}{r^2} = 0 . \quad (2.22)$$

Equation (2.22) now has the z and r variables independent of each other. This means the variables have been separated accordingly. For the full separation of the variables, they must be equal to a separation constant as follows:

$$\frac{1}{Z(z)} \frac{d^2 Z(z)}{dz^2} = - \left[\frac{1}{R(r)} \frac{d^2 R(r)}{dr^2} + \frac{1}{R(r)} \frac{dR(r)}{dr} - \frac{1}{r^2} \right] = c_k . \quad (2.23)$$

c_k is the separation constant. Since the z and r are independent of each other, a solution can be found for each variable separately. Two independent linear differential equations are derived for each variable and later solved. The z variable therefore equates to c_k as

$$\frac{1}{Z(z)} \frac{d^2 Z(z)}{dz^2} = c_k , \quad (2.24a)$$

which can be written as

$$\frac{d^2 Z(z)}{dz^2} - c_k Z(z) = 0 . \quad (2.24b)$$

Equation (2.24b) is a second order linear differential equation of the form

$$Z'' - c_k Z = 0 . \quad (2.25)$$

The r variable is handled in the same way as the z variable by equating to c_k as follows:

$$- \left[\frac{1}{R(r)} \frac{d^2 R(r)}{dr^2} + \frac{1}{R(r)} \frac{dR(r)}{dr} - \frac{1}{r^2} \right] = c_k \quad (2.26)$$

and can be written as

$$\frac{1}{R(r)} \frac{d^2 R(r)}{dr^2} + \frac{1}{R(r)} \frac{dR(r)}{dr} - \frac{1}{r^2} + c_k = 0 . \quad (2.27)$$

Multiplying equation (2.27) by r^2 and also by $R(r)$ results into

$$r^2 \frac{d^2 R(r)}{dr^2} + r \frac{dR(r)}{dr} + (r^2 c_k - 1) R(r) = 0 , \quad (2.28)$$

which is a second linear differential equation represented as

$$r^2 R'' + r R' + (r^2 c_k - 1) R = 0 . \quad (2.29)$$

So far, the Laplace equation (2.19) has been separated into equation (2.25) and (2.29). However, the solutions vary depending on the case value of c_k which leads three possible solutions may be obtained. The three case values of c_k are: $c_k = 0$, $c_k > 0$, and $c_k < 0$.

2.4.1.1 Solution due to Case 1

In case 1. the solution for $c_k = 0$ is as follows: When c_k is zero, equation (2.25) becomes

$$Z(z)'' = 0 \quad (2.30)$$

The general solution to equation (2.30) after direct integration is

$$Z(z) = D_1 + D_2 z \quad (2.31)$$

while equation (2.29) becomes

$$r^2 R'' + r R' - R = 0 , \quad (2.32)$$

which is a Cauchy-Euler equation and is solved by assuming that the solution has the form

$$R(r) = r^s . \quad (2.33)$$

The likely values of m are solved by inserting equation (2.33) into equation (2.32) to produce the solution

$$\begin{aligned} s(s-1)r^s + sr^s - r^s &= 0 \\ r^s(s^2 - s + s - 1) &= 0 \\ s &= \pm 1 \end{aligned} \quad (2.34)$$

Therefore, the general solution for $R(r)$ is

$$R(r) = C_1 r + C_2 r^{-1} . \quad (2.35)$$

Inserting both equations (2.31) and (2.35) into equation (2.20) gives a particular solution

$$A_\phi(r, z) = R(r)Z(z) = (C_1 r + C_2 r^{-1})(D_1 + D_2 z) , \quad (2.36)$$

which can also be written as a general solution

$$A_\phi(r, z) = \sum_{n=1,2,\dots}^{\infty} [E_n r + F_n r^{-1} + G_n r z + H_n r^{-1} z] . \quad (2.37)$$

Since the required solution for $A_\phi(r, z)$ has to be periodic in the z direction, the above equation (2.37) does not qualify as the solution to the Laplace equation.

2.4.1.2 Solution due to case 2

In case 2. the solution for $c_k > 0$ is presented below. Taking $c_k = k^2$ and that $k^2 > 0$, equation (2.25)) becomes

$$Z'' - k^2 Z = 0 . \quad (2.38)$$

The general solution to equation (2.38)) in exponential form and in hyperbolic sine and cosine is presented as

$$Z(z) = d_3 e^{kz} + d_4 e^{-kz} \quad (2.39a)$$

$$Z(z) = D_3 \cosh(kz) + D_4 \sinh(kz) \quad (2.39b)$$

Turning the attention to equation (2.29) which in this case becomes

$$r^2 R'' + r R' + (r^2 k^2 - 1) R = 0 . \quad (2.40)$$

Comparing equation (2.40) to the equation (2.41) below

$$x^2 y'' + x y' + (x^2 - n^2) y = 0 , \quad (2.41)$$

it is observed that the two equations are the similar except that in equation (2.41) $n = 1$. Thus equation (2.40) has a particular solution of the form

$$R(r) = C_3 J_0(kr) + C_4 Y_0(kr) \quad (2.42)$$

which is a Bessel's equation of the first and second kind of order zero. Inserting equations (2.39) and (2.42) into equation (2.20) gives a particular solution of

$$A_\phi(r, z) = [C_3 J_0(kr) + C_4 Y_0(kr)][D_3 \cosh(kz) + D_4 \sinh(kz)] \quad (2.43)$$

which can be written in a general format as

$$A_\phi(r, z) = \sum_{n=1,2,\dots}^{\infty} ([E_n J_0(kr) + F_n Y_0(kr)] \cosh(kz) + [G_n J_0(kr) + H_n Y_0(kr)] \sinh(kz)) . \quad (2.44)$$

Again in this particular case, $A_\phi(r, z)$ is not periodic in z and thus does not qualify to be the solution to the Laplace equation.

2.4.1.3 Solution due to case 3

In case 3. the solution for $c_k < 0$ is presented. Taking $c_k = -k^2$ and that $k^2 < 0$, equation (2.25) becomes

$$Z'' + k^2 Z = 0 \quad (2.45)$$

Equation (2.45) has a general solution which is presented both in exponential form and in the hyperbolic sine and cosine as

$$Z(z) = d_5 e^{jkz} + d_6 e^{-jkz} \quad (2.46a)$$

$$Z(z) = D_5 \cos(kz) + D_6 \sin(kz) \quad (2.46b)$$

Turning the attention to equation (2.29) which in this case becomes

$$r^2 R'' + rR' - (r^2 k^2 + 1)R = 0 , \quad (2.47)$$

In standard form, (2.48) appears as

$$x^2 y'' + xy'' - (x^2 + n^2)y = 0 \quad (2.48)$$

again comparing equation (2.48) to equation (2.49) it is observed that the two equations are the similar except that in equation (2.48) $n = 1$. Therefore the general solution to equation (2.48) is

$$R(r) = C_5 I_1(kr) + C_6 K_1(kr) \quad (2.49)$$

which is a Modified Bessel's equation of the first and second kind of order 1 with a real argument kr . Inserting equation (2.48) and (2.50) into equation (2.20) gives

$$A_\phi(r, z) = [C_5 I_1(mr) + C_6 K_1(mr)][D_5 \cos(mz) + D_6 \sin(mz)] \quad (2.50)$$

which can be presented in general format as

$$A_\phi(r, z) = \sum_{n=1,2,\dots}^{\infty} ([E_n I_1(mr) + F_n K_1(mr)] \cos(mz) + [G_n I_1(mr) + H_n K_1(mr)] \sin(mz)) \quad (2.51)$$

where m in this case is a real number and defined by $k = jm$. Equation (2.52) is periodic in the z direction and could be the solution to the Laplace equation.

Due to the fact that the axial component of flux density is very minimal on $z = 0$, $B_z|_{z=0}$. Inserting equation (2.52) into equation (2.7) produces $\nabla \times \mathbf{A}_\phi = \frac{-1}{r} \frac{\partial r A_\phi}{\partial z} \mathbf{e}_r + \frac{1}{r} \frac{\partial r A_\phi}{\partial r} \mathbf{e}_z$ which is the same as $B = -B_r \mathbf{e}_r + B_z \mathbf{e}_z$. With $B_z|_{z=0} = 0$ and also considering that I_1 and K_1 are independent of each other, which implies that one cannot be expressed in terms of the other, then E_n and F_n are then taken as

$$E_n = 0$$

and

$$F_n = 0$$

Therefore, the solution to the Laplace equation becomes

$$A_\phi(r, z) = [a_n I_1(mr) + b_n K_1(mr)] \sin(mz) \quad (2.52)$$

where $a_n = G_n$ and $b_n = H_n$ are constants that are to be determined later. To form a complete series solution, superposition principal is applied to obtain

$$A_\phi(r, z) = \sum_{n=1,2,\dots}^{\infty} [A_n I_1(mr) + B_n K_1(mr)] \sin(mz) . \quad (2.53)$$

2.4.2 General solution to the Poisson equation for the O.C analysis

For the regions of the PMs *II* and *IV*, the Poisson equation in cylindrical coordinates is

$$\frac{\partial^2 A_\phi}{\partial z^2} + \frac{\partial^2 A_\phi}{\partial r^2} + \frac{1}{r} \frac{\partial A_\phi}{\partial r} - \frac{1}{r^2} A_\phi = -\mu_0 \nabla \times \mathbf{M} . \quad (2.54)$$

From the left side of the equal sign in equation (2.54), it is observed that the solution derived in 2.4.1 is the Poisson equation's corresponding homogeneous equation. The equation (2.53) is rewritten below for the sake of convenience

$$A_\phi(r, z) = \sum_{n=1,\dots}^{\infty} [A_n I_1(mr) + B_n K_1(mr)] \sin(mz) .$$

The solution to the Poisson equation (2.54) cannot be achieved without the harmonic expansion of the magnetisation vector \mathbf{M} which is on the right side of the equal sign. With the magnetisation vector solved, then separation of variable technique is again adopted to obtain the solutions. Separate variables are later recombined for the general solution to the Poisson equation.

2.4.2.1 Formulation of the Magnetisation vector for the O.C analysis

The magnetisation vector \mathbf{M} assumes only the radial component as the LOG has radially magnetised magnets. Figure 2.3 displays the method employed in formulating the magnetisation vector.

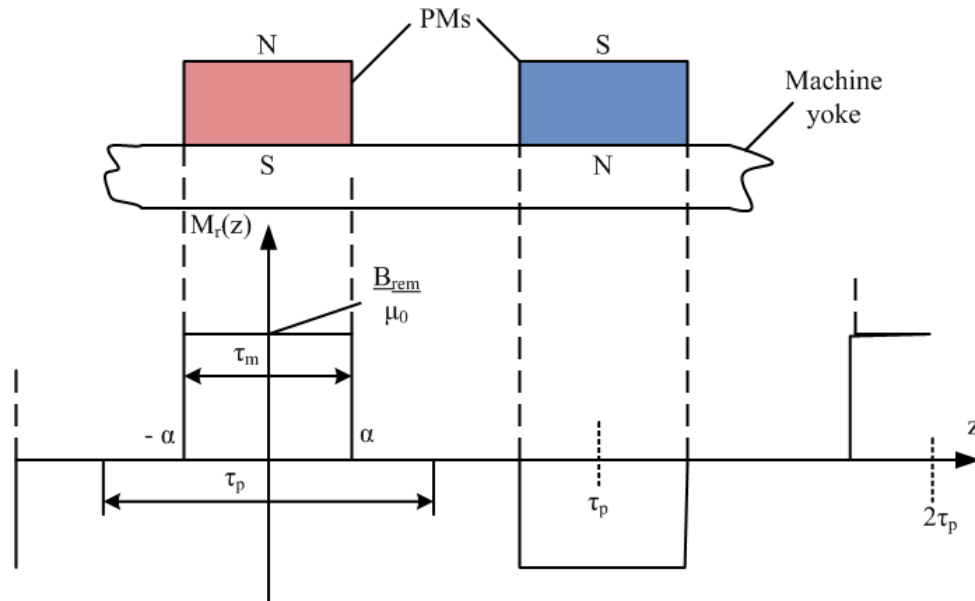


Figure 2.3: Radial component of magnetic flux along the axial coordinate

Since the current topology only has radial magnets with interpolar spaces, \mathbf{M} has only the component of M_r in the r direction. Therefore,

$$\mathbf{M} = M_r \mathbf{e}_r \quad (2.55)$$

where M_r can be expressed as a Fourier series

$$M_r(z) = \frac{a_0}{2} + \sum_{n=1, \dots}^{\infty} a_n \cos(\omega_n z) . \quad (2.56)$$

With a period of $2\tau_p$, $\omega_n = \frac{n\pi}{\tau_p}$. From Figure 2.3, it is clear that

$$a_n = \frac{1}{\tau_p} \int_{-\tau_p}^{\tau_p} f(z) \cos(\omega_n z) dz \quad (2.57a)$$

which is equal to

$$a_n = \frac{2}{\tau_p} \int_0^{\tau_p} f(z) \cos(\omega_n z) dz \quad (2.57b)$$

Splitting the integral leads to

$$a_n = \frac{2}{\tau_p} \left[\frac{B_{rem}}{\mu_0} \int_0^{\frac{\tau_m}{2}} \cos(\omega_n z) dz - \frac{B_{rem}}{\mu_0} \int_{\frac{2\tau_p - \tau_m}{2}}^{\tau_p} \cos(\omega_n z) dz \right] \quad (2.57c)$$

which results into

$$a_n = \frac{2B_{rem}}{\tau_p \mu_0} \left\{ \frac{\sin(\omega_n z)}{\omega_n} \Big|_0^{\frac{\tau_m}{2}} - \frac{\sin(\omega_n z)}{\omega_n} \Big|_{\frac{2\tau_p - \tau_m}{2}}^{\tau_p} \right\} \quad (2.57d)$$

$$a_n = \frac{2B_{rem}}{\tau_p \mu_0 \omega_n} \left\{ \sin\left(\omega_n \frac{\tau_m}{2}\right) + \sin\left(\omega_n \left(\frac{2\tau_p - \tau_m}{2}\right)\right) \right\} \quad (2.57e)$$

$$a_n = \frac{2B_{rem}}{n\pi \mu_0} \left\{ \sin\left(\frac{\omega_n \tau_m}{2}\right) + \sin\left(n\pi - \frac{\omega_n \tau_p}{2}\right) \right\}. \quad (2.57f)$$

Applying the trigonometric identity $\{\sin(a - b) = \sin a \cos b - \sin b \cos a\}$ to equation (2.57f) produces

$$a_n = \frac{2B_{rem}}{n\pi \mu_0} (1 - (-1)^n) \sin\left(\frac{n\pi \tau_m}{2 \tau_p}\right) \quad (2.58)$$

where $(-1)^n = \cos(n\pi)$. It is observed that only odd harmonic numbers will be summed up and therefore, a_n is taken as a_{2n-1} which equals

$$a_{2n-1} = \frac{4B_{rem}}{(2n-1)\pi \mu_0} \sin\left(\frac{(2n-1)\pi \tau_m}{2 \tau_p}\right). \quad (2.59)$$

The expression for $M_r(z)$ is therefore

$$\begin{aligned} M_r(z) &= \frac{a_0}{2} + \sum_{n=1}^{\infty} a_{2n-1} \cos(\omega_{2n-1} z) \\ &= \frac{a_0}{2} + \frac{4B_{rem}}{\pi \mu_0} \sum_{n=1}^{\infty} \frac{1}{(2n-1)} \sin\left(\frac{(2n-1)\pi \tau_m}{2 \tau_p}\right) \cos(m_n z), \end{aligned} \quad (2.60)$$

where

$$m_n = (2n-1) \frac{\pi}{\tau_p}. \quad (2.61)$$

2.4.2.2 Inserting the magnetisation vector solution back into the Poisson equation

It must be noted that \mathbf{M} is a member of the Poisson equation's $(-\mu_0 \nabla \times \mathbf{M})$, which must be solved beginning with the curl of \mathbf{M} . The curl of \mathbf{M} is obtained as

$$\nabla \times \mathbf{M} = \frac{1}{r} \begin{bmatrix} \mathbf{e}_r & r\mathbf{e}_\phi & \mathbf{e}_z \\ \frac{\partial}{\partial r} & \frac{\partial}{\partial \phi} & \frac{\partial}{\partial z} \\ M_r & 0 & 0 \end{bmatrix} = \frac{\partial M_r}{\partial z} \mathbf{e}_\phi - \frac{1}{r} \frac{\partial M_r}{\partial \phi} \mathbf{e}_z \quad (2.62)$$

since $\partial \phi = 0$

$$\nabla \times \mathbf{M} = \frac{\partial M_r}{\partial z} \mathbf{e}_\phi \quad (2.63)$$

which implies that the whole right side of the equal-sign in Poisson equation (2.54), after differentiating and multiplying by μ_0 equals

$$\nabla \times (\nabla \times A_\phi) = \frac{4B_{rem}}{\tau_p} \sum_{n=1}^{\infty} \sin\left(\frac{(2n-1)\pi \tau_m}{2 \tau_p}\right) \sin(m_n z) \quad (2.64)$$

The general solution to Poisson equation becomes

$$A_\phi(r, z) = \sum_{n=1, \dots}^{\infty} [a_n I_1(m_n r) + b_n K_1(m_n r)] \sin(m_n z) + S(r, z) \quad (2.65)$$

where

$$S(r, z) = R(r)Z(z) \quad (2.66)$$

The Poisson equation in cylindrical coordinates becomes

$$\frac{\partial^2 A_\phi}{\partial z^2} + \frac{\partial^2 A_\phi}{\partial r^2} + \frac{1}{r} \frac{\partial A_\phi}{\partial r} - \frac{1}{r^2} A_\phi = P_n \sin(m_n z), \quad (2.67)$$

where

$$P_n = \frac{4B_{rem}}{\tau_p} \sin\left[(2n-1) \frac{\pi \tau_m}{2 \tau_p}\right]. \quad (2.68)$$

Separation of variables is employed on (2.67) by replacing A_ϕ with $R(r)Z(z)$ and thereafter dividing each side by $R(r)Z(z)$

$$\frac{1}{Z(z)} \frac{d^2 Z(z)}{dz^2} + \frac{1}{R(r)} \frac{d^2 R(r)}{dr^2} + \frac{1}{R(r)r} \frac{dR(r)}{dr} - \frac{1}{r^2} = \frac{1}{R(r)Z(z)} P_n \sin(m_n z). \quad (2.69)$$

Letting

$$\frac{1}{Z(z)} \frac{d^2 Z(z)}{dz^2} = m_n^2 \quad (2.70)$$

$Z(z)$ is then equal to

$$Z(z) = \sin(m_n z) \quad (2.71)$$

The r variable is determined through the equation

$$\frac{1}{R(r)} \frac{d^2 R(r)}{dr^2} + \frac{1}{R(r)r} \frac{dR(r)}{dr} - \frac{1}{r^2} + m_n^2 = \frac{P_n}{R(r)}. \quad (2.72)$$

Both sides are multiplied by r^2 and $R(r)$ to get

$$r^2 \frac{d^2 R(r)}{dr^2} + r \frac{dR(r)}{dr} - R(r)(m_n^2 r^2 + 1) = r^2 P_n, \quad (2.73)$$

which can be expressed as

$$r^2 R'' + rR' - (m_n^2 r^2 + 1)R = r^2 P_n. \quad (2.74)$$

Equation (2.74) can be expressed as

$$x^2y'' + xy' - (x^2 + 1)y = \frac{2x^2}{\sqrt{\pi}\Gamma(\frac{3}{2})} = \frac{2x^2}{\pi}, \quad (2.75)$$

where Γ is the Gamma function. Assuming that

$$x^2y'' + xy' - (a^2x^2 + 1)y = bx^2, \quad (2.76)$$

and letting $y(x) = AL_1(Bx)$ and $B^2 = a^2$, obtains

$$x^2y'' + xy' - (B^2x^2 + 1)y = \frac{2AB^2x^2}{\pi} \quad (2.77)$$

where $\frac{2AB^2}{\pi} = b$, replacing B^2 with a^2 , gives $A = \frac{b\pi}{2a^2}$ and therefore:

$$y(x) = \frac{\pi b}{2a^2} L_1(ax). \quad (2.78)$$

In equation (2.78), $b = P_n$, $a = m_n$ and $x = r$ therefore the result for $R(r)$ is

$$R(r) = \frac{\pi P_n}{2m_n^2} L_1(m_n r), \quad (2.79)$$

The expression for $S(r, z)$ is obtained from

$$S(r, z) = R(r)Z(z) = \frac{\pi L_1(m_n r)}{2m_n^2} P_n \sin(m_n z) \quad (2.80)$$

where $L_1(x)$ is the solution to the inhomogeneous Bessel's equation and it is called a modified Struve function or the partial Struve function [76, Part 1, Chap. 2, Sec. 28], [77, Chap. 12, Sec. 2]. The Poisson equation is finally expressed as a summation of its homogeneous solution and the particular solution (2.80) to obtain

$$A_\phi(r, z) = [a_n I_1(m_n r) + b_n K_1(m_n r)] \sin(m_n z) + \frac{\pi L_1(m_n r)}{2m_n^2} P_n \sin(m_n z) \quad (2.81)$$

The general solutions to Poisson equations is therefore

$$A_\phi(r, z) = \sum_{n=1, \dots}^{\infty} \left[a_n I_1(m_n r) + b_n K_1(m_n r) + \frac{\pi L_1(m_n r)}{2m_n^2} P_n \right] \sin(m_n z) \quad (2.82)$$

2.4.3 General solutions to the magnetic vector potential for all subdomains for O.C analysis

The magnetic vector potential \mathbf{A} for each subdomain I, II, III, IV and V is therefore expressed as

$$A_{\phi I}(r, z) = \sum_{n=1, \dots}^{\infty} [a_{nI} I_1(m_n r) + b_{nI} K_1(m_n r)] \sin(m_n z), \quad (2.83)$$

$$A_{\phi II}(r, z) = \sum_{n=1, \dots}^{\infty} \left[a_{nII} I_1(m_n r) + b_{nII} K_1(m_n r) + \frac{\pi L_1(m_n r)}{2m_n^2} P_n \right] \sin(m_n z), \quad (2.84)$$

$$A_{\phi III}(r, z) = \sum_{n=1, \dots}^{\infty} [a_{nIII} I_1(m_n r) + b_{nIII} K_1(m_n r)] \sin(m_n z), \quad (2.85)$$

$$A_{\phi IV}(r, z) = \sum_{n=1, \dots}^{\infty} \left[a_{nIV} I_1(m_n r) + b_{nIV} K_1(m_n r) + \frac{\pi L_1(m_n r)}{2m_n^2} P_n \right] \sin(m_n z), \quad (2.86)$$

$$A_{\phi V}(r, z) = \sum_{n=1, \dots}^{\infty} [a_{nV} I_1(m_n r) + b_{nV} K_1(m_n r)] \sin(m_n z). \quad (2.87)$$

2.5 General solution to the PM magnetic flux density

The curl of the magnetic vector potential previously determined in (2.83) - (2.87) results into the determination of the magnetic flux density \mathbf{B} . Similar to the determination of the curl of the magnetisation vector (2.62), the curl of the magnetic vector potential is determined in a similar pattern. The general solutions of the magnetic flux densities are obtained from employing equation (2.7) on equation (2.83) - (2.87) as follows:

$$\mathbf{B} = \nabla \times \mathbf{A} = \frac{1}{r} \begin{bmatrix} \mathbf{e}_r & r\mathbf{e}_\phi & \mathbf{e}_z \\ \frac{\partial}{\partial r} & \frac{\partial}{\partial \phi} & \frac{\partial}{\partial z} \\ A_r & rA_\phi & A_z \end{bmatrix} = -\frac{1}{r} \frac{\partial r A_\phi}{\partial z} \mathbf{e}_r + \frac{1}{r} \frac{\partial r A_\phi}{\partial r} \mathbf{e}_z \quad (2.88)$$

The equation above (2.88) is a result obtained by considering that A_ϕ is only a component of ϕ which implies that $A_r = 0$ and $A_z = 0$. Therefore,

$$\mathbf{B} = B_r \mathbf{e}_r + B_z \mathbf{e}_z = -\frac{1}{r} \frac{\partial r A_\phi}{\partial z} \mathbf{e}_r + \frac{1}{r} \frac{\partial r A_\phi}{\partial r} \mathbf{e}_z \quad (2.89)$$

The radial component of \mathbf{B} is equal to

$$B_r = -\frac{1}{r} \frac{\partial r A_\phi}{\partial z} = -\frac{\partial A_\phi}{\partial z} \quad (2.90)$$

and the axial component of \mathbf{B} , B_z is evaluated by

$$B_z = \frac{1}{r} \frac{\partial r A_\phi}{\partial r} \quad (2.91)$$

The evaluation of the magnetic flux densities takes into consideration some properties of modified Bessel equations [78],

$$\frac{\partial(z^v I_v(z))}{\partial z} = z^v I_{v-1}(z) , \quad \left(\frac{1}{z} \frac{\partial}{\partial z}\right)^k (z^v \ell_v(z)) = z^{v-k} \ell_{v-k}(z) \quad (2.92)$$

where ℓ denotes I_v or K_v .

2.5.1 Radial magnetic flux density general solutions for all subdomains in O.C analysis

The expression for the radial and axial components of the magnetic flux density in accordance with subdomains they represent after differentiation of the equations (2.90) and (2.91) are evaluated by

$$B_{rI}(r, z) = \sum_{n=1, \dots}^{\infty} -m_n [a_{nI} I_1(m_n r) + b_{nI} K_1(m_n r)] \cos(m_n z) , \quad (2.93)$$

$$B_{rII}(r, z) = \sum_{n=1, \dots}^{\infty} -m_n \left[a_{nII} I_1(m_n r) + b_{nII} K_1(m_n r) + \frac{\pi L_1(m_n r)}{2m_n^2} P_n \right] \cos(m_n z) , \quad (2.94)$$

$$B_{rIII}(r, z) = \sum_{n=1, \dots}^{\infty} -m_n [a_{nIII} I_1(m_n r) + b_{nIII} K_1(m_n r)] \cos(m_n z) , \quad (2.95)$$

$$B_{rIV}(r, z) = \sum_{n=1, \dots}^{\infty} -m_n \left[a_{nIV} I_1(m_n r) + b_{nIV} K_1(m_n r) + \frac{\pi L_1(m_n r)}{2m_n^2} P_n \right] \cos(m_n z) , \quad (2.96)$$

$$B_{rV}(r, z) = \sum_{n=1, \dots}^{\infty} -m_n [a_{nV} I_1(m_n r) + b_{nV} K_1(m_n r)] \cos(m_n z) . \quad (2.97)$$

2.5.2 Axial magnetic flux density general solutions for all subdomains

Whereas the axial component of the magnetic flux density are evaluated per subdomain resulting from the implementation of equation (2.91) as,

$$B_{zI}(r, z) = \sum_{n=1, \dots}^{\infty} m_n [a_{nI} I_0(m_n r) - b_{nI} K_0(m_n r)] \sin(m_n z) , \quad (2.98)$$

$$B_{zII}(r, z) = \sum_{n=1, \dots}^{\infty} m_n \left[a_{nII} I_0(m_n r) - b_{nII} K_0(m_n r) + \frac{\pi L_0(m_n r)}{2m_n^2} P_n \right] \sin(m_n z) , \quad (2.99)$$

$$B_{zIII}(r, z) = \sum_{n=1, \dots}^{\infty} m_n [a_{nIII} I_0(m_n r) - b_{nIII} K_0(m_n r)] \sin(m_n z) , \quad (2.100)$$

$$B_{zIV}(r, z) = \sum_{n=1, \dots}^{\infty} m_n \left[a_{nIV} I_0(m_n r) - b_{nIV} K_0(m_n r) + \frac{\pi L_0(m_n r)}{2m_n^2} P_n \right] \sin(m_n z) , \quad (2.101)$$

$$B_{zV}(r, z) = \sum_{n=1, \dots}^{\infty} m_n [a_{nV} I_0(m_n r) - b_{nV} K_0(m_n r)] \sin(m_n z) . \quad (2.102)$$

The functions I_0 and K_0 are modified Bessel functions of the first kind of orders zero.

2.6 Boundary Conditions for the O.C. analysis

In order to evaluate the magnetic flux density, boundary conditions have to be implemented. The boundary conditions ensures that the coefficients (a_{nI} , a_{nII} , a_{nIII} , a_{nIV} and a_{nV}) and (b_{nI} , b_{nII} , b_{nIII} , b_{nIV} and b_{nV}) are evaluated accordingly. Magnetic boundary conditions are defined as conditions which magnetic flux density \mathbf{B} and the magnetic flux intensity \mathbf{H} between two different magnetic media of different permeability μ_1 and μ_2 must satisfy. From the Figure 2.4, boundary conditions are derived by firstly applying Gauss's Law [79, Sec. 9.7],

$$\oint_s \mathbf{B} \cdot d\mathbf{S} = 0 \quad (2.103)$$

where dS is a differential cylindrical Gaussian surface. Equation (2.103) implies that the amount of flux leaving one magnetic material in the normal direction is equal to the amount of flux entering another magnetic material i.e continuous. Therefore,

$$B_{N1} = B_{N2} . \quad (2.104)$$

The magnetic flux intensity is not continuous and is expressed by

$$H_{N2} = \frac{\mu_1}{\mu_2} H_{N1} \quad (2.105)$$

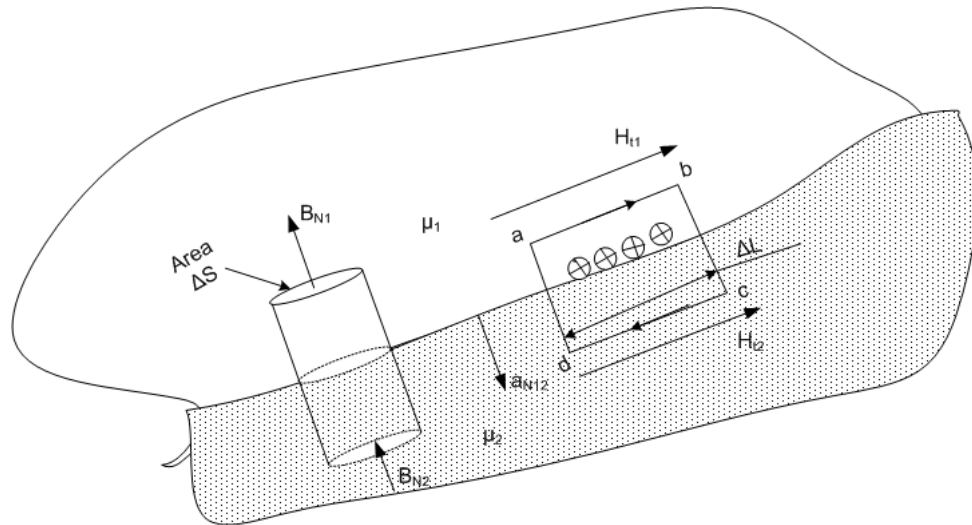


Figure 2.4: Gaussian surface and a closed path constructed between two media [79]

From the application of Ampere's circuital law to a closed path $abcd$

$$\oint_L \mathbf{H} \cdot d\mathbf{L} = I \quad (2.106)$$

where dL is differential length along the closed path and I being the total current. Employing this analysis on path $abcd$ on Figure 2.4 in clockwise direction

$$H_{t1}\Delta L - H_{t2}\Delta L = K\Delta L \quad \text{which means that } H_{t1} - H_{t2} = K \quad (2.107)$$

where K is the assumed surface current density. In case the surface current density is zero, $H_{t1} = H_{t2}$. The tangential component of the magnetic flux density \mathbf{B} is therefore expressed through

$$\frac{B_{t1}}{\mu_1} - \frac{B_{t2}}{\mu_2} = K \quad (2.108)$$

The continuous boundary conditions are mostly referred to as Neumann Boundary conditions, whereas the discontinuous boundary conditions are called the Dirichlet Boundary condition. With the Dirichlet boundary, a fixed value of a potential is assigned to a boundary. The Neumann conditions on the other hand, a normal derivative is assigned to a potential on the boundary line as illustrated on Figure 2.5.

For the analysis of the linear oscillatory machine in this dissertation, the basic boundary conditions mentioned above will suffice. Further study of boundary conditions can be obtained in Bargallo [80]

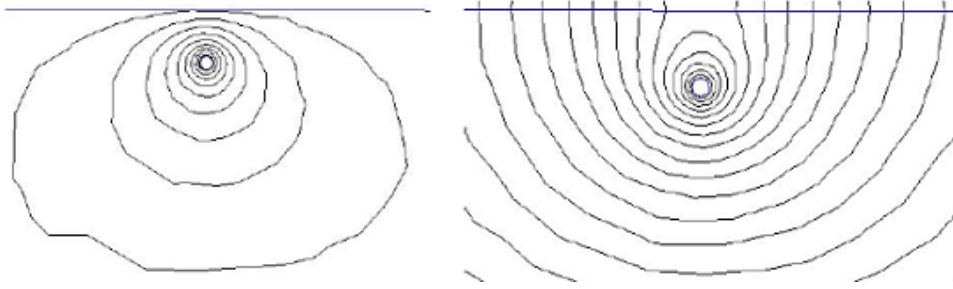


Figure 2.5: Left: Dirichlet Boundary Conditions; Right: Neumann Boundary Conditions [80]

2.7 Implementation of boundary conditions to solve for the magnetic vector potential and the magnetic flux density in the O.C analysis

Boundary conditions applied to the Linear oscillatory generator under study as referred to the boundary lines in Figure 2.2 and also pertaining to the equations of the magnetic vector potential of (2.83) - (2.87) as well as to the equations of the magnetic flux density in both the radial and axial directions (2.93) - (2.102) are:

$$A_{\phi I}|_{r=iR_s} = 0 \quad (2.109)$$

$$B_{rI}|_{r=iR_r} = B_{rII}|_{r=iR_r} \quad (2.110)$$

$$H_{zI}|_{r=iR_r} = H_{zII}|_{r=iR_r} \quad (2.111)$$

$$B_{rII}|_{r=iR_m} = B_{rIII}|_{r=iR_m} \quad (2.112)$$

$$H_{zII}|_{r=iR_m} = H_{zIII}|_{r=iR_m} \quad (2.113)$$

$$B_{rIII}|_{r=oR_m} = B_{rIV}|_{r=oR_m} \quad (2.114)$$

$$H_{zIII}|_{r=oR_m} = H_{zIV}|_{r=oR_m} \quad (2.115)$$

$$B_{rIV}|_{r=oR_s} = B_{rV}|_{r=oR_s} \quad (2.116)$$

$$H_{zIV}|_{r=oR_s} = H_{zV}|_{r=oR_s} \quad (2.117)$$

$$A_{\phi V}|_{r=R_o} = 0 \quad (2.118)$$

It should be noted that the magnetic flux density is related to the magnetic flux intensity by $\mathbf{B} = \mu\mathbf{H}$ from which \mathbf{H} is obtained and applied in terms of boundary condition (2.108) when K is zero. Absolute permeability $\mu = \mu_0\mu_r$, where μ_r is the relative permeability, while μ_0 is the permeability of free space and equal to $4\pi \times 10^{-7}[H/m]$ or $[Wb/(A \cdot m)]$. The following equations are obtained after the implementation of boundary conditions.

2.7.1 Internal bore radius boundary of subdomain I

Starting with boundary condition (2.109) ($A_{\phi I}|_{r=iR_s} = 0$) on boundary line of $r = iR_s$ where the equation becomes

$$a_{nI}I_1(m_n iR_s) + b_{nI}K_1(m_n iR_s) = 0 . \quad (2.119)$$

2.7.2 Boundary between subdomain I and II - O.C. analysis

For the boundary between subdomain *I* and *II* with condition (2.110) ($B_{rI}|_{r=iR_r} = B_{rII}|_{r=iR_r}$) at iR_r line,

$$m_n [a_{nI}I_1(m_n iR_r) + b_{nI}K_1(m_n iR_r)] = m_n \left[a_{nII}I_1(m_n iR_r) + b_{nII}K_1(m_n iR_r) + \frac{\pi L_1(m_n iR_r)}{2m_n^2} P_n \right] , \quad (2.120)$$

and condition (2.111) ($H_{zI}|_{r=iR_r} = H_{zII}|_{r=iR_r}$) results into

$$\mu_{rII}m_n [a_{nI}I_0(m_n iR_r) - b_{nI}K_0(m_n iR_r)] = \mu_{rI}m_n \left[a_{nII}I_0(m_n iR_r) - b_{nII}K_0(m_n iR_r) + \frac{\pi L_0(m_n iR_r)}{2m_n^2} P_n \right] , \quad (2.121)$$

where $\mu_{II} = \mu_0\mu_{rII}$ and according to the assumptions 2.2.1, $\mu_{rII} = \mu_{rIV} = 1$. $\mu_I = \mu_V$ due to $\mu_{rI} = \mu_{rV} = 1000$.

2.7.3 Boundary between subdomain II and III - O.C. analysis

For the boundary between subdomain *II* and *III* with condition (2.112) ($B_{rII}|_{r=iR_m} = B_{rIII}|_{r=iR_m}$) at iR_m line,

$$m_n \left[a_{nII}I_1(m_n iR_m) + b_{nII}K_1(m_n iR_m) + \frac{\pi L_1(m_n iR_m)}{2m_n^2} P_n \right] = m_n [a_{nIII}I_1(m_n iR_m) + b_{nIII}K_1(m_n iR_m)] , \quad (2.122)$$

and for condition (2.113) ($H_{zII}|_{r=iR_m} = H_{zIII}|_{r=iR_m}$) the equation is

$$m_n \left[a_{nII}I_0(m_n iR_m) - b_{nII}K_0(m_n iR_m) + \frac{\pi L_0(m_n iR_m)}{2m_n^2} P_n \right] = \mu_{rII}m_n [a_{nIII}I_0(m_n iR_m) - b_{nIII}K_0(m_n iR_m)] , \quad (2.123)$$

where $\mu_{III} = \mu_0$.

2.7.4 Boundary between subdomain III and IV - O.C. analysis

For the boundary between subdomain *III* and *IV* with condition (2.114) ($B_{rIII}|_{r=oR_m} = B_{rIV}|_{r=oR_m}$) at oR_m line,

$$m_n [a_{nIII}I_1(m_n oR_m) + b_{nIII}K_1(m_n oR_m)] = m_n \left[a_{nIV}I_1(m_n oR_m) + b_{nIV}K_1(m_n oR_m) + \frac{\pi L_1(m_n oR_m)}{2m_n^2} P_n \right] . \quad (2.124)$$

For condition (2.115) ($H_{zIII}|_{r=oR_m} = H_{zIV}|_{r=oR_m}$) equation becomes

$$\begin{aligned} & \mu_{rIV} m_n [a_{nIII} I_0(m_n oR_m) - b_{nIII} K_0(m_n oR_m)] = \\ & m_n \left[a_{nIV} I_0(m_n oR_m) - b_{nIV} K_0(m_n oR_m) + \frac{\pi L_0(m_n oR_m)}{2m_n^2} P_n \right] . \end{aligned} \quad (2.125)$$

2.7.5 Boundary between subdomain IV and V - O.C. analysis

For the boundary between subdomain IV and V with condition (2.116) ($B_{rIV}|_{r=oR_s} = B_{rV}|_{r=oR_s}$) at oR_s line,

$$\begin{aligned} & m_n \left[a_{nIV} I_1(m_n oR_s) + b_{nIV} K_1(m_n oR_s) + \frac{\pi L_1(m_n oR_s)}{2m_n^2} P_n \right] = \\ & m_n [a_{nV} I_1(m_n oR_s) + b_{nV} K_1(m_n oR_s)] , \end{aligned} \quad (2.126)$$

and for condition (2.117) ($H_{zIV}|_{r=oR_s} = H_{zV}|_{r=oR_s}$) the equation is

$$\begin{aligned} & \mu_{rV} m_n \left[a_{nIV} I_0(m_n oR_s) - b_{nIV} K_0(m_n oR_s) + \frac{\pi L_0(m_n oR_s)}{2m_n^2} P_n \right] = \\ & \mu_{rIV} m_n [a_{nV} I_0(m_n oR_s) - b_{nV} K_0(m_n oR_s)] . \end{aligned} \quad (2.127)$$

2.7.6 Outer radius boundary of subdomain V - O.C. analysis

Finally the last condition (2.118) ($A_{\phi V}|_{r=R_o} = 0$) gives

$$a_{nV} I_1(m_n R_o) + b_{nV} K_1(m_n R_o) = 0 . \quad (2.128)$$

2.7.7 Solving the ten simultaneous equations - O.C. analysis

The above equations formulated can only be evaluated once the coefficients are determined. To determine the coefficients, the 10 equations (2.119) to (2.128) are simplified

and simultaneously solved using the matrix method. The 10 equations are expressed as,

$$1. \quad a_{nI} I_1(m_n i R_s) - b_{nI} K_1(m_n i R_s) = 0, \quad (2.129)$$

$$2. \quad m_n [a_{nII} I_1(m_n i R_r) + b_{nI} K_1(m_n i R_r) - a_{nIII} I_1(m_n i R_r) - b_{nIII} K_1(m_n i R_r)] = m_n \frac{\pi L_1(m_n i R_r)}{2m_n^2} P_n, \quad (2.130)$$

$$3. \quad m_n [\mu_{rII} a_{nII} I_0(m_n i R_r) - \mu_{rII} b_{nII} K_0(m_n i R_r) - \mu_{rI} a_{nIII} I_0(m_n i R_r) + \mu_{rI} b_{nIII} K_0(m_n i R_r)] = \mu_{rI} m_n \frac{\pi L_0(m_n i R_r)}{2m_n^2} P_n, \quad (2.131)$$

$$4. \quad m_n [a_{nIII} I_1(m_n i R_m) + b_{nII} K_1(m_n i R_m) - a_{nIII} I_1(m_n i R_m) - b_{nIII} K_1(m_n i R_m)] = -m_n \frac{\pi L_1(m_n i R_m)}{2m_n^2} P_n, \quad (2.132)$$

$$5. \quad m_n [a_{nIII} I_0(m_n i R_m) - b_{nII} K_0(m_n i R_m) - \mu_{rII} a_{nIII} I_0(m_n i R_m) + \mu_{rII} b_{nIII} K_0(m_n i R_m)] = -m_n \frac{\pi L_0(m_n i R_m)}{2m_n^2} P_n, \quad (2.133)$$

$$6. \quad m_n [a_{nIII} I_1(m_n o R_m) + b_{nIII} K_1(m_n o R_m) - a_{nIV} I_1(m_n o R_m) - b_{nIV} K_1(m_n o R_m)] = m_n \frac{\pi L_1(m_n o R_m)}{2m_n^2} P_n, \quad (2.134)$$

$$7. \quad m_n [\mu_{rIV} a_{nIII} I_0(m_n o R_m) - \mu_{rIV} b_{nIII} K_0(m_n o R_m) - a_{nIV} I_0(m_n o R_m) + b_{nIV} K_0(m_n o R_m)] = m_n \frac{\pi L_0(m_n o R_m)}{2m_n^2} P_n, \quad (2.135)$$

$$8. \quad m_n [a_{nIV} I_1(m_n o R_s) + b_{nIV} K_1(m_n o R_s) - a_{nV} I_1(m_n o R_s) - b_{nV} K_1(m_n o R_s)] = -m_n \frac{\pi L_1(m_n o R_s)}{2m_n^2} P_n, \quad (2.136)$$

$$9. \quad m_n [\mu_{rV} a_{nIV} I_0(m_n o R_s) - \mu_{rV} b_{nIV} K_0(m_n o R_s) - \mu_{rIV} a_{nV} I_0(m_n o R_s) + \mu_{rIV} b_{nV} K_0(m_n o R_s)] = -\mu_{rV} m_n \frac{\pi L_0(m_n o R_s)}{2m_n^2} P_n, \quad (2.137)$$

$$10. \quad a_{nV} I_1(m_n R_o) + b_{nV} K_1(m_n R_o) = 0. \quad (2.138)$$

The matrix method is employed to determine the coefficients $a_{nI} - a_{nV}$ and $b_{nI} - b_{nV}$ as

$$\begin{bmatrix}
 I_1(M^a) & +K_1(M^a) & 0 & 0 & 0 & 0 & 0 & 0 & 0 & 0 \\
 I^b(M^b) & K^b(M^b) & -I^b(M^b) & -K^b(M^b) & 0 & 0 & 0 & 0 & 0 & 0 \\
 I^a(M^b) & -K^a(M^b) & -\mu_{rI} I^a(M^b) & \mu_{rI} K^a(M^b) & 0 & 0 & 0 & 0 & 0 & 0 \\
 0 & 0 & I^b(M^c) & K^b(M^c) & -I^b(M^c) & -K^b(M^c) & 0 & 0 & 0 & 0 \\
 0 & 0 & I^a(M^c) & -K^a(M^c) & -I^a(M^c) & K^a(M^c) & 0 & 0 & 0 & 0 \\
 0 & 0 & 0 & 0 & I^b(M^d) & K^b(M^d) & -I^b(M^d) & -K^b(M^d) & 0 & 0 \\
 0 & 0 & 0 & 0 & I^a(M^d) & -K^a(M^d) & -I^a(M^d) & K^a(M^d) & 0 & 0 \\
 0 & 0 & 0 & 0 & 0 & 0 & I^b(M^e) & K^b(M^e) & -I^b(M^e) & -K^b(M^e) \\
 0 & 0 & 0 & 0 & 0 & 0 & \mu_{rV} I^a(M^e) & -\mu_{rV} K^a(M^e) & -I^a(M^e) & K^a(M^e) \\
 0 & 0 & 0 & 0 & 0 & 0 & 0 & 0 & I_1(M^f) & +K_1(M^f)
 \end{bmatrix}$$

$$\begin{bmatrix}
 a_{nI} \\
 b_{nI} \\
 a_{nII} \\
 b_{nII} \\
 a_{nIII} \\
 b_{nIII} \\
 a_{nIV} \\
 b_{nIV} \\
 a_{nV} \\
 b_{nV}
 \end{bmatrix}
 =
 \begin{bmatrix}
 0 \\
 m_n \frac{\pi L_1(M^b)}{2m_n^2} P_n \\
 \mu_{rI} m_n \frac{\pi L_0(M^b)}{2m_n^2} P_n \\
 -m_n \frac{\pi L_1(M^c)}{2m_n^2} P_n \\
 -m_n \frac{\pi L_0(M^c)}{2m_n^2} P_n \\
 m_n \frac{\pi L_1(M^d)}{2m_n^2} P_n \\
 m_n \frac{\pi L_0(M^d)}{2m_n^2} P_n \\
 -m_n \frac{\pi L_1(M^e)}{2m_n^2} P_n \\
 -\mu_{rV} m_n \frac{\pi L_0(M^e)}{2m_n^2} P_n \\
 0
 \end{bmatrix}
 \quad (2.139)$$

where $M^a = m_n i R_s$, $M^b = m_n i R_r$, $M^c = m_n i R_m$, $M^d = m_n o R_m$, $M^e = m_n o R_s$, $M^f = m_n R_o$; $I^a = m_n I_0$, $I^b = m_n I_1$, $K^a = m_n K_0$, and $K^b = m_n K_1$.

For the sake of demonstrating the matrix onto a page, the first row and the last row have been left untouched, while in the second row up until the ninth row, functions have been represented by Capital letters M, I and K with small-letter superscripts to differentiate their representation. Bessel functions in multiplication with m_n have been represented by same letters as the Bessel functions for easier understanding.

2.8 Final solutions to the magnetic vector potential and the magnetic flux densities (O.C. analysis)

2.8.1 Solutions to the magnetic vector potential- O.C. analysis

Once the coefficients are established from the matrix (2.139), the final solutions are obtained by inserting the derived coefficients $a_{nI} - a_{nV}$ and $b_{nI} - b_{nV}$ into the expressions for the magnetic vector potential in Sec. 2.4.3 (2.83) - (2.87).

2.8.2 Solution to the radial magnetic flux densities - O.C. analysis

The final solutions to the radial magnetic flux densities are obtained by inserting the calculated coefficients from (2.139) into the expressions for the radial magnetic flux densities given in Sec. 2.5.1 (2.93) - (2.97).

2.8.3 Solution to the axial magnetic flux densities - O.C. analysis

The final solutions to the axial magnetic flux densities are determined by inserting the coefficient solutions determined through (2.139) into Sec. 2.5.2 in (2.98) - (2.102).

2.8.4 Solution to the total magnetic flux - O.C. analysis

The total magnetic flux density $B_T(r, z)$ is then determined from the algebraic sum of the radial magnetic flux densities $B_r(r, z)$ and the axial magnetic flux density $B_z(r, z)$ for the different subdomains as shown in Figure 2.2 present in the linear machine.

$$B_T(r, z) = \sqrt{B_r^2(r, z) + B_z^2(r, z)} \quad (2.140)$$

The flux density contour plots can be plotted from equation (2.140) and is demonstrated in the validation section below.

2.9 Validation of the model (PM field only) with finite element method (FEM)

The model in the FEM package MagNet is modelled such that the axial boundaries of the machine are given periodic boundary conditions in accordance with the assumption of the machine being infinitely long. The type of permanent magnets adopted are rare earth Neodymium Iron Boron (NdFeB) permanent magnets. The remanent magnetisation of NdFeB is $B_{rem} = 1.3T$ and the relative recoil permeability is $\mu_r = 1.04$ which is very close to unit. For this reason, $\mu_r = 1$ was adopted the analytical models. The analytical solution has been tested on a large variety of machine dimensions and the model has been consistent with the results correlating with those of the finite element package MagNet by infolytica inc.. To be presented are the predictions of the magnetic flux distribution in the machine subdomains. The machine dimensions adopted for both the analytical model and the FEM simulations are depicted in Table 2.1,

Table 2.1: Machine dimensions

symbol	value	symbol	value
iR_s	10.0 mm	g_1	1 mm
iR_r	35.5 mm	g_2	1 mm
iR_m	44.2 mm	τ_p	45 mm
iR_{coil}	45.2 mm	τ_m	30 mm
oR_{coil}	57.2 mm	τ_{wp}	45 mm
oR_m	58.2 mm	τ_w	35 mm
oR_s	67.9 mm	l_{ms}	15 mm
R_o	82.2 mm	l_{ws}	10 mm

2.9.1 Radial PM Flux density distribution - with PM field only

The magnetic flux density in the radial direction for the domains *II*, *III* and *IV* as compared to the finite element method is presented in this section. In the FEM simulations, the machine axial ends are given periodic boundary condition so that the machine is infinitely long.

In Figures 2.6 and 2.7, the radii; $R_{pma} = iR_s + h_{ics} + h_{ipm}/2$, $rn = iR_s + h_{ics} + h_{ipm} + g_1 + h_{coil}/2$ and $R_{pmb} = iR_s + h_{ics} + h_{ipm} + g_1 + h_{coil} + g_2 + h_{opm}/2$. The radial flux density in the air-gap $B_{r,III}$, i.e at radius rn in subdomain *III*, relates very well to the theoretical approximation of the air-gap flux density which is given by,

$$B_{gPM} \approx \frac{B_{rem}}{2} = 0.65T \quad (2.141)$$

where B_{gPM} is the theoretical approximation of the air-gap flux density. The magnetic flux density predicted in subdomain *II* at R_{pma} is shown as $B_{r,II}$ and that for the subdomain

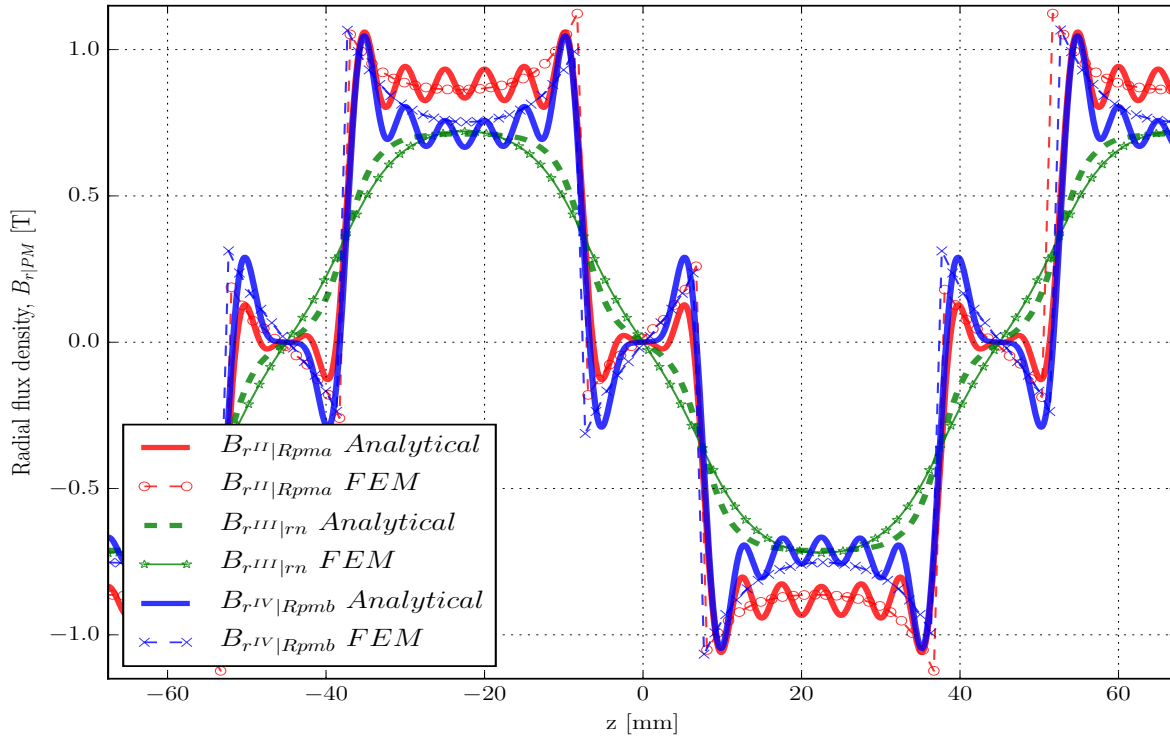


Figure 2.6: Radial flux density distribution due to PMs

III at radius R_{pmb} is shown as $B_{r,III}$ in Figure 2.6. The oscillations observed in both the lower and upper PMs results for the analytical model are due to the coefficient calculation matrix becoming unstable for higher $(2n - 1)^{th}$ harmonics. This is very common with calculations involving Bessel functions and the phenomenon has also been observed by Gysen *et al* [81]. The results for the radial flux density indicates that the prediction is valid with reference to (2.141) and the comparison with FEM.

2.9.2 Axial PM Flux density distribution - with PM field only

In this section, the axial flux densities of the analytical model for subdomains II , III and IV are compared with FEM. The comparison is done in the same way as for the radial flux density distribution.

It is observed from Figure 2.7 that there is good correlation between the analytical model and FEM in all the three subdomains II , III and IV for the axial flux densities.

2.9.3 Flux density distribution in the yokes and saturation monitoring

The analytical model developed has a provision the predicting the magnetic flux density distribution in the yokes. This is achieved by taking the relative permeability of the yoke to be finite. The boundary between the PMs and the yoke are assigned with Neumann

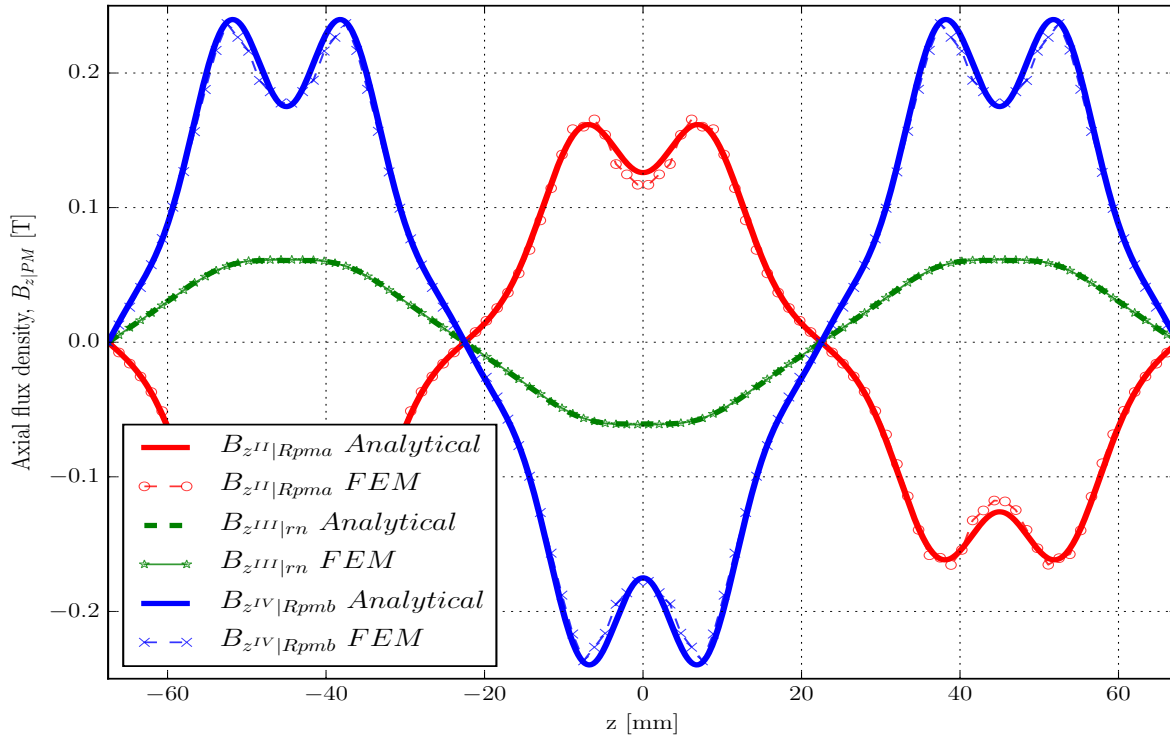


Figure 2.7: Axial flux density distribution due to PMs

boundary conditions while the radial edges of the yokes are assigned with Dirichlet boundary conditions. This implies that both the lower and upper yoke domains have radial and axial flux density expressions through which levels of flux density in the yokes can be observed. If the yoke material B-H Curve is available, one can be able to observe the levels of yoke saturation by simply plotting the flux density distribution in the yokes and compare whether the levels are below or above the knee of the B-H curve. It should be noted that the analytical model does not take saturation into consideration in the development of the mathematical equations. It only provides the designer insight on the level of saturation. This information can then be employed to adjust the parameters such as the yoke thickness or PM thickness to reduce saturation levels in the yokes. In this study, Cold Rolled 1010 Steel (*CR1010*) was adopted for the yoke material. The B-H curve of the material is shown in Figure 2.8.

From Figure 2.8, *CR1010* has a linear characteristic of the material observed to up to $1.5T$. However, the linear characteristic is more pronounced with a fairly constant relative permeability up to about $1.2T$ which gives the relative permeability to be equivalent to 941. It is for this reason that an initial relative permeability value of 1000 is adopted in the analytical calculations and it can be adjusted to 550 which is obtained at a more less linear characteristic $1.5T$ on the B-H Curve of *CR1010*.

The yoke flux density distribution are demonstrated in both the unsaturated and the saturated inner yoke of subdomain *I*.

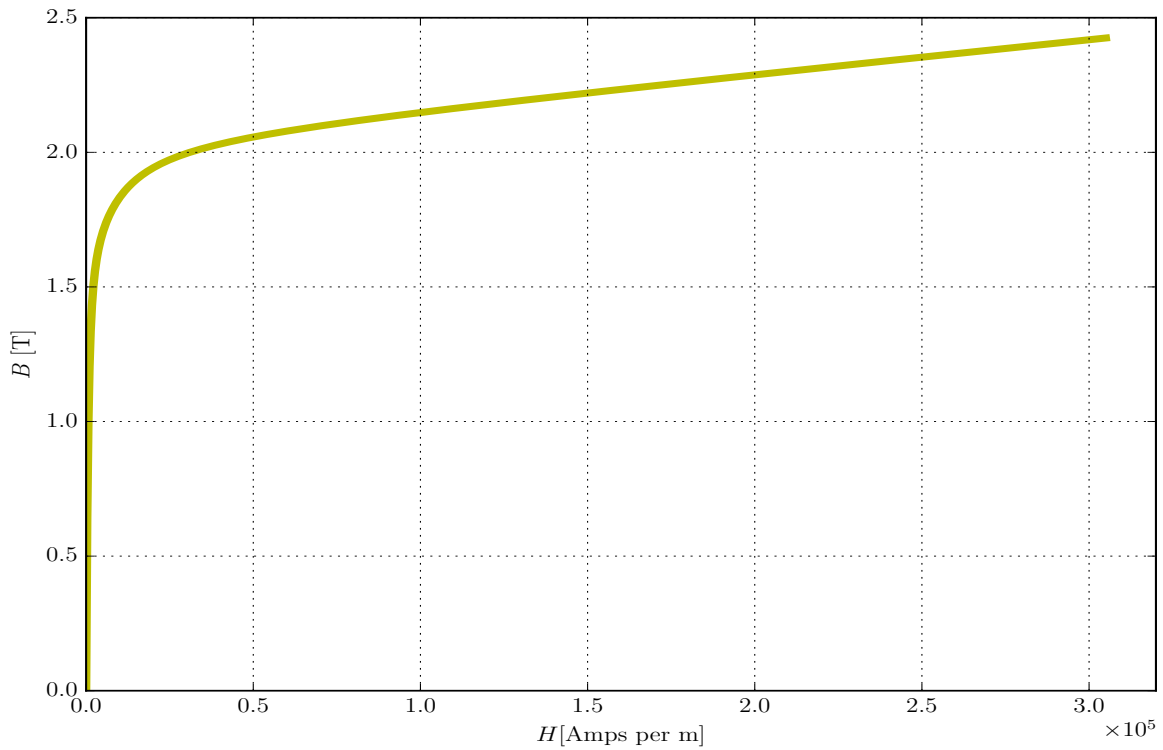


Figure 2.8: B-H Curve of Cold Rolled 1010 Steel [Infolytica MagNet]

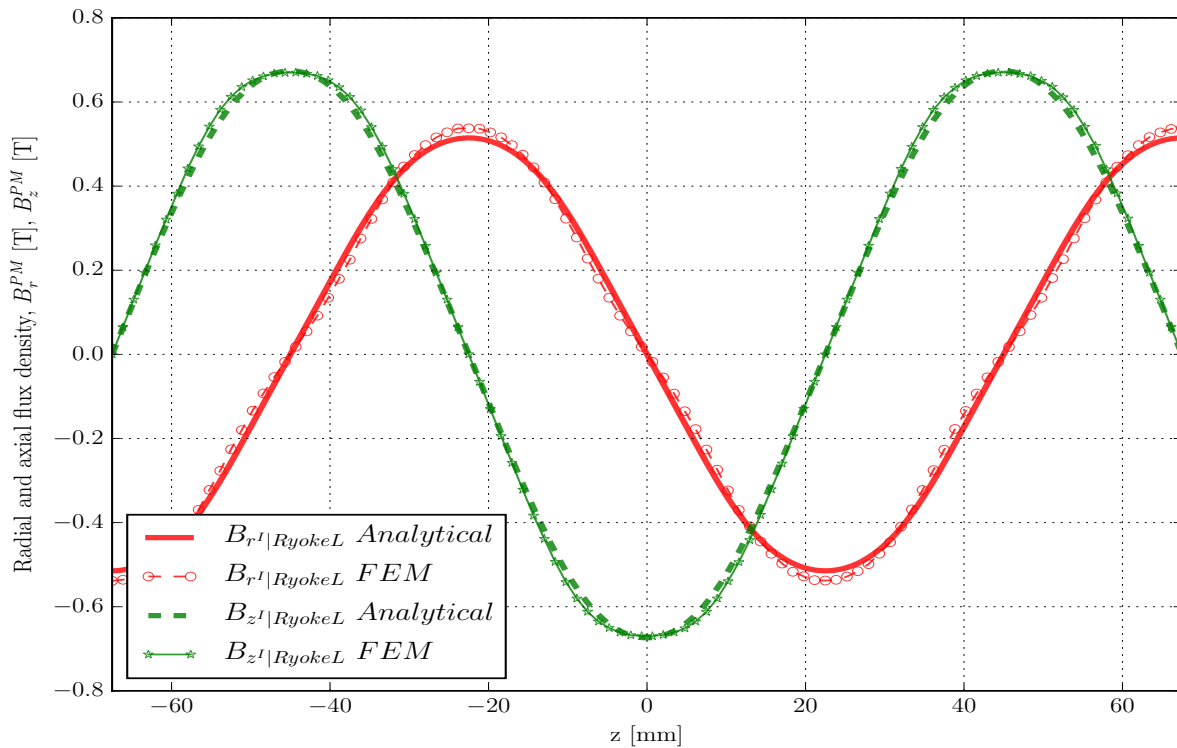


Figure 2.9: Axial and radial flux density of the inner yoke (unsaturated case)

From Figure 2.9, the magnetic flux density levels in the inner yoke are unsaturated and below the knee point of the B-H curve of *CR1010*. The reading of the flux density in the yoke is taken on the middle horizontal line of H_{ics} .

On the other hand, the inner yoke is deliberately reduced in thickness while the dimensions of the permanent magnets are maintained. The inner and yoke thickness are reduced to 5 mm (from 25.5 mm) and 4 mm (from 14.5 mm) respectively in order to demonstrate the saturated case as shown in Figures 2.10 and 2.12.

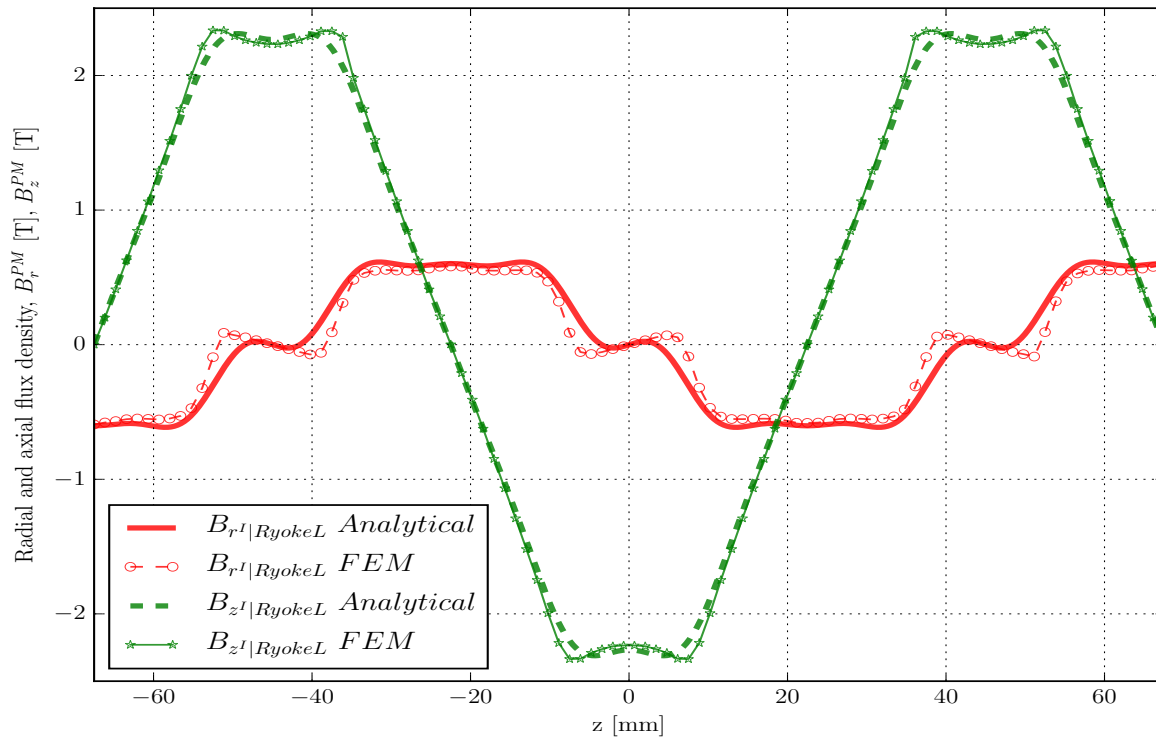


Figure 2.10: Axial and radial flux density of the inner yoke (saturated case)

Saturation monitoring is further illustrated for the outer yoke for the flux density distribution both with the yoke unsaturated and saturated for subdomain V .

Figure 2.11 shows that the levels of the magnetic flux densities especially the axial flux density in the upper yoke are below the knee of $CR1010$ and may therefore be considered as unsaturated.

By reducing the yoke thickness just to demonstrate the monitoring, it is observed in Figure 2.12 that the yoke flux density levels go beyond the knee point of $CR1010$

2.9.4 Contour plot comparison - with PM field only

The analytical model generated contour plots and magnetic field line plots are compared with FEM in this section.

Figures 2.13 and 2.14 are compared and it is observed that the field lines and the contour plot obtained by the analytical model correlates fairly well with a slight overestimation in the lower magnet poles which shows some flux concentration on the inner edges of the magnets.

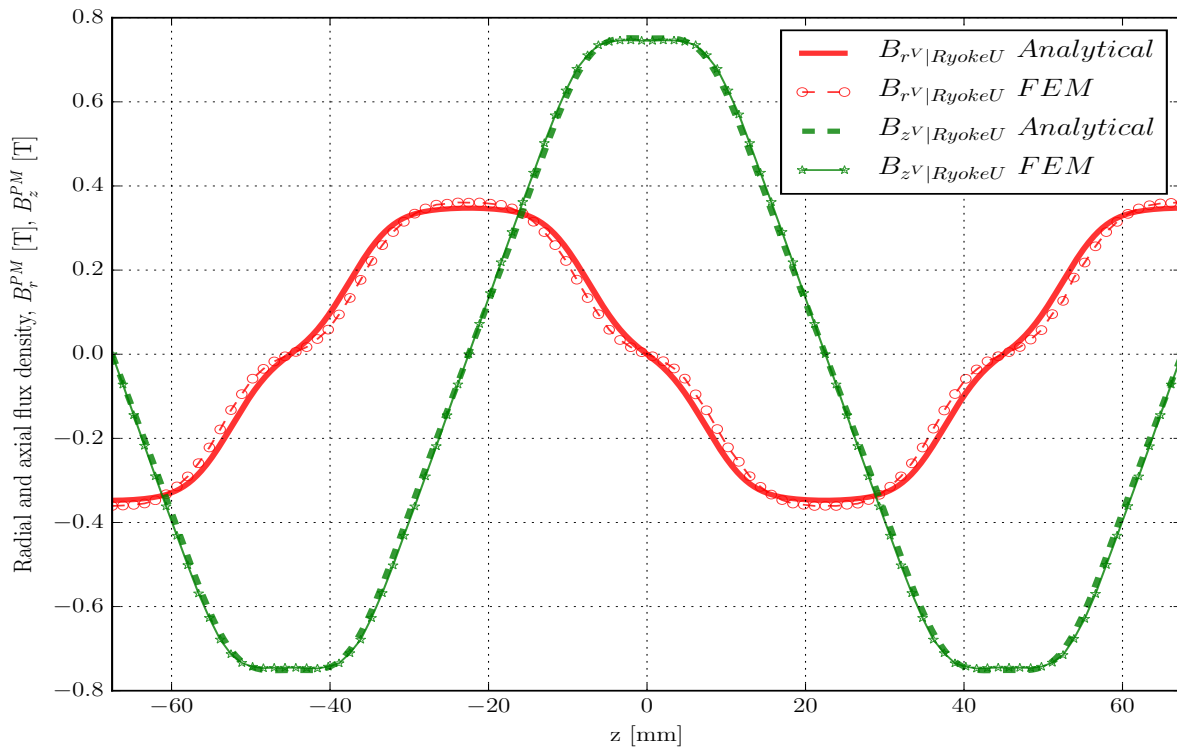


Figure 2.11: Axial and radial flux density of the outer yoke (unsaturated case)

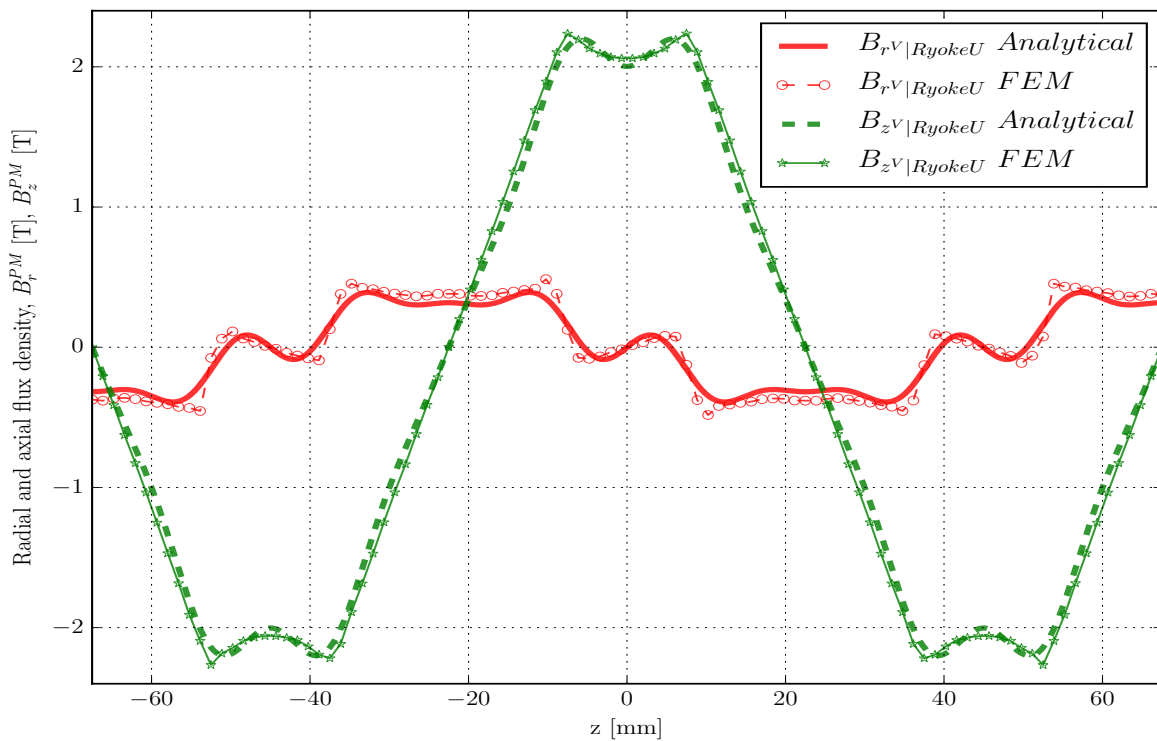


Figure 2.12: Axial and radial flux density of the outer yoke (saturated case)

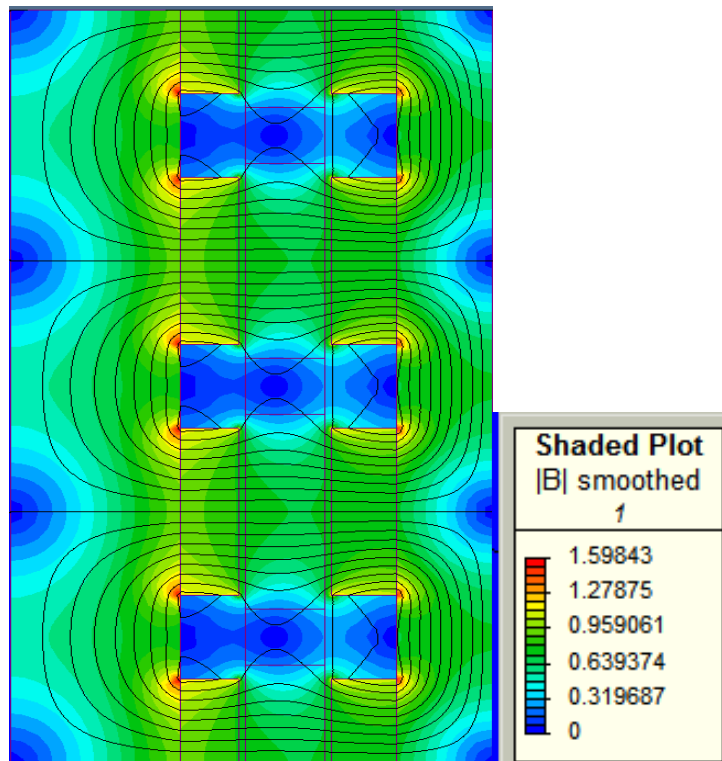


Figure 2.13: Contour plot obtained from FEM

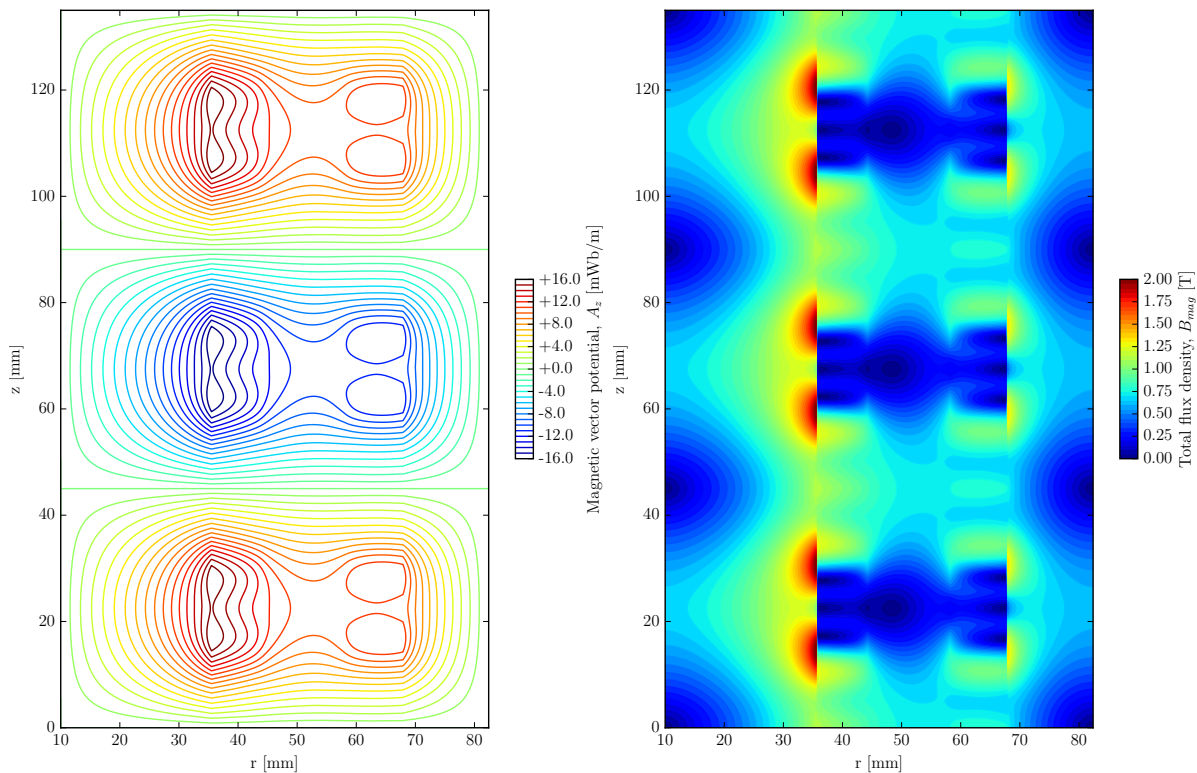


Figure 2.14: Field line plot and contour plot obtained from the analytical model

2.10 Summary and conclusion - with PM field only

In this chapter, the analytical model for the PM as the only source of the magnetic field has been developed. The model has been compared to a FEM model under the

same conditions and assumptions among which are the infinite length of the machine. The relative permeability of the yoke is considered to be a finite value allowing for the monitoring of the saturation in the yokes. The model shows that it is capable of predicting the magnetic flux distribution in all the domains of the machine. The model developed is capable of predicting the magnetic flux density distribution in the class of radially magnetised linear machines. The oscillations observed in Figure 2.6 as earlier explained are caused by the unconditional behaviour of the matrix with increase to higher harmonics especially with the employment of Bessel functions. The results displayed were obtained for harmonics up to the 17th. The Bessel function being independent of each other results in difficulty in conditioning the matrix to obtain coefficients that can allow for higher harmonics calculations. Gysen *et al* did experience the same challenges in [81].

The proposed consideration of the finite permeability of the yokes has been demonstrated in Figures 2.11 where the model upper yoke is not saturated and within the linear section of the B-H Curve as shown in Figure 2.8. This shows that the model is capable of being utilised as saturation monitoring tool which is important in the optimisation procedure especially in minimising the mass. Figure 2.12 demonstrates a saturated upper yoke in which the axial flux densities are over 2 T. Compared to the B-H Curve, it is observed that the axial flux densities are above the knee point. Again the analytical model correlates well with FEM to show the saturation level in the yoke. It should be noted that, the model does not calculate saturation but because the yokes are given a finite permeability, each yoke subdomain has an equation for the magnetic flux density through which the levels of flux concentration can be monitored.

The magnetic field line plots and contour plots are also compared and shows a fairly good correlation. The analytical model can be adopted as a pre-optimisation design tool to predict the magnetic field distribution in the linear machine.

The low flux densities obtained from the PMs in this machine is as expected because by FEM

$$B_{PM} \approx \frac{B_{rem}}{2} \quad (2.142)$$

where B_{rem} is the remanent magnetisation of value $1.3T$. This work differs from that of Wang *et al* [62] in that is considered double iron yokes which increases the number of variables to be considered in the calculation because the domains become five instead of three. Besides that Wang considers the iron yokes infinitely permeable and infinitely thick which is not the case in this work.

Chapter 3

Prediction of the armature field flux density

3.1 Introduction

The main magnetic field in the air-gap may be distorted by the field generated from the coil when a current passes through it and this phenomenon is called armature reaction **AR**. The armature reaction for air-cored armature machines is relatively low [40; 82; 83], however the importance of the armature reaction calculation for the purpose of machine control design schemes, inductance levels and real time control is still very high. A high armature reaction is detrimental to the force output of the machine. To solve the Maxwell equations, separation of variable with Fourier Series techniques are employed. This approach has also been adopted by many authors among which are [62; 84; 85; 86; 42; 81; 65; 66; 67; 49]. Among these authors, Wang *et al* [62] coils that are surface mounted to a core where as Yan *et al* [49] considered the air-cored windings for the development of the analytical models for the calculation of the armature reaction. The remaining authors as cited above considered slotted coils in their analytical models. The armature reaction analytical models have mostly focused on low permeability subdomains which is mostly the winding subdomain and the air-gaps subdomain with assumptions that the yokes are infinitely permeable and thick. In the determination of the armature reaction, the iron yokes are given a finite relative permeability as well as thickness so as to monitor the saturation levels which has only been done for rotating machines [70; 71]. The proposed approach for this linear machine has been demonstrated by Chembe *et al* in [87] for different machine dimension as compared to the dimensions adopted in this analysis. The armature reaction is also key in determining the machine inductance. Figure 3.1 shows the model employed in the armature reaction analysis with the PMs considered switched off. The subdomains $II' = h_{ipm} + g1$ and $IV' = h_{opm} + g2$.

3.2 Governing equations - armature field flux density analysis (AR-analysis)

In order to calculate the armature reaction field distribution, the inner permanent magnets are replaced by air and added to the inner air-gap g_i to form region $II' = II + g_i$ whereas

the upper permanent magnets are also replaced by air and added to the outer air-gap go to form region $IV' = IV + go$.

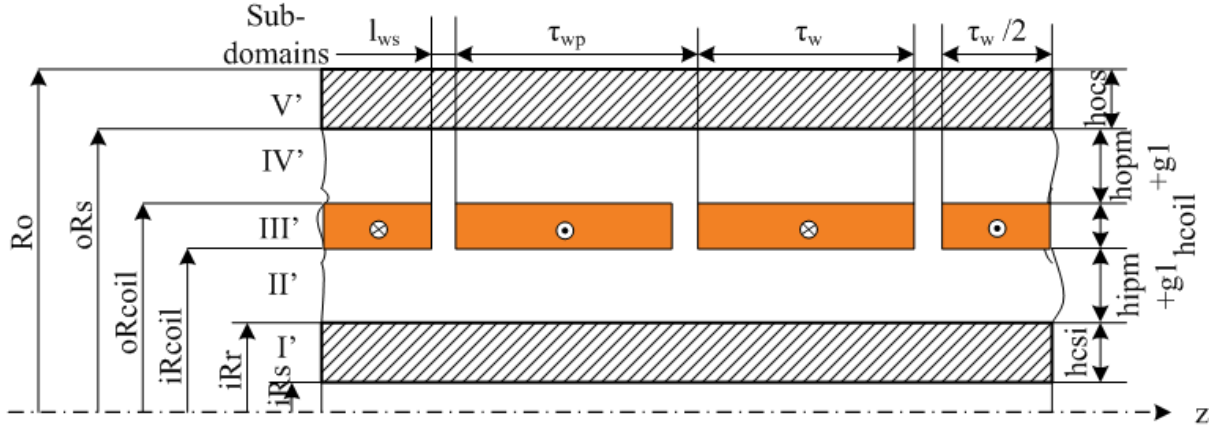


Figure 3.1: Armature reaction subdomain representation

The regions I' , $II' = II + gi$, IV' and V' are solved using the Laplace equation

$$\nabla \times \nabla \times A_{\phi^i} = 0 , \quad (3.1)$$

where i represents regions I' , II' , IV' and V' . However, the coil region in this case is solved using the Poisson equation

$$\nabla \times \nabla \times A_{\phi^i} = -\mu J . \quad (3.2)$$

as can be seen in the armature reaction domain presented on Figure 3.1.

3.2.1 Assumptions for the AR analysis

For the calculation of the magnetic field distribution considering only the field from the coil current that is referred to as the armature reaction, the following assumptions have to be taken into consideration.

1. The stator is assigned a finite permeability for the purpose of considering saturation levels in the stator;
2. Permanent magnets are assumed with permeability of air;
3. Eddy-current effects are not considered
4. The axial length of the machines is considered infinite so as to eliminate end effects. Fringing can be incorporated by following [88].

3.2.2 Representation of the Laplace and the Poisson equations in cylindrical coordinate system

The Laplace equation then for the non-current density carrier domains is

$$\frac{\partial^2 A_{\phi^i}}{\partial z^2} + \frac{\partial^2 A_{\phi^i}}{\partial r^2} + \frac{1}{r} \frac{\partial A_{\phi^i}}{\partial r} - \frac{1}{r^2} A_{\phi^i} = 0 \quad (3.3)$$

where i represents the domains I', II', IV', V' . The Poisson equation for the winding region is

$$\frac{\partial^2 A_{\phi_{III'V'}}}{\partial z^2} + \frac{\partial^2 A_{\phi_{III'V'}}}{\partial r^2} + \frac{1}{r} \frac{\partial A_{\phi_{III'V'}}}{\partial r} - \frac{1}{r^2} A_{\phi_{III'V'}} = -\mu_0 J_z \quad (3.4)$$

3.3 General solution to the Laplace equation - AR analysis

The general solution to (3.4) is obtained in the same way as in Sec. 2.4.1 which is presented below for the sake of convenience,

$$A_{\phi}^{AR}(r, z) = \sum_{n=1,2,..}^{\infty} ([E_n I_1(mr) + F_n K_1(mr)] \cos(mz) + [G_n I_1(mr) + H_n K_1(mr)] \sin(mz)). \quad (3.5)$$

For the analysis of the armature reaction, G_n and H_n are taken as

$$G_n = 0$$

and

$$H_n = 0$$

It should be noted that I_1 and K_1 are Modified Bessel functions of the first and second kind of order 1 and are independent of each other. Therefore the solution to the Laplace equation for the armature reaction is expressed as

$$A_{\phi}^{AR}(r, z) = \sum_{n=1,..}^{\infty} [a_n I_1(m_n r) + b_n K_1(m_n r)] \cos(m_n z), \quad (3.6)$$

where $a_n = E_n$ and $b_n = F_n$ are coefficients to be determined later.

3.4 General solution to the Poisson equation - AR analysis

To obtain the general solution to 3.5, one has to firstly find the expression for the current density J_z by employing Fourier expansion method. Separation of variables is then applied to solve the Poisson equation and determine the particular solution.

3.4.1 Solution to the current density

Figure 3.2 is employed for the determination of the current density expression. In the Figure, the coils with conductors moving out of the page are taken as positive current densities and the coils entering into the page are taken as negative.

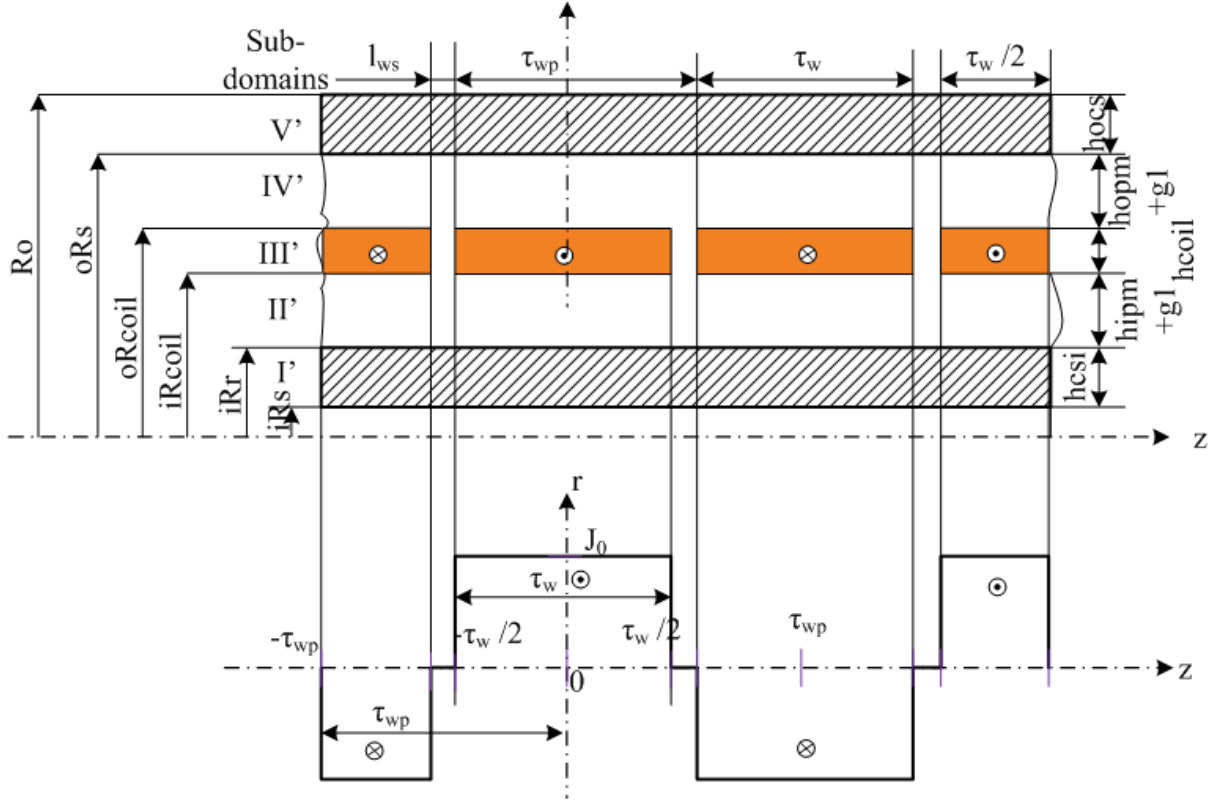


Figure 3.2: Domain representation for armature reaction field distribution

The current density is expressed as a Fourier series

$$J(z) = \sum_{n=1,2,\dots}^{\infty} J_n \cos(m_n^{AR} z) . \quad (3.7)$$

The period in this case is $2\tau_{wp}$, $\omega_n^{AR} = \frac{n\pi}{\tau_{wp}}$. From Figure 3.2, it is observed that

$$J_n = \frac{1}{\tau_{wp}} \int_{-\tau_{wp}}^{\tau_{wp}} f(z) \cos(\omega_n^{AR} z) dz . \quad (3.8a)$$

The equation can be also expressed as

$$J_n = \frac{2}{\tau_{wp}} \int_0^{\tau_{wp}} f(z) \cos(\omega_n^{AR} z) dz . \quad (3.8b)$$

(3.8b) is then split into two integrals as

$$J_n = \frac{2}{\tau_{wp}} \left[J_0 \int_0^{\frac{\tau_w}{2}} \cos(\omega_n^{AR} z) dz - J_0 \int_{\frac{2\tau_{wp}-\tau_w}{2}}^{\tau_{wp}} \cos(\omega_n^{AR} z) dz \right] . \quad (3.8c)$$

After integration, (3.8c) is expressed as

$$J_n = \frac{2J_0}{\tau_{wp}} \left\{ \frac{\sin(\omega_n^{AR}z)}{\omega_n^{AR}} \Big|_0^{\frac{\tau_w}{2}} - \frac{\sin(\omega_n^{AR}z)}{\omega_n^{AR}} \Big|_{\frac{2\tau_{wp}-\tau_w}{2}}^{\tau_{wp}} \right\}, \quad (3.8d)$$

which when simplified is given by

$$J_n = \frac{2J_0}{n\pi} \left\{ \sin\left(\frac{\omega_n^{AR}\tau_w}{2}\right) + \sin\left(n\pi - \frac{\omega_n^{AR}\tau_{wp}}{2}\right) \right\}. \quad (3.8e)$$

Further simplification can only be achieved by applying a trigonometric identity $\{\sin(a - b) = \sin a \cos b - \sin b \cos a\}$ to (3.8e) to obtain

$$J_n = \frac{2J_0}{n\pi} (1 - (-1)^n) \sin\left(\frac{n\pi}{2} \frac{\tau_w}{\tau_{wp}}\right), \quad (3.9)$$

where it is known that $(-1)^n = \cos(n\pi)$. This implies that only odd harmonics will be summed up and therefore, J_n is taken as J_{2n-1} resulting into

$$J_{2n-1} = \frac{4J_0}{(2n-1)\pi} \sin\left(\frac{(2n-1)\pi}{2} \frac{\tau_w}{\tau_{wp}}\right). \quad (3.10)$$

The expression for the current density $J(z)$ is therefore equal to

$$J(z) = \frac{4J_0}{\pi} \sum_{n=1}^{\infty} \frac{1}{(2n-1)} \sin\left(\frac{(2n-1)\pi}{2} \frac{\tau_w}{\tau_{wp}}\right) \cos(m_n^{AR}z), \quad (3.11)$$

where

$$m_n^{AR} = (2n-1) \frac{\pi}{\tau_{wp}}. \quad (3.12)$$

J_0 is the input current density value; τ_w and τ_{wp} are the coil length and coil pole pitch respectively. From (3.4), the right side the Poisson equation for the armature must be equal to $\mu_0 J(z)$, that is

$$J(z) = \frac{4J_0\mu_0}{\pi} \sum_{n=1}^{\infty} \frac{1}{(2n-1)} \sin\left(\frac{(2n-1)\pi}{2} \frac{\tau_w}{\tau_{wp}}\right) \cos(m_n^{AR}z), \quad (3.13)$$

3.4.2 Inserting the solution to the current density into the Poisson equation

The general solution to the Poisson equation is the summation of the homogeneous solution and the particular solution $S(r, z)$ as

$$A_\phi^{AR}(r, z) = \sum_{n=1, \dots}^{\infty} [a_n I_1(m_n^{AR}r) + b_n K_1(m_n^{AR}r)] \cos(m_n^{AR}z) + S(r, z)^{AR} \quad (3.14)$$

where

$$S(r, z) = R(r)Z(z). \quad (3.15)$$

The Separation of Variables technique is applied to the cylindrical equation of the Poisson equation which is given by

$$\frac{\partial^2 A_\phi^{AR}}{\partial z^2} + \frac{\partial^2 A_\phi^{AR}}{\partial r^2} + \frac{1}{r} \frac{\partial A_\phi^{AR}}{\partial r} - \frac{1}{r^2} A_\phi^{AR} = P_n^{AR} \cos(m_n^{AR} z), \quad (3.16)$$

to determine the particular solution. In (3.16)

$$P_n^{AR} = \frac{-4J_0\mu_0}{(2n-1)\pi} \sin\left(\frac{(2n-1)\pi\tau_w}{2\tau_{wp}}\right). \quad (3.17)$$

Applying separation of variables to (3.17), the particular solution $S(r, z)^{AR}$ is obtained with the same procedure as in Sec. 2.4.2.2 and is given by

$$S(r, z)^{AR} = \frac{\pi L_1(m_n^{AR} z)}{2m_n^2 AR} P_n^{AR} \cos(m_n^{AR} z), \quad (3.18)$$

where L_1 is a Modified Struve function [78; 49]. The solution to the Poisson equation is then expressed as

$$A_\phi^{AR}(r, z) = \sum_{n=1, \dots}^{\infty} \left[a_n I_1(m_n^{AR} r) + b_n K_1(m_n^{AR} r) + \frac{\pi L_1(m_n^{AR} r)}{2m_n^2 AR} P_n^{AR} \right] \cos(m_n^{AR} z). \quad (3.19)$$

3.5 General solutions to the magnetic vector potential for all the subdomains for the AR analysis

The magnetic vector potential \mathbf{A}^{AR} for each of the subdomains I', II', III', IV' and V' of Figure 3.1 are expressed as

$$A_{\phi I'}^{AR}(r, z) = \sum_{n=1, \dots}^{\infty} [a_{nI'} I_1(m_n^{AR} r) + b_{nI'} K_1(m_n^{AR} r)] \cos(m_n^{AR} z), \quad (3.20)$$

$$A_{\phi II'}^{AR}(r, z) = \sum_{n=1, \dots}^{\infty} [a_{nII'} I_1(m_n^{AR} r) + b_{nII'} K_1(m_n^{AR} r)] \cos(m_n^{AR} z), \quad (3.21)$$

$$A_{\phi III'}^{AR}(r, z) = \sum_{n=1, \dots}^{\infty} [a_{nIII'} I_1(m_n^{AR} r) + b_{nIII'} K_1(m_n^{AR} r) + S r_1^{AR}] \cos(m_n^{AR} z), \quad (3.22)$$

$$A_{\phi IV'}^{AR}(r, z) = \sum_{n=1, \dots}^{\infty} [a_{nIV'} I_1(m_n^{AR} r) + b_{nIV'} K_1(m_n^{AR} r)] \cos(m_n^{AR} z), \quad (3.23)$$

$$A_{\phi V'}^{AR}(r, z) = \sum_{n=1, \dots}^{\infty} [a_{nV'} I_1(m_n^{AR} r) + b_{nV'} K_1(m_n^{AR} r)] \cos(m_n^{AR} z). \quad (3.24)$$

where

$$S r_1^{AR} = \frac{\pi L_1(m_n^{AR} r)}{2m_n^2 AR} P_n^{AR} \quad (3.25)$$

The expression for the inner and outer yokes are to serve as guidance in the monitoring of the magnetic flux levels in the yokes.

3.6 General solution to the AR magnetic flux density

The magnetic flux density for the armature reaction fields are calculated from the curl of the magnetic vector potential determined in (3.20) - (3.24). The steps to determine the The curl of \mathbf{A} have been demonstrated in Sec. 2.5 in (2.89), which is repeated below but unnumbered,

$$\mathbf{B} = \nabla \times \mathbf{A} = B_r \mathbf{e}_r + B_z \mathbf{e}_z = -\frac{1}{r} \frac{\partial r A_\phi}{\partial z} \mathbf{e}_r + \frac{1}{r} \frac{\partial r A_\phi}{\partial r} \mathbf{e}_z$$

3.6.1 Radial magnetic flux density general solutions for all subdomains in AR analysis

The expression for the radial flux densities per subdomain are obtained from the differentiation of (3.20) - (3.24) in accordance with (2.89)

$$B_{rI'}^{AR}(r, z) = \sum_{n=1, \dots}^{\infty} m_n^{AR} [a_{nI'} I_1(m_n^{AR} r) + b_{nI'} K_1(m_n^{AR} r)] \sin(m_n^{AR} z), \quad (3.26)$$

$$B_{rII'}^{AR}(r, z) = \sum_{n=1, \dots}^{\infty} m_n^{AR} [a_{nII'} I_1(m_n^{AR} r) + b_{nII'} K_1(m_n^{AR} r)] \sin(m_n^{AR} z), \quad (3.27)$$

$$B_{rIII'}^{AR}(r, z) = \sum_{n=1, \dots}^{\infty} m_n^{AR} [a_{nIII'} I_1(m_n^{AR} r) + b_{nIII'} K_1(m_n^{AR} r) + Sr_1^{AR}] \sin(m_n^{AR} z), \quad (3.28)$$

$$B_{rIV'}^{AR}(r, z) = \sum_{n=1, \dots}^{\infty} m_n^{AR} [a_{nIV'} I_1(m_n^{AR} r) + b_{nIV'} K_1(m_n^{AR} r)] \sin(m_n^{AR} z), \quad (3.29)$$

$$B_{rV'}^{AR}(r, z) = \sum_{n=1, \dots}^{\infty} m_n^{AR} [a_{nV'} I_1(m_n^{AR} r) + b_{nV'} K_1(m_n^{AR} r)] \sin(m_n^{AR} z). \quad (3.30)$$

where Sr_1^{AR} is given by 3.25 on Sec. 3.5

3.6.2 General solution for the axial magnetic flux density in all subdomains

The axial flux densities per subdomain are also obtained from the differentiation of (3.20) - (3.24) for the axial component through (2.89) and obtained as

$$B_{zI'}^{AR}(r, z) = \sum_{n=1, \dots}^{\infty} m_n^{AR} [a_{nI'} I_0(m_n^{AR} r) - b_{nI'} K_0(m_n^{AR} r)] \cos(m_n^{AR} z), \quad (3.31)$$

$$B_{zII'}^{AR}(r, z) = \sum_{n=1, \dots}^{\infty} m_n^{AR} [a_{nII'} I_0(m_n^{AR} r) - b_{nII'} K_0(m_n^{AR} r)] \cos(m_n^{AR} z), \quad (3.32)$$

$$B_{zIII'}^{AR}(r, z) = \sum_{n=1, \dots}^{\infty} m_n^{AR} [a_{nIII'} I_0(m_n^{AR} r) - b_{nIII'} K_0(m_n^{AR} r) + Sr_0^{AR}] \cos(m_n^{AR} z), \quad (3.33)$$

$$B_{zIV'}^{AR}(r, z) = \sum_{n=1, \dots}^{\infty} m_n^{AR} [a_{nIV'} I_0(m_n^{AR} r) - b_{nIV'} K_0(m_n^{AR} r)] \cos(m_n^{AR} z), \quad (3.34)$$

$$B_{zV'}^{AR}(r, z) = \sum_{n=1, \dots}^{\infty} m_n^{AR} [a_{nV'} I_0(m_n^{AR} r) - b_{nV'} K_0(m_n^{AR} r)] \cos(m_n^{AR} z), \quad (3.35)$$

where I_0 and K_0 are modified Bessel functions of the first kind of orders zero and

$$Sr_0^{AR} = \frac{\pi L_0(m_n^{AR} r)}{2m_n^{2AR}} P_n^{AR} \quad (3.36)$$

3.7 Implementation of boundary conditions for the AR analysis

An introduction to boundary conditions has been presented in Sec. 2.6 and therefore, the approach in this section is to focus on the implementation of the boundary conditions for the armature reaction analysis. In the subdomain method, boundary conditions at the interfaces of the material leads to the calculation of the coefficients. Dirichlet boundary condition are applied at the inner bore radius of the machine as well as at the circumferential radius of the machine. Neumann boundary conditions are applied on the material interfaces of the machine. The boundary conditions applied for the AR reaction model

are provided by

$$A_{\phi I'}^{AR}|_{r=iR_s} = 0 \quad (3.37)$$

$$B_{r I'}^{AR}|_{r=iR_r} = B_{r II'}^{AR}|_{r=iR_r} \quad (3.38)$$

$$H_{z I'}^{AR}|_{r=iR_r} = H_{z II'}^{AR}|_{r=iR_r} \quad (3.39)$$

$$B_{r III'}^{AR}|_{r=iR_{coil}} = B_{r III'}^{AR}|_{r=iR_{coil}} \quad (3.40)$$

$$H_{z III'}^{AR}|_{r=iR_{coil}} = H_{z III'}^{AR}|_{r=iR_{coil}} \quad (3.41)$$

$$B_{r III'}^{AR}|_{r=oR_{coil}} = B_{r IV'}^{AR}|_{r=oR_{coil}} \quad (3.42)$$

$$H_{z III'}^{AR}|_{r=oR_{coil}} = H_{z IV'}^{AR}|_{r=oR_{coil}} \quad (3.43)$$

$$B_{r IV'}^{AR}|_{r=oR_s} = B_{r V'}^{AR}|_{r=oR_s} \quad (3.44)$$

$$H_{z IV'}^{AR}|_{r=oR_s} = H_{z V'}^{AR}|_{r=oR_s} \quad (3.45)$$

$$A_{\phi V'}^{AR}|_{r=R_o} = 0 \quad (3.46)$$

The magnetic flux intensity \mathbf{H} in the boundary conditions is solved through the relation $\mathbf{B} = \mu\mathbf{H}$. It is known that $\mu = \mu_r\mu_0$, where μ_r is the relative permeability of the material and $\mu_0 = 4\pi \times 10^{-7} [H/m]$ or $[Wb/(A \cdot m)]$. In this case, the relative permeability of the yoke material Cold Rolled Steel 1010 is taken as $\mu_r^{CR1010} = 1000$. Presented below are the equations obtained from the boundary condition implementation

3.7.1 Internal bore radius boundary of subdomain I' - AR analysis

At $r = iR_s$, applying the boundary condition (3.37) ($A_{\phi I'}^{AR}|_{r=iR_s} = 0$) yields

$$a_{n I'} I_1(m_n^{AR} iR_s) + b_{n I'} K_1(m_n^{AR} iR_s) = 0. \quad (3.47)$$

3.7.2 Boundary between subdomain I' and II' - AR analysis

At $r = iR_r$, applying the boundary condition (3.38) ($B_{r I'}^{AR}|_{r=iR_r} = B_{r II'}^{AR}|_{r=iR_r}$) yields

$$\begin{aligned} m_n^{AR} [a_{n I'} I_1(m_n^{AR} iR_r) + b_{n I'} K_1(m_n^{AR} iR_r)] = \\ m_n^{AR} [a_{n II'} I_1(m_n^{AR} iR_r) + b_{n II'} K_1(m_n^{AR} iR_r)] , \end{aligned} \quad (3.48)$$

Boundary condition (3.39) ($H_{z I'}^{AR}|_{r=iR_r} = H_{z II'}^{AR}|_{r=iR_r}$) yields

$$\begin{aligned} m_n^{AR} [a_{n I'} I_0(m_n^{AR} iR_r) - b_{n I'} K_0(m_n^{AR} iR_r)] = \\ \mu_{r II'} m_n^{AR} [a_{n II'} I_0(m_n^{AR} iR_r) - b_{n II'} K_0(m_n^{AR} iR_r)] . \end{aligned} \quad (3.49)$$

3.7.3 Boundary between subdomain II' and III' - AR analysis

At iR_{coil} , boundary condition (3.40) ($B_{r_{II'}}^{AR}|_{r=iR_{coil}} = B_{r_{III'}}^{AR}|_{r=iR_{coil}}$) yields

$$\begin{aligned} m_n^{AR} [a_{n_{II'}} I_1(m_n^{AR} iR_{coil}) + b_{n_{II'}} K_1(m_n^{AR} iR_{coil})] = \\ m_n^{AR} \left[a_{n_{III'}} I_1(m_n^{AR} iR_{coil}) + b_{n_{III'}} K_1(m_n^{AR} iR_{coil}) + \frac{\pi L_1(m_n^{AR} iR_{coil})}{2m_n^2 AR} P_n^{AR} \right], \end{aligned} \quad (3.50)$$

and the boundary condition (3.41) ($H_{z_{II'}}^{AR}|_{r=iR_{coil}} = H_{z_{III'}}^{AR}|_{r=iR_{coil}}$) gives

$$\begin{aligned} m_n^{AR} [a_{n_{II'}} I_0(m_n^{AR} iR_{coil}) - b_{n_{II'}} K_0(m_n^{AR} iR_{coil})] = \\ m_n^{AR} \left[a_{n_{III'}} I_0(m_n^{AR} iR_{coil}) - b_{n_{III'}} K_0(m_n^{AR} iR_{coil}) + \frac{\pi L_0(m_n^{AR} iR_{coil})}{2m_n^2 AR} P_n^{AR} \right]. \end{aligned} \quad (3.51)$$

3.7.4 Boundary between subdomain III' and IV' - AR analysis

At oR_{coil} , boundary condition (3.42) ($B_{r_{III'}}^{AR}|_{r=oR_{coil}} = B_{r_{IV'}}^{AR}|_{r=oR_{coil}}$) yields

$$\begin{aligned} m_n^{AR} \left[a_{n_{III'}} I_1(m_n^{AR} oR_{coil}) + b_{n_{III'}} K_1(m_n^{AR} oR_{coil}) + \frac{\pi L_1(m_n^{AR} oR_{coil})}{2m_n^2 AR} P_n^{AR} \right] = \\ m_n^{AR} [a_{n_{IV'}} I_1(m_n^{AR} oR_{coil}) + b_{n_{IV'}} K_1(m_n^{AR} oR_{coil})], \end{aligned} \quad (3.52)$$

and the boundary condition (3.43) ($H_{z_{III'}}^{AR}|_{r=oR_{coil}} = H_{z_{IV'}}^{AR}|_{r=oR_{coil}}$) gives

$$\begin{aligned} m_n^{AR} \left[a_{n_{III'}} I_0(m_n^{AR} oR_{coil}) - b_{n_{III'}} K_0(m_n^{AR} oR_{coil}) + \frac{\pi L_0(m_n^{AR} oR_{coil})}{2m_n^2 AR} P_n^{AR} \right] = \\ m_n^{AR} [a_{n_{IV'}} I_0(m_n^{AR} oR_{coil}) - b_{n_{IV'}} K_0(m_n^{AR} oR_{coil})]. \end{aligned} \quad (3.53)$$

3.7.5 Boundary between subdomain IV' and V' - AR analysis

At oR_s , boundary condition (3.44) ($B_{r_{IV'}}^{AR}|_{r=oR_s} = B_{r_{V'}}^{AR}|_{r=oR_s}$) yields

$$\begin{aligned} m_n^{AR} [a_{n_{IV'}} I_1(m_n^{AR} oR_s) + b_{n_{IV'}} K_1(m_n^{AR} oR_s)] = \\ m_n^{AR} [a_{n_{V'}} I_1(m_n^{AR} oR_s) + b_{n_{V'}} K_1(m_n^{AR} oR_s)], \end{aligned} \quad (3.54)$$

and boundary condition (3.45) ($H_{z_{IV'}}^{AR}|_{r=oR_s} = H_{z_{V'}}^{AR}|_{r=oR_s}$) gives

$$\begin{aligned} \mu_{r,v} m_n^{AR} [a_{n_{IV'}} I_0(m_n^{AR} oR_s) - b_{n_{IV'}} K_0(m_n^{AR} oR_s)] = \\ m_n^{AR} [a_{n_{V'}} I_0(m_n^{AR} oR_s) - b_{n_{V'}} K_0(m_n^{AR} oR_s)]. \end{aligned} \quad (3.55)$$

3.7.6 Outer radius boundary of subdomain V' - AR analysis

At last, the boundary condition (3.46) ($A_{\phi_{V'}}^{AR}|_{r=R_o} = 0$) yields

$$a_{n_{V'}} I_1(m_n^{AR} R_o) + b_{n_{V'}} K_1(m_n^{AR} R_o) = 0. \quad (3.56)$$

3.7.7 Solving the ten simultaneous equations - AR analysis

The equation developed after the implementation of boundary condition are further simplified to separate the constant variables for the coefficient linked variables. Thereafter, the equations are solved simultaneously through the matrix method. (3.47) - (3.56) are rearranged as

$$1. a_{nI'} I_1(m_n^{AR} i R_s) + b_{nI'} K_1(m_n^{AR} i R_s) = 0, \quad (3.57)$$

$$2. m_n^{AR} [a_{nI'} I_1(m_n^{AR} i R_r) + b_{nI'} K_1(m_n^{AR} i R_r) - a_{nII'} I_1(m_n^{AR} i R_r) - b_{nII'} K_1(m_n^{AR} i R_r)] = 0, \quad (3.58)$$

$$3. m_n^{AR} [a_{nI'} I_0(m_n^{AR} i R_r) - b_{nI'} K_0(m_n^{AR} i R_r) - \mu_{rI'} a_{nII'} I_0(m_n^{AR} i R_r) + \mu_{rI'} b_{nII'} K_0(m_n^{AR} i R_r)] = 0, \quad (3.59)$$

$$4. m_n^{AR} [a_{nIII'} I_1(m_n^{AR} i R_{coil}) + b_{nIII'} K_1(m_n^{AR} i R_{coil}) - a_{nIII'} I_1(m_n^{AR} i R_{coil}) - b_{nIII'} K_1(m_n^{AR} i R_{coil})] = m_n^{AR} \frac{\pi L_1(m_n^{AR} i R_{coil})}{2m_n^2 AR} P_n^{AR}, \quad (3.60)$$

$$5. m_n^{AR} [a_{nIII'} I_0(m_n^{AR} i R_{coil}) - b_{nIII'} K_0(m_n^{AR} i R_{coil}) - a_{nIII'} I_0(m_n^{AR} i R_{coil}) + b_{nIII'} K_0(m_n^{AR} i R_{coil})] = m_n^{AR} \frac{\pi L_0(m_n^{AR} i R_{coil})}{2m_n^2 AR} P_n^{AR}, \quad (3.61)$$

$$6. m_n^{AR} [a_{nIV'} I_1(m_n^{AR} o R_{coil}) + b_{nIV'} K_1(m_n^{AR} o R_{coil}) - a_{nIV'} I_1(m_n^{AR} o R_{coil}) - b_{nIV'} K_1(m_n^{AR} o R_{coil})] = -m_n^{AR} \frac{\pi L_1(m_n^{AR} o R_{coil})}{2m_n^2 AR} P_n^{AR}, \quad (3.62)$$

$$7. m_n^{AR} [a_{nIII'} I_0(m_n^{AR} o R_{coil}) - b_{nIII'} K_0(m_n^{AR} o R_{coil}) - a_{nIV'} I_0(m_n^{AR} o R_{coil}) + b_{nIV'} K_0(m_n^{AR} o R_{coil})] = -m_n^{AR} \frac{\pi L_0(m_n^{AR} o R_{coil})}{2m_n^2 AR} P_n^{AR}, \quad (3.63)$$

$$8. m_n^{AR} [a_{nIV'} I_1(m_n^{AR} o R_s) + b_{nIV'} K_1(m_n^{AR} o R_s) - a_{nV'} I_1(m_n^{AR} o R_s) - b_{nV'} K_1(m_n^{AR} o R_s)] = 0, \quad (3.64)$$

$$9. m_n^{AR} [\mu_{rV} a_{nIV'} I_0(m_n^{AR} o R_s) - \mu_{rV} b_{nIV'} K_0(m_n^{AR} o R_s) - a_{nV'} I_0(m_n^{AR} o R_s) + b_{nV'} K_0(m_n^{AR} o R_s)] = 0, \quad (3.65)$$

$$10. a_{nV'} I_1(m_n^{AR} R_o) + b_{nV'} K_1(m_n^{AR} R_o) = 0. \quad (3.66)$$

The ten equation have been rearranged and the solution to the coefficients are determined through the matrix method as shown below

$$\begin{bmatrix}
 I_1(M^{a'}) & -K_1(M^{a'}) & 0 & 0 & 0 & 0 & 0 & 0 & 0 & 0 & 0 \\
 I^b(M^{b'}) & K^{b'}(M^{b'}) & -I^{b'}(M^{b'}) & -K^{b'}(M^{b'}) & 0 & 0 & 0 & 0 & 0 & 0 & 0 \\
 I^{a'}(M^{b'}) & -K^{a'}(M^{b'}) & -\mu_{r,I'} I^{a'}(M^{b'}) & \mu_{r,I'} K^{a'}(M^{b'}) & 0 & 0 & 0 & 0 & 0 & 0 & 0 \\
 0 & 0 & I^{b'}(M^{c'}) & K^{b'}(M^{c'}) & -I^{b'}(M^{c'}) & -K^{b'}(M^{c'}) & 0 & 0 & 0 & 0 & 0 \\
 0 & 0 & I^{a'}(M^{c'}) & -K^{a'}(M^{c'}) & -I^{a'}(M^{c'}) & K^{a'}(M^{c'}) & 0 & 0 & 0 & 0 & 0 \\
 0 & 0 & 0 & 0 & I^{b'}(M^{d'}) & K^{b'}(M^{d'}) & -I^{b'}(M^{d'}) & -K^{b'}(M^{d'}) & 0 & 0 & 0 \\
 0 & 0 & 0 & 0 & I^{a'}(M^{d'}) & -K^{a'}(M^{d'}) & -I^{a'}(M^{d'}) & K^{a'}(M^{d'}) & 0 & 0 & 0 \\
 0 & 0 & 0 & 0 & 0 & 0 & I^{b'}(M^{e'}) & K^{b'}(M^{e'}) & -I^{b'}(M^{e'}) & -K^{b'}(M^{e'}) & 0 \\
 0 & 0 & 0 & 0 & 0 & 0 & \mu_{r,V'} I^{a'}(M^{e'}) & -\mu_{r,V'} K^{a'}(M^{e'}) & -I^{a'}(M^{e'}) & K^{a'}(M^{e'}) & 0 \\
 0 & 0 & 0 & 0 & 0 & 0 & 0 & 0 & I_1(M^{f'}) & +K_1(M^{f'}) & 0
 \end{bmatrix}$$

$$\begin{bmatrix}
 a_{nI'} \\
 b_{nI'} \\
 a_{nII'} \\
 b_{nII'} \\
 a_{nIII'} \\
 b_{nIII'} \\
 a_{nIV'} \\
 b_{nIV'} \\
 a_{nV'} \\
 b_{nV'}
 \end{bmatrix}
 =
 \begin{bmatrix}
 0 \\
 0 \\
 0 \\
 m_n^{AR} \frac{\pi L_1(M^{c'})}{2m_n^2 AR} P_n^{AR} \\
 m_n^{AR} \frac{\pi L_0(M^{c'})}{2m_n^2 AR} P_n^{AR} \\
 -m_n^{AR} \frac{\pi L_1(M^{d'})}{2m_n^2 AR} P_n^{AR} \\
 -m_n^{AR} \frac{\pi L_0(M^{d'})}{2m_n^2 AR} P_n^{AR} \\
 0 \\
 0 \\
 0
 \end{bmatrix}
 \quad (3.67)$$

where $M^{a'} = m_n^{AR} i R_s$, $M^{b'} = m_n^{AR} i R_r$, $M^{c'} = m_n^{AR} i R_{coil}$, $M^{d'} = m_n^{AR} o R_{coil}$, $M^{e'} = m_n^{AR} o R_s$, $M^{f'} = m_n^{AR} R_o$; $I^{a'} = m_n^{AR} I_0$, $I^{b'} = m_n^{AR} I_1$, $K^{a'} = m_n^{AR} K_0$, and $K^{b'} = m_n^{AR} K_1$.

Again, the matrix has been assigned the above symbols for the sake of illustration. It should be noted that the first and last row in the matrix has been left with the actual Bessel functions.

3.8 AR Final solutions to the magnetic vector potential and the magnetic flux densities

3.8.1 Solutions to the magnetic vector potential - AR analysis

Establishment of the coefficients from the matrix (3.67) provides for the final determination of the magnetic vector potential equations given in Section 3.5 in (3.20) - (3.24). Therefore, inserting the coefficients into (3.20) - (3.24) gives the final solution to the magnetic vector potential.

3.8.2 Solutions to the radial magnetic flux densities

The final solution to the radial magnetic flux densities in the armature reaction analysis are obtained by inserting the determined solutions of the coefficients from (3.67) into Section 3.6.1 (3.26) - (3.30).

3.8.3 Solutions to the axial flux densities

The final solutions to the axial flux densities are determined by inserting the determined solutions to the coefficients from (3.67) into Section 3.6.2 (3.31) - (3.35)

3.8.4 The total magnetic flux density for the armature reaction

The total magnetic flux densities for the armature reaction B_T^{AR} are obtained by the algebraic sum of the radial magnetic flux densities and the axial magnetic flux densities for each of the subdomains of Figure 3.1 of the linear machine as

$$B_T^{AR}(r, z) = \sqrt{B_r^{2AR}(r, z) + B_z^{2AR}(r, z)} \quad (3.68)$$

The contour plots can be plotted from (3.68) and will be demonstrated in the validation section below.

3.9 Inductance calculation

Determination of the inductance of a linear oscillatory machine with radial magnetisation can be achieved by either calculating it from the flux linkage due to the machines own armature reaction field as in

$$L = \frac{\lambda}{i} \quad (3.69)$$

where L , λ and i are the inductance, flux linkage due to armature reaction and current through the coil, respectively,

or calculating it from the stored magnetic energy

$$L = \frac{2W}{i^2} \quad (3.70)$$

where W is the stored energy. The stored energy W has to be the summation of the stored energies in each considered subdomain e.g $W = W_{II} + W_{III} + W_{IV}$. Since the magnetic vector potential and magnetic fields in the coil subdomain have been determined in the previous section, inductance is calculated by employing (3.69). This implies that the flux linkage calculations due to the armature reaction field precedes the inductance calculations. It should be considered that since the machine under analysis is a single-phase machine, only the self-inductance is determined [62].

3.9.1 Flux linkage due to the armature reaction

The flux linkage due to machines armature reaction is obtained by

$$\psi_{AR} = \sum_{n=1,2,..}^{\infty} \phi_{ar} \quad (3.71)$$

where

$$\phi_{ar} = \frac{4\pi N_p N_t K_{dpm}}{m_n (oR_{coil} - iR_{coil})} \int_{iR_{coil}}^{oR_{coil}} r [a_{nIII'} I_1(m_n^{AR} r) + b_{nIII'} K_1(m_n^{AR} r) + Sr_1^{AR}] dr . \quad (3.72)$$

In (3.72), N_p , N_t are the number of number of pole pairs and number of series turns per phase per pole respectively. $N_t = \frac{N_{wp}}{2N_p}$ where N_{wp} is the number of series turns per phase. Sr_1^{AR} and K_{dpm} in (3.72) are given as in (3.25)

$$Sr_1^{AR} = \frac{\pi L_1(m_n^{AR} r)}{2m_n^2 AR} P_n^{AR} ,$$

$$K_{dpm} = \sin(m_n \tau_w / 2) / (m_n \tau_w / 2) \sin(m_n \tau_{wp} / 2) , \quad (3.73)$$

3.9.2 Self-inductance calculation

With the phase winding flux linkage due to its own armature obtained in 3.9.1, the self-inductance of the winding is determined by

$$L_{si} = \frac{\psi_{AR}}{J_0 \tau_w (oR_{coil} - iR_{coil}) / N_t} \quad (3.74)$$

3.10 Comparison of the armature reaction model with finite element method (FEM)

For the validation of the armature reaction model, the dimensions presented in 2.1 are employed for both the analytical model and FEM. A commercial FEM package called MagNet by infolytica inc. is utilised to compare the field distribution due to the armature reaction with the analytical model. In the FEM model, as explained in the previous chapter, periodic boundaries at the axial edges of the machine are adopted to ensure the model suits the assumption that the machine is infinitely long along the axial edges. As shown in the Figure 3.1, the machine has three coil poles with one split in half and placed near the axial edges of the machine. This implies that, whatever number of turns the full coils are assigned, half that number is assigned to the split coil poles. The machine is calculated at a current density of 5 A/mm^2 and a fill factor of 0.55. In Figures 3.3 and 3.4, the radii; $R_{ag1} = iR_s + h_{ics} + (h_{ipm} + g_1)/2$, $rn = iR_s + h_{ics} + h_{ipm} + g_1 + h_{coil}/2$ and $R_{ag2} = iR_s + h_{ics} + h_{ipm} + g_1 + h_{coil} + (g_2 + h_{opm})/2$.

3.10.1 AR - Radial flux density distribution

The radial flux densities in the subdomains II' , III' and IV' as compared to FEM are presented in Figure 3.3.

The analytical model in comparison to the FEM model matches well as can be seen in Figure 3.3. Since the machine is assumed infinitely long on the axial edges, there is no need to move the coil within the machine to show how the coil movements might influence the flux concentration in the yokes.

3.10.2 AR - Axial flux density distribution

The axial flux densities in the subdomains II' , III' and IV' are compared between the FEM package and the analytical model. The results obtained are presented in Figure 3.4.

From Figure 3.4, it can be seen that there is good correlation between the results of FEM and those of the analytical model. It should be noted that the plots are obtained at the center line of each II' , III' and IV' subdomains

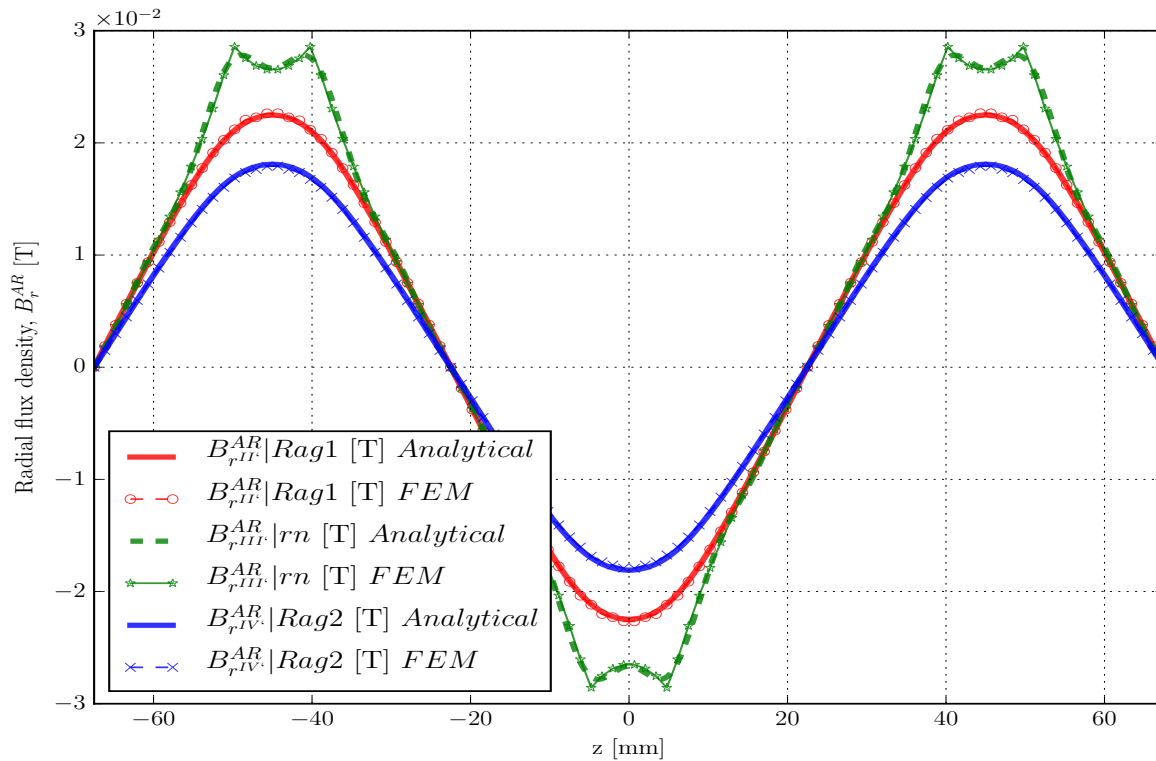


Figure 3.3: Radial flux density distribution due to AR

3.10.3 AR - Contour plot comparison

In this section, a comparison between the contour plots generated by FEM and the contour plots as well as the field line plots generated by the analytical model is undertaken. For better illustration the plots generated from the analytical model are separated so as to provide a better understanding and comparison.

From Figure 3.5 and 3.6, it can be seen that the analytical model predicts the field behaviour very well and correlates well with the results obtained from FEM.

3.11 Summary and conclusion for the AR analysis

The Armature reaction results presented on in the validation section indicates that the model has been developed accordingly and correlates well with the results obtained from FEM. A current density of $5A/mm^2$ was adopted with a fill factor of 0.55. The simulation, just as for the PM analysis, had periodic boundaries at the edges of the axial edges of the machine according to the assumptions considered. The axial and radial flux densities for the armature reaction are low because the coils are air-cored which also allows the machines to have lower inductance. This is expected for these types of machines as can be seen in [86; 40]. The radial and axial flux densities compare well with FEM just as the contour plots in Figure 3.5 and 3.6.

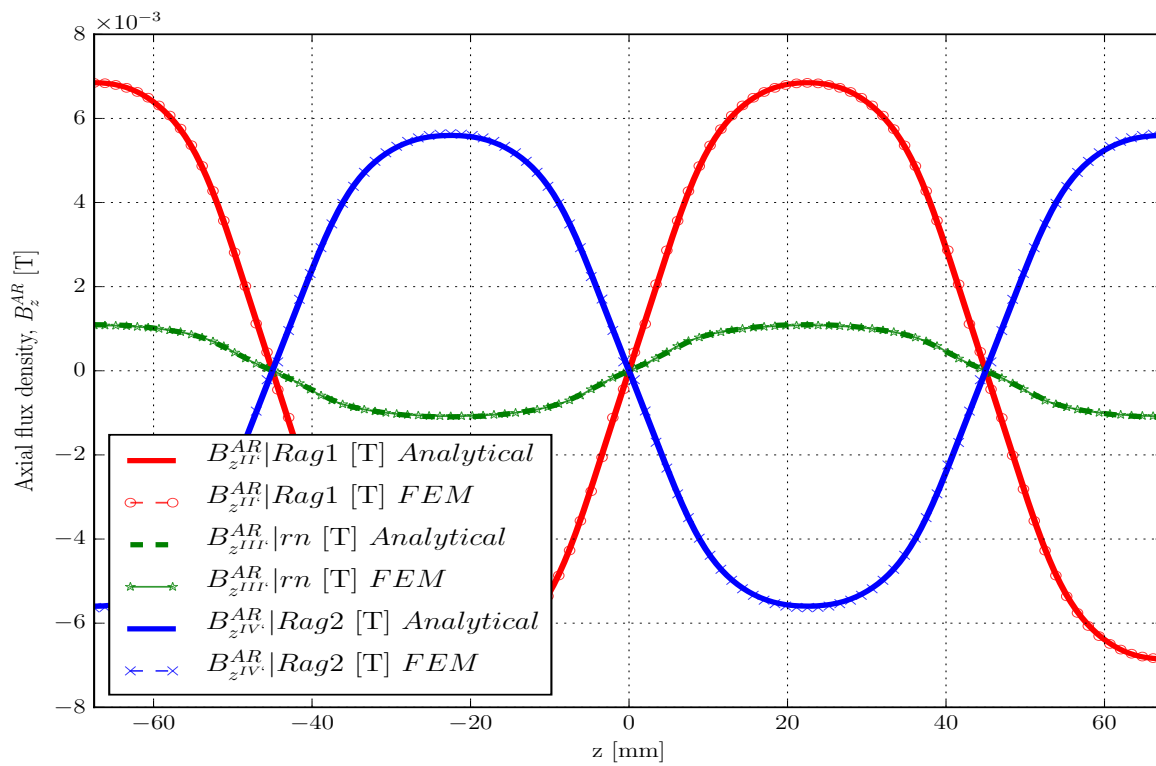


Figure 3.4: Radial flux density distribution due to AR

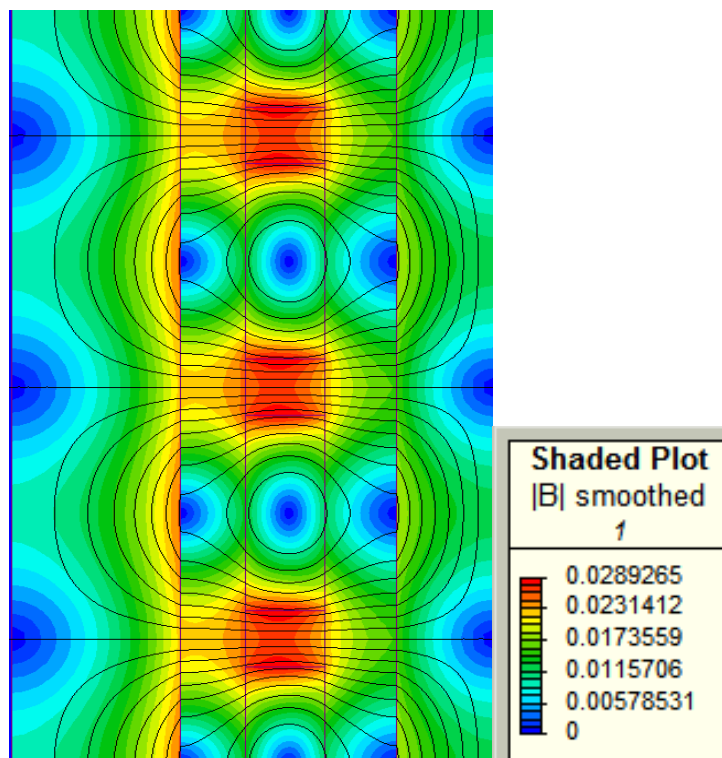


Figure 3.5: Contour plot obtained from FEM

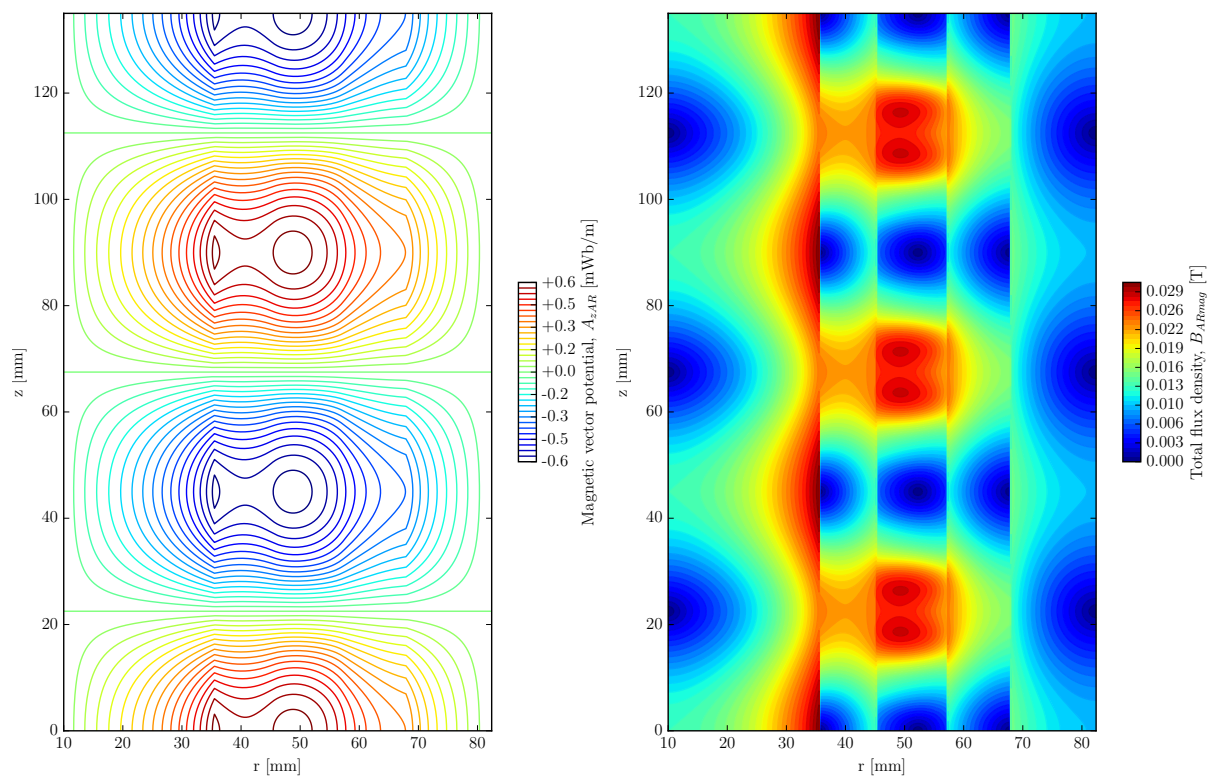


Figure 3.6: Field line plot and contour plot obtained from the analytical model

Chapter 4

Prediction of Force and EMF

4.1 Introduction

In the same way as for rotary permanent magnet machines, linear oscillatory machines are guided by Faraday's laws and Ampere's laws in the development of electromagnetic forces. This implies that electromotive force has to come from either a current source or a permanent magnet source. In the magnetic fields, force can be classified as electromagnetic and electrodynamic. Electromagnetic forces occur mostly due to field alignment or attraction. For this reason electromagnetic forces focuses on minimising the magnetic stored energy. Therefore if the magnetic stored energy or the co-energy is determined, it is possible to determine the electromagnetic force which can be obtained from

$$F_{em} = -\frac{\partial W_m}{\partial x}(\lambda, x) = \frac{1}{2}i^2 \frac{\partial L}{\partial x} N \quad (4.1)$$

where the flux linkage λ and the displacement x are taken as independent variables. W_m, F_{em}, L and i are the magnetic stored energy, the developed force, the inductance and the current. In a case where the co-energy is considered, the force is obtained from

$$F_{em} = \frac{\partial W'_m}{\partial x}(i, x) = \frac{1}{2}L^2 \frac{\partial L}{\partial x} N \quad (4.2)$$

where W'_m is the co-energy. The derivative of the magnetic stored energy or the co-energy can therefore be employed to determine the required force. The accuracy of the co-energy method is however low because of the adoption of finite difference approximations [34].

The second method for the determination of the force is the Maxwell Stress Tensor (MST) method. This method involves obtaining the stress at the surfaces of the permanent magnet array at the boundary between the permanent magnets and the air-gap region and summing them up. In short the MST can be described as a method involving calculation of the surface integral over a subdomain. The MST method has been considered an accurate method especially with iron-cored coil topologies that do also experience cogging forces due to slotted coils [81; 65; 89]. The MST can be expressed as

$$\mathbf{F} = \frac{1}{2\mu_0} \oint_s B_n^2 \hat{\mathbf{n}} ds, \quad (4.3)$$

where B_n is the normal component of \mathbf{B} to the surface [75].

The MST was adopted in the calculation of the cogging torque for a surface permanent magnet motor by Zarko *et al* in [61]. The MST has also been utilised by Krop *et al* for

the formulation of the forces on a surface mounted permanent magnet linear synchronous motor with slotted armature coils. He further explains that the Lorentz force method could not be adopted for his slotted structure because it does not consider the magnetisation of the steel teeth [60]. Amara *et al* adopts the MST to determine the force for surface mounted permanent magnet tubular linear machine for the same reason as Krop *et al*. Most recent work by Ouagued *et al*, the cogging forces for a linear permanent magnet machine is calculated by employing the MST method [64]. Gysen *et al* determines the force in the analysis of a tubular permanent-magnet actuator with a slotted armature by adopting the MST [81].

It is therefore observed that for the sake of considering the magnetisation of the steel teeth in slotted translators or stators of permanent-magnet machines, the Maxwell Stress Tensor method, which is capable of taking steel teeth into consideration, is suitable. The method has been adopted for calculation of forces, cogging forces and cogging torques by a number of authors among others [58; 90; 91; 92; 93]. The selection of the line of integration and the model discretisation are the most critical for the Maxwell Stress Tensor method to be accurate [94].

In the third method, which has been adopted in this work, electrodynamic forces are achieved by the interactions between a current carrying conductor and the magnetic field, in which case its called the Ampere's force

$$F_{em} = l_{ac} I \times \mathbf{B} \text{ N} , \quad (4.4)$$

where l_{ac} is the conductor length, \mathbf{B} is the magnetic flux density and I is the current. Similarly, the Lorentz Force Method can be employed to determine the force developed due to the current density and the magnetic flux density interactions and can be expressed as,

$$F_{em} = \mathbf{J} \times \mathbf{B} \text{ N/m}^2 , \quad (4.5)$$

or in the integral format as,

$$\mathbf{F} = \int_v (\mathbf{J} \times \mathbf{B}) dv , \quad (4.6)$$

where \mathbf{J} is the current density, A/m^2 . In a region consisting of the current density \mathbf{J} and the magnetic flux density \mathbf{B} , a force \mathbf{F} per volume is obtained. The volume integral of the Lorentz force is therefore the calculation of the total magnetic force on an object. Once the magnetic flux densities are accurately determined in the machines air-gap, the Lorentz force method can be applied to accurately calculate the force density. The Lorentz force method is very accurate and suitable for air-cored machines and not iron cored as the cogging forces affect the accuracy of the determination of the force.

Kim *et al* adopts the Lorentz force method to determine the thrust force for a linear brushless DC motor [95]. In a similar procedure, Li *et al* in [96] calculates for the thrust force by employing the Lorentz force for an air-cored flat double-sided PM linear synchronous machine. In [62; 88], Wang *et al* employs the Lorentz force method to determine the force of the radially magnetised linear tubular machine. Tsai and Chiang in [72] employs the Lorentz method to determine the force of an actuator. the Lorentz force method application can also be found in [71; 75].

The Lorentz method is suitable for electrical machines with air-cored coils. The Lorentz force method is therefore adopted for the calculation of thrust force and total force for this work and is demonstrated later.

When operating the linear oscillatory machine at no-load, the magnetic flux linkage across the coils calculated is a result of the field produced by the permanent magnets only. From Faraday's magnetic induction, the induced voltage can be determined from the obtained flux linkage by

$$v_{\lambda} = \frac{d\lambda}{dt}, \quad (4.7)$$

where v_{λ} is the induced voltage. From Figure ??, at no-load, the induced voltage v_{λ} is equal to the electromotive force voltage (emf) of the machine. The resultant magnetic flux linkage can be obtained by the algebraic summation of the flux linkage obtained from the permanent magnet field and the armature reaction field in the *III* subdomain for the permanent magnet analysis as obtained in Chapter 2 and *III'* subdomain for the armature reaction calculations illustrated in Chapter 3.

The analytical formulation of the magnetic flux linkage and the electromotive force is presented in the sections to below.

4.2 Force Prediction formulations

4.2.1 Assumptions for the formulation of global quantities

The following assumptions are taken for the formulation of the force and the EMF.

1. The stator cores are assumed to have a relative permeability of $\mu_r = 1000$ which incorporates the yokes in the calculations and provides means to monitor saturation within the yokes,
2. The effects of the eddy currents are neglected.
3. The axial length of the machine is assumed infinitely long and periodic in the z -direction,

4.2.2 Thrust Force predictions

For the sake of convenience, the magnetic vector potential and the magnetic flux density expressions obtained from the influence of the permanent magnet field only (Chapter 2) for the air-gap region are again rewritten from Sections; 2.4.3, 2.5.1 and 2.5.2 as

The magnetic vector potential for the open circuit field

$$A_{\phi III}(r, z) = \sum_{n=1, \dots}^{\infty} [a_{n III} I_1(m_n r) + b_{n III} K_1(m_n r)] \sin(m_n z) \quad (2.85) .$$

The radial magnetic flux density for the open circuit field

$$B_{r III}(r, z) = \sum_{n=1, \dots}^{\infty} -m_n [a_{n III} I_1(m_n r) + b_{n III} K_1(m_n r)] \cos(m_n z) \quad (2.95) .$$

The axial magnetic flux density for the open circuit field

$$B_{z III}(r, z) = \sum_{n=1, \dots}^{\infty} m_n [a_{n III} I_0(m_n r) - b_{n III} K_0(m_n r)] \sin(m_n z) \quad (2.100) ,$$

where

$$m_n = (2n - 1) \frac{\pi}{\tau_p} \quad (2.61) .$$

In addition to the equations again for convenience is Figure 4.1 in which the coil displacement z_d is clearly seen. It should also be noted that $iR_{coil} = iR_m + g1$ and $oR_{coil} = oR_m - g2$ from the same figure. Other machine parameters are also illustrated to give a quick grasp to the mathematical formulations for the forces and the electromotive force.

Thrust force is the force along the direction of the oscillatory linear motion. Accordingly, the coil experiences a force caused by the PM field and the winding current when a coil carries a current density J . By employing the Lorentz force method, the formulation for the thrust force is given by

$$F_w = - \int_{z - \frac{\tau_w}{2}}^{z + \frac{\tau_w}{2}} \int_{iR_{coil}}^{oR_{coil}} 2\pi r J B_{r III}(r, z) dr dz \quad (4.8)$$

where $B_{r III}$ is the radial magnetic flux density in the air-gap considering only the field from the permanent magnets. The boundaries of a winding coil area are considered to be $r_i = iR_{coil}$, $r_o = oR_{coil}$, $z_{l1} = z - \tau_w/2$ and $z_{l2} = z + \tau_w/2$. (4.8) can be expressed as

$$F_w = \sum_{n=1, 2, \dots}^{\infty} F_n \cos(m_n z) , \quad (4.9)$$

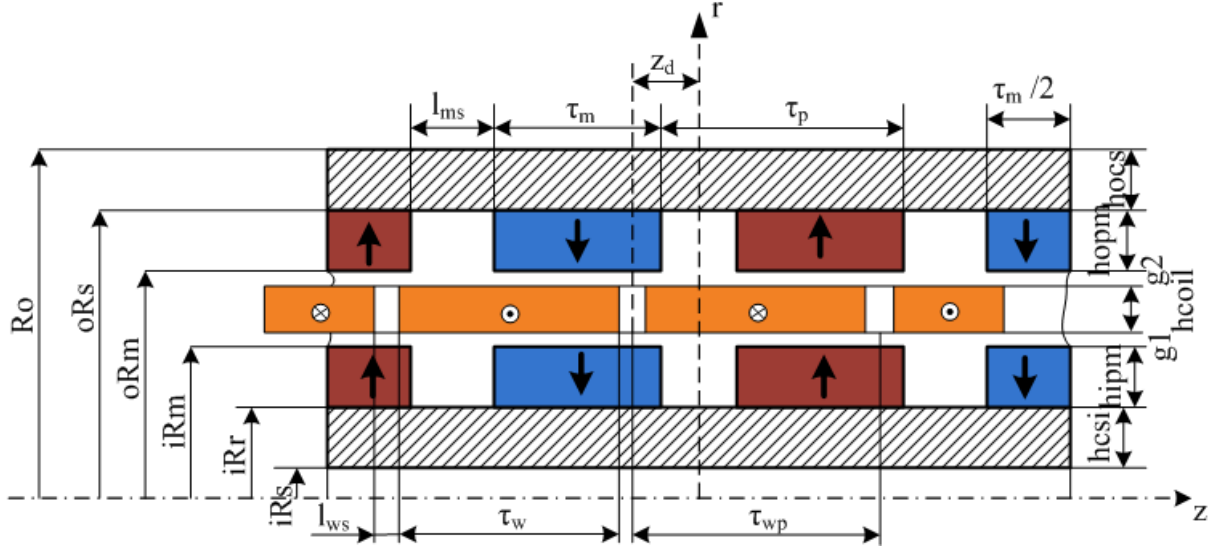


Figure 4.1: Linear machine to illustrate displacement of the coil

where

$$F_n = 2\pi\tau_w JK_{dn} \int_{iR_{coil}}^{oR_{coil}} r [a_{nIII} I_1(m_n r) + b_{nIII} K_1(m_n r)] dr . \quad (4.10)$$

In (4.10), τ_w is the winding axial length and K_{dn} is the $(2n - 1)^{th}$ harmonic winding distribution factor, which is given by

$$K_{dn} = \frac{\sin \frac{m_n \tau_w}{2}}{\frac{m_n \tau_w}{2}} . \quad (4.11)$$

4.2.3 Total force

Taking into consideration a number of series connected coils in a phase winding with each coil having a winding pitch τ_{wp} , the total force on a phase winding with a current i is predicted by

$$F_{wp} = \left[\sum_{n=1,2,\dots}^{\infty} K_{tn} \sin \left(m_n z - \frac{m_n \tau_{wp}}{2} \right) \right] i \quad (4.12)$$

where

$$K_{tn} = \frac{2\pi K_{dpm} N_{wp}}{(oR_{coil} - iR_{coil})} \int_{iR_{coil}}^{oR_{coil}} r [a_{nIII} I_1(m_n r) + b_{nIII} K_1(m_n r)] dr . \quad (4.13)$$

K_{tn} being the torque constant of the $(2n - 1)^{th}$ harmonic. $K_{dpm} = K_{pm} K_{dn}$ is called the winding factor; N_{wp} is the number of series turns per phase. K_{pm} , the winding pitch factor is given by

$$K_{pm} = \sin \left(\frac{m_n \tau_{wp}}{2} \right) \quad (4.14)$$

4.3 Flux linkage and EMF calculations

The linear machine presented having a moving coil entails that there are two radii parameters that are key to determining the flux linkage of the armature coil. The radii are boundaries of the coil region with iR_{coil} being the inner armature winding radius and oR_{coil} being the outer radius of the armature windings respectively. $z_1 = z - \frac{\tau_w}{2}$ and $z_2 = z + \frac{\tau_w}{2}$ the difference of which is the width of the coil. Therefore, the area of the coil is $\tau_w(oR_{coil} - iR_{coil})$. The coil flux linkage for a single coil due to the flux linkage from the permanent magnet field is then obtained from

$$\psi_w = \frac{N_w}{\tau_w(oR_{coil} - iR_{coil})} \int_{z - \frac{\tau_w}{2}}^{z + \frac{\tau_w}{2}} \int_{iR_{coil}}^{oR_{coil}} 2\pi \times A_{\phi III}(r, z) dr dz . \quad (4.15)$$

Which can also be expressed as

$$\psi_w = \sum_{n=1,2,\dots}^{\infty} \phi_n \sin(m_n z) , \quad (4.16)$$

where ϕ_n represents

$$\phi_n = \frac{2\pi\tau_w K_{dn}}{m_n} \int_{iR_{coil}}^{oR_{coil}} r [a_{nIII} I_1(m_n r) + b_{nIII} K_1(m_n r)] dr . \quad (4.17)$$

Taking the time derivative of the flux linkage ψ_w results into the determination of the induced electromotive force per phase

$$e_w = -\frac{d\psi_w}{dt} = -v \frac{d\psi_w}{dz} = \left[-\sum_{n=1,2,\dots}^{\infty} K_{en} \sin\left(m_n z - \frac{m_n \tau_{wp}}{2}\right) \right] v \quad (4.18)$$

where v is the translator linear velocity.

$$K_{en} = -\frac{2\pi K_{dpn} N_w}{(oR_{coil} - iR_{coil})} \int_{iR_{coil}}^{oR_{coil}} r [a_{nIII} I_1(m_n r) + b_{nIII} K_1(m_n r)] dr \quad (4.19)$$

is the $(2n - 1)$ th harmonic back-emf constant. The winding factor K_{dpn} is the product of two factors namely the distribution factor, $K_{dn} = \sin(m_n \tau_w / 2) / (m_n \tau_w / 2)$ and the winding pitch factor, $K_{pn} = \sin(m_n \tau_{wp} / 2)$. Therefore $K_{dpn} = K_{pn} K_{dn}$.

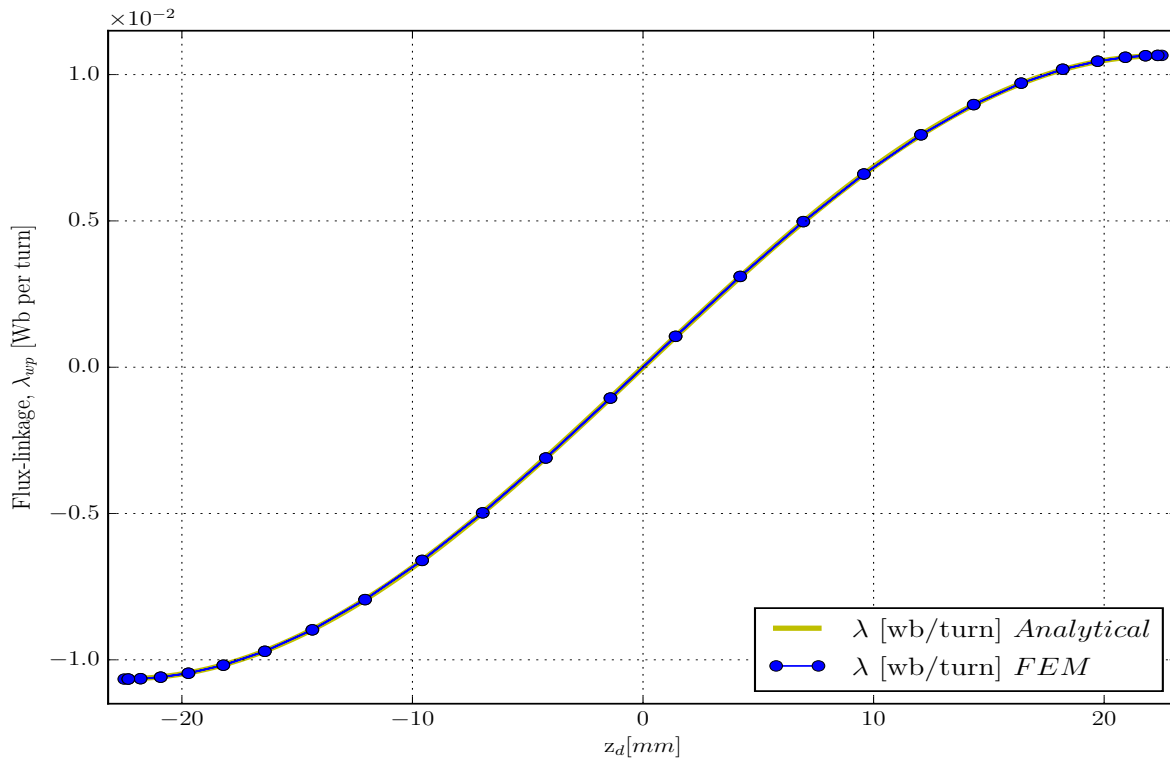


Figure 4.2: Flux linkage with armature position

4.4 Validation of the analytically derived global quantities by FEM

4.4.1 Flux linkage and EMF comparison between FEM and analytical

Flux linkage results are presented below. The ideal flux linkage plot against armature displacement position is a straight line. The actual flux linkage against the armature position and compared to FEM appears as shown in Figure 4.2.

In non-ideal terms, flux linkage cannot be obtained as a straight line. Therefore, the Figure 4.2 shows a non-ideal form of a flux linkage. From Figure 4.2, it can also be observed that the flux linkage is lowest when the permanent magnet poles are in vertical line with the coils ($z_d = 0 \text{ mm}$).

The EMF is obtained by taking the derivative of the flux linkage with time as can be seen in Figure 4.3. The EMF is analytically obtained through taking employing the splines on the flux linkage and taking the derivative to obtain the electromotive force.

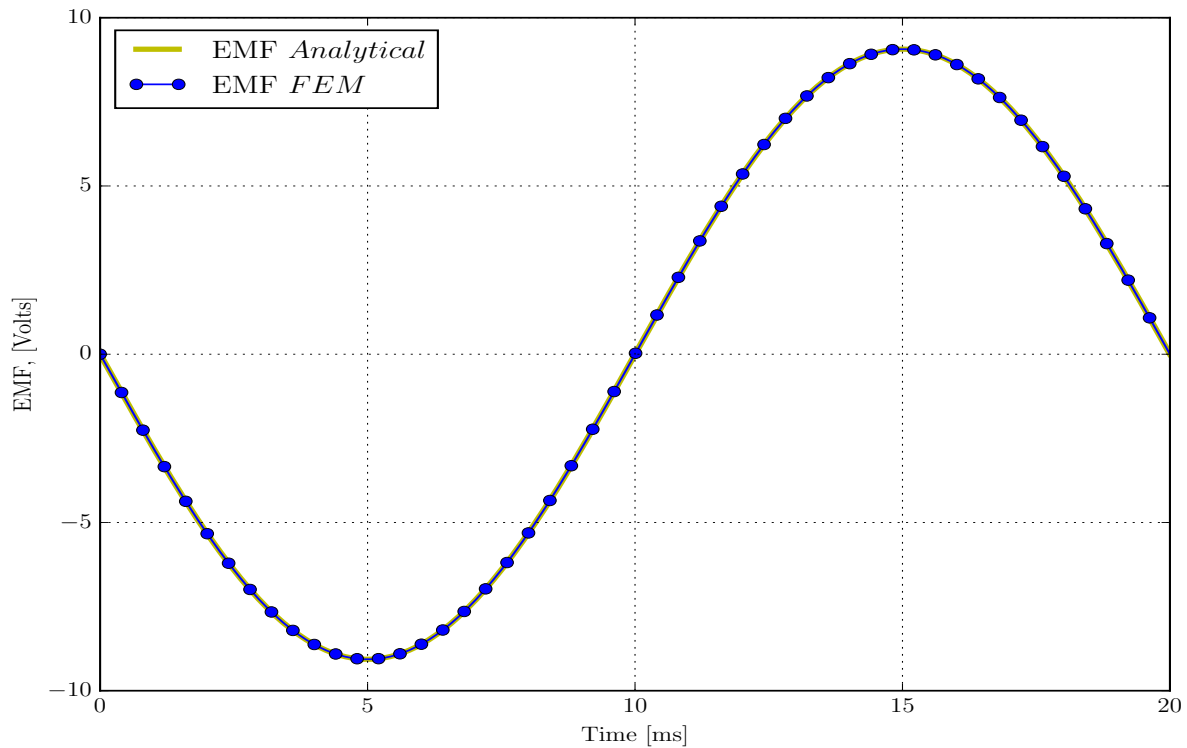


Figure 4.3: Induced voltage obtained against time

4.4.2 Thrust force comparison between FEM and analytical

The analytically determined thrust force is compared with FEM can be seen in Figure 4.4. The maximum thrust force is obtained when the coil aligns with its pair of PMs. Again, good correlation is obtained between FEM and the analytical model.

4.5 Summary and conclusion

The analytical formulations for the global quantities have been developed. A limited number of harmonics upto the 17th harmonics of the $(2n - 1)^{th}$ harmonic for obtaining the magnetic flux densities of the open-circuit field and the armature reaction circuit. The as higher harmonics are attempted the coefficient matrix becomes ill conditioned resulting into some coefficients becoming too large and too small which becomes computationally difficult. Per subdomain however, higher harmonics could be reached especially in the air-gap subdomains (28th harmonic could be obtained) for both the open circuit and the armature reaction. The accuracy of the global quantities were not much affected by the number of harmonics as observed in the results of the thrust force (Figure 4.4) and those obtained for the no load flux linkage (Figure 4.2) which are in good agreement with the results obtained from FEM.

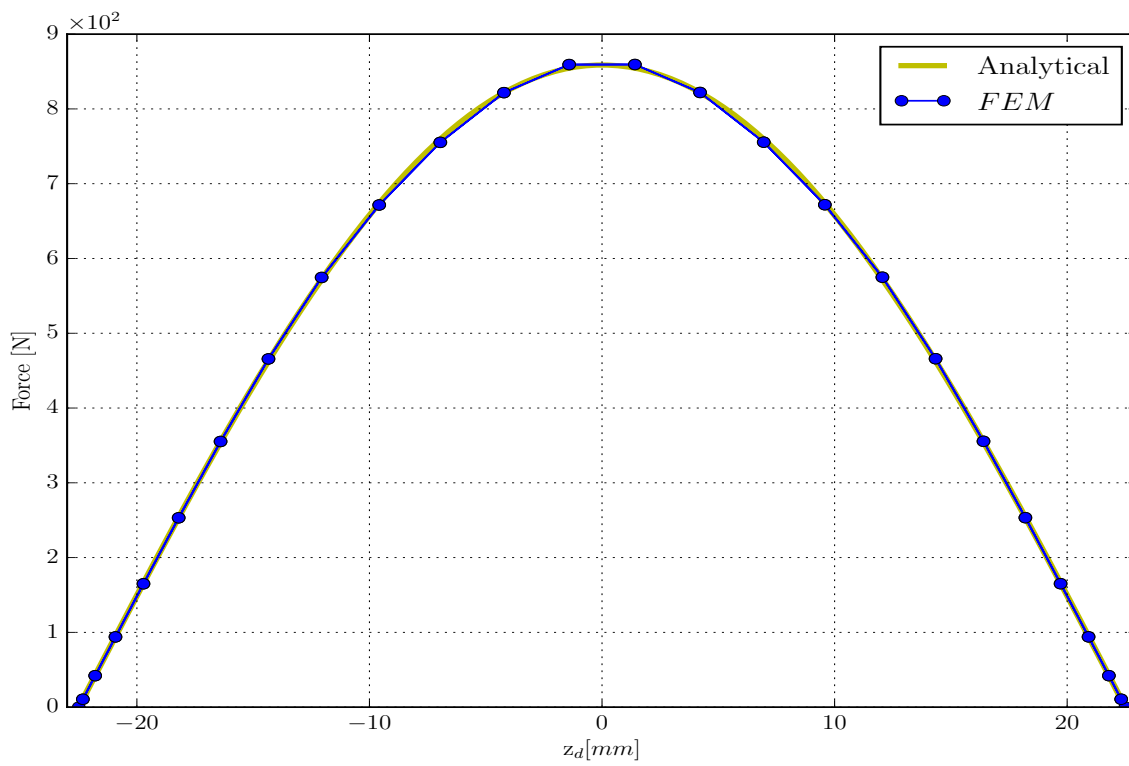


Figure 4.4: Thrust force with displacement

Chapter 5

Discrete PM series analytical model

5.1 Introduction

In this Chapter, an analytical model is developed to approximate the behaviour of a finite length tubular permanent magnet longitudinal flux oscillating machine. The consideration of the machine in its actual geometry as a finite length machine implies that the machine, like any other linear machine, will have some end effects at the axial edges of the linear machine. In rotary machines, end effects are not present because the coil flux is linked in a closed loop with other coils. In linear machines however, the flux from the permanent magnets placed at the axial edges of the machine, is not fully linked to the next permanent magnet. Some magnetic flux from the permanent magnets takes a path through the air and back into the machine yoke (fringing flux), while some flux leaks out of the machine. These effects are designated as *longitudinal end effects* and are caused by a finite length structure. Transverse end effects may also occur but for a transverse flux topology. In this case, the topology under study is a longitudinal flux machine.

Selcuk and Kurum [97] distinguishes longitudinal end effects into static and dynamic. Static effects are differences in flux distribution because of the finite length of the machine geometry; also end effects caused by the finite geometry due to induced currents in the translator. Dynamic longitudinal end effects are effects caused by the movement of the translator. When the translator is longer than the permanent magnet structure, its translational movements cause it to move beyond the machines length, thereby creating fringing flux. In a similar paper, Cupertino *et al* in [?] and Vermaak [98] looked at the importance of understanding the end effects and their influence on machine performance.

The main difference between the analytically obtained results for the assumption where axial edges of the machine are considered infinitely long, illustrated in Chapters 2, 3 and 4, and the infinitely long but with discrete permanent magnet arrangement is that end effects can be demonstrated to some extent. With the model developed in Chapter 2, the amplitude of the flux density distribution remains constant even at the axial edges of the machine, while for an infinitely long machine with discrete PM arrangements, most of the end effects can be demonstrated.

A fully finite length analytical model employing the subdomain method has not been presented in any literature analysed so far. Approximate approaches have been considered as observed in [88], where Wang *et al* considered a finite armature length which is

replicated at τ_l distance apart, while the PM and yoke structures are maintained to be infinitely long. With a similar concept, Wang *et al* in [63; 54] takes the single sided Halbach permanent magnet array with a finite length, but replicated infinitely with τ_l between the Halbach arrays. The iron yokes were assumed infinitely permeable and infinitely long. Wang *et al* in both papers [88; 54] argues that by taking either the armature or the PM array as discrete finite geometries replicated infinitely, analytical formulations could illustrate the end effects such as fringing end effects on the variation of flux distribution at the axial edges of the machine.

Chen *et al* [42] also adopts the method employed by Wang *et al* by assuming the moving permanent magnet array to be replicated infinitely and in so doing a Fourier expansion method is possible to solve for the Maxwell equations. The iron yokes are taken as infinitely long and permeable.

5.2 Challenges to obtain a finite machine length analytical model and alternative approach

A finite length machine is illustrated in Figure 5.1. The analytical solution developed in the previous chapters considered the machine edges as infinitely long and hence could be truncated at any point without any distortions to the magnetic flux densities peak values. In this chapter, the full permanent magnets are considered as it is deemed more practical to construct.

The finite length machine experiences end effects at the axial edges of the machine which have been illustrated in Figure 5.1.

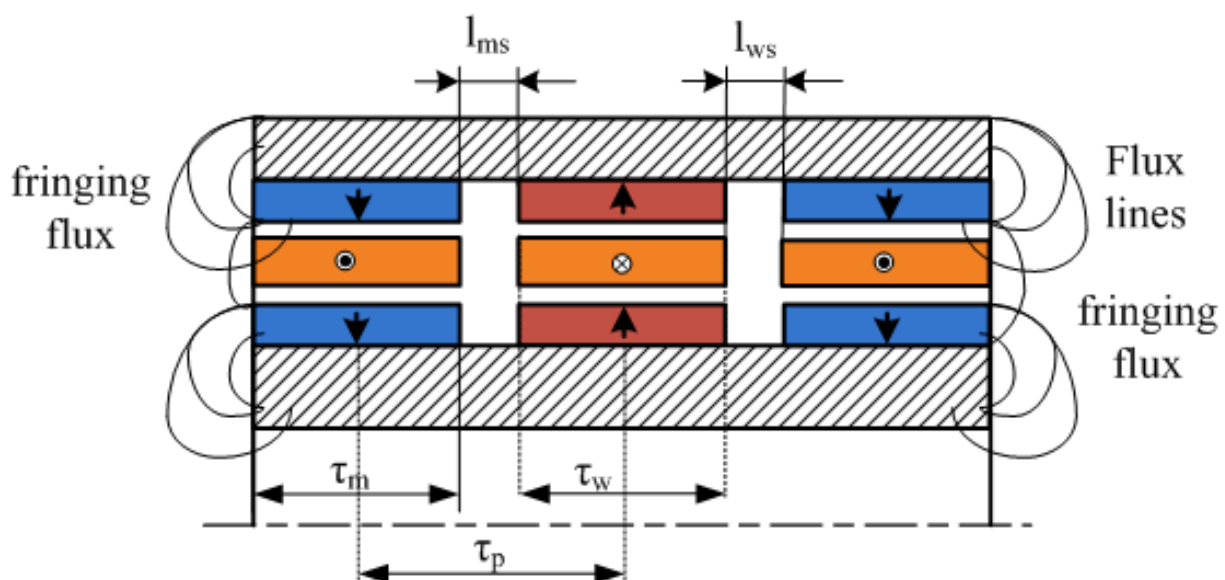


Figure 5.1: Illustration of a finite length machine with end effects

Determining the magnetic flux density distribution for a finite length machine by employing the subdomain method (Fourier expansion and separation of variables technique) is very involving according to the many attempts that were conducted. The complexity is mainly because of the many additional boundary conditions introduced on the axial edges of the linear machine. The magnetic flux behaviour at the machine axial ends is such that some flux fringes and some flux leaks out from both the PMs and the yokes of the machine. It should be noted that some flux does not cross the axial boundary of the iron yoke.

In the quest to finding the solution to the finite length machine model and also by observing the behaviour of the flux at the axial edges of the machine, an attempt was made to employ asymptotic boundary conditions at all axial edges of the machine. Asymptotic boundary conditions are simply a mixture of boundary conditions, that is a combination of the Dirichlet boundary conditions (the field lines are tangential to the boundary line/ field lines do not cross the boundary line) and the Neumann boundary condition (Flux lines cross the boundary line in a certain known pattern).

$$\frac{\partial A(z)}{\partial n} + h(z)A(z) = w(z) \quad (5.1)$$

where $h(z)$ and $w(z)$ are explicit known functions on a boundary. The asymptotic boundary condition is mainly employed in finite element methods in creating open boundaries as explained by Bargallo [80, Page 20 - 29]. Implementing the asymptotic boundary conditions in a fully analytical approach results into a complex of equations with which the determination of coefficients, because of an ill-conditioned matrix, does not lead to the required coefficients. As the advantage of the analytical model is being faster than FEM, with the asymptotic boundary approach, getting top the solutions becomes computationally expensive and impractical.

Yet another attempt was made where an infinite series of linear machines are placed τ_l apart as shown on Figure 5.2. In this case the magnetisation vector can easily be obtained through the Fourier expansion. However, boundary conditions still have to be applied on the axial edges of the machine yokes.

In Figure 5.2, the distance τ_l must be much larger than τ_p and at the same time a multiple of τ_p to ensure that τ_l is also a multiple of τ_p .

Wang *et al* [53, Part I] calculated fringing effects on a tubular PM linear machine. In their work, Wang *et al* takes the radial flux density to be zero at the axial boundary of the iron yokes of the armature which is replicated with a distance of τ_l in between. The iron yokes are assumed infinitely permeable and infinitely thick. However, there is an equation developed for the air-gap between the iron yokes. It is not clear how Wang *et al* developed the expression for the armature iron yoke subdomain and also how the coefficients were determined.

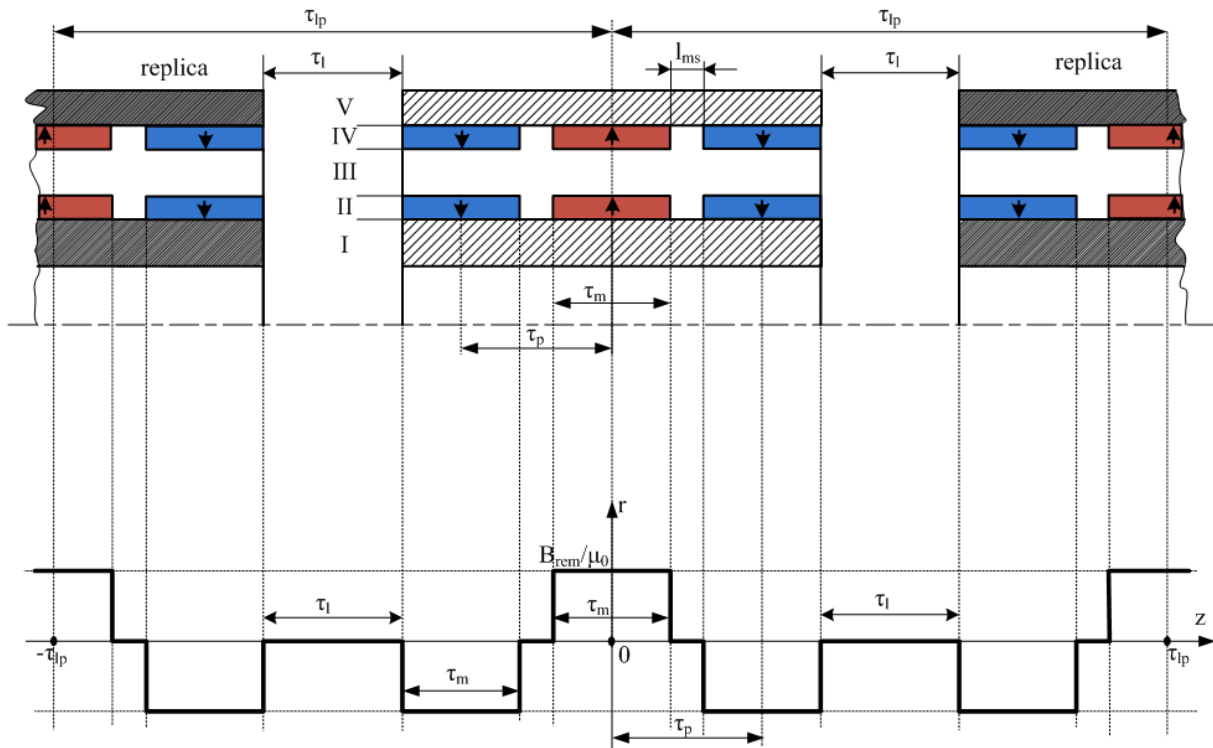


Figure 5.2: Discrete linear machines in infinite series

In the attempt made for this work, it was discovered that the calculations still needed to involve the similar boundary conditions to the asymptotic conditions which again leads to ill conditioned coefficient solution matrices. Wang *et al* could easily find the solution to the coefficients in the gap between the armatures because the permanent magnets and the yoke was assumed infinitely long and provided the flux density between the discrete armatures. This is not the case while observing Figure 5.2.

These challenges led to an alternative approach to analytically predict the magnetic flux density distribution of a finite length machine by taking the yoke as infinitely long and having discrete PM arrays which depict the arrangement of the PMs in the finite length machine. The iron yokes are considered with finite permeability.

5.3 Alternative analytical model approximating the magnetic flux density distribution of a finite length machine

The alternative approach involves taking the iron yokes as infinitely long but with finite permeability while considering the permanent magnets as an infinite series of discrete arrays. Figure 5.3 illustrates the diagram for the alternative approach to developing the analytical model that approximates the magnetic flux density distribution similar to the finite length machine. The determination of the magnetisation vector does not differ

from the assumption taken in the previous model from Figure 5.2. The Fourier series for the magnetisation vector, which is determined later in this chapter, provides an accurate behaviour of the field from the PMs as long as the distance between the discrete PMs (τ_l) is much larger than the pole pitch τ_p .

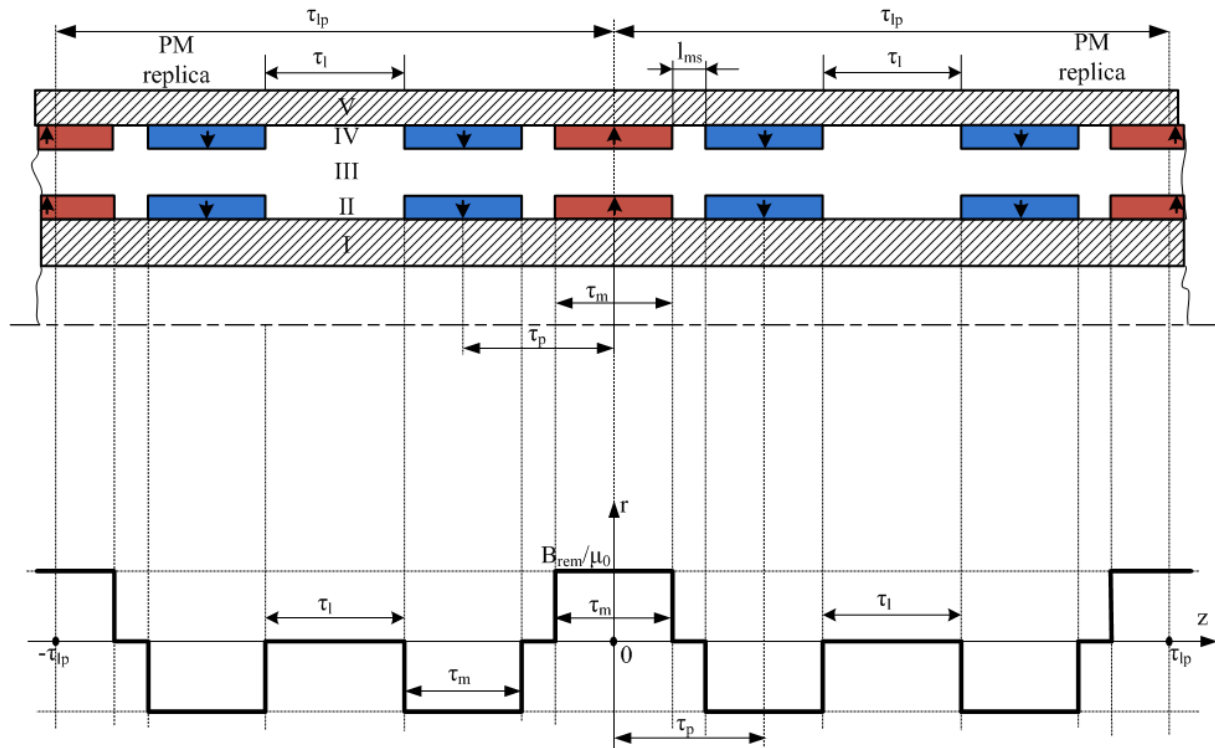


Figure 5.3: An axisymmetrical structure of the LOG with infinitely long iron yokes and with finite permeability (series PM-array). Below the machine is the magnetisation vector for radial magnetisation

5.3.1 Assumptions

For the calculation of the magnetic field due to the permanent magnet field, the following assumptions are taken into consideration.

1. Discrete series of the permanent magnet arrays, which are separated by τ_l , are arranged in an infinitely long series while the iron yokes are infinitely long,
2. The iron yokes are considered to have finite permeability so that saturation levels can be monitored,

5.3.2 General solution to the Laplace Equation (PM -finite-length)

In cylindrical coordinates, the Laplace is represented by

$$\frac{\partial^2 A_{\phi^i}}{\partial z^2} + \frac{\partial^2 A_{\phi^i}}{\partial r^2} + \frac{1}{r} \frac{\partial A_{\phi^i}}{\partial r} - \frac{1}{r^2} A_{\phi^i} = 0, \quad (5.2)$$

with i representing the subdomains which have no field sources. For the finite length of the machine, the solution obtained for the Laplace equation in the previous model is adopted

$$A_{\phi^f}(r, z) = \sum_{n=1,2..}^{\infty} ([E_n I_1(mr) + F_n K_1(mr)] \cos(mz) + [G_n I_1(mr) + H_n K_1(mr)] \sin(mz)). \quad (5.3)$$

For the analysis of the finite length model,

$$G_n = 0$$

and

$$H_n = 0$$

where I_1 and K_1 are Modified Bessel functions of the first and second kind of order 1 which are independent of each other. The Laplace equation is therefore expressed as

$$A_{\phi^f}(r, z) = \sum_{n=1,..}^{\infty} [a_n I_1(m_n r) + b_n K_1(m_n r)] \cos(m_n z), \quad (5.4)$$

where $a_n = E_n$ and $b_n = F_n$ are coefficients which are solved later.

5.3.3 General solution to the Poisson equation (PM - finite-length)

In cylindrical coordinates, the Poisson appears as

$$\frac{\partial^2 A_{\phi^s}}{\partial z^2} + \frac{\partial^2 A_{\phi^s}}{\partial r^2} + \frac{1}{r} \frac{\partial A_{\phi^s}}{\partial r} - \frac{1}{r^2} A_{\phi^s} = -\mu_0 \nabla \times \mathbf{M} \quad (5.5)$$

where s represents the subdomains which have magnetic field sources present. The solution to the Poisson equation is only obtainable after the solution to the magnetisation vector has been determined and for the discrete finite length of the machine, a different approach is taken as illustrated in the next section.

5.3.3.1 Solution to the magnetisation vector (finite length)

The magnetisation vector \mathbf{M} formulation is determined with consideration of the arrangement of the PMs arrays and also the period taken τ_{lp} . For this reason, the magnetisation vector formulation has to be formulated specifically for the topology being analysed. Any change in the PM pertain which may change the period τ_{lp} , leads to a new formulation for the magnetisation vector.

From Figure 5.3, it can be seen that

$$\tau_{lp} = 3\tau_m + 2l_{ms} + \tau_l, \quad (5.6)$$

where τ_l is the separation distance between the discrete PM arrays. The separation distance has to be in multiples of the pole pitch τ_p to obtain solutions that are consistent and it must be much larger than the pole pitch τ_p .

With radial permanent magnets, the magnetisation vector is determined from

$$\mathbf{M} = M_r \mathbf{e}_r \quad (5.7)$$

Employing the Fourier expansion and again with reference to Figure 5.3,

$$M_r = \frac{a_0}{2} + \sum_{1,2,..}^{\infty} a_{rn} \cos(m_{nf} z), \quad (5.8)$$

Since in this case the period is τ_{lp} , then $m_{nf} = 2n\pi/\tau_{lp}$. Hence,

$$a_{rn} = \frac{1}{\tau_{lp}} \int_{-\tau_{lp}}^{\tau_{lp}} f(z) \cos(m_{nf} z) dz, \quad (5.9a)$$

which is doubled when taken from 0 to τ_{lp} as

$$a_{rn} = \frac{2}{\tau_{lp}} \int_0^{\tau_{lp}} f(z) \cos(m_{nf} z) dz. \quad (5.9b)$$

Expanding the integral leads to

$$a_{rn} = \frac{2B_{rem}}{\mu_0 \tau_{lp}} \left[\int_0^{\frac{\tau_m}{2}} \cos(m_{nf} z) dz - \int_{\frac{\tau_m}{2} + l_{ms}}^{\tau_p + \frac{\tau_m}{2}} \cos(m_{nf} z) dz - \int_{\frac{L}{2} + \tau_l}^{\tau_{lp} - (\frac{\tau_m}{2} + l_{ms})} \cos(m_{nf} z) dz + \int_{\tau_{lp} - \frac{\tau_m}{2}}^{\tau_{lp}} \cos(m_{nf} z) dz \right], \quad (5.9c)$$

where $L = \frac{3\tau_m}{2} + l_{ms}$. Solving the integrals gives

$$a_{rn} = \frac{B_{rem}}{\mu_0 n \pi} \left[\sin\left(\frac{m_{nf} \tau_m}{2}\right) - \left\{ \sin\left[m_{nf} \left(\frac{\tau_m + 2\tau_p}{2}\right)\right] - \sin\left[m_{nf} \left(\frac{\tau_m + 2l_{ms}}{2}\right)\right] \right\} - \left\{ \sin\left[m_{nf} \left(\frac{2\tau_{lp} - 2l_{ms} - \tau_m}{2}\right)\right] - \sin\left[m_{nf} \left(\frac{2\tau_l + L}{2}\right)\right] \right\} + \left\{ \sin(m_{nf} \tau_{lp}) - \sin\left[m_{nf} \left(\frac{2\tau_{lp} - \tau_m}{2}\right)\right] \right\} \right] \quad (5.9d)$$

The expression on the right side of the equal-sign of the Poisson equation is $\mu_0 \nabla \times \mathbf{M}$ from which it is known that the curl on the magnetisation vector is

$$\nabla \times M = \frac{\partial M_r}{\partial z} \mathbf{e}_\phi \quad (5.10)$$

Taking the partial derivative of the magnetisation vector and multiplying the obtained solution by μ_0 gives the complete solution to the right hand side of the Poisson equation to be

$$\mu_0 \nabla \times \mathbf{M} = P_{nf} \sin(m_{nf} z) \quad (5.11)$$

where

$$\begin{aligned} P_{nf} = & \frac{2B_{rem}}{\tau_{lp}} \left[\sin\left(\frac{m_{nf}\tau_m}{2}\right) - \left\{ \sin\left[m_{nf}\left(\frac{\tau_m + 2\tau_p}{2}\right)\right] - \sin\left[m_{nf}\left(\frac{\tau_m + 2l_{ms}}{2}\right)\right] \right\} \right. \\ & - \left. \left\{ \sin\left[m_{nf}\left(\frac{2\tau_{lp} - 2l_{ms} - \tau_m}{2}\right)\right] - \sin\left[m_{nf}\left(\frac{2\tau_l + L}{2}\right)\right] \right\} \right. \\ & \left. + \left\{ \sin(m_{nf}\tau_{lp}) - \sin\left[m_{nf}\left(\frac{2\tau_{lp} - \tau_m}{2}\right)\right] \right\} \right]. \end{aligned} \quad (5.12)$$

5.3.3.2 General solution to the Poisson equation incorporating the magnetisation vector

Replacing the obtained solution to the magnetisation vector, then the Poisson equation after mathematical manipulations similarly to Section 2.4.2.2 is obtained as

$$A_{\phi f}(r, z) = \sum_{n=1, \dots}^{\infty} \left[a_n I_1(m_{nf} r) + b_n K_1(m_{nf} r) + \frac{\pi L_1(m_{nf} r)}{2m_{nf}^2} P_{nf} \right] \sin(m_{nf} z). \quad (5.13)$$

5.3.4 General solutions to the magnetic vector potential for all the subdomains (PM field only)

The magnetic vector potential for all the subdomains are expressed as

$$A_{\phi I f} = \sum_{n=1, \dots}^{\infty} [a_{nI} I_1(m_{nf} r) + b_{nI} K_1(m_{nf} r)] \sin(m_{nf} z), \quad (5.14)$$

$$A_{\phi II f} = \sum_{n=1, \dots}^{\infty} \left[a_{nII} I_1(m_{nf} r) + b_{nII} K_1(m_{nf} r) + \frac{\pi L_1(m_{nf} r)}{2m_{nf}^2} P_{nf} \right] \sin(m_{nf} z), \quad (5.15)$$

$$A_{\phi III f} = \sum_{n=1, \dots}^{\infty} [a_{nIII} I_1(m_{nf} r) + b_{nIII} K_1(m_{nf} r)] \sin(m_{nf} z), \quad (5.16)$$

$$A_{\phi IV f} = \sum_{n=1, \dots}^{\infty} \left[a_{nIV} I_1(m_{nf} r) + b_{nIV} K_1(m_{nf} r) + \frac{\pi L_1(m_{nf} r)}{2m_{nf}^2} P_{nf} \right] \sin(m_{nf} z), \quad (5.17)$$

$$A_{\phi V f} = \sum_{n=1, \dots}^{\infty} [a_{nV} I_1(m_{nf} r) + b_{nV} K_1(m_{nf} r)] \sin(m_{nf} z). \quad (5.18)$$

where the subscripts I, \dots, V represent the subdomains of the machine considering only the influence of the PM fields.

5.3.5 General solution to the magnetic flux density

The curl of the magnetic vector potential $\mathbf{B} = \nabla \times \mathbf{A}$ leads to the solution of the magnetic flux density in radial and axial directions. The obtained expressions are given as

5.3.5.1 The radial flux density

$$B_{rIf} = \sum_{n=1, \dots}^{\infty} m_{nf} [a_{nI} I_1(m_{nf} r) + b_{nI} K_1(m_{nf} r)] \cos(m_{nf} z) , \quad (5.19)$$

$$B_{rIIIf} = \sum_{n=1, \dots}^{\infty} m_{nf} \left[a_{nII} I_1(m_{nf} r) + b_{nII} K_1(m_{nf} r) + \frac{\pi L_1(m_{nf} r)}{2m_{nf}^2} P_{nf} \right] \cos(m_{nf} z) , \quad (5.20)$$

$$B_{rIIIIf} = \sum_{n=1, \dots}^{\infty} m_{nf} [a_{nIII} I_1(m_{nf} r) + b_{nIII} K_1(m_{nf} r)] \cos(m_{nf} z) , \quad (5.21)$$

$$B_{rIVf} = \sum_{n=1, \dots}^{\infty} m_{nf} \left[a_{nIV} I_1(m_{nf} r) + b_{nIV} K_1(m_{nf} r) + \frac{\pi L_1(m_{nf} r)}{2m_{nf}^2} P_{nf} \right] \cos(m_{nf} z) , \quad (5.22)$$

$$B_{rVf} = \sum_{n=1, \dots}^{\infty} m_{nf} [a_{nV} I_1(m_{nf} r) + b_{nV} K_1(m_{nf} r)] \cos(m_{nf} z) . \quad (5.23)$$

5.3.5.2 The axial flux density

$$B_{zIf} = \sum_{n=1, \dots}^{\infty} m_{nf} [a_{nI} I_0(m_{nf} r) - b_{nI} K_0(m_{nf} r)] \sin(m_{nf} z) , \quad (5.24)$$

$$B_{zIIIf} = \sum_{n=1, \dots}^{\infty} m_{nf} \left[a_{nII} I_0(m_{nf} r) - b_{nII} K_0(m_{nf} r) + \frac{\pi L_0(m_{nf} r)}{2m_{nf}^2} P_{nf} \right] \sin(m_{nf} z) , \quad (5.25)$$

$$B_{zIIIIf} = \sum_{n=1, \dots}^{\infty} m_{nf} [a_{nIII} I_0(m_{nf} r) - b_{nIII} K_0(m_{nf} r)] \sin(m_{nf} z) , \quad (5.26)$$

$$B_{zIVf} = \sum_{n=1, \dots}^{\infty} m_{nf} \left[a_{nIV} I_0(m_{nf} r) - b_{nIV} K_0(m_{nf} r) + \frac{\pi L_0(m_{nf} r)}{2m_{nf}^2} P_{nf} \right] \sin(m_{nf} z) , \quad (5.27)$$

$$B_{zVf} = \sum_{n=1, \dots}^{\infty} m_{nf} [a_{nV} I_0(m_{nf} r) - b_{nV} K_0(m_{nf} r)] \sin(m_{nf} z) . \quad (5.28)$$

5.3.6 Implementation of boundary conditions

The boundary conditions in this case are only considered for the radial directions because the iron yokes are assumed infinitely long. For this reason, the boundary conditions remains similar to the conditions in 2.109 - 2.118.

5.3.6.1 Inner radius of subdomain I Boundary

At iR_s , applying boundary condition (2.109), obtains

$$[a_{nI} I_1(m_{nf} iR_s) + b_{nI} K_1(m_{nf} iR_s)] = 0 . \quad (5.29)$$

5.3.6.2 Boundary between subdomains I and II

At iR_r , applying boundary condition (2.110) gives

$$\begin{aligned} m_{nf} [a_{nI} I_1(m_{nf} iR_r) + b_{nI} K_1(m_{nf} iR_r) - a_{nII} I_1(m_{nf} iR_r) \\ - b_{nII} K_1(m_{nf} iR_r)] = \frac{m_{nf} \pi L_1(m_{nf} iR_r) P_{nf}}{2m_{nf}^2} . \end{aligned} \quad (5.30)$$

Implementation of boundary condition (2.111) leads to

$$\begin{aligned} m_{nf} [a_{nI} I_0(m_{nf} iR_r) - b_{nI} K_0(m_{nf} iR_r) - \mu_{rI} a_{nII} I_0(m_{nf} iR_r) \\ + \mu_{rI} b_{nII} K_0(m_{nf} iR_r)] = \mu_{rI} \frac{m_{nf} \pi L_0(m_{nf} iR_r) P_{nf}}{2m_{nf}^2} . \end{aligned} \quad (5.31)$$

where $\mu_{rI} = 1000$ is the relative permeability of the yoke material.

5.3.6.3 Boundary between subdomains II and III

At iR_m , applying boundary condition (2.112) leads to

$$\begin{aligned} m_{nf} [a_{nII} I_1(m_{nf} iR_m) + b_{nII} K_1(m_{nf} iR_m) - a_{nIII} I_1(m_{nf} iR_m) \\ - b_{nIII} K_1(m_{nf} iR_m)] = -\frac{m_{nf} \pi L_1(m_{nf} iR_m) P_{nf}}{2m_{nf}^2} . \end{aligned} \quad (5.32)$$

Condition (2.113) on the other hand gives

$$\begin{aligned} m_{nf} [a_{nII} I_0(m_{nf} iR_m) - b_{nII} K_0(m_{nf} iR_m) - a_{nIII} I_0(m_{nf} iR_m) \\ + b_{nIII} K_0(m_{nf} iR_m)] = -\frac{m_{nf} \pi L_0(m_{nf} iR_m) P_{nf}}{2m_{nf}^2} . \end{aligned} \quad (5.33)$$

5.3.6.4 Boundary between subdomains III and IV

At oR_m , applying boundary condition (2.114)

$$\begin{aligned} m_{nf} [a_{nIII} I_1(m_{nf} oR_m) + b_{nIII} K_1(m_{nf} oR_m) - a_{nIV} I_1(m_{nf} oR_m) \\ - b_{nIV} K_1(m_{nf} oR_m)] = \frac{m_{nf} \pi L_1(m_{nf} oR_m) P_{nf}}{2m_{nf}^2} . \end{aligned} \quad (5.34)$$

Condition (2.115) gives

$$\begin{aligned} m_{nf} [a_{nIII} I_0(m_{nf} oR_m) - b_{nIII} K_0(m_{nf} oR_m) - a_{nIV} I_0(m_{nf} oR_m) \\ + b_{nIV} K_0(m_{nf} oR_m)] = \frac{m_{nf} \pi L_0(m_{nf} oR_m) P_{nf}}{2m_{nf}^2} . \end{aligned} \quad (5.35)$$

5.3.6.5 Boundary between subdomains IV and V

At oR_s , applying boundary condition (2.116)

$$\begin{aligned} m_{nf} [a_{nIV} I_1(m_{nf} oR_s) + b_{nIV} K_1(m_{nf} oR_s) - a_{nV} I_1(m_{nf} oR_s) \\ - b_{nV} K_1(m_{nf} oR_s)] = -\frac{m_{nf} \pi L_1(m_{nf} oR_s) P_{nf}}{2m_{nf}^2} . \end{aligned} \quad (5.36)$$

Boundary condition (2.117) gives

$$\begin{aligned} m_{nf} [\mu_{rV} a_{nIV} I_0(m_{nf} oR_s) - \mu_{rV} b_{nIV} K_0(m_{nf} oR_s) - a_{nV} I_0(m_{nf} oR_s) \\ + b_{nV} K_0(m_{nf} oR_s)] = \mu_{rV} \frac{m_{nf} \pi L_0(m_{nf} oR_s) P_{nf}}{2m_{nf}^2} . \end{aligned} \quad (5.37)$$

where $\mu_{rV} = 1000$ is the relative permeability of the yoke material

5.3.6.6 Outer radius of subdomain V boundary

At R_o , application of boundary condition (2.118)

$$[a_{nV} I_1(m_{nf} R_o) - b_{nV} K_1(m_{nf} R_o)] = 0 . \quad (5.38)$$

Similar to the process in chapter 2.7.7, equations are rearranged accordingly in order from 1 – 10 and a matrix formulated to determine the coefficients.

5.3.7 Solving the ten simultaneous equations by matrix method

The coefficients in the formulated ten equations are solved by employing the matrix method as

$$\begin{bmatrix}
 I_1(M^{a^f}) & +K_1(M^{a^f}) & 0 & 0 & 0 & 0 & 0 & 0 & 0 & 0 \\
 I^{bf}(M^{b^f}) & K^b(M^{b^f}) & -I^{bf}(M^{b^f}) & -K^{bf}(M^{b^f}) & 0 & 0 & 0 & 0 & 0 & 0 \\
 I^{af}(M^{b^f}) & -K^{af}(M^{b^f}) & -\mu_{rI}I^{af}(M^{b^f}) & \mu_{rI}K^{af}(M^{b^f}) & 0 & 0 & 0 & 0 & 0 & 0 \\
 0 & 0 & I^{bf}(M^{c^f}) & K^{bf}(M^{c^f}) & -I^{bf}(M^{c^f}) & -K^{bf}(M^{c^f}) & 0 & 0 & 0 & 0 \\
 0 & 0 & I^{af}(M^{c^f}) & -K^{af}(M^{c^f}) & -I^{af}(M^{c^f}) & K^{af}(M^{c^f}) & 0 & 0 & 0 & 0 \\
 0 & 0 & 0 & 0 & I^{bf}(M^{d^f}) & K^{bf}(M^{d^f}) & -I^{bf}(M^{d^f}) & -K^{bf}(M^{d^f}) & 0 & 0 \\
 0 & 0 & 0 & 0 & I^{af}(M^{d^f}) & -K^{af}(M^{d^f}) & -I^{af}(M^{d^f}) & K^{af}(M^{d^f}) & 0 & 0 \\
 0 & 0 & 0 & 0 & 0 & 0 & I^{bf}(M^{e^f}) & K^{bf}(M^{e^f}) & -I^{bf}(M^{e^f}) & -K^{bf}(M^{e^f}) \\
 0 & 0 & 0 & 0 & 0 & 0 & \mu_{rV}I^{af}(M^{e^f}) & -\mu_{rV}K^{af}(M^{e^f}) & -I^{af}(M^{e^f}) & K^{af}(M^{e^f}) \\
 0 & 0 & 0 & 0 & 0 & 0 & 0 & 0 & I_1(M^{f^f}) & +K_1(M^{f^f})
 \end{bmatrix}$$

$$\begin{bmatrix}
 a_{nI} \\
 b_{nI} \\
 a_{nII} \\
 b_{nII} \\
 a_{nIII} \\
 b_{nIII} \\
 a_{nIV} \\
 b_{nIV} \\
 a_{nV} \\
 b_{nV}
 \end{bmatrix}
 =
 \begin{bmatrix}
 0 \\
 m_{nf} \frac{\pi L_1(M^b)}{2m_{nf}^2} P_{nf} \\
 \mu_{rI} m_{nf} \frac{\pi L_0(M^{b^f})}{2m_{nf}^2} P_{nf} \\
 -m_{nf} \frac{\pi L_1(M^{c^f})}{2m_{nf}^2} P_{nf} \\
 -m_{nf} \frac{\pi L_0(M^{c^f})}{2m_{nf}^2} P_{nf} \\
 m_{nf} \frac{\pi L_1(M^{d^f})}{2m_{nf}^2} P_{nf} \\
 m_{nf} \frac{\pi L_0(M^{d^f})}{2m_{nf}^2} P_{nf} \\
 -m_{nf} \frac{\pi L_1(M^{e^f})}{2m_{nf}^2} P_{nf} \\
 -\mu_{rV} m_{nf} \frac{\pi L_0(M^{e^f})}{2m_{nf}^2} P_{nf} \\
 0
 \end{bmatrix}
 \tag{5.39}$$

where $M^{af} = m_{nf}iR_s$, $M^{bf} = m_{nf}iR_r$, $M^{cf} = m_{nf}iR_m$, $M^{df} = m_{nf}oR_m$, $M^{ef} = m_{nf}oR_s$, $M^{ff} = m_{nf}R_o$; $I^{af} = m_{nf}I_0$, $I^{bf} = m_{nf}I_1$, $K^{af} = m_{nf}K_0$, and $K^{bf} = m_{nf}K_1$.

5.3.8 Validation of the Model with FEM

The coefficients obtained in the matrix are then inserted into the magnetic vector potential expressions (5.14) - (5.18), the radial flux density expressions (5.19) - (5.23) and the axial flux density expressions (5.24) - (5.28).

5.3.8.1 Setup of the finite length model with a FEM-Package (MagNet)

A brief description of the finite length machine simulation settings are discussed in this section. The simulation is conducted with the help of a FEM package from Infolytica incorporation called MagNet. As the machine is axisymmetrical, the linear machine is positioned in a vertical position accordingly with MagNet requirements for axisymmetrical machine setup. The linear machine is placed in an air-box which set-up with flux tangential boundary conditions around it as shown in figure 5.4. A static simulation is conducted firstly with the coil switched off to capture the magnetic flux distribution with the influence of the permanent magnets only. Then the simulation is run with the coil switched on with a current density while the permanent magnets are switched off. A peak current is considered to fully capture the influence of the armature reaction field. The solution mesh is displayed in the figure below illustrate how the mesh was considered.

Figure 5.4a shows an axisymmetrical machine in an air-box where the radial permanent magnets, placed around the middle most part of the coil, are magnetised radially outward while the other magnetic pole sets are magnetised radially inward. On Figure 5.4b, the solution mesh is displayed to demonstrate that the mesh has been set with different dimensions to provide a more accurate solution to the simulation. As it is known that the mesh density especially in the coil areas or in moving parts of the machine affect the accuracy of the solution. It can be observed from Figure 5.4b that the mesh is much denser in the air-gaps between the coils; in the PMs and slightly less denser in the core materials and in-between the PMs. The air-box around the machine has a much less dense mesh.

5.3.8.2 Radial magnetic flux density

Figure 5.5 shows the radial flux density plotted for the machine length plus an additional small distance from the edges of the machine to indicate the fringing flux. As can be seen the analytically produced results matches well with FEM simulation results. The FEM simulation is given a large air-box so that fringing flux can be captured.

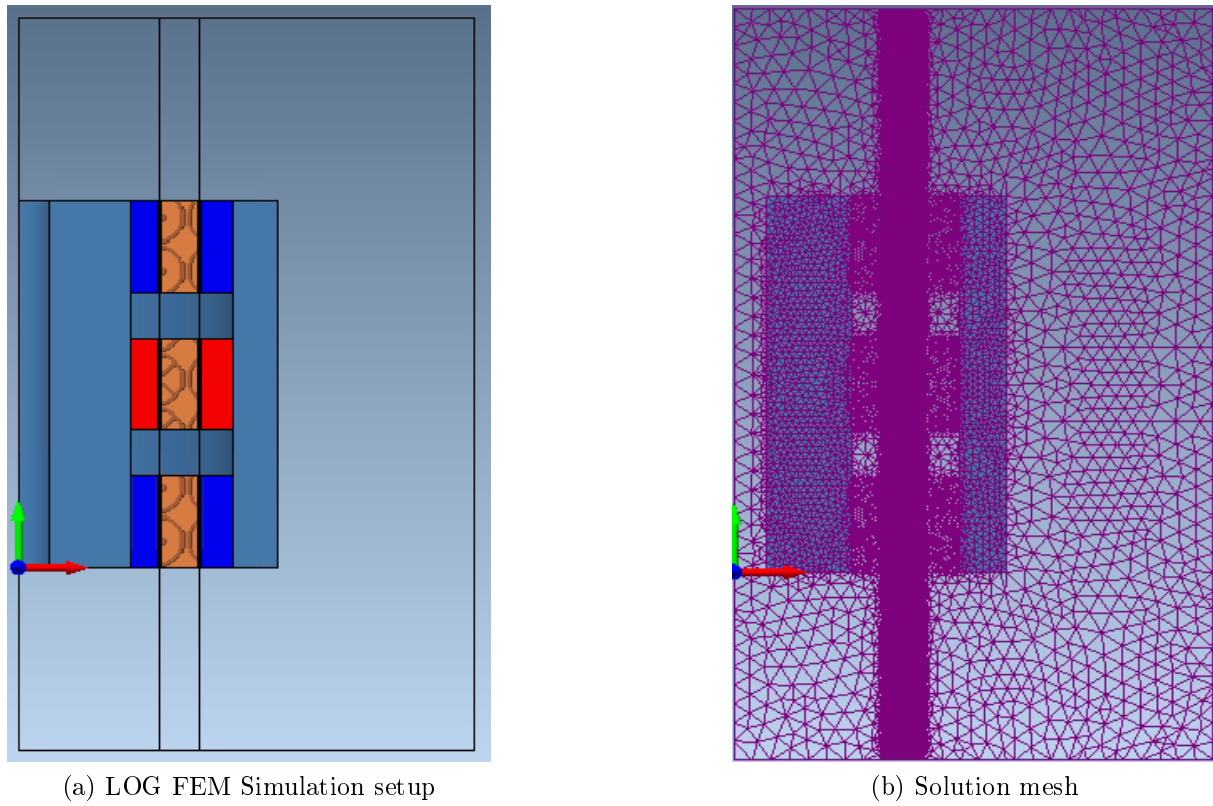


Figure 5.4: An illustration of the MagNet set-up of the simulation and a solution mesh

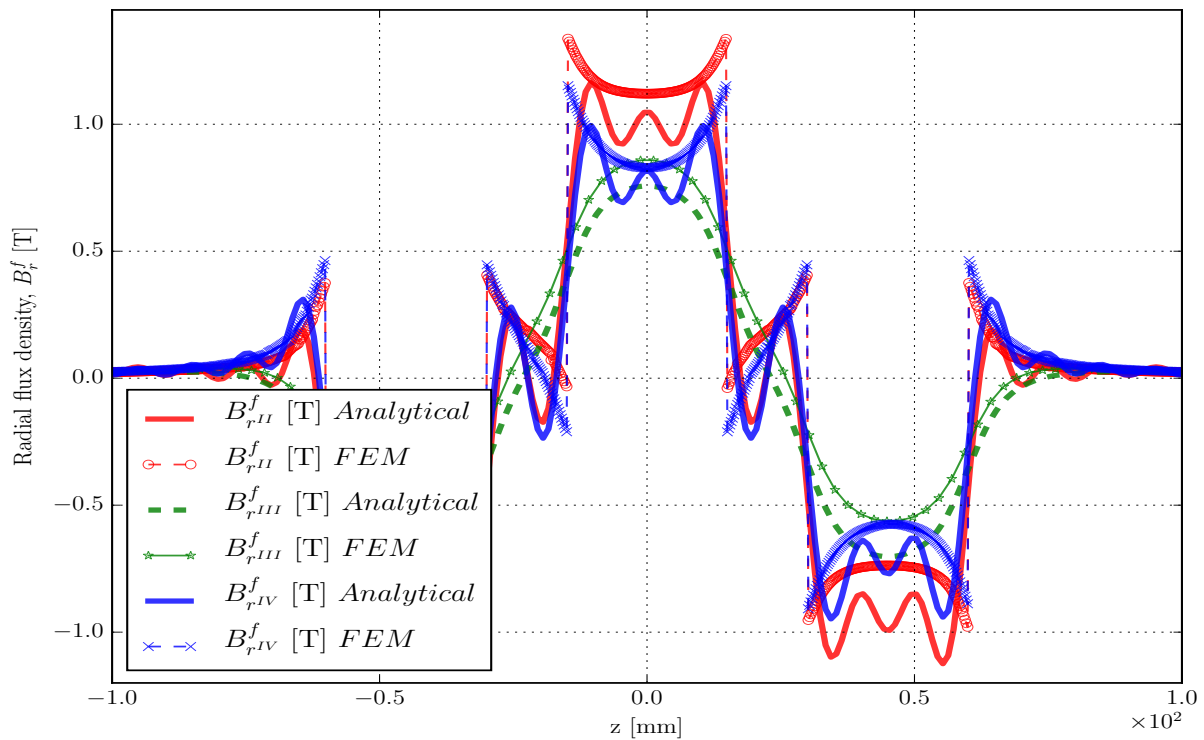


Figure 5.5: Radial flux densities obtained analytically and compared to a finite length FEM model

From Figure 5.5, a small deviation observed in the flux densities especially at the machine edges and the flux densities plots for $B_r^f_{III}$ are due to the analytical model having an assumption of infinitely long yokes. The flux densities can be observed diminishing to almost zero a few mm from the axial edges of the linear machine. The analytical model, therefore, predicts the levels of the flux densities in the linear machine and matches well with the finite element model (FEM) results. The analytical model is designed to consider a discrete series of permanent magnets so that an approximation of the field behaviour that relates to a finite length machine model can be modelled. In between the discrete permanent magnets is a distance τ_l that can be seen in Figure 5.6, where the flux density is near zero. Taking the behaviour of the flux distribution only for the machine length with a small extension at the axial edges is what is displayed on Figure 5.5.

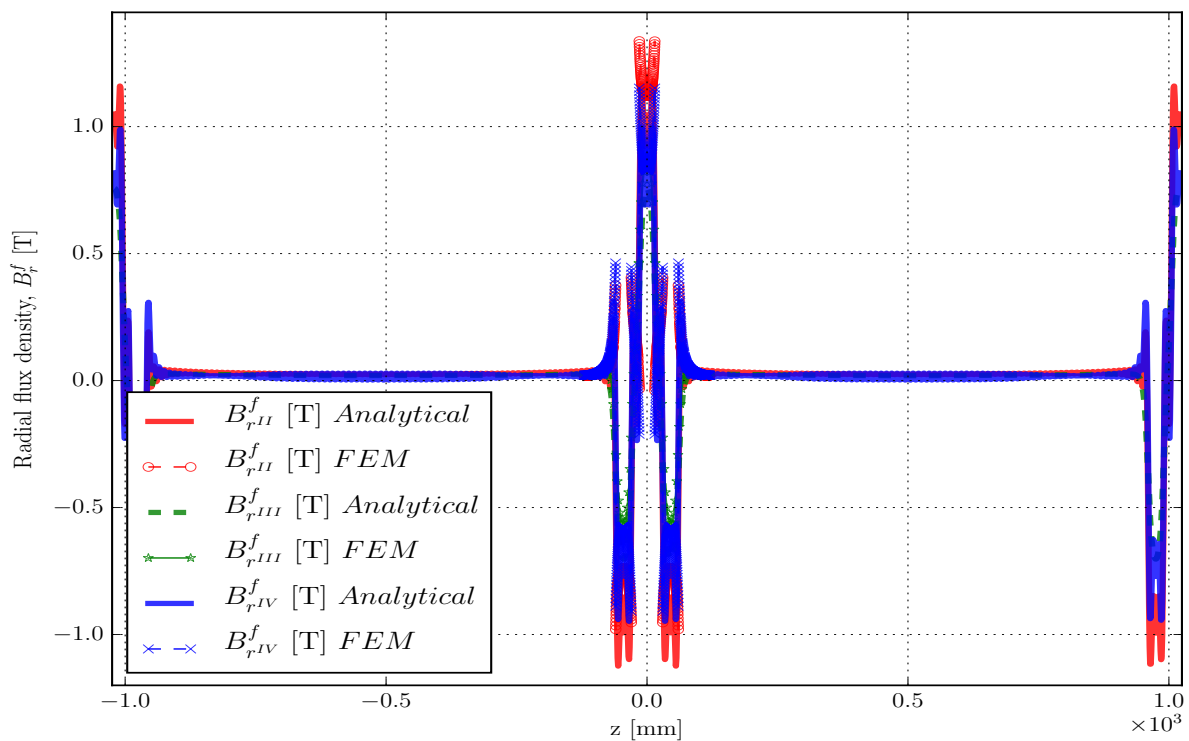


Figure 5.6: Full spectrum radial flux density plot compared to a finite length FEM model

5.3.8.3 Axial magnetic flux density

Figure 5.7 shows a zoomed version of the axial flux density plots obtained analytically and compared to FEM results. Good correlation is shown, indicating that the model is capable of predicting the flux densities for finite length machine. A slight overestimation of the flux densities at the machine edges occurs as seen in Figure 5.7 which is again stemming from taking the iron yokes to be infinitely long in the analytical model.

Figure 5.8, displays the results for $z = 2\tau_{lp}$ for the axial flux densities.

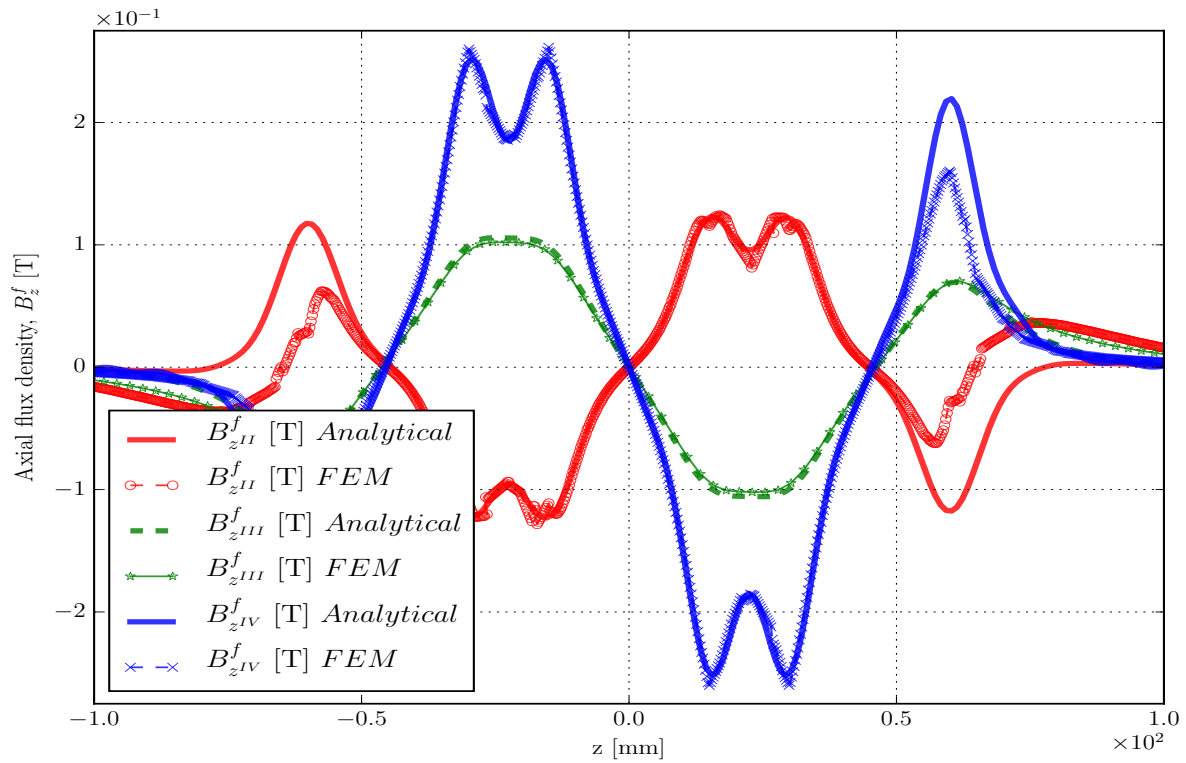


Figure 5.7: Analytically obtained axial flux density compared to a finite length FEM model

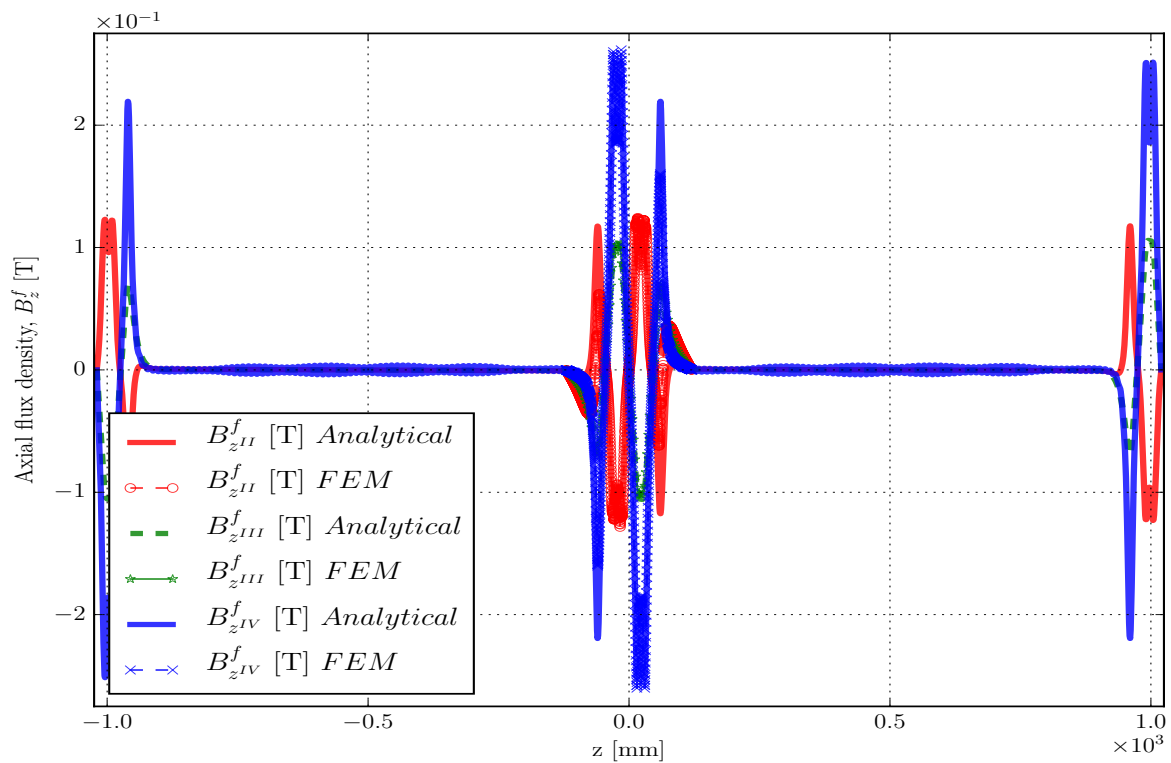


Figure 5.8: Full spectrum of axial flux density plot compared to a finite length FEM model

5.3.8.4 Comparison of the contour plots

The contour plots generated from the analytical model are compared to the contour plots from the FEM software. The FEM contour plot for a finite length machine model is displayed on Figure 5.9.

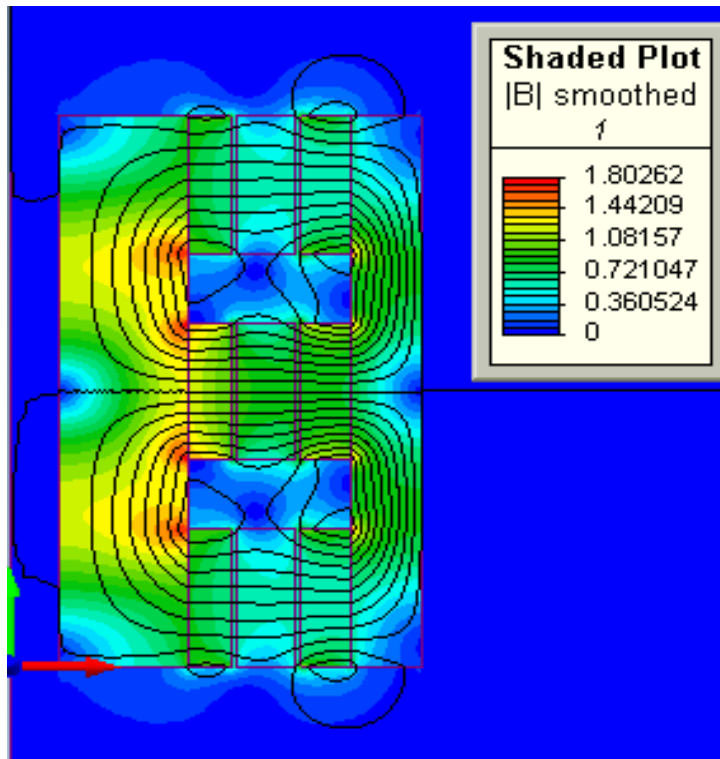


Figure 5.9: Contour plot of the FEM model

The contour plots obtained from the analytical model can be seen on Figure 5.10. It can be observed that the total flux density obtained by the analytical model has an overestimation by about $0.2 T$ or 10% which is within the considered levels and is due to the consideration of the yokes to be infinitely long. This can be observed on Figure 5.10 where the field lines can be seen extending out through the yokes of the machine. The effect of the infinitely long yoke on the magnitudes of the magnetic flux densities is minimal and therefore, the results from the analytical model in comparison to the FEM model match well as illustrated on Figures 5.5 and 5.8.

The full spectrum of the both the contour plots and the field lines are illustrated on Figure 5.11. The Figure 5.10 considered the linear machine length while Figure 5.11 illustrates the replication of the magnetic poles with a separation distance of τ_l . As already mentioned the separation distance must be a multiple of τ_p and must be much larger than τ_p .

From figure 5.11 it is observed that the fringing fields are higher than anticipated and as explained earlier this may be attributed to the infinitely long yokes and also having a

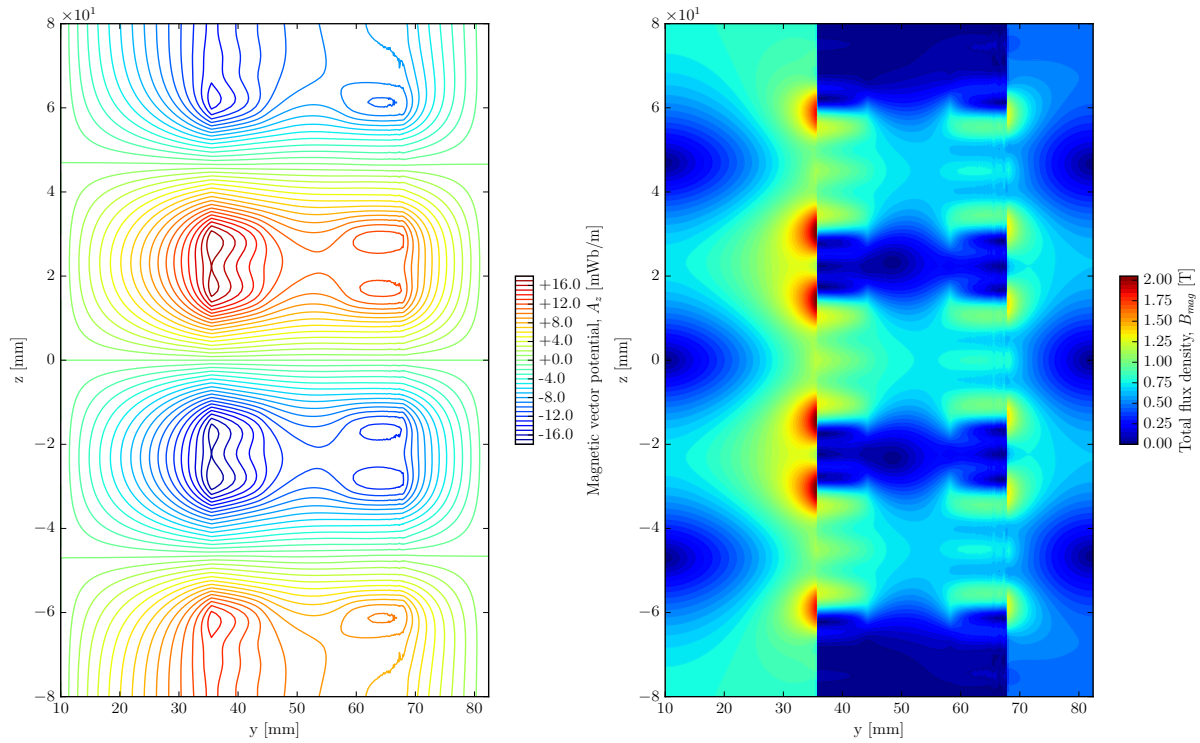


Figure 5.10: The magnetic field lines and a contour plot as obtained from the analytical model

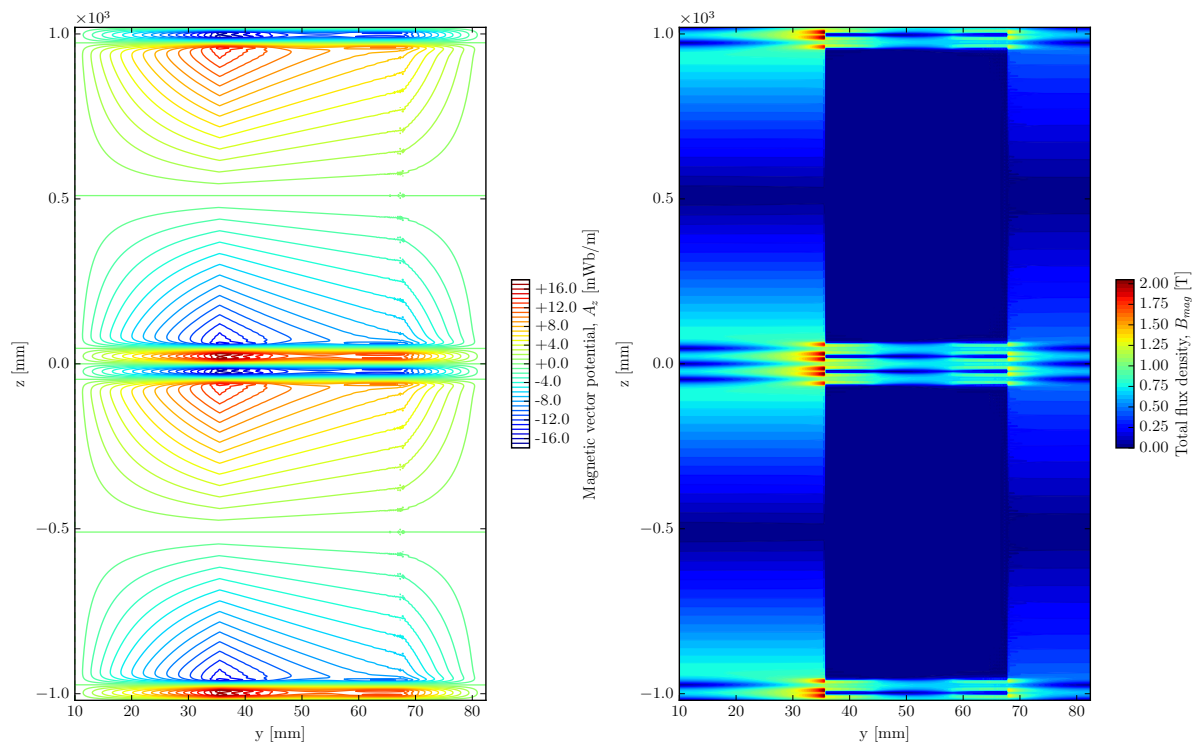


Figure 5.11: Analytically determined magnetic field lines and contour plot considering an axial length of $2\tau_{lp}$

full magnet at the machine axial edges provides more field lines that cannot pair with the field lines from the centrally placed (non-axial edge) permanent magnets. This can be

seen when compared to the analytical model in which the half length permanent magnets are placed at the axial edges of the linear machine as shown on Figure B.1. The field plots as well as the contour plots obtained from the model considering half PMs at the axial edges are illustrated on Figure 5.12.

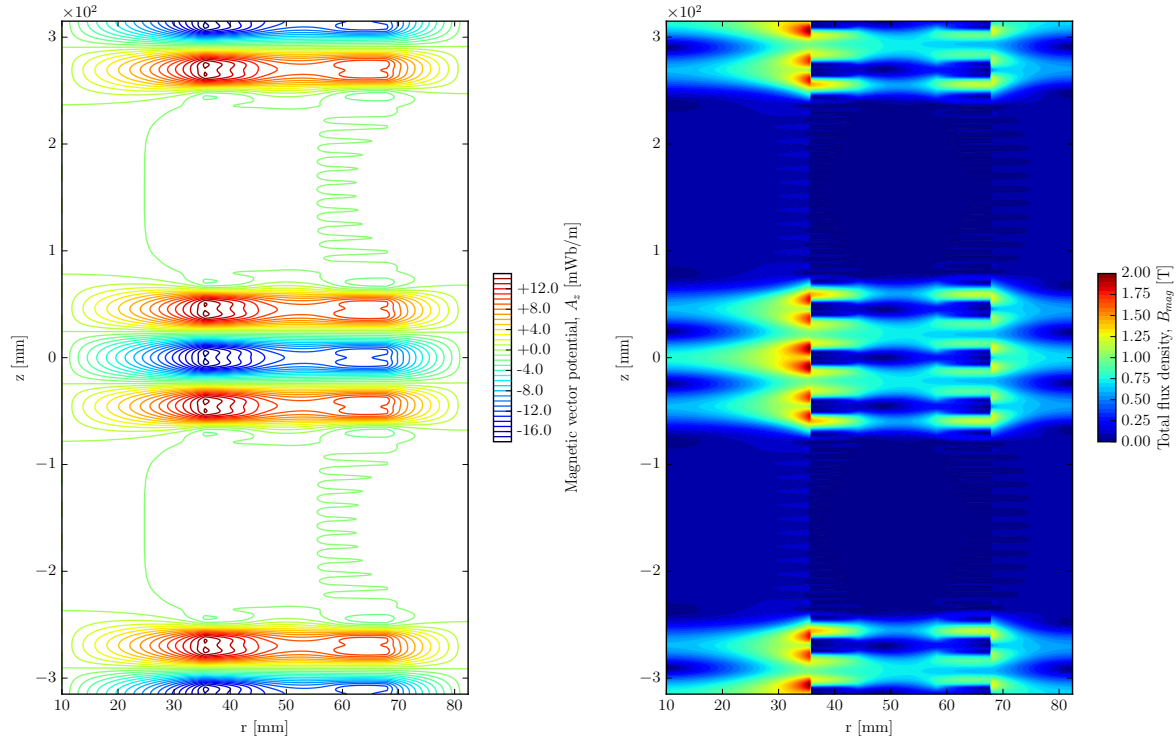


Figure 5.12: Analytically determined magnetic field lines and contour plot considering an axial length of $2\tau_{lp}$ with half PMs at axial edges of the machine

From Figures 5.12, it is observed that there is less fringing fields which is attributed to the half PMs having most of the field lines paired with the other PMs. For the sake of optimisation, the model with three full permanent magnet pole pairs is preferred.

5.4 Summary and conclusion

The development of the analytical model that considers the machine to have a finite length and also considers the machine to have a finite permeability has been developed. This chapter focused on the influence of the permanent magnets as the only field source. The armature is considered switched off. The solutions obtained were achieved after considering the iron yokes as infinitely long. Various boundary conditions were tested on the axial edges of the machine which could have highly improved the results if suitable and mathematically workable boundary conditions were applied. However, conditioning of the matrix with the various boundary conditions tested could not be achieved. Taking the

iron yokes as infinitely long has minimal deviation from the solutions as the comparisons with FEM show in the validation section.

Chapter 6

Discrete AR series analytical model

6.1 Introduction

In the determination of the armature reaction field distribution in this section, the governing equations are taken with the same approach as in Chapter 3. Just as for the permanent magnet field distribution, the harmonic expansion (Fourier Series Technique) of Maxwell equation and separation of variables is adopted. In this analysis, the armature length is considered finite but arranged as infinitely long discrete finite-length armatures. This arrangement ensures that the harmonic expansion solution becomes possible. The distance between the armatures should be much greater than the pole pitch so that fringing of one armature does not influence the field of another armature as Wang *et al* concluded in [53].

The concept taken in the armature reaction prediction has been presented by Wang *et al* in [88; 99] where a quasi-Halbach moving magnet tubular linear motor was considered with infinitely long array of discrete finite length PM arrays [99]. The region in between the PMs is considered as having permanent magnets which are not activated as the relative permeability in the PM regions, the air regions are taken as equal. The justification is that the relative permeability of NdFeb Magnets is $\mu_r = 1.05$. The iron yokes in [99] are considered having infinite permeability and thickness but in [53], Wang *et al* considers the finite length armature winding connected to an iron core also of finite length but infinite thickness. Then the radial permanent magnets are axially infinitely long together with the iron core to which the PMs are connected. A harmonic based analytical model is developed by Wang *et al* nevertheless, his analytical model does not clearly indicate how he derived the equation for the air-region between the armature iron yokes. Repeating the work in [53] proved extremely difficult because of lack of clarity of the equation for the air-gap between the armature cores. Also among the authors illustrating their solutions for a finite length armature for a linear tubular moving-coil machine is Yan *et al* [49]. Yan *et al* employs the harmonic expansion of the Maxwell's equation and incorporates the permeance model in order to achieve a solution for a finite length armature. Some constraints are adopted and for one of the adopted constraints, Yan *et al* solves using the equivalent magnetic circuit. All the authors mentioned in this chapter did not take into consideration the iron yokes to have a finite permeability and finite thickness. While the analysis done in this section considers the iron yokes with finite permeability and

thickness.

6.2 Armature reaction and inductance formulation

The armature reaction field is analysed by taking the permanent magnets as having the permeability of air. The field obtained in the tubular machine is only provided by the armature with a defined current density. The set-up is shown in Figure 6.1.

6.2.1 Assumptions

The following assumptions are employed in the finite-length armature reaction prediction:

1. The armature length is considered finite but set up as infinitely long finite-length discrete armatures
2. The iron yokes are considered to be infinitely long with finite permeability and finite thickness so that saturation can be monitored
3. The iron yoke is considered as infinitely long
4. The permanent magnets are to have the same permeability as that of air (switched off).

6.2.2 Laplace and Poisson equations in cylindrical coordinates

The Laplace and the Poisson equation that represent the armature reaction prediction analysis are governed by the same expressions as in Section 3.2 and are repeated here in cylindrical coordinates for the sake of convenience. The subdomains in which the current density does not exist, i.e. the iron yokes, the lower and upper air-gaps are represented by

$$\frac{\partial^2 A_{\phi^k}}{\partial z^2} + \frac{\partial^2 A_{\phi^k}}{\partial r^2} + \frac{1}{r} \frac{\partial A_{\phi^k}}{\partial r} - \frac{1}{r^2} A_{\phi^k} = 0 \quad (6.1)$$

where k represents the subdomains I', II', IV', V' . The coil subdomains is governed by the Poisson equation of the form,

$$\frac{\partial^2 A_{\phi_{III'}}}{\partial z^2} + \frac{\partial^2 A_{\phi_{III'}}}{\partial r^2} + \frac{1}{r} \frac{\partial A_{\phi_{III'}}}{\partial r} - \frac{1}{r^2} A_{\phi_{III'}} = -\mu_0 J_z \quad (6.2)$$

6.2.3 General solutions to Laplace and Poisson equations

The general solution to (6.1) which is the Laplace equation is given by

$$A_{\phi^{AR}} = \sum_{n=1, \dots}^{\infty} [a_n I_1(m_n r) + b_n K_1(m_n r)] \cos(m_n z) . \quad (6.3)$$

For the Poisson equation, the general solution is given by

$$A_{\phi AR} = \sum_{n=1,..}^{\infty} [a_{n^k} I_1(m_{n^f} r) + b_{n^k} K_1(m_{n^f} r) + S(r, z)] \cos(m_{n^f} z) , \quad (6.4)$$

where $S(r, z)$ is the particular solution of the Poisson equation of which the solution to the current density vector plays a key role. The formulation for the current density vector starts with the formulation presented in Figure 6.1.

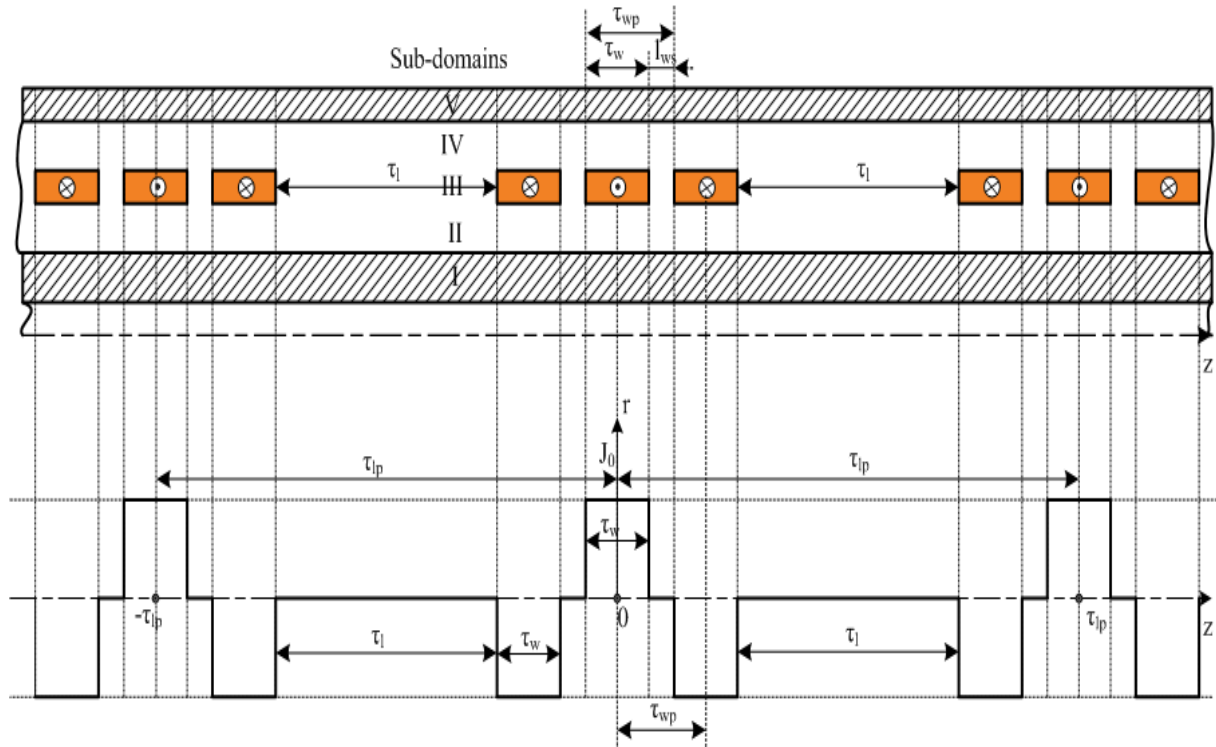


Figure 6.1: The LOG with PMs removed and only showing the discrete finite length armatures in series separated by τ_l . Also shown is a current density vector formulation

6.2.3.1 Solution to the current density J

Just as for the distribution of the field supplied by only the permanent magnets, the distance τ_l must be a multiple of coil pole pitch τ_{wp} but must be much greater than τ_{wp} . The current density $J(z^f)$ for the model with a finite length armature is formulated from a Fourier series with a period given by $2\tau_{lp}$ as

$$J(z^f) = \sum_{n=1,..}^{\infty} J_{n^f} \cos(m_{n^f} z) , \quad (6.5a)$$

With the help of the bottom section of Figure 6.1, J_{n^f} is expressed by

$$J_{n^f} = \frac{1}{\tau_{lp}} \int_{-\tau_{lp}}^{\tau_{lp}} f(z) \cos(m_{n^f} z) dz , \quad (6.5b)$$

which can be doubled when the range is taken from $0 - \tau_{lp}$ as

$$J_{nf} = \frac{2}{\tau_{lp}} \int_0^{\tau_{lp}} f(z) \cos(m_{nf} z) dz . \quad (6.5c)$$

Considering the initial current density J_0 and expressing the integrals in sections based on Figure 6.1

$$J_{nf} = \frac{2J_0}{\tau_{lp}} \left[\int_0^{\frac{\tau_w}{2}} \cos(m_{nf} z) dz - \int_{\frac{\tau_w}{2} + l_{ws}}^{\tau_{wp} + \frac{\tau_w}{2}} \cos(m_{nf} z) dz - \int_{\frac{L_w}{2} + \tau_l}^{\tau_{lp} - (\frac{\tau_w}{2} + l_{ws})} \cos(m_{nf} z) dz + \int_{\tau_{lp} - \frac{\tau_w}{2}}^{\tau_{lp}} \cos(m_{nf} z) dz \right] \quad (6.5d)$$

where $L_w = \frac{3\tau_w}{2} + l_{ws}$ and $m_{nf} = \frac{2n\pi}{\tau_{lp}}$. Solving each integral leads to

$$J_{nf} = \frac{2J_0}{m_{nf} \tau_{lp}} \left[\sin\left(\frac{m_{nf} \tau_w}{2}\right) - \left\{ \sin\left[m_{nf} \left(\frac{\tau_w + 2\tau_{wp}}{2}\right)\right] - \sin\left[m_{nf} \left(\frac{\tau_w + 2l_{ws}}{2}\right)\right] \right\} - \left\{ \sin\left[m_{nf} \left(\frac{2\tau_{lp} - 2l_{ws} - \tau_w}{2}\right)\right] - \sin\left[m_{nf} \left(\frac{2\tau_l + L_w}{2}\right)\right] \right\} + \left\{ \sin(m_{nf} \tau_{lp}) - \sin\left[m_{nf} \left(\frac{2\tau_{lp} - \tau_w}{2}\right)\right] \right\} \right] . \quad (6.5e)$$

Since the right side of the Poisson equation is given by $-\mu_0 J(z)$ which is equal to

$$-\mu_0 J(z) = P_{nfAR} \cos(m_{nf} z) \quad (6.6)$$

where

$$P_{nfAR} = \frac{-2J_0\mu_0}{m_{nf} \tau_{lp}} \left[\sin\left(\frac{m_{nf} \tau_w}{2}\right) - \left\{ \sin\left[m_{nf} \left(\frac{\tau_w + 2\tau_{wp}}{2}\right)\right] - \sin\left[m_{nf} \left(\frac{\tau_w + 2l_{ws}}{2}\right)\right] \right\} - \left\{ \sin\left[m_{nf} \left(\frac{2\tau_{lp} - 2l_{ws} - \tau_w}{2}\right)\right] - \sin\left[m_{nf} \left(\frac{2\tau_l + L_w}{2}\right)\right] \right\} + \left\{ \sin(m_{nf} \tau_{lp}) - \sin\left[m_{nf} \left(\frac{2\tau_{lp} - \tau_w}{2}\right)\right] \right\} \right] \quad (6.7)$$

The particular solution obtained after the separation of variables just as obtained in Sec. 2.4.2.2 and $S(r, z) = R(r)Z(z) = \frac{\pi L_1(m_{nf} r)}{2m_{nf}^2} P_{nfAR} \cos(m_{nf} z)$ therefore the Poisson equation is given by

$$A_{\phi AR}(r, z) = \sum_{n=1, \dots}^{\infty} \left[a_n I_1(m_{nf} r) + b_n K_1(m_{nf} r) + \frac{\pi L_1(m_{nf} r)}{2m_{nf}^2} P_{nfAR} \right] \cos(m_{nf} z) . \quad (6.8)$$

6.2.4 General solution to the magnetic vector potential for finite length armature reaction

The solution determined for the Poisson equation provides for the full formulation of the magnetic vector potential in all the subdomains of the machine. From the magnetic vector

potential, the magnetic flux density in both the radial and axial directions are formulated through $\mathbf{B} = \nabla \times \mathbf{A}$. \mathbf{A} is expressed as

$$A_{\phi IAR}(r, z) = \sum_{n=1, \dots}^{\infty} [a_{nI} I_1(m_{nf} r) + b_{nI} K_1(m_{nf} r)] \cos(m_{nf} z), \quad (6.9)$$

$$A_{\phi IIAR}(r, z) = \sum_{n=1, \dots}^{\infty} [a_{nII} I_1(m_{nf} r) + b_{nII} K_1(m_{nf} r)] \cos(m_{nf} z), \quad (6.10)$$

$$A_{\phi IIIAR}(r, z) = \sum_{n=1, \dots}^{\infty} [a_{nIII} I_1(m_{nf} r) + b_{nIII} K_1(m_{nf} r) + S(r^{AR})] \cos(m_{nf} z), \quad (6.11)$$

$$A_{\phi IVAR}(r, z) = \sum_{n=1, \dots}^{\infty} [a_{nIV} I_1(m_{nf} r) + b_{nIV} K_1(m_{nf} r)] \cos(m_{nf} z), \quad (6.12)$$

$$A_{\phi VAR}(r, z) = \sum_{n=1, \dots}^{\infty} [a_{nV} I_1(m_{nf} r) + b_{nV} K_1(m_{nf} r)] \cos(m_{nf} z), \quad (6.13)$$

where

$$S(r^{AR}) = \frac{\pi L_1(m_{nf} r)}{2m_{nf}^2} P_{n^{fAR}}. \quad (6.14)$$

In the expressions above, I, II, III, IV and V identifies with the subdomains and the iron yokes have also been integrated into the equation to monitor the field behaviour.

6.2.5 General solution to the magnetic flux density in the radial direction

The formulation of the magnetic flux density in the radial direction is employed from the first section of the solution of the curl of the magnetic vector potential $B_r \mathbf{e}_r = -\frac{1}{r} \frac{\partial r A_{\phi}}{\partial z} \mathbf{e}_r$. From the differentiation

$$B_{r IAR}(r, z) = \sum_{n=1, \dots}^{\infty} m_{nf} [a_{nI} I_1(m_{nf} r) + b_{nI} K_1(m_{nf} r)] \sin(m_{nf} z), \quad (6.15)$$

$$B_{r IIAR}(r, z) = \sum_{n=1, \dots}^{\infty} m_{nf} [a_{nII} I_1(m_{nf} r) + b_{nII} K_1(m_{nf} r)] \sin(m_{nf} z), \quad (6.16)$$

$$B_{r IIIAR}(r, z) = \sum_{n=1, \dots}^{\infty} m_{nf} [a_{nIII} I_1(m_{nf} r) + b_{nIII} K_1(m_{nf} r) + S(r^{AR})] \sin(m_{nf} z), \quad (6.17)$$

$$B_{r IVAR}(r, z) = \sum_{n=1, \dots}^{\infty} m_{nf} [a_{nIV} I_1(m_{nf} r) + b_{nIV} K_1(m_{nf} r)] \sin(m_{nf} z), \quad (6.18)$$

$$B_{r VAR}(r, z) = \sum_{n=1, \dots}^{\infty} m_{nf} [a_{nV} I_1(m_{nf} r) + b_{nV} K_1(m_{nf} r)] \sin(m_{nf} z), \quad (6.19)$$

and $S(r^{AR})$ is considered as (6.14).

6.2.6 General solution to the magnetic flux density in the axial direction

The formulation for the magnetic flux density in the axial direction is deduced from $B_z \mathbf{e}_z = \frac{1}{r} \frac{\partial r A_\phi}{\partial r} \mathbf{e}_z$. Recall that $\mathbf{B} = \nabla \times \mathbf{A} = B_r \mathbf{e}_r + B_z \mathbf{e}_z$. Therefore, for each subdomain, B_z is given by

$$B_{zIAR}(r, z) = \sum_{n=1, \dots}^{\infty} m_{nf} [a_{nI} I_0(m_{nf} r) - b_{nI} K_0(m_{nf} r)] \cos(m_{nf} z), \quad (6.20)$$

$$B_{zIIAR}(r, z) = \sum_{n=1, \dots}^{\infty} m_{nf} [a_{nII} I_0(m_{nf} r) - b_{nII} K_0(m_{nf} r)] \cos(m_{nf} z), \quad (6.21)$$

$$B_{zIIIAR}(r, z) = \sum_{n=1, \dots}^{\infty} m_{nf} [a_{nIII} I_0(m_{nf} r) - b_{nIII} K_0(m_{nf} r) + S(z^{AR})] \cos(m_{nf} z), \quad (6.22)$$

$$B_{zIVAR}(r, z) = \sum_{n=1, \dots}^{\infty} m_{nf} [a_{nIV} I_0(m_{nf} r) - b_{nIV} K_0(m_{nf} r)] \cos(m_{nf} z), \quad (6.23)$$

$$B_{zVAR}(r, z) = \sum_{n=1, \dots}^{\infty} m_{nf} [a_{nV} I_0(m_{nf} r) - b_{nV} K_0(m_{nf} r)] \sin(m_{nf} z), \quad (6.24)$$

where in this case,

$$S(z^{AR}) = \frac{\pi L_0(m_{nf} r)}{2m_{nf}^2} P_{n^{fAR}}. \quad (6.25)$$

These equations obtained (6.9) - (6.13), (6.15) - (6.19) and (6.20) - (6.24) are then employed with the help of boundary conditions to determine the coefficients of the expressions.

6.2.7 Boundary conditions

Boundaries of the machine are considered only in the radial direction. The consideration of the discrete armatures of finite length already illustrates that between the distance τ_l , the flux density is almost zero and hence the Fourier expansion of the current density vector covers the axial boundaries. For this reason, only the radial boundaries are considered

which are:

$$A_{\phi IAR}|_{r=iR_s} = 0 \quad (6.26)$$

$$B_{rIAR}|_{r=iR_r} = B_{rIIAR}|_{r=iR_r} \quad (6.27)$$

$$H_{zIAR}|_{r=iR_r} = H_{zIIAR}|_{r=iR_r} \quad (6.28)$$

$$B_{rIIAR}|_{r=iR_{coil}} = B_{rIIIAR}|_{r=iR_{coil}} \quad (6.29)$$

$$H_{zIIAR}|_{r=iR_{coil}} = H_{zIIIAR}|_{r=iR_{coil}} \quad (6.30)$$

$$B_{rIIIAR}|_{r=oR_{coil}} = B_{rIVAR}|_{r=oR_{coil}} \quad (6.31)$$

$$H_{zIIIAR}|_{r=oR_{coil}} = H_{zIVAR}|_{r=oR_{coil}} \quad (6.32)$$

$$B_{rIVAR}|_{r=oR_s} = B_{rVAR}|_{r=oR_s} \quad (6.33)$$

$$H_{zIVAR}|_{r=oR_s} = H_{zVAR}|_{r=oR_s} \quad (6.34)$$

$$A_{\phi VAR}|_{r=R_o} = 0 \quad (6.35)$$

The magnetic flux density and the magnetic field intensity have a relation through $\mathbf{B} = \mu\mathbf{H}$. Therefore the boundary condition, for example, $H_{zIAR}|_{r=iR_r} = H_{zIIAR}|_{r=iR_r}$ indicates that $\frac{B_{zIAR}}{\mu_I} = \frac{B_{zIIAR}}{\mu_{II}}$.

6.2.7.1 Boundary at the inner bore radius

The implementation of the first boundary condition (6.26) ($A_{\phi IAR}|_{r=iR_s} = 0$) at $r = iR_s$ leads to

$$a_{nI} I_1(m_{nf} iR_s) + b_{nI} K_1(m_{nf} iR_s) = 0 . \quad (6.36)$$

6.2.7.2 Boundary between I and II - refer to Figure 6.1

Applying the boundary condition (6.27) ($B_{rIAR}|_{r=iR_r} = B_{rIIAR}|_{r=iR_r}$) at $r = iR_r$ yields

$$\begin{aligned} m_{nf} [a_{nI} I_1(m_{nf} iR_r) + b_{nI} K_1(m_{nf} iR_r)] = \\ m_{nf} [a_{nII} I_1(m_{nf} iR_r) + b_{nII} K_1(m_{nf} iR_r)] , \end{aligned} \quad (6.37)$$

While considering boundary condition (6.28) ($H_{zIAR}|_{r=iR_r} = H_{zIIAR}|_{r=iR_r}$) gives

$$\begin{aligned} m_{nf} [a_{nI} I_0(m_{nf} iR_r) - b_{nI} K_0(m_{nf} iR_r)] = \\ \mu_{rI} m_{nf} [a_{nII} I_0(m_{nf} iR_r) - b_{nII} K_0(m_{nf} iR_r)] . \end{aligned} \quad (6.38)$$

6.2.7.3 Boundary between II and III with reference to Figure 6.1

Implementation of the boundary condition (6.29) ($B_{rIIAR}|_{r=iR_{coil}} = B_{rIIIAR}|_{r=iR_{coil}}$) at iR_{coil} gives

$$\begin{aligned} m_{nf} [a_{nII} I_1(m_{nf} iR_{coil}) + b_{nII} K_1(m_{nf} iR_{coil})] = \\ m_{nf} \left[a_{nIII} I_1(m_{nf} iR_{coil}) + b_{nIII} K_1(m_{nf} iR_{coil}) + \frac{\pi L_1(m_{nf} iR_{coil})}{2m_{nf}^2} P_{n^f AR} \right] , \end{aligned} \quad (6.39)$$

while applying the boundary condition (6.30) ($H_{zIIAR}|_{r=iR_{coil}} = H_{zIII}|_{r=iR_{coil}}$) leads to

$$\begin{aligned} m_{nf} [a_{nII} I_0(m_{nf} iR_{coil}) - b_{nII} K_0(m_{nf} iR_{coil})] = \\ m_{nf} \left[a_{nIII} I_0(m_{nf} iR_{coil}) - b_{nIII} K_0(m_{nf} iR_{coil}) + \frac{\pi L_0(m_{nf} iR_{coil})}{2m_{nf}^2} P_{n^fAR} \right]. \end{aligned} \quad (6.40)$$

6.2.7.4 Boundary between III and IV with reference to Figure 6.1

Implementing the boundary condition (6.31) ($B_{rIII}^{AR}|_{r=oR_{coil}} = B_{rIV}^{AR}|_{r=oR_{coil}}$) at oR_{coil} yields

$$\begin{aligned} m_{nf} \left[a_{nIII} I_1(m_{nf} oR_{coil}) + b_{nIII} K_1(m_{nf} oR_{coil}) + \frac{\pi L_1(m_{nf} oR_{coil})}{2m_{nf}^2} P_{n^fAR} \right] = \\ m_{nf} [a_{nIV} I_1(m_{nf} oR_{coil}) + b_{nIV} K_1(m_{nf} oR_{coil})], \end{aligned} \quad (6.41)$$

and applying the boundary condition (6.32) ($H_{zIIIAR}|_{r=oR_{coil}} = H_{zIVAR}|_{r=oR_{coil}}$) gives

$$\begin{aligned} m_{nf} \left[a_{nIII} I_0(m_{nf} oR_{coil}) - b_{nIII} K_0(m_{nf} oR_{coil}) + \frac{\pi L_0(m_{nf} oR_{coil})}{2m_{nf}^2} P_{n^fAR} \right] = \\ m_{nf} [a_{nIV} I_0(m_{nf} oR_{coil}) - b_{nIV} K_0(m_{nf} oR_{coil})]. \end{aligned} \quad (6.42)$$

6.2.7.5 Boundary between IV and V - refer to Figure 6.1

Applying the boundary condition (6.33) ($B_{rIVAR}|_{r=oR_s} = B_{rVAR}|_{r=oR_s}$) at oR_s leads to

$$\begin{aligned} m_{nf} [a_{nIV} I_1(m_{nf} oR_s) + b_{nIV} K_1(m_{nf} oR_s)] = \\ m_{nf} [a_{nV} I_1(m_{nf} oR_s) + b_{nV} K_1(m_{nf} oR_s)], \end{aligned} \quad (6.43)$$

while applying the boundary condition (6.34) ($H_{zIVAR}|_{r=oR_s} = H_{zVAR}|_{r=oR_s}$) gives

$$\begin{aligned} \mu_{rV} m_{nf} [a_{nIV} I_0(m_{nf} oR_s) - b_{nIV} K_0(m_{nf} oR_s)] = \\ m_{nf} [a_{nV} I_0(m_{nf} oR_s) - b_{nV} K_0(m_{nf} oR_s)]. \end{aligned} \quad (6.44)$$

6.2.7.6 Boundary at the outer radius of the machine

Applying the boundary condition (6.35) ($A_{\phi VAR}|_{r=R_o} = 0$) at R_o yields

$$a_{nV} I_1(m_{nf} R_o) + b_{nV} K_1(m_{nf} R_o) = 0. \quad (6.45)$$

6.2.8 Solving the ten equations simultaneously for AR analysis

The equations formed after the implementation of the boundary conditions must be solved simultaneously to solve for the coefficients. The rearranged equations are as follows

$$1. \quad a_{nI} I_1(m_{nf} i R_s) + b_{nI} K_1(m_{nf} i R_s) = 0, \quad (6.46)$$

$$2. \quad m_{nf} [a_{nI} I_1(m_{nf} i R_r) + b_{nI} K_1(m_{nf} i R_r) - a_{nII} I_1(m_{nf} i R_r) - b_{nII} K_1(m_{nf} i R_r)] = 0, \quad (6.47)$$

$$3. \quad m_{nf} [a_{nI} I_0(m_{nf} i R_r) - b_{nI} K_0(m_{nf} i R_r) - \mu_{rI} a_{nII} I_0(m_{nf} i R_r) + \mu_{rI} b_{nII} K_0(m_{nf} i R_r)] = 0, \quad (6.48)$$

$$4. \quad m_{nf} [a_{nII} I_1(m_{nf} i R_{coil}) + b_{nII} K_1(m_{nf} i R_{coil}) - a_{nIII} I_1(m_{nf} i R_{coil}) - b_{nIII} K_1(m_{nf} i R_{coil})] = m_{nf} \frac{\pi L_1(m_{nf} i R_{coil})}{2m_{nf}^2} P_{n^{fAR}}, \quad (6.49)$$

$$5. \quad m_{nf} [a_{nII} I_0(m_{nf} i R_{coil}) - b_{nII} K_0(m_{nf} i R_{coil}) - a_{nIII} I_0(m_{nf} i R_{coil}) + b_{nIII} K_0(m_{nf} i R_{coil})] = m_{nf} \frac{\pi L_0(m_{nf} i R_{coil})}{2m_{nf}^2} P_{n^{fAR}}, \quad (6.50)$$

$$6. \quad m_{nf} [a_{nIII} I_1(m_{nf} o R_{coil}) + b_{nIII} K_1(m_{nf} o R_{coil}) - a_{nIV} I_1(m_{nf} o R_{coil}) - b_{nIV} K_1(m_{nf} o R_{coil})] = -m_{nf} \frac{\pi L_1(m_{nf} o R_{coil})}{2m_{nf}^2} P_{n^{fAR}}, \quad (6.51)$$

$$7. \quad m_{nf} [a_{nIII} I_0(m_{nf} o R_{coil}) - b_{nIII} K_0(m_{nf} o R_{coil}) - a_{nIV} I_0(m_{nf} o R_{coil}) + b_{nIV} K_0(m_{nf} o R_{coil})] = -m_{nf} \frac{\pi L_0(m_{nf} o R_{coil})}{2m_{nf}^2} P_{n^{fAR}}, \quad (6.52)$$

$$8. \quad m_{nf} [a_{nIV} I_1(m_{nf} o R_s) + b_{nIV} K_1(m_{nf} o R_s) - a_{nV} I_1(m_{nf} o R_s) - b_{nV} K_1(m_{nf} o R_s)] = 0, \quad (6.53)$$

$$9. \quad m_{nf} [\mu_{rV} a_{nIV} I_0(m_{nf} o R_s) - \mu_{rV} b_{nIV} K_0(m_{nf} o R_s) - a_{nV} I_0(m_{nf} o R_s) + b_{nV} K_0(m_{nf} o R_s)] = 0, \quad (6.54)$$

$$10. \quad a_{nV} I_1(m_{nf} R_o) + b_{nV} K_1(m_{nf} R_o) = 0. \quad (6.55)$$

The matrix method is adopted to find the coefficients as shown on (6.56)

$$\begin{bmatrix}
 I_1(M^{af}) & -K_1(M^{af}) & 0 & 0 & 0 & 0 & 0 & 0 & 0 & 0 \\
 I^{bf}(M^{bf}) & K^{bf}(M^{bf}) & -I^{bf}(M^{bf}) & -K^{bf}(M^{bf}) & 0 & 0 & 0 & 0 & 0 & 0 \\
 I^{af}(M^{bf}) & -K^{af}(M^{bf}) & -\mu_{r,I}I^{af}(M^{bf}) & \mu_{r,I}K^{af}(M^{bf}) & 0 & 0 & 0 & 0 & 0 & 0 \\
 0 & 0 & I^{bf}(M^{cf}) & K^{bf}(M^{cf}) & -I^{bf}(M^{cf}) & -K^{bf}(M^{cf}) & 0 & 0 & 0 & 0 \\
 0 & 0 & I^{af}(M^{cf}) & -K^{af}(M^{cf}) & -I^{af}(M^{cf}) & K^{af}(M^{cf}) & 0 & 0 & 0 & 0 \\
 0 & 0 & 0 & 0 & I^{bf}(M^{df}) & K^{bf}(M^{df}) & -I^{bf}(M^{df}) & -K^{bf}(M^{df}) & 0 & 0 \\
 0 & 0 & 0 & 0 & I^{af}(M^{df}) & -K^{af}(M^{df}) & -I^{af}(M^{df}) & K^{af}(M^{df}) & 0 & 0 \\
 0 & 0 & 0 & 0 & 0 & 0 & I^{bf}(M^{ef}) & K^{bf}(M^{ef}) & -I^{bf}(M^{ef}) & -K^{bf}(M^{ef}) \\
 0 & 0 & 0 & 0 & 0 & 0 & \mu_{r,V}I^{af}(M^{ef}) & -\mu_{r,V}K^{af}(M^{ef}) & -I^{af}(M^{ef}) & K^{af}(M^{ef}) \\
 0 & 0 & 0 & 0 & 0 & 0 & 0 & 0 & I_1(M^{ff}) & +K_1(M^{ff})
 \end{bmatrix}$$

$$\begin{bmatrix}
 a_{nI} \\
 b_{nI} \\
 a_{nII} \\
 b_{nII} \\
 a_{nIII} \\
 b_{nIII} \\
 a_{nIV} \\
 b_{nIV} \\
 a_{nV} \\
 b_{nV}
 \end{bmatrix}
 =
 \begin{bmatrix}
 0 \\
 0 \\
 0 \\
 m_{nf} \frac{\pi L_1(M^{cf})}{2m_{nf}^2} P_{n^{fAR}} \\
 m_{nf} \frac{\pi L_0(M^{cf})}{2m_{nf}^2} P_{n^{fAR}} \\
 -m_{nf} \frac{\pi L_1(M^{df})}{2m_{nf}^2} P_{n^{fAR}} \\
 -m_{nf} \frac{\pi L_0(M^{df})}{2m_{nf}^2} P_{n^{fAR}} \\
 0 \\
 0 \\
 0
 \end{bmatrix}
 \tag{6.56}$$

where $M^{af} = m_{nf}iR_s$, $M^{fb} = m_{nf}iR_r$, $M^{cf} = m_{nf}iR_{coil}$, $M^{df} = m_{nf}oR_{coil}$, $M^{ef} = m_{nf}oR_s$, $M^{ff} = m_{nf}R_o$; $I^{af} = m_{nf}I_0$, $I^{bf} = m_{nf}I_1$, $K^{af} = m_{nf}K_0$, and $K^{bf} = m_{nf}K_1$. It should be noted that the matrix simplification is done so that the matrix can be illustrated in its full composition. First line and the last line has been left with the Bessel functions unrepresented.

6.2.9 Final Solutions to the magnetic vector potential and the magnetic flux densities

The obtained coefficient expressions from the matrix (6.56) for $a_{nI} - a_{nV}$ and $b_{nI} - b_{nV}$ must be replaced back into various general solutions.

Solutions to the magnetic vector potential are obtained by inserting the coefficient expressions obtained from the matrix into the equations for the magnetic vector potential in (6.9) - (6.13). Numerical values can then be inserted for Validation with a finite element software.

Solutions to the radial magnetic flux densities are obtained also by inserting the expressions derived from the matrix for the coefficients into the equations for the radial magnetic flux densities in (6.15) - (6.19).

Solutions to the axial magnetic flux densities are finalised by inserting the solutions for the coefficients that are obtained from the matrix into (6.20) - (6.24).

Total magnetic flux density is then obtained by the algebraic sum of the radial magnetic flux density and the axial magnetic flux density as shown in (3.68).

6.2.10 Determination of inductance

The two methods that can be employed for the determination of the inductance have been outlined in 3.9. Therefore, the route to the determination of the self-inductance, as the machine under analysis is a single phase machine, is the evaluation of the flux linkage due to the armature reaction. The formulation for the flux linkage is not unique from 3.72 but includes the consideration of the armature as having finite length arranged in series with a separation distance of τ_l . This approach demonstrates the actual behaviour of the field generated by the armature only and this can be illustrated, in this case, by zooming on one armature in the obtained results. The flux linkage obtained because of the armature reaction is given by

$$\psi_f = \sum_{n=1,2,..}^{\infty} \phi_f \quad (6.57)$$

where

$$\phi_f = \frac{4\pi N_p N_t K_{dpn}}{m_n(oR_{coil} - iR_{coil})} \int_{iR_{coil}}^{oR_{coil}} r [a_{nIII} I_1(m_{nf}r) + b_{nIII} K_1(m_{nf}r) + S(r^{AR})] dr . \quad (6.58)$$

In (6.58), $S(r^{AR}) = \frac{\pi L_1(m_{nf}r)}{2m_{nf}^2} P_{nfAR}$ as provided in (6.14). Other factors of (6.58) have already been explained in 3.9.1 and are therefore not repeated in this sub-section. The self inductance of the winding is calculated from

$$L_{self} = \frac{\psi_f}{J_0 \tau_w (oR_{coil} - iR_{coil}) / N_t} \quad (6.59)$$

6.2.11 Validation of the armature reaction field with finite element software, MagNet by infolytica inc..

The accuracy of the analytical model is verified by comparing with the finite-element software. In the finite-element simulation, the permanent magnets are taken as air while the coils are considered as single turn (three) coils connected in series. The machine is taken as a finite length machine and therefore, only a boundary box is inserted as regards boundary conditions. The analytical model on the other hand, takes a series of armatures with τ_l in between to emulate a finite-length armature and its field behaviour. The machine current however is large due taking the coils as single turn but take note that with many turns in the coil, the current levels are normalised. The same applies to the voltage levels which must increase with the increase in the number of coil turns. For the prediction of the armature reaction field, the maximum current is considered and calculated in both the analytical and finite-element models by

$$I_{max} = J_0 \times h_{coil} \times \tau_w \times Fillfactor, \quad (6.60)$$

where h_{coil} - is the coil thickness, τ_w - is the coil length. The *Fillfactor* is taken as 0.55. The finite-element simulation set-up is illustrated on Figure 6.2 while the solution mesh remains just demonstrated on Figure 5.4b.

6.2.11.1 Radial magnetic flux density comparison with FEM for armature reaction

horizontal lines on the middle of the subdomains *II, III, IV*, which are the armature reaction model lower air-gap ($h_{ipm} + g_1$), the coil area (h_{coil}) and the upper air-gap ($g_2 + h_{opm}$) see Figure 4.1, have been taken for the comparisons of the analytical model to the finite-element package. The radial flux density comparison illustrated on Figure 6.3 is obtained from taking the machine length plus a small distance from the machine axial edges to demonstrate the fringing fields.

Figure 6.3 shows that the analytical model correlates well with the finite-length finite-element simulation. The differences at the axial ages are attributed to the analytical model taking the iron yokes as infinitely long. From the figure, it can be seen that the machine length plus a few *mm* on the axial edges of the machine are shown. The full

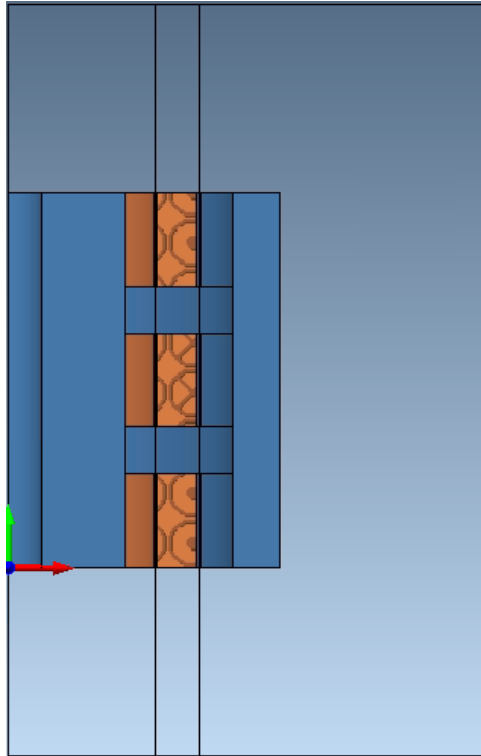


Figure 6.2: An illustration of MagNet set-up for the armature reaction field

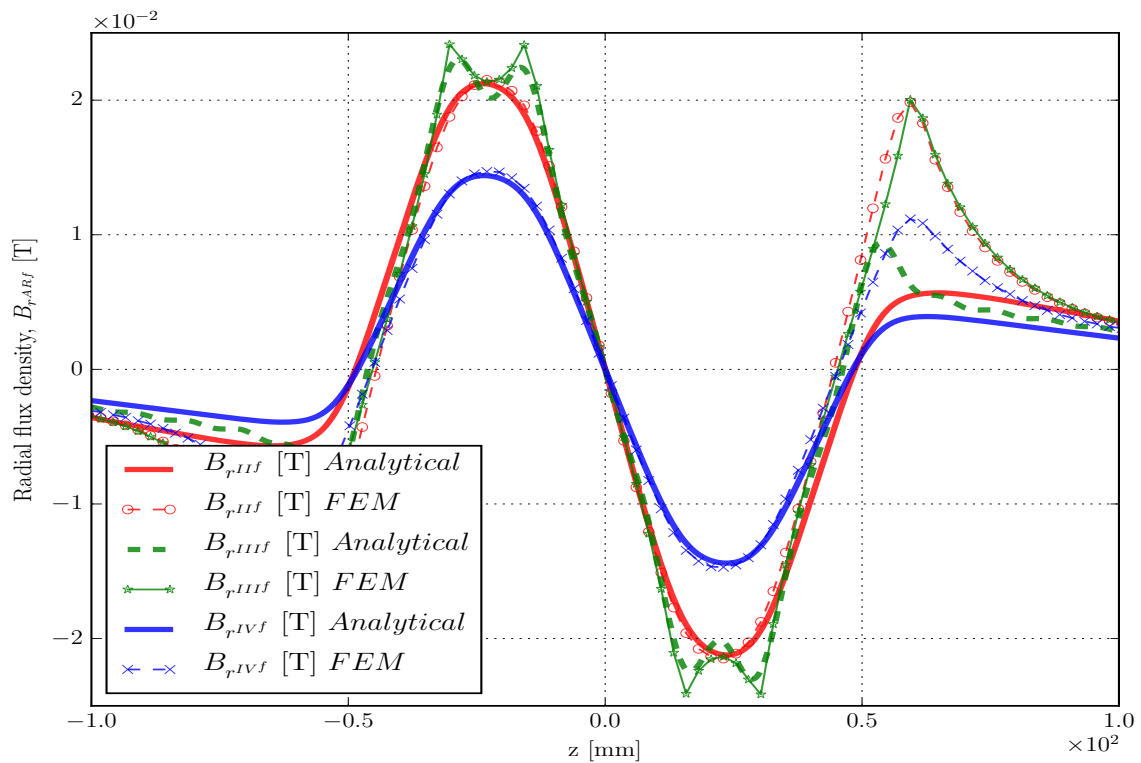


Figure 6.3: Radial flux density compared to a finite length FEM model

analytical model calculation takes into consideration $2\tau_{lp}$ and the extract illustrated from Figure is obtained from Figure

Figure 6.4 shows the full spectrum of the analytical model predictions of the field

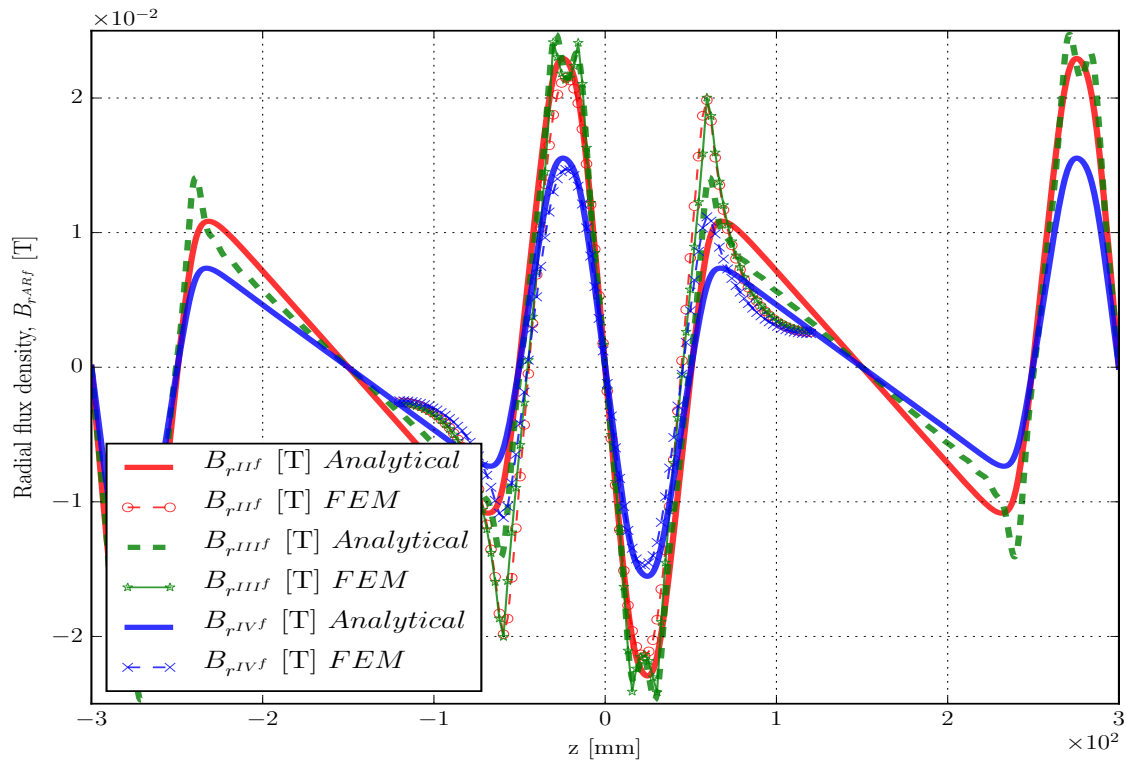


Figure 6.4: Radial flux density compared to a finite length FEM model with full analytical model axial length analysis

behavior in the radial direction. The correlation can be observed as good correlation.

6.2.11.2 Axial magnetic flux density comparison with FEM for armature reaction

For the axial direction of the field, the comparison is illustrated on Figure 6.5. In a similar manner, two figures are displayed, one for the machine length and another incorporating the full analytical model spectrum.

The figure shows good correlation with some deviations for the lower air-gap at the axial edges of the machine. However, since the level of the armature reaction is very low for this machine, such small deviations as noticed for the axial flux density has almost no effect on the overall flux density in the machine.

6.2.11.3 Countour plot comparison with FEM for armature reaction

The contour plots and the field lines for the armature reaction obtained from calculation of the total magnetic field ($B_T = \sqrt{B_r^2 + B_z^2}$). As FEM automatically calculates the total magnetic field, the formula shown is employed in the analytical model. The comparison between the analytical model and the finite-element method are illustrated on Figure 6.7 and Figure 6.8.

Figure 6.7 shows the contour plot obtained from FEM. The analytically obtained contour plots are demonstrated on Figures 6.8 and 6.9

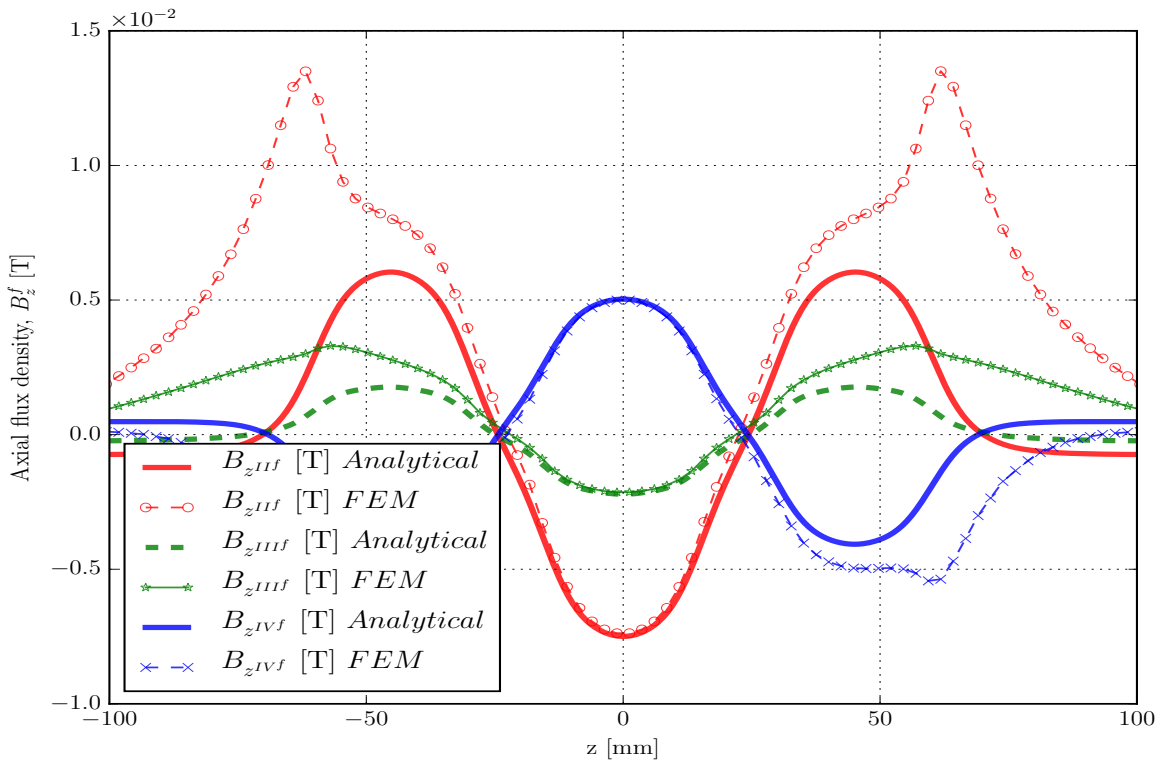


Figure 6.5: Axial flux density compared to a finite length FEM model

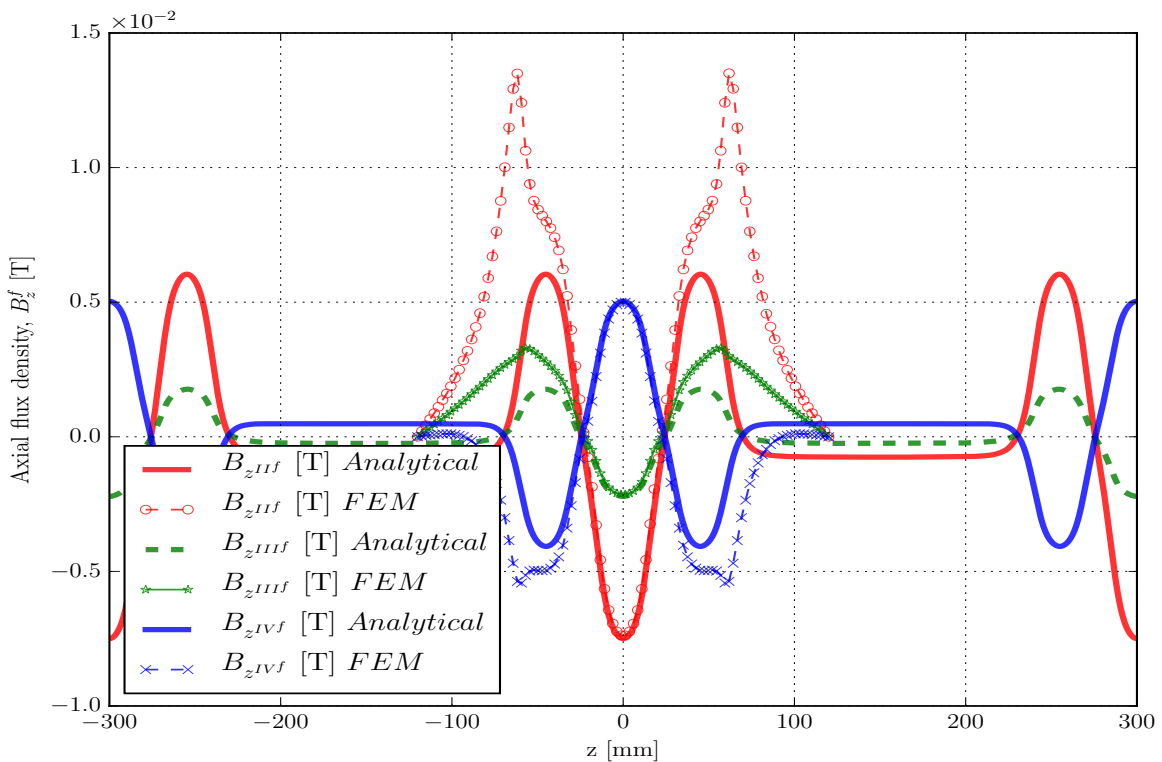


Figure 6.6: Axial flux density compared to a finite length FEM model considering the full analytical spectrum

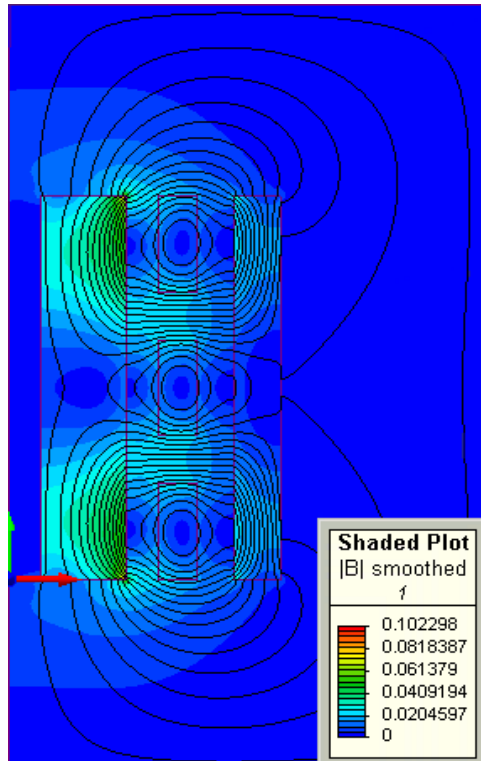


Figure 6.7: Contour plot obtained from the finite-element solution

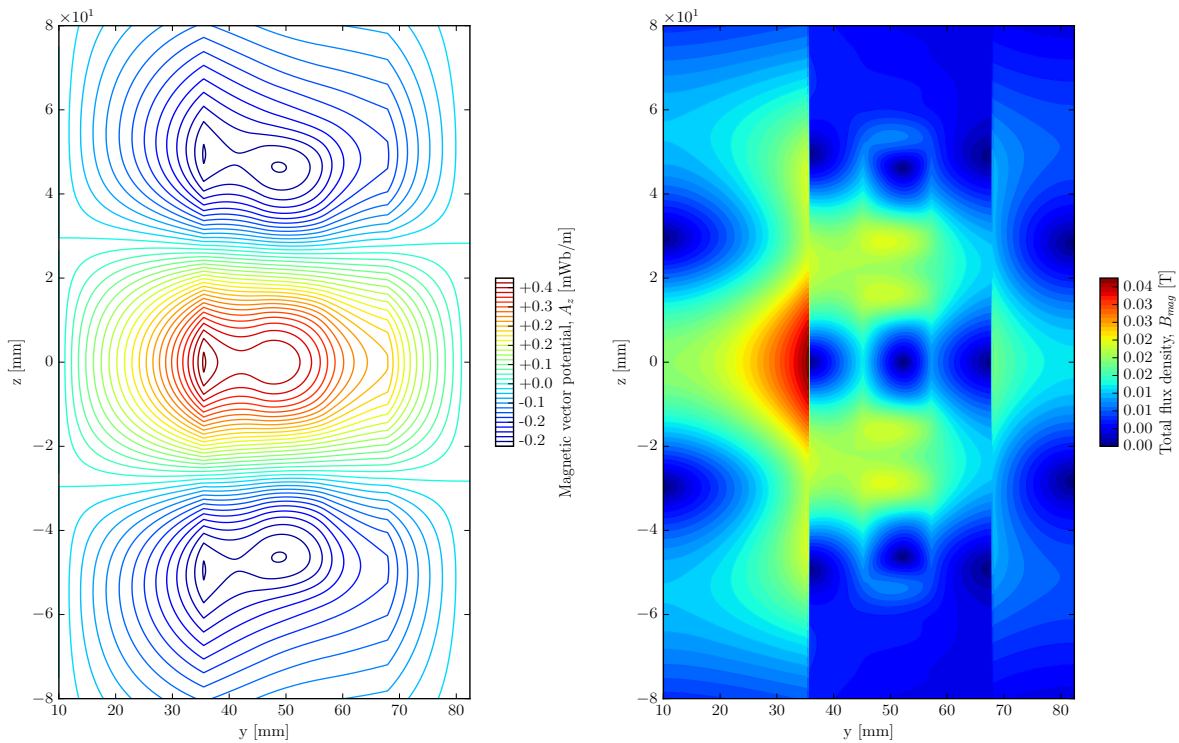


Figure 6.8: Analytically determined magnetic field lines and contour plot considering the machine length plus extra mm on the axial edges for the armature reaction fields prediction

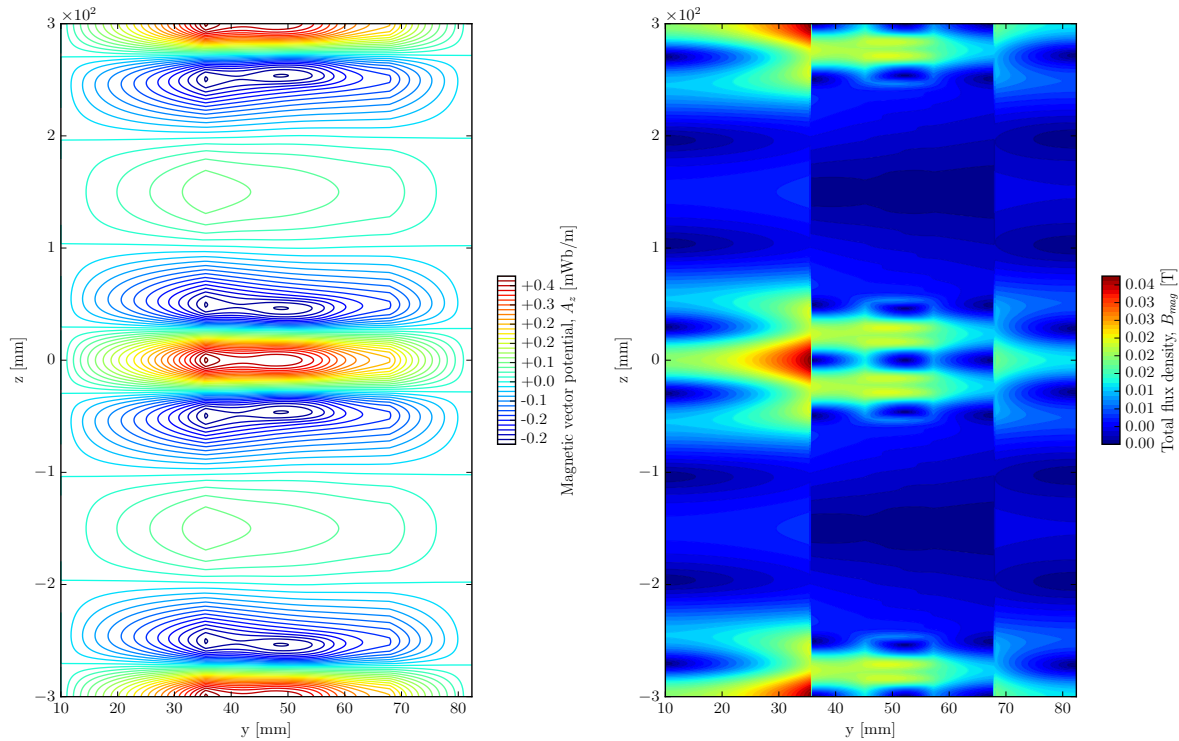


Figure 6.9: Analytically determined magnetic field lines and contour plot considering an axial length of $2\tau_{lp}$ for the armature reaction fields prediction

6.3 Global quantities - finite length

The formulation for the global quantities are considered with the procedure similar to what is illustrated in Chapter 4 but taking the permanent magnet arrays and the coils with finite length. As explained already, the finite length armature and permanent magnet array are replicated in series with a separation distance of τ_l .

6.3.1 Force prediction

The explanation of the electromagnetic force and the methods through which it can be derived has been discussed in Section 4.1. The methods commonly employed to determine the forces are the co-energy method - (4.2), the Maxwell Stress Tensor (MST) method - (4.3) and the Lorentz Force method - (4.5). The Lorentz force method has been adopted for the formulation of force for this machine. Certain assumptions must be in place for the formulation to be in order.

6.3.2 Assumptions (Finite length model)

The following assumptions are taken for the formulation of the global quantities:

1. The axial length of the permanent magnets-array and the armature are assumed to be finite but arranged in series with a separation distance of τ_l ,

2. The stator cores are assumed to be infinitely long but with finite thickness,
3. The stator cores are also assumed to have a relative permeability of $\mu_r = 1000$ to allow for the monitoring of the iron yoke saturation.

The formulation for the **thrust force** on a coil with a current density is then given by

$$F_{wf} = - \int_{z-\frac{\tau_w}{2}}^{z+\frac{\tau_w}{2}} \int_{iR_{coil}}^{oR_{coil}} 2\pi r J B_{rIII f}(r, z) dr dz \quad (6.61)$$

where $B_{rIII f}$ is the magnetic flux density obtained in (5.21) for the open circuit model. The expression can then be expanded as

$$F_{wf} = \sum_{n=1,2,..}^{\infty} \left[2\pi \tau_w J K_{dn} \int_{iR_{coil}}^{oR_{coil}} r [a_{nIII} I_1(m_n f r) + b_{nIII} K_1(m_n f r)] dr \right] \cos(m_n f z). \quad (6.62)$$

where τ_w is the winding axial length and the winding distribution factor in this case is given by

$$K_{dn} = \frac{\sin \frac{m_n f \tau_w}{2}}{\frac{m_n f \tau_w}{2}}. \quad (6.63)$$

The **total force** on a series of coils connected in one phase winding carrying a current i is predicted by

$$F_{wpf} = \sum_{n=1,2,..}^{\infty} \left[\frac{2\pi K_{dpm} N_{wp}}{(oR_{coil} - iR_{coil})} \int_{iR_{coil}}^{oR_{coil}} r [a_{nIII} I_1(m_n f r) + b_{nIII} K_1(m_n f r)] dr \sin \left(m_n f z - \frac{m_n f \tau_{wp}}{2} \right) \right] i. \quad (6.64)$$

where τ_{wp} is the winding pitch, N_{wp} is the number of series turns per phase and $K_{dpm} = K_{pn} K_{dn}$ is called the winding factor. K_{pn} , the winding pitch factor in this case is given by

$$K_{pn} = \sin \left(\frac{m_n f \tau_{wp}}{2} \right) \quad (6.65)$$

6.3.3 Flux linkage and EMF prediction

The formulation of the flux linkage considering the PM array and the armature to have a finite length is similar to (4.15) and is determined from

$$\psi_{wf} = \frac{N_w}{\tau_w (oR_{coil} - iR_{coil})} \int_{z-\frac{\tau_w}{2}}^{z+\frac{\tau_w}{2}} \int_{iR_{coil}}^{oR_{coil}} 2\pi \times A_{\phi III f}(r, z) dr dz, \quad (6.66)$$

When expanded ψ_{wf} can be given by

$$\psi_{wf} = \sum_{n=1,2,\dots}^{\infty} \left[\frac{2\pi\tau_w K_{dn}}{m_{nf}} \int_{iR_{coil}}^{oR_{coil}} r [a_{nIII} I_1(m_{nf}r) + b_{nIII} K_1(m_{nf}r)] dr \right] \sin(m_{nf}z) . \quad (6.67)$$

The coil induced EMF that is created by the motion between the armature and the permanent magnet array stator is then calculated from taking the time derivative of the flux linkage and given by

$$e_{wf} = -\frac{d\psi_w}{dt} = -v \frac{d\psi_w}{dz} \quad (6.68)$$

which can be expressed as

$$e_{wf} = \sum_{n=1,2,\dots}^{\infty} \left[-\frac{2\pi K_{dpm} N_w}{(oR_{coil} - iR_{coil})} \int_{iR_{coil}}^{oR_{coil}} r [a_{nIII} I_1(m_{nf}r) + b_{nIII} K_1(m_{nf}r)] dr \sin\left(m_{nf}z - \frac{m_{nf}\tau_{wp}}{2}\right) \right] v \quad (6.69)$$

6.3.4 Comparison with FEM

The linear machine under study has a stroke length of 45 mm and is to operate at a frequency of 50 Hz. To understand the comparisons between the analytical model and the FEM, it is imperative that certain concepts are clearly defined. The motion component is one such concept that must be explained well. In this analysis, the coil's starting position is offset 90 degrees from the magnet poles. That is, while the motion component is calculated as:

$$X = \frac{l_{stroke}}{2} \sin(2\pi ft) \quad (6.70)$$

where X represents the motion component while f and t represent the frequency and time respectively. For the coil to be offset 90 degrees, $\frac{\pi}{2}$ is subtracted as shown in (6.71)

$$X = \frac{l_{stroke}}{2} \sin\left(2\pi ft - \frac{\pi}{2}\right) . \quad (6.71)$$

The coil begins its movements from -22.5 mm through to 0 mm (when magnet poles are aligned with coil poles) and out to 22.5 mm when it finally returns to -22.5 mm.

The next concept is that of the current which is taken to be

$$i = I_{max} \sin(\omega t) = J_{max} \times \tau_w \times h_{coil} \times Fillfactor \sin(2\pi ft) \quad (6.72)$$

where I_{max} is the amplitude of the current, J_{max} being the maximum current density while τ_w and h_{coil} represent the coil dimensions - width and height respectively. The copper fill factor is taken as 0.55. The current appears large because the coil is regarded as a single

turn. With many turns considered, the current value will significantly reduce to normal levels, while on the other hand the voltage values which appear quite small values as will be observed later will increase.

The flux linkage and the emf obtained analytically and displayed in the next subsection are carried on when there is no current in the coils

6.3.4.1 Comparison of flux linkage obtained analytically with FEM

Figure 6.10 shows the comparison of the flux linkage obtained analytically compared to the flux linkage obtained by employing FEM. The analytically obtained flux linkage correlates well with FEM. It must be mentioned that since the subdomain method is employed, only the total flux linkage can be obtained for the analytical model. The electromotive force is obtained by taking the time derivative of the of the flux linkage as shown in (6.68).

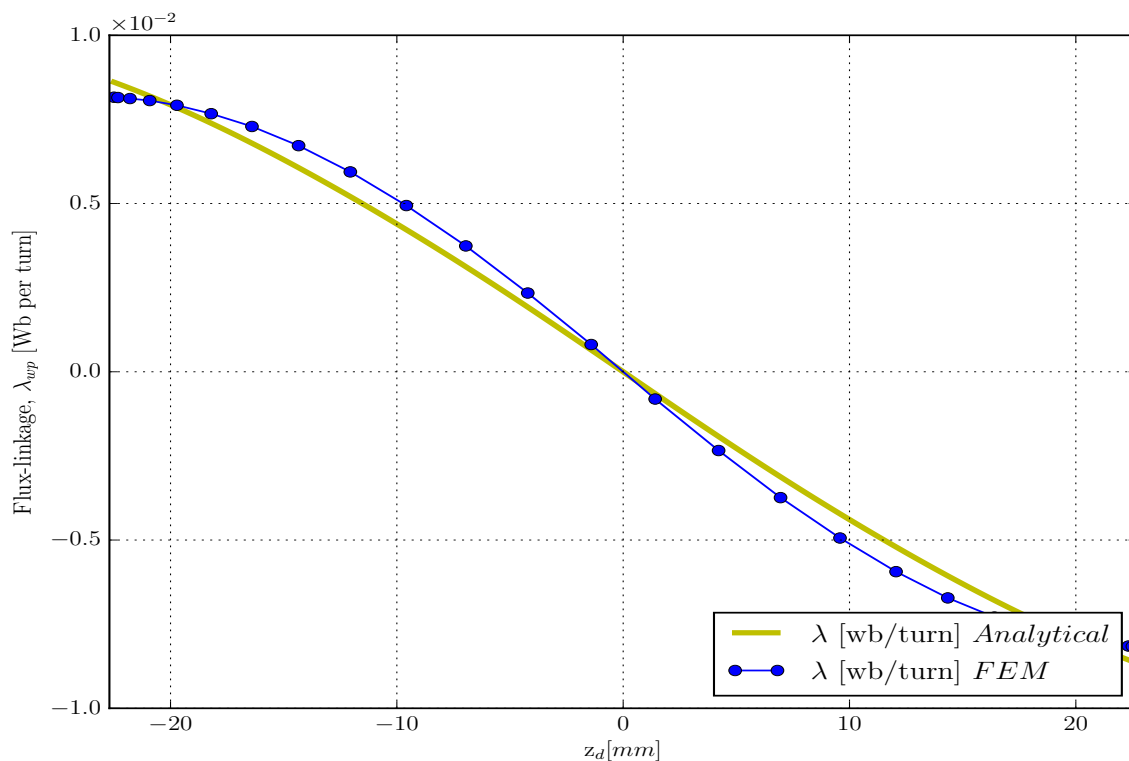


Figure 6.10: Flux linkage in relation with the armature displacement

In addition to this comparison, the flux linkage can also be compared in terms of the armature position against time. The flux linkage against time is displayed for total flux linkages obtained from FEM in comparison to the analytically obtained. This is because individual coils cannot be considered in the subdomain method, and therefore the whole domain is considered resulting in getting the total flux linkage from the FEM for comparison reasons with the analytically obtained flux linkage. As explained earlier

the coil moves from the extreme left to the extreme right and back and therefore the flux linkage against time is shown in Figure 6.11

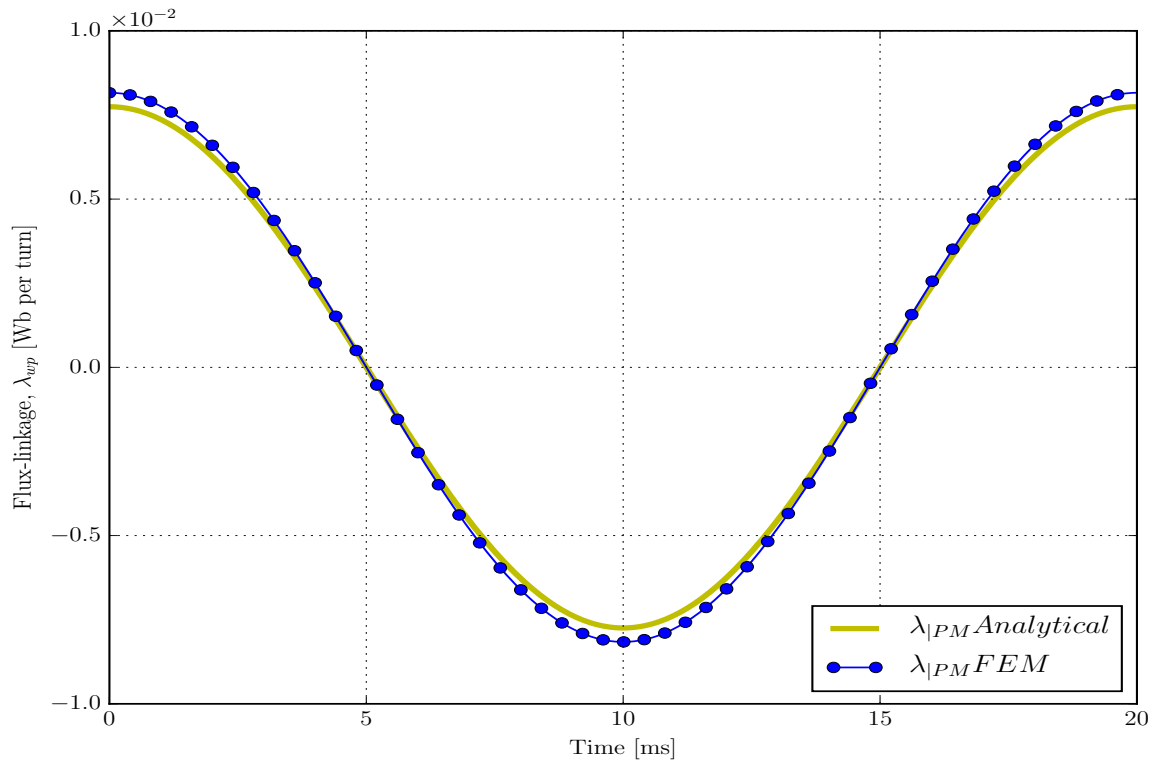


Figure 6.11: Flux linkage in relation with time

6.3.4.2 Comparison of EMF obtained analytically with FEM

At fixed frequency, the coil movements or oscillations leads to the changes in the flux linkages. This leads to the back EMF being induced in the moving coil. The induced electromotive force is obtained when the coil current is zero. Therefore the induced voltage is equal to $V_{emf} = V_{\lambda}$ with reference to Figure ???. To obtain the EMF, the flux linkage obtained (no current in coils) is differentiated against time as in (6.68). The obtained results are compared in Figure 6.12. From Figure 6.12, it can be seen that the back EMF voltage is minimal-to-zero during the periods of low-to-zero coil velocity which occur during the the coil oscillations.

From Figure 6.12, the analytical model compares favourably well with the simulated value. The peak values match very well and could be used to predict the emf of a model.

6.3.4.3 Comparison of Thrust force obtained analytically with FEM

Figure 6.13 show the comparison of the thrust force obtained analytically to that of FEM. As can be seen, the analytically obtained thrust force correlates well with that of FEM. The calculation was conducted while considering the displacement z of the coil. The

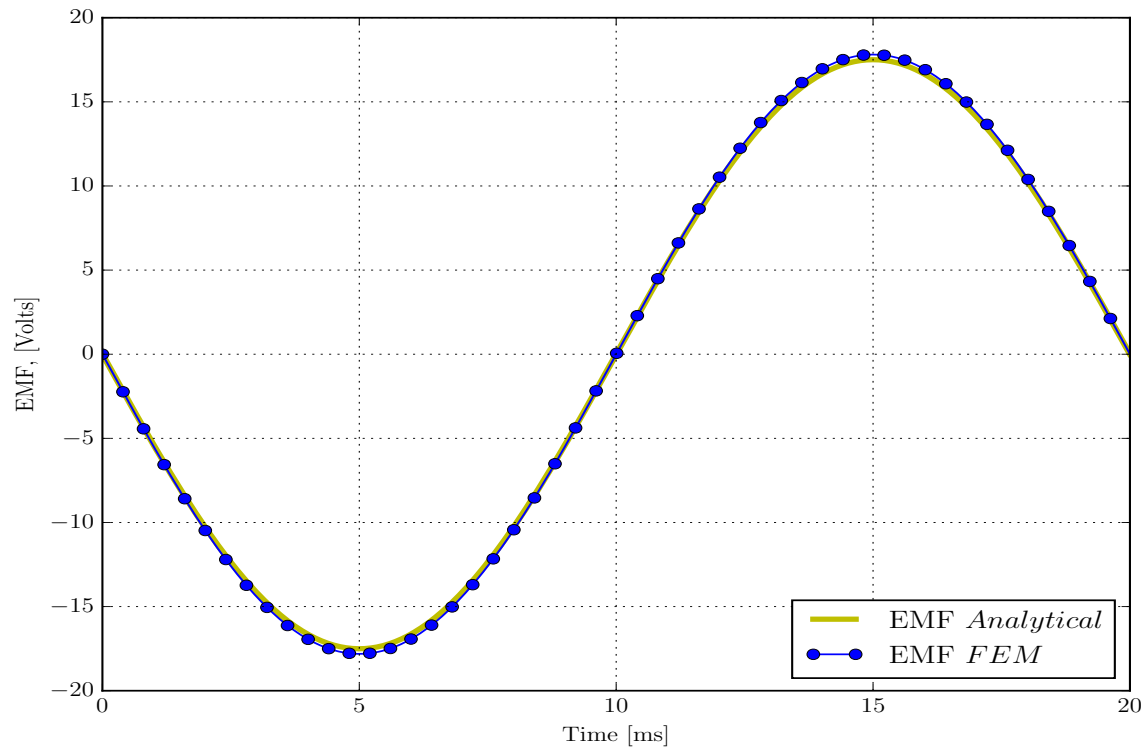


Figure 6.12: Simulated and analytically obtained voltages

maximum force is obtained when the coils are in vertical alignment with the magnetic poles and almost zeros when the coil reaches its displacement axial limit. FEM simulation is done a steps where at each positional step, starting from the negative motion amplitude (-22.5 mm), a simulation is conducted and the value of the force is stored until the positive amplitude is reached.

In addition to this comparison, another Force comparison between the analytical model and FEM is considered in relation to time. Figure 6.14 demonstrates the comparison between the simulated force and the analytically derived force.

The analytically obtained force against time is sinusoidal and close to a more ideal force. However, the prediction in comparison to the simulated model is still valid. The small discrepancies in the plots could be attributed to the assumption that the yokes are infinitely long in the analytical model, a challenge yet to be concurred.

6.4 Summary and conclusion

The development of the analytical model that considers the machine to have a finite length and also considers the machine to have a finite permeability has been developed. The complexity in the development of this model has been on the prediction of the armature reaction field. The incorporation of the air-gap between the iron yokes proved extremely complex and resulted in assuming the iron yokes as infinitely long but considering the

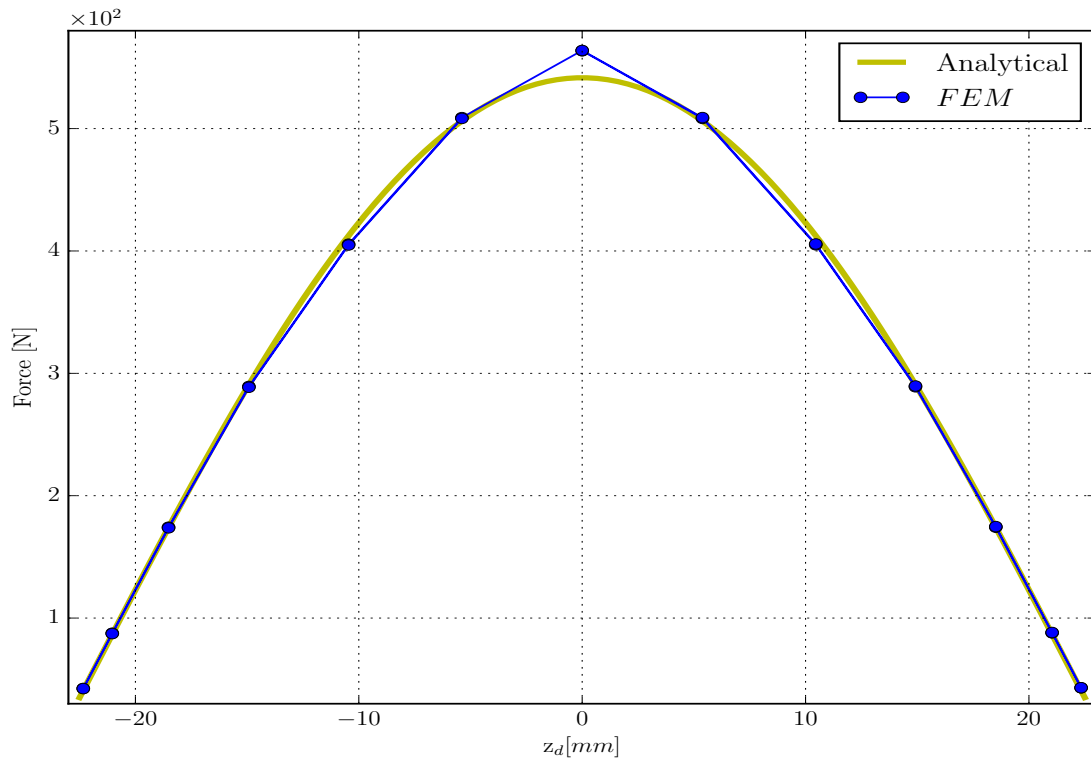


Figure 6.13: Thrust force against translational position

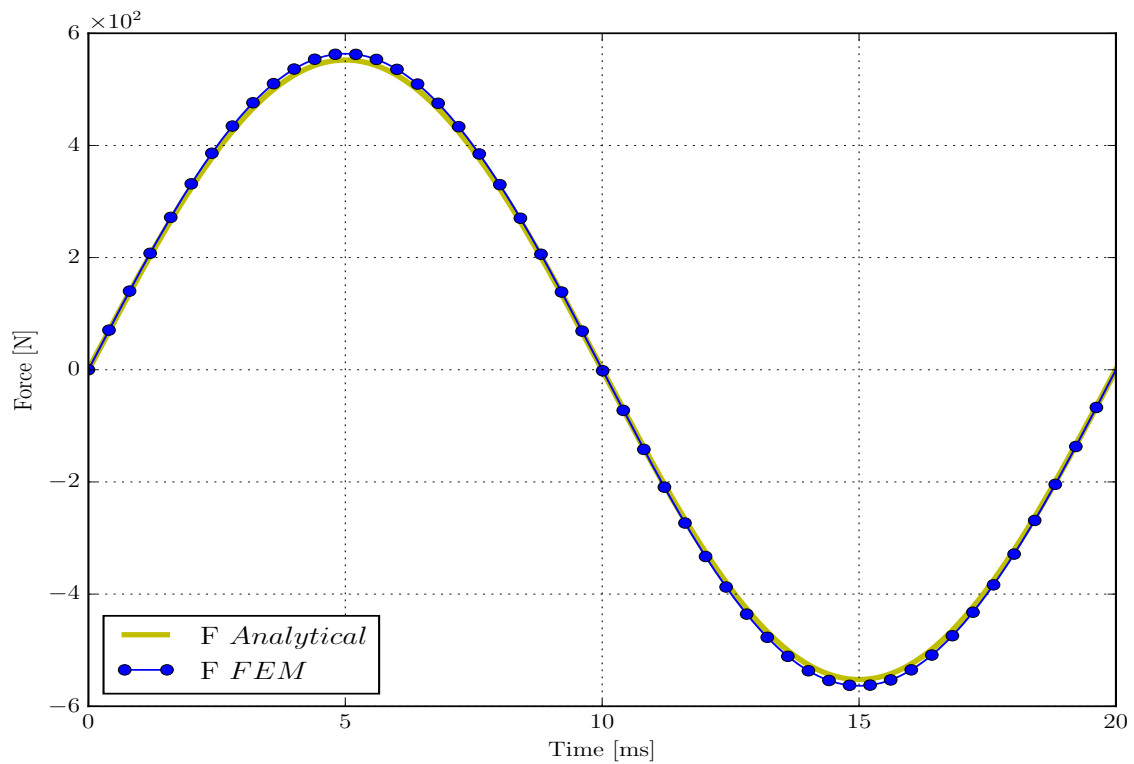


Figure 6.14: Thrust force against time

magnetic arrays and the armature as having a finite length but repeated in discrete series. This approach is taken because without the Fourier series subdomain method, it would

be difficult to formulate expression for the prediction of the magnetic flux density for a finite length machine.

The analytical model has been validated with the finite element method and it matches well with FEM. The assumption of the iron yokes as infinitely long created some level of difficulty in obtaining the actual fringing flux fields pattern as seen in Figures 6.9 compared to Figure 6.7.

Chapter 7

Conclusions and recommendations

7.1 Introduction

A two stage analytical model-one that considers a simulation of the linear machine to be infinitely long and another that considers a simulation of the finite length of the linear machine has been developed in this work for a dual radially magnetised tubular longitudinal flux linear air-cored machine for application in free-piston Stirling engines. The linear machine has 3 magnetic poles surface mounted on the inner yoke and another set of 3 poles on the outer yoke. The number of poles (3 poles) were chosen following the optimisation results obtained by Strauss [50] as indicative of the lowest total active mass in comparison to 2, 4 and 5 poles. Although the Halbach PM array machine produces more radial flux densities in the air-gap and reduces axial flux densities in the stator core thereby reducing the thickness of the stator core, the proposed radially magnetised machine has the advantage of easier manufacturing and assembly. Halbach array is extremely difficult to assemble as the PMs constantly exert high opposite forces causing miss-alignment of the PMs. The proposed air-cored topology has numerous advantages over the iron-cored counterpart linear generators in that there are no cogging forces and attraction forces between the translator and the stator which are more pertinent in iron-cored machines. With air-cored machine, low inductance is obtained which leads to a high power factor.

The initial stage of the analytical model development focused on the infinitely long linear machine to understand the underlying principles that are required to approach the development of an analytical model for a finite length linear machine. For the infinitely long analytical model, comparisons are undertaken with FEM which show that the model matches well to each other. On the other hand, the infinitely long analytical model serves as a benchmark for the development of the analytical model that focusses on the actual finite length of the linear machine. Both analytical models are then tested and compared to the finite element software MagNet by infolytica inc. for validation.

7.2 Conclusions

7.2.1 Analytical model developed for an infinitely long machine

The analytical model developed considering the machine to be infinitely long compared well with the finite element software. With this approach, boundary conditions were only

applied in the radial direction of the linear machine. The model was staged in three sections-open circuit, armature reaction and global quantities. The open circuit section considered the influence of only the magnetic field generated by the permanent magnets while the coil is considered switched off. The armature reaction then considered the influence of the coil or armature supplied with a current while the permanent magnets were taken as switched off. Global quantities involved the solution to the power, the induced voltage and the flux linkage. The subdomain method involving the Fourier expansion of Maxwell's equation was adopted. The general solution formulated resulted in having the modified Bessel functions of the first and second kind. This complicated the solution of the magnetic flux densities in that higher harmonic solutions could not be achieved. The conditioning of the matrix for the determination of the coefficients for the Fourier Bessel solutions was getting distorted the higher the number of harmonics were taken. The Fourier series solutions are known to provide a more accurate solution with an infinite number of harmonics. In this work, however, the solution were obtained with a finite number of harmonics of about 17^{th} and 18^{th} of the $(2n - 1)^{th}$ harmonics.

The obtained solution albeit a finite number of harmonic solutions matched well with the finite element software as seen in Chapters 2.9, 3.10 and 4.4. If each domain is taken separately, then the air-gap subdomain solutions could reach slightly higher harmonics in comparison to the PM subdomain solutions and the yoke subdomain solutions. The challenge of obtaining solutions with a finite number of harmonics has been experienced and discussed by Gysen *et al* in [81] and also by Gerber in [100, Chap. 5, Sec. 3.2], and the causes of such solutions have been attributed to the presence of the modified Bessel functions in the Fourier solutions. The actual case is that as n increases, the modified Bessel functions of first kind and second kind I_n and K_n become extremely large terms and small terms respectively. This leads to the matrix becoming ill conditioned with increase in the harmonic numbers. Besides that, the modified Bessel functions of the first kind multiplied by the modified Bessel functions of the second kind in the magnetic field expressions experiences the same challenge with increase in n because of the product of extremely large numbers and also extremely small numbers.

7.2.2 Analytical model developed for a finite length machine

To approach the development of an analytical model that can accurately simulate a finite length machine, a few notes were taken from the initial analytical model for an infinitely long machine. The main question was how to obtain a solution that does not involve series such as the Fourier series. This approach, after several attempts resulted in solutions that were far from what was expected. Another approach was then taken to take the finite length machine and repeat it several times and in so doing making a series of discrete finite length linear machines. This approach created more room because the subdomain method

(Fourier series) could be adopted to develop the solutions. Open circuit, armature reaction and global quantities calculation stages were adopted just as in the initial analytical model development. A separation distance τ_l between the discrete linear machine series that is considered to be a multiple of τ_p and much larger than τ_p . Mathematically formulating boundary conditions for the iron yokes to be considered having a finite length proved extremely complex. Attempted solutions were outside the expected solutions. Finally, it was decided to take the iron yokes as infinitely long while the armatures and the PM arrays were considered as having finite lengths.

7.3 Dissertation contribution made to this work

The following contributions have been made to this work.

- An analytical model of the LFPM moving coil linear machine has been developed by employing the subdomain (Fourier series) method and the separation of variables. The model (assuming the machine is infinitely long) is capable of predicting the magnetic flux density distribution in the open circuit and the armature reaction. The model considers the permeability of the yokes to be finite and with a finite thickness with expressions developed that help to monitor the saturation level in the iron yokes.
- Another analytical model with consideration of the machine's finite length has been developed. The model predicts the flux density distribution of a machine's actual finite length and flux behaviour. The model compares well with finite element software.

7.4 Recommendations to be considered for future work

- Research needs to be conducted on the asymptotic boundary condition [80] for implementation on a finite length linear machine. Although the method is utilised in finite element software, successful implementation of asymptotic boundary condition in an analytical model will lead to the full capturing of the natural magnetic field behaviour within the machine and the fringing flux behaviour pattern.
- Formulation of the Laplace and Poisson solution without the Modified Bessel functions could improve the overall solution by achieving higher harmonic solutions or even infinite harmonic solutions.

- Tailor Series is another option that need to be considered in the development of the analytical model but with a meticulous approach,
- Further research is required on the conditioning of the coefficient solution matrices. This would require employing the approximations of the modified Bessel functions of both the first and second kind instead of the python defined I_n and K_n . This recommendation would be entirely a mathematical field approach, the publishing of which may be acceptable in mathematical specialised journals.
- An comparative optimisation study is further recommended to observe that both FEM and the analytical model do conclude with the similar dimensions after optimisations.

Appendices

Appendix A

Magnetisation vector determination for various magnet arrangements

A.1 Magnetisation vector for four pole double sided machine with two configurations

A.1.1 One central complete magnet length and two half length size magnets on each side

Below is a diagram to illustrate the magnet arrangement for which the magnetisation vector is to be determined.

From Figure A.1, the radial magnetisation vector is determined from

$$M = M_r \mathbf{e}_r , \quad (\text{A.1})$$

where

$$M_r(z) = \frac{a_0}{2} + \sum_{n=1, \dots}^{\infty} a_n \cos(w_n z) . \quad (\text{A.2})$$

Since the period is $2\tau_p$, then $w_n = n\pi/\tau_p$. Therefore,

$$a_n = \frac{1}{\tau_p} \int_{-\tau_p}^{\tau_p} f(z) \cos(w_n z) dz , \quad (\text{A.3})$$

which can be doubled if considered from 0 to τ_p as

$$a_n = \frac{2}{\tau_p} \int_0^{\tau_p} f(z) \cos(w_n z) dz . \quad (\text{A.4})$$

Considering only the positive and negative field areas while excluding the areas where the field is deemed zero

$$a_n = \frac{2B_{rem}}{\tau_p \mu_0} \left[\int_0^{\tau_m/2} \cos(w_n z) dz - \int_{(2\tau_p - \tau_m)/2}^{\tau_p} \cos(w_n z) dz \right] . \quad (\text{A.5})$$

Solving the integrals results into

$$a_n = \frac{2B_{rem}}{\tau_p \mu_0 w_n} \left\{ \sin\left(\frac{w_n \tau_m}{2}\right) + \sin\left[w_n \left(\frac{2\tau_p - \tau_m}{2}\right)\right] \right\} . \quad (\text{A.6})$$

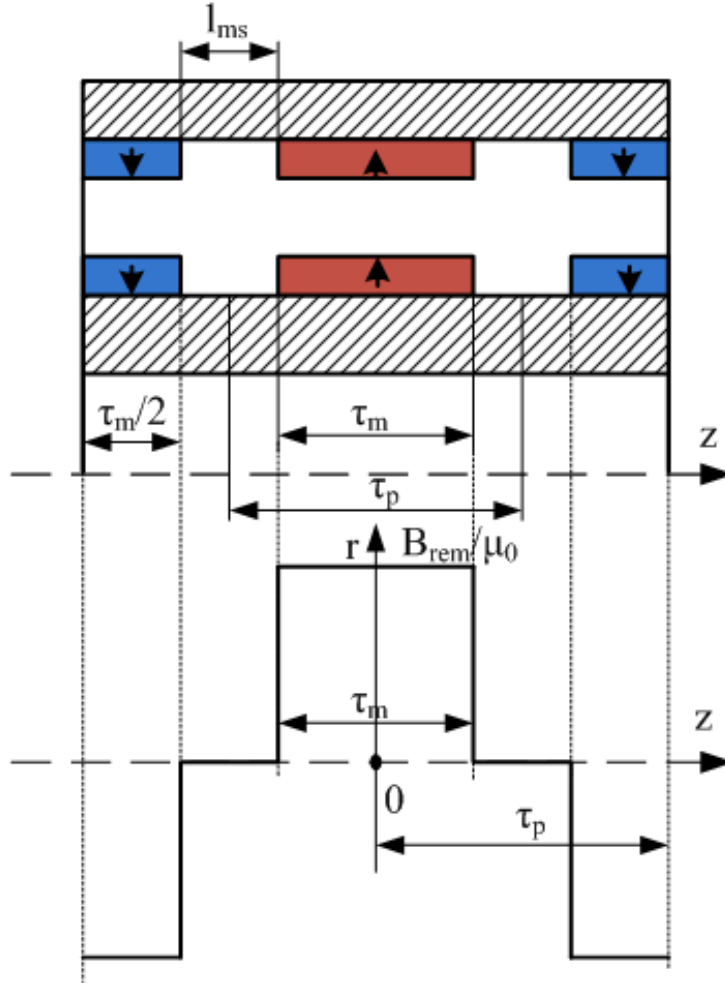


Figure A.1: Four pole double sided PM linear machine with one complete central magnet and two half length magnets

Considering the trigonometric identity ($\sin(a - b) = \sin a \cos b - \sin b \cos a$),

$$a_n = \frac{2B_{rem}}{n\pi\mu_0} (1 - (-1)^n) \sin\left(\frac{n\pi\tau_m}{2\tau_p}\right), \quad (\text{A.7})$$

where $\cos(n\pi) = (-1)^n$ and also $\sin(n\pi) = 0$. The obtained solution is zero for even numbers of n and solutions can be obtained for odd numbers and for this reason n is taken as $2n - 1$

$$a_{2n-1} = \frac{4B_{rem}}{(2n-1)\pi\mu_0} \sin\left(\frac{(2n-1)\pi\tau_m}{2\tau_p}\right). \quad (\text{A.8})$$

The magnetisation vector is finally obtained as

$$M_r(z) = \frac{a_0}{2} + \frac{4B_{rem}}{\pi\mu_0} \sum_{n=1, \dots}^{\infty} \frac{1}{(2n-1)} \sin\left(\frac{(2n-1)\pi\tau_m}{2\tau_p}\right) \cos(m_n z), \quad (\text{A.9})$$

where

$$m_n = (2n-1) \frac{\pi}{\tau_p}. \quad (\text{A.10})$$

A.1.2 Two full magnet arrangement for a four pole machine double sided

The diagram below shows a set-up of the PMs on a machine with the same pole pitch length as the previously presented machine in A.1.1.

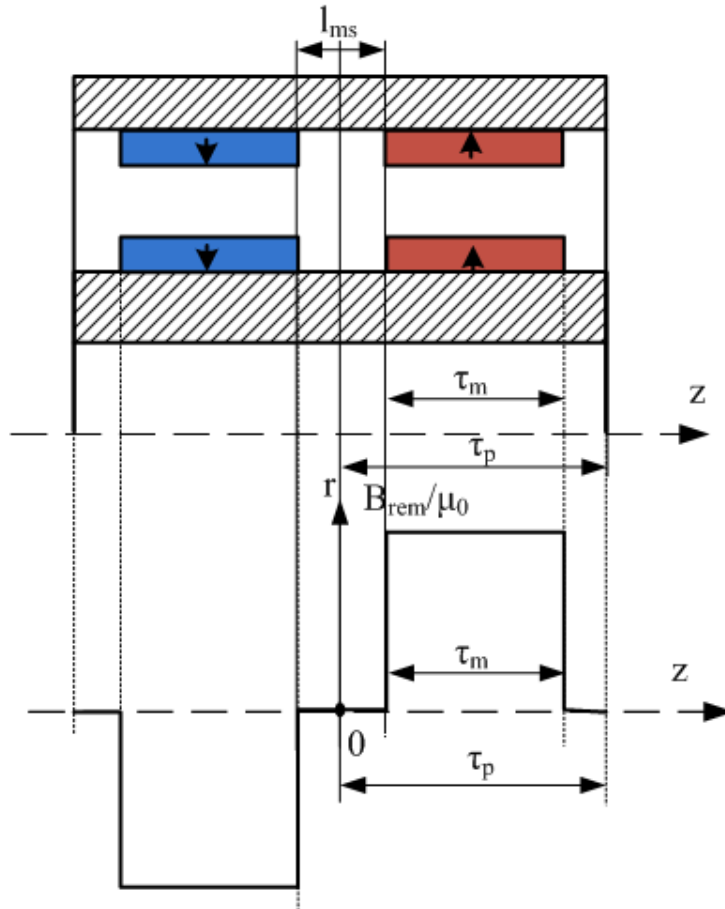


Figure A.2: Four pole double sided PM linear machine with two full length magnets

From Figure A.2, the magnetisation vector is determined from

$$M = M_r \mathbf{e}_r , \quad (\text{A.11})$$

where

$$M_r = \frac{a_0}{2} + \sum_{n=1}^{\infty} b_n \sin(w_n z) . \quad (\text{A.12})$$

The period for this machine is also $2\tau_p$ and hence $w_n = n\pi/\tau_p$. b_n is determined from

$$b_n = \frac{1}{\tau_p} \int_{-\tau_p}^{\tau_p} f(z) \sin(w_n z) dz , \quad (\text{A.13})$$

which when taken from 0 to τ_p is doubled as

$$b_n = \frac{2}{\tau_p} \int_0^{\tau_p} f(z) \sin(w_n z) dz . \quad (\text{A.14})$$

Considering the remanence flux density over the permeability of free space B_{rem}/μ_0 into A.14 leads to

$$b_n = \frac{2B_{rem}}{\tau_p\mu_0} \int_{(\tau_p-\tau_m)/2}^{((\tau_p-\tau_m)/2)+\tau_m} \sin(w_n z) dz, \quad (\text{A.15})$$

which when the integration is done results into

$$b_n = \frac{2B_{rem}}{\tau_p\mu_0} \left\{ \frac{2 \sin\left(\frac{w_n\tau_m}{2}\right) \sin\left(\frac{w_n\tau_p}{2}\right)}{w_n} \right\}. \quad (\text{A.16})$$

Taking w_n outside the brackets and also taking n as $2n - 1$ gives

$$b_{2n-1} = \frac{4B_{rem}}{(2n-1)\pi\mu_0} \left\{ \sin\left(\frac{(2n-1)\pi\tau_m}{2\tau_p}\right) \sin\left(\frac{(2n-1)\pi}{2}\right) \right\} \quad (\text{A.17})$$

The magnetisation vector for the machine of Figure A.2 is given by

$$M_r(z) = \frac{a_0}{2} + \frac{4B_{rem}}{\pi\mu_0} \sum_{n=1,..\infty} \frac{1}{(2n-1)} \sin\left(\frac{(2n-1)\pi\tau_m}{2\tau_p}\right) \sin\left(\frac{(2n-1)\pi}{2}\right) \sin(m_n z) \quad (\text{A.18})$$

where m_n is the same as in (A.10)

Appendix B

Simplified analytical model -open circuit only

B.1 Magnetic field distribution due to permanent magnets (coil switched off)

This appendix takes a look at predicting the magnetic field distribution due to permanent magnets field only as an illustration of a simplified version. Also, to avoid repetition, the machine topology is selected from the topology looked at in Chapters 2 - 4. The permanent magnets setup is similar to Figure 2.2 shown in Chapter 2 but replicated at a distance of τ_l which is much larger than τ_p . While the iron yokes are considered as infinitely long. This topology has small effects on the reduction of fringing fields at the machine edges because of having half length permanent magnetic poles at the edges of the machine whose most flux lines have magnetic coupling with the inner full length magnetic poles. Figure B.1 illustrates the topology for which a simplified analytical model is developed. The iron yokes are infinitely long and only the permanent magnets are replicated. The approach involves taking three subdomains: the inner PMs (subdomain I), the air-gap (subdomain II) with the armature removed and the outer PMs (subdomain III), for which the Laplace and Poisson equations for determining the magnetic flux density expressions are solved and coefficients calculated.

B.1.1 Assumptions for the simplified model

Below are the assumptions considered for this analysis:

1. The axial length of the machine is considered infinite, with discrete series of permanent magnet arrays which are separated by τ_l ,
2. The iron yokes are considered to have infinite permeability,

B.1.1.1 Solution to the magnetisation vector for the simplified model

Taking the period to be τ_{lp} which is given as

$$\tau_{lp} = 3\tau_p + \tau_l, \quad (\text{B.1})$$

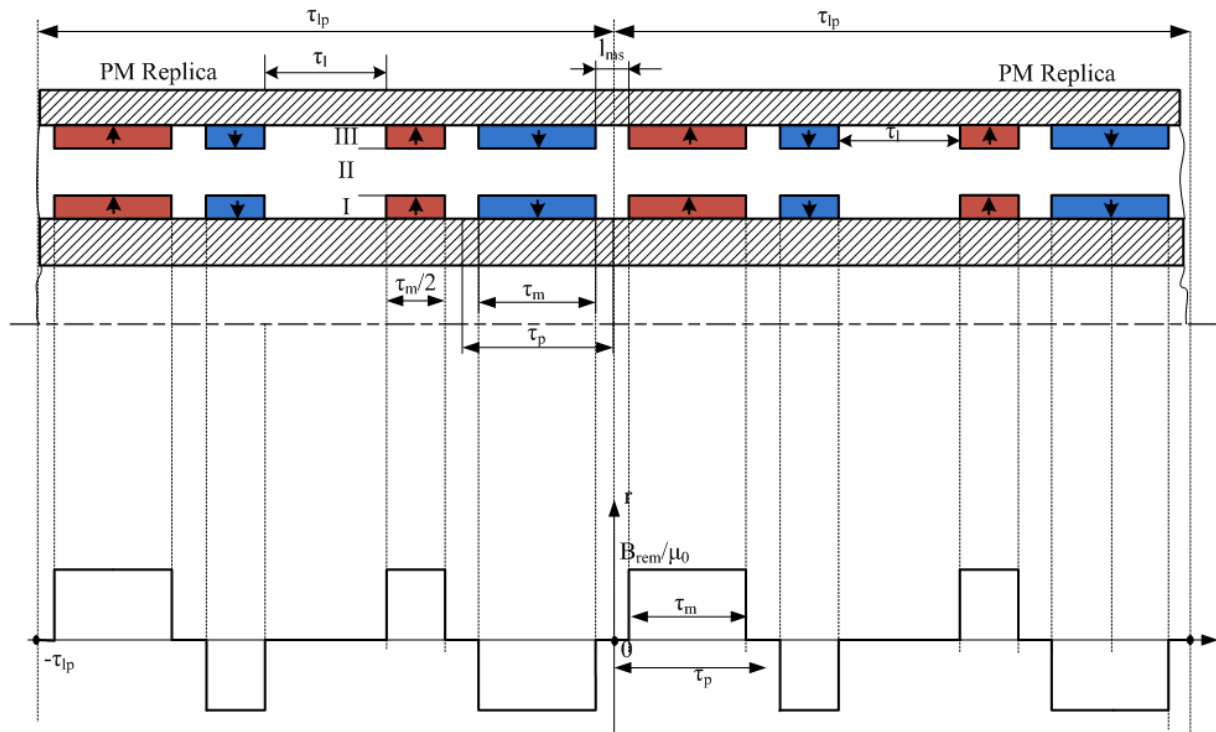


Figure B.1: LOG with infinite PM series and infinitely long and permeable iron yokes

with τ_l being the separation distance. Since the permanent magnets are radially magnetised, the Fourier expansion is given by

$$M = \sum_{1,2,..}^{\infty} m_{rn} \sin(m_{nf} z) , \quad (\text{B.2})$$

where $m_{nf} = 2n\pi/\tau_{lp}$ same as in Chapter 5. m_{nf} is calculated from

$$m_{rn} = \frac{1}{\tau_{lp}} \int_{-\tau_{lp}}^{\tau_{lp}} f(z) \sin(m_{nf} z) dz = \frac{2}{\tau_{lp}} \int_0^{\tau_{lp}} f(z) \sin(m_{nf} z) dz . \quad (\text{B.3})$$

Taking 0 (with reference to Figure B.1) as the initial position, the flux distribution pattern is calculated as

$$m_{rn} = \frac{2B_{rem}}{\tau_{lp}\mu_0} \left[\int_{l_{ms}/2}^{\tau_m+l_{ms}/2} f(z) \sin(m_{nf} z) dz - \int_{\tau_p+l_{ms}/2}^{3\tau_p/2} f(z) \sin(m_{nf} z) dz \right] . \quad (\text{B.4})$$

The solution to the integration is obtained as

$$m_{rn} = \frac{B_{rem}}{\mu_0 n \pi} \left\{ \cos\left(\frac{3m_{nf}\tau_p}{2}\right) - \cos\left[m_{nf}\left(\tau_p + \frac{l_{ms}}{2}\right)\right] \right. \\ \left. + \cos\left(\frac{m_{nf}l_{ms}}{2}\right) - \cos\left[m_{nf}\left(\frac{l_{ms}}{2} + \tau_m\right)\right] \right\} . \quad (\text{B.5})$$

Finally, the expression for the magnetisation vector is given by

$$M = \frac{B_{rem}}{\mu_0 n \pi} \left\{ \cos\left(\frac{3m_{nf}\tau_p}{2}\right) - \cos\left[m_{nf}\left(\tau_p + \frac{l_{ms}}{2}\right)\right] \right. \\ \left. + \cos\left(\frac{m_{nf}l_{ms}}{2}\right) - \cos\left[m_{nf}\left(\frac{l_{ms}}{2} + \tau_m\right)\right] \right\} \sin(m_{nf} z) . \quad (\text{B.6})$$

Completing the right side of the Poisson equation being $\mu_0 \nabla \times \mathbf{M}$, it is known that $\nabla \times M = \frac{\partial M_r}{\partial z} \mathbf{e}_\phi$ from which the partial derivative leads to

$$\mu_0 \nabla \times \mathbf{M} = P_{nf} \cos(m_{nf} z) \quad (\text{B.7})$$

with

$$P_{nf} = \frac{2B_{rem}}{\tau_{lp}} \left\{ \cos\left(\frac{3m_{nf}\tau_p}{2}\right) - \cos\left[m_{nf}\left(\tau_p + \frac{l_{ms}}{2}\right)\right] + \cos\left(\frac{m_{nf}l_{ms}}{2}\right) - \cos\left[m_{nf}\left(\frac{l_{ms}}{2} + \tau_m\right)\right] \right\}. \quad (\text{B.8})$$

Incorporating the magnetisation vector into the Poisson equation leads to

$$A_{\phi f}(r, z) = \sum_{n=1, \dots}^{\infty} \left[a_n I_1(m_{nf} r) + b_n K_1(m_{nf} r) + \frac{\pi L_1(m_{nf} z)}{2m_{nf}^2} P_{nf} \right] \cos(m_{nf} z). \quad (\text{B.9})$$

B.1.1.2 General solutions to the magnetic vector potential and the magnetic flux densities

In this analysis the magnetic vector potential is given by

$$A_{\phi I f} = \sum_{n=1, \dots}^{\infty} \left[a_{nI} I_1(m_{nf} r) + b_{nI} K_1(m_{nf} r) + \frac{\pi L_1(m_{nf} z)}{2m_{nf}^2} P_{nf} \right] \cos(m_{nf} z), \quad (\text{B.10})$$

$$A_{\phi II f} = \sum_{n=1, \dots}^{\infty} [a_{nII} I_1(m_{nf} r) + b_{nII} K_1(m_{nf} r)] \cos(m_{nf} z), \quad (\text{B.11})$$

$$A_{\phi III f} = \sum_{n=1, \dots}^{\infty} \left[a_{nIII} I_1(m_{nf} r) + b_{nIII} K_1(m_{nf} r) + \frac{\pi L_1(m_{nf} z)}{2m_{nf}^2} P_{nf} \right] \cos(m_{nf} z) \dots \quad (\text{B.12})$$

The magnetic flux density in the radial direction is given by

$$B_{r I f} = \sum_{n=1, \dots}^{\infty} m_{nf} \left[a_{nI} I_1(m_{nf} r) + b_{nI} K_1(m_{nf} r) + \frac{\pi L_1(m_{nf} z)}{2m_{nf}^2} P_{nf} \right] \sin(m_{nf} z), \quad (\text{B.13})$$

$$B_{r II f} = \sum_{n=1, \dots}^{\infty} m_{nf} [a_{nII} I_1(m_{nf} r) + b_{nII} K_1(m_{nf} r)] \sin(m_{nf} z), \quad (\text{B.14})$$

$$B_{r III f} = \sum_{n=1, \dots}^{\infty} m_{nf} \left[a_{nIII} I_1(m_{nf} r) + b_{nIII} K_1(m_{nf} r) + \frac{\pi L_1(m_{nf} z)}{2m_{nf}^2} P_{nf} \right] \sin(m_{nf} z), \quad (\text{B.15})$$

and the magnetic flux density in the axial direction by

$$B_{z I f} = \sum_{n=1, \dots}^{\infty} m_{nf} \left[a_{nI} I_0(m_{nf} r) - b_{nI} K_0(m_{nf} r) + \frac{\pi L_0(m_{nf} z)}{2m_{nf}^2} P_{nf} \right] \cos(m_{nf} z), \quad (\text{B.16})$$

$$B_{z II f} = \sum_{n=1, \dots}^{\infty} m_{nf} [a_{nII} I_0(m_{nf} r) - b_{nII} K_0(m_{nf} r)] \cos(m_{nf} z), \quad (\text{B.17})$$

$$B_{z III f} = \sum_{n=1, \dots}^{\infty} m_{nf} \left[a_{nIII} I_0(m_{nf} r) - b_{nIII} K_0(m_{nf} r) + \frac{\pi L_0(m_{nf} z)}{2m_{nf}^2} P_{nf} \right] \cos(m_{nf} z), \dots \quad (\text{B.18})$$

B.1.2 Solving the simultaneous equations for the simplified model

Boundary condition are only considered in the radial direction just as in Chapter 5. In a similar pattern, six equations are obtained and a matrix is obtained to calculate for the coefficients to the Laplace and the Poisson equations as

$$\begin{bmatrix}
 \frac{m_{nf}}{\mu_0} I_0(m_{nf} i R_r) & -\frac{m_{nf}}{\mu_0} K_1(m_{nf} i R_r) & 0 & 0 & 0 & 0 \\
 m_{nf} I_1(m_{nf} i R_m) & m_{nf} K_1(m_{nf} i R_m) & -m_{nf} I_1(m_{nf} i R_m) & -m_{nf} K_1(m_{nf} i R_m) & 0 & 0 \\
 m_{nf} I_0(m_{nf} i R_m) & -m_{nf} K_0(m_{nf} i R_m) & -m_{nf} I_0(m_{nf} i R_m) & +m_{nf} K_0(m_{nf} i R_m) & 0 & 0 \\
 0 & 0 & m_{nf} I_1(m_{nf} o R_m) & +m_{nf} K_1(m_{nf} o R_m) & -m_{nf} I_1(m_{nf} o R_m) & -m_{nf} K_1(m_{nf} o R_m) \\
 0 & 0 & m_{nf} I_0(m_{nf} o R_m) & -m_{nf} K_0(m_{nf} o R_m) & -m_{nf} I_0(m_{nf} o R_m) & +m_{nf} K_0(m_{nf} o R_m) \\
 0 & 0 & 0 & 0 & \frac{m_{nf}}{\mu_0} I_0(m_{nf} o R_s) & -\frac{m_{nf}}{\mu_0} K_1(m_{nf} o R_s)
 \end{bmatrix}
 \begin{bmatrix}
 a_{nI} \\
 b_{nI} \\
 a_{nII} \\
 b_{nII} \\
 a_{nIII} \\
 b_{nIII}
 \end{bmatrix}
 =
 \begin{bmatrix}
 -\frac{m_{nf} \pi L_0(m_{nf} i R_r) P_{nf}}{\mu_0 2m_{nf}^2} \\
 \frac{m_{nf} \pi L_1(m_{nf} i R_m) P_{nf}}{2m_{nf}^2} \\
 -\frac{m_{nf} \pi L_0(m_{nf} i R_m) P_{nf}}{2m_{nf}^2} \\
 \frac{m_{nf} \pi L_1(m_{nf} o R_m) P_{nf}}{2m_{nf}^2} \\
 \frac{m_{nf} \pi L_0(m_{nf} o R_m) P_{nf}}{2m_{nf}^2} \\
 \frac{m_{nf} \pi L_0(m_{nf} o R_s) P_{nf}}{\mu_0 2m_{nf}^2}
 \end{bmatrix}
 \tag{B.19}$$

B.1.3 Comparison with finite element model

Inserting the coefficients into the magnetic vector potential expressions (B.10) - (B.12), the radial flux density expressions (B.13) - (B.15) and the axial flux density expressions (B.16) - (B.18) with numerical values, a comparison to FEM can be obtained.

B.1.4 Comparison of the radial magnetic flux density from the simplified model with FEM

Figure B.2 considers the actual length of the machine. On the other hand, a full spectrum of the machine is shown in Figure B.3

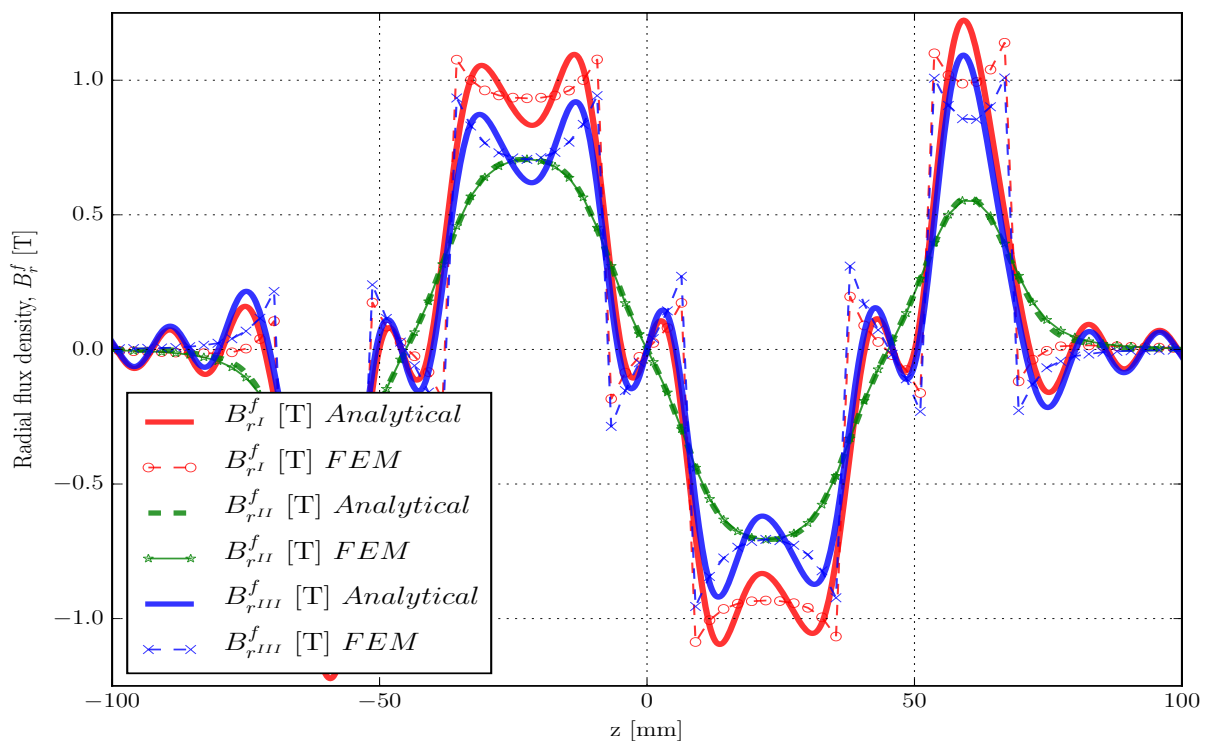


Figure B.2: Analytically Radial flux density plot compared to a finite length FEM model

The results show good correlation between FEM and the simplified analytical model. The results obtained considered upto the 24th harmonics.

B.1.5 Comparison of the axial magnetic flux density from the simplified model to FEM

A machine length comparison of the axial flux densities are illustrated in Figure B.4 where as the full spectrum is captured in Figure B.5. Again good correlation between the simplified analytical model and FEM is observed in the results.

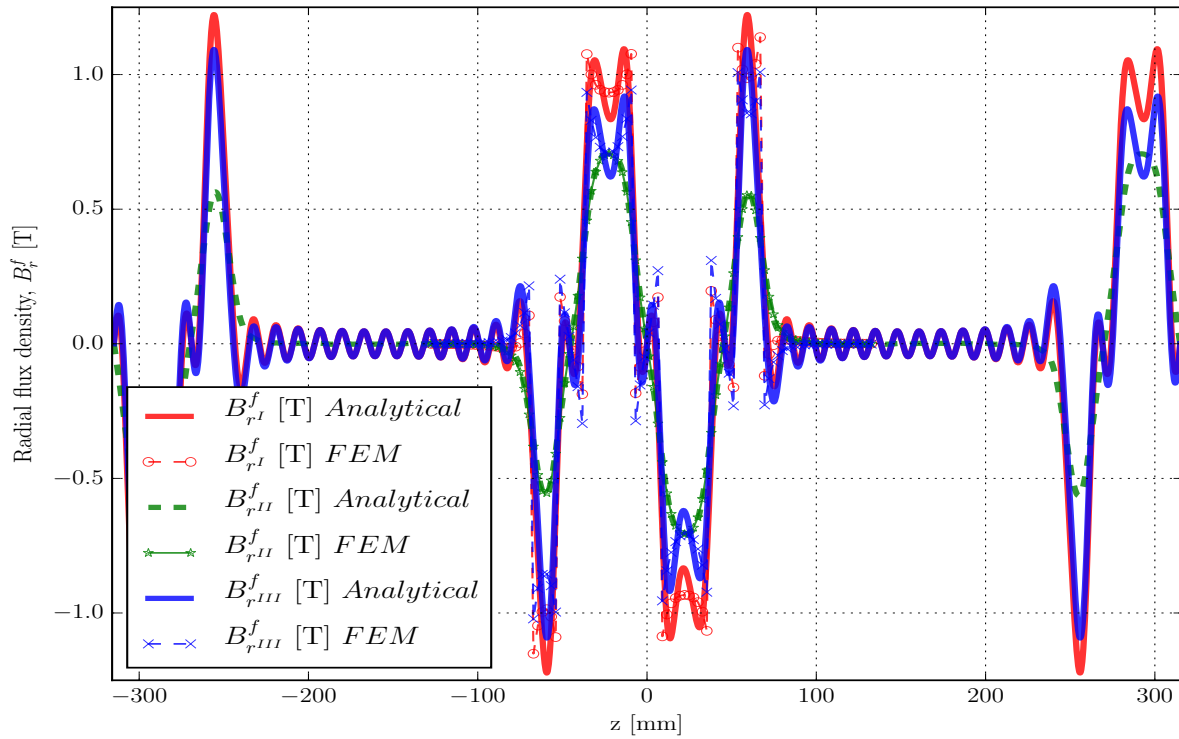


Figure B.3: Full spectrum radial flux density plot compared to a finite length FEM model

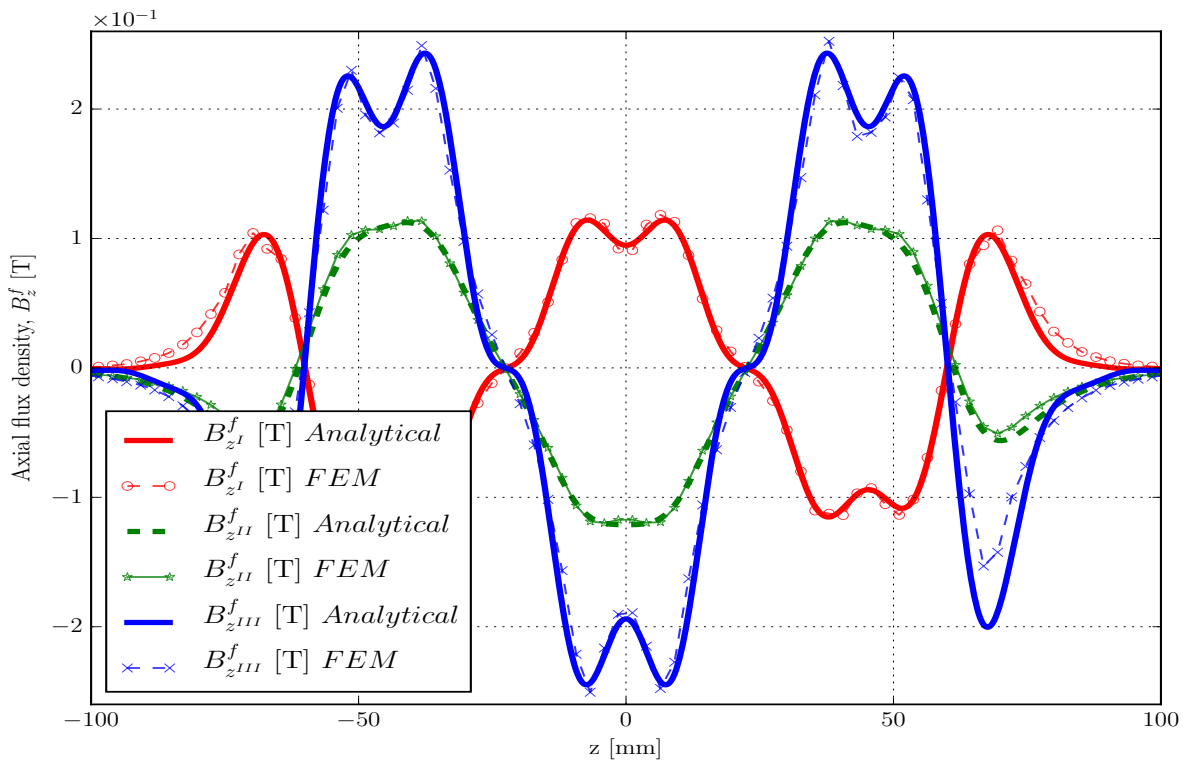


Figure B.4: Axial flux density plot compared to a finite length FEM model

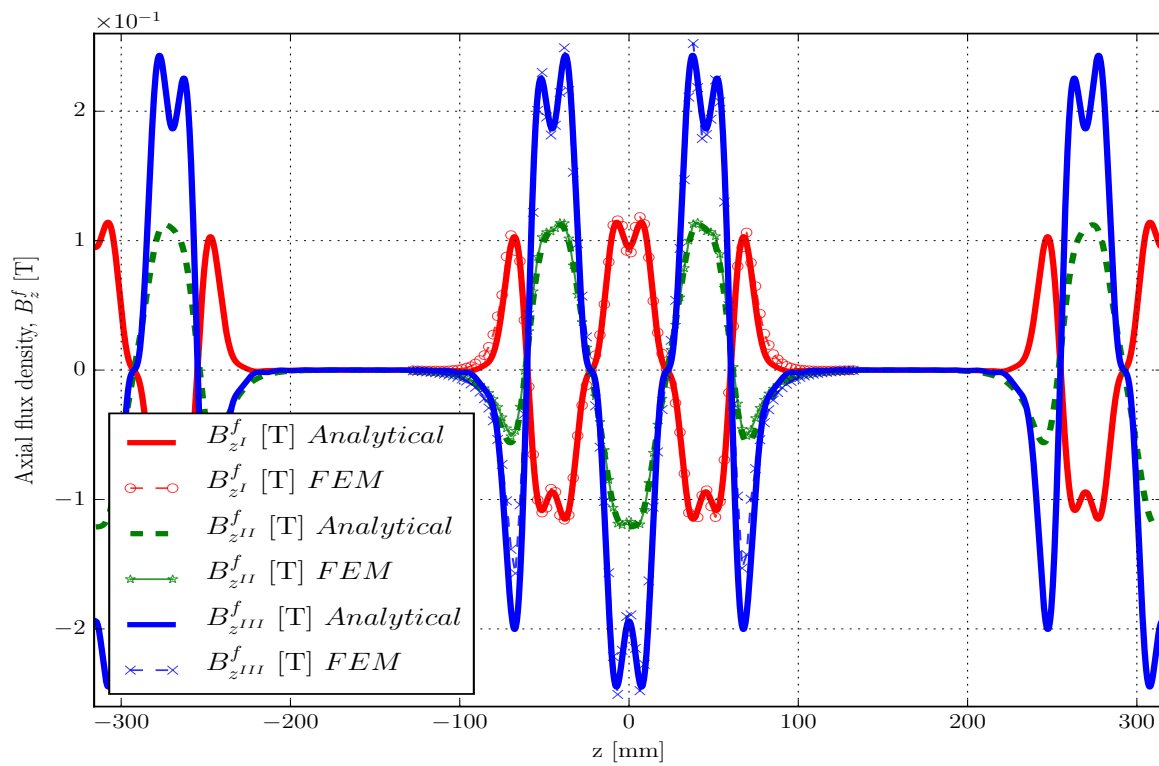


Figure B.5: Full spectrum of axial flux density plot compared to a finite length FEM model

Appendix C

Bessel Functions

C.1 Brief Introduction to Bessel functions

C.1.1 Bessel function of the first kind

A brief introduction is given here to simply highlight the Bessel functions and types that exist. According to [76], the linear differential equation of the second order of the form

$$z^2 \frac{d^2 u}{dz^2} + z \frac{du}{dz} + (z^2 - v^2)u = 0 \quad (\text{C.1})$$

can be expressed as

$$u(z) = C_1 u_1(z) + C_2 u_2(z) \quad (\text{C.2})$$

in its integral form where $u_1(z)$ and $u_2(z)$ become partial solutions of (C.1) but as linearly independent. Employing the Bessel operator

$$\nabla_v = z^2 \frac{d^2}{dz^2} + z \frac{d}{dz} + z^2 - v^2 \quad (\text{C.3})$$

and taking $\nabla_v u = 0$ of (C.1) using the power series of the argument z , the solutions of (C.1) appears as

$$u(z) = \sum_{m=0}^{\infty} a_m z^{m+\alpha} \quad (\text{C.4})$$

with $a_0 \neq 0$. To calculate the coefficients a_m and also α of (C.4) the first and second derivatives of $u(z) = \sum_{m=0}^{\infty} a_m z^{m+\alpha}$ are obtained as

$$u'(z) = \sum_{m=0}^{\infty} a_m (m + \alpha) z^{m+\alpha-1} \quad (\text{C.5})$$

$$u''(z) = \sum_{m=0}^{\infty} a_m (m + \alpha)(m + \alpha - 1) z^{m+\alpha-2} \quad (\text{C.6})$$

Replacing the left hand side of (C.1) with the series obtained leads to the following series

$$\begin{aligned} \nabla_v u &= a_0(\alpha^2 - v^2)z^\alpha + a_1[(\alpha + 1)^2 - v^2]z^{\alpha+1} \\ &+ \sum_{m=2}^{\infty} \{a_m[(\alpha + m)^2 - v^2] + a_{m-2}\}z^{\alpha+m} \end{aligned} \quad (\text{C.7})$$

An infinite system of equations are obtained when considering that $\nabla_v u = 0$ with all the coefficients of $z^{\alpha+m}$ in (C.7) becoming zero. Using the systems of equations obtained (not shown here) and taking $\alpha = v$ then the first partial solution to (C.1) as

$$u_1(z) = a_0 z^v \left[1 - \frac{z^2}{4 \cdot 1 \cdot (v+1)} + \frac{z^4}{4^2 \cdot 2!(v+1)(v+2)} - \frac{z^6}{4^3 \cdot 3!(v+1)(v+2)(v+3)} + \dots \right], \quad (\text{C.8})$$

where as the second partial solution is obtained for $\alpha = -v$ as

$$u_2(z) = a'_0 z^{-v} \left[1 - \frac{z^2}{4 \cdot 1 \cdot (-v+1)} + \frac{z^4}{4^2 \cdot 2!(-v+1)(-v+2)} - \frac{z^6}{4^3 \cdot 3!(-v+1)(-v+2)(-v+3)} + \dots \right], \quad (\text{C.9})$$

The constants a_0 and a'_0 are taken as;

$$a_0 = \frac{1}{2^v \Gamma(v+1)} \quad (\text{C.10})$$

and

$$a'_0 = \frac{1}{2^{-v} \Gamma(-v+1)} \quad (\text{C.11})$$

Employing gamma function properties, $u_1(z)$ in (C.8) defines the Bessel function or cylindrical functions of the first kind

$$J_v = \left(\frac{z}{2}\right)^v \sum_{m=0}^{\infty} \frac{(-1)^m (z/2)^{2m}}{m! \Gamma(v+m+1)} \quad (\text{C.12})$$

while the second series (C.9) gives

$$J_{-v} = \left(\frac{z}{2}\right)^{-v} \sum_{m=0}^{\infty} \frac{(-1)^m (z/2)^{2m}}{m! \Gamma(-v+m+1)} \quad (\text{C.13})$$

The series $J_v(z)$ converges extremely well in any bounded domain of index v and of variation of z except for $z = 0$.

C.1.2 Bessel functions of the second kind

The Bessel function of the second kind $Y_v(z)$ is often called the Neumann function and it is represented as

$$Y_v(z) = \frac{J_v(z) \cos v\pi - J_{-v}(z)}{\sin v\pi} \quad (\text{C.14})$$

Various solutions to the Bessel equations are formed from the combination of the Neumann function $Y_v(z)$ and the $J_v(z)$ for any integer or index. This can be demonstrated in the Hankel functions which are the Bessel functions of the third kind as

$$H_v^{(1)}(z) = J_v(z) + iY_v(z), \quad H_v^{(2)}(z) = J_v(z) - iY_v(z) \quad (\text{C.15})$$

C.1.3 Modified Bessel functions

If the variable in (C.1) is replaced by $z = ix$ the equation

$$x^2 \frac{d^2 u}{dx^2} + x \frac{du}{dx} - (x^2 + v^2)u = 0 \quad (\text{C.16})$$

is obtained. The solution to this (C.16) is known as the Bessel function with an imaginary argument $J_v(ix)$. The real argument is then taken as the modified Bessel function of first kind

$$I_v(x) = e^{-v\pi i/2} J_v(ix) \quad (\text{C.17})$$

which in power series is given by

$$I_v(x) = \sum_{m=0}^{\infty} \frac{(x/2)^{2m+v}}{m! \Gamma(v+m+1)}. \quad (\text{C.18})$$

The modified Bessel function of the second kind is obtained from the second integral of (C.16) as

$$K_v(x) = \frac{1}{2} \pi i e^{v\pi i/2} H_v^{(1)}(ix) \quad (\text{C.19})$$

and in power series for $v = n$

$$\begin{aligned} K_n(x) = & (-1)^{n+1} I_n(x) \ln \frac{x}{2} + \frac{1}{2} \sum_{m=0}^{n-1} (-1)^m \left(\frac{x}{2}\right)^{-n+2m} \frac{(n-m-1)!}{m!} \\ & + (-1)^{n+1} \frac{1}{2} \sum_{m=0}^{\infty} \frac{(x/2)^{n+2m}}{m!(n+m)!} \left[2C - \sum_{k=1}^{m+n} \frac{1}{k} - \sum_{k=1}^m \frac{1}{k} \right] \end{aligned} \quad (\text{C.20})$$

where C is the Euler constant. The modified Bessel functions of the first and second kind form the solution for the linear equations for the work in this dissertation. The differentiation and the integrals for the Bessel function can further be studied in [76; 78].

List of References

- [1] Hargreaves, C.M.: *The Philips Stirling Engine*. Elsevier Science Publishers, 1991.
- [2] Walker, G.: *Robert Stirling and his family*. 1980.
Available at: <https://books.google.co.uk/books?id=HNBSAAAAMAAJ>
- [3] Darlington, R. and Strong, K.: *Stirling and hot air engines*. 1st edn. Crowood Press, 2005. ISBN 9781861266880.
- [4] William, R.M.: *Stirling Engine Design Manual*. US Department of Energy, NASA, 1978.
- [5] Walker, G. and Senft, J.R.: *Free-piston Stirling Engines*. 1st edn. Springer-Verlag Berlin, Heidelberg, 1985. ISBN 9783540154952.
- [6] Beale, W.: Free Piston Stirling Engines - Some Model Tests and Simulations. In: *Soc. Automot. Eng.* 1969.
- [7] Beale, W.: Some Stirling Engine Designs for Solar Energy Concepts Analysis and Test Results. 1977.
- [8] Taylor, G.: Free piston Stirling engines increase solar/thermal efficiency. *Int. Power Gener.*, vol. 2, pp. 45,47–48, 1979.
- [9] Beale, W.: *The Free Piston Stirling Engine 20 Years of Development*. 1983.
- [10] Beale, W.T.: *Solar-Powered-Stirling-Engines-and-their-Potential-Uses-in-Developing-Countries*. Tech. Rep., United Nations Industrial Development Organisation, 1986.
- [11] Bean, J.R. and Kubo, I.: *Development of the CPG 5 KW Dish/Stirling System*. Tech. Rep., Cummings Power Generation, Inc., 1990.
- [12] Stine, W.B. and Diver, R.B.: *A compendium of Solar Dish/Stirling Technology*. Tech. Rep., California State Polytechnic University, Sandia National Laboratories, 1994.
- [13] Bean, J.R. and Diver, R.B.: *Technical Status of the Dish/Stirling Joint Venture Program*. Tech. Rep., Cummins Power Generation, Sandia National Laboratories -DOE, 1995.
- [14] Wood, J.G., Chagnot, B.J. and Penswick, L.B.: *Design of a Low Pressure Air Engine for Third World Use*. 1982.
- [15] Berchowit, D.: *Stirling-Engines-in-Developing-Countries*. 1984.
- [16] Sternlicht, B.: The Stirling Engine: prime mover of the 21st century. *Endeav. Ser. Vol. 8, No 1*, pp. 21 –28, 1984.

- [17] Beale, W., Heltsley, F.L., Feeney, M.F., Wagman, R.C. and Woodling, F.E.: Understanding Stirling Engines. Tech. Rep., Volunteers in Technical Assistance, Inc (VITA), 1985.
- [18] Beale, W.T.: A Free-Piston Stirling Engine Using Rough Biomass. In: *Fifth Int. Conf. small Engines, their fuels Environ.* 1995.
- [19] Beale, W.T. and Chen, G.: Small Stirling Free Piston Engines for Cogeneration. 1992.
- [20] Bowman, L. and Lane, N.W.: Micro-Scale Biomass Power. In: *Fourth Biomass Conf. Am.*, pp. 75 –80. Oakland, California, 1999.
- [21] Wood, J.G., Lane, N.W. and Beale, W.T.: Preliminary Design of a 7 kWe Free-Piston Stirling Engine with Rotary Generator Output. In: *10th Int. Stirling Engine Conf.*, pp. 24–27. 2001.
- [22] Lane, N.W., Wood, J.G. and Unger, R.Z.: Free-piston Stirling Machine Commercialization Status at Sunpower. *Int. Stirling Engine Conf.*, vol. 1, no. November, p. 9, 2003.
- [23] Lane, N.W.: Commercialization Status of Free-piston Stirling Machines. Tech. Rep. September 2005, Sunpower Incorporation, USA, 2005.
- [24] Wood, J.G., Carroll, C., Matejczyk, D., Penswick, L.B. and Lane, N.: Development of the Sunpower 35 We Free-Piston Stirling Convertor. In: *3rd Int. Energy Convers. Eng. Conf.*, August 15 -18, pp. 96 – 108. 2005. ISBN 0735402302.
- [25] Boldea, I. and Nasar, S.A.: Linear electric actuators and generators. *IEEE Trans. Energy Convers.*, vol. 14, no. 3, pp. 712–717, 1999. ISSN 08858969.
- [26] Laithwaite, E.R.: linear Electric Machines-. *Proc. IEEE, Febr. 1975*, vol. 63, no. 2, 1975.
- [27] Boldea, I.: *Variable Speed Generators*. 2nd edn. CRC Press, Taylor and Francis Group, 2016. ISBN 9781498723589.
- [28] Jansen, P.L., Li, L.-j., Lorenz, R.D. and Member, S.: Analysis of Competing Topologies of Linear Induction Machines for High-speed Material Transport Systems. *IEEE Trans. Ind. Appl.*, vol. 31, no. 4, pp. 925 –932, 1995.
- [29] Danielsson, O. and Leijon, M.: Flux Distribution in Linear Permanent-Magnet Synchronous Machines Including Longitudinal End Effects. *IEEE Trans. Magn.*, vol. 43, 2007. ISSN 0018-9464.
- [30] Vaez-zadeh, S. and Isfahani, A.H.: Multiobjective Design Optimization of Air-Core Linear Permanent-Magnet Synchronous Motors for Improved Thrust and Low Magnet Consumption. *IEEE Trans. Magn.*, vol. 42, no. 3, pp. 446–452, 2006.
- [31] Duan, Y. and Ionel, D.M.: A Review of Recent Developments in Electrical Machine Design Optimization Methods With a Permanent-Magnet Synchronous Motor Benchmark Study. *IEEE Trans. Ind. Electron.*, vol. 49, no. 3, pp. 1268–1275, 2013.

- [32] Garcia-Amorós, J., Andrada, P. and Blanqué, B.: Design Procedure for a Longitudinal Flux Flat Linear Switched Reluctance Motor. 2011.
- [33] Baoming, G., Almeida, A. and Ferreira, F.: Design of Transverse Flux Linear Switched Reluctance Motor. *IEEE Trans. Magn.*, vol. 45, no. 1, pp. 113–119, 2009. ISSN 0018-9464.
- [34] Boldea, I. and Nasar, S.A.: *LINEAR ELECTRIC ACTUATORS AND GENERATORS*. Cambridge University Press, 1997. ISBN 0-7803-3946-0.
- [35] Schutte, J. and Strauss, J.: Optimisation of a transverse flux linear PM generator using 3D finite element analysis. In: *Electr. Mach. (ICEM), 2010 XIX Int. Conf.* 2010. ISBN 978-1-4244-4174-7.
- [36] Joubert, L.H., Schutte, J., Strauss, J.M. and Dobson, R.T.: Design Optimisation of a Transverse Flux , Short Stroke , Linear Generator. In: *Electr. Mach. (ICEM), 2012 XXth Int. Conf.*, pp. 640–646. 2012. ISBN 9781467301428.
- [37] Zheng, P., Chen, A., Thelin, P., Arshad, W.M. and Sadarangani, C.: Research on a Tubular Longitudinal Flux PM Linear Generator Used for Free-Piston Energy Converter. *IEEE Trans. Magn.*, vol. 43, no. 1, pp. 447–449, jan 2007. ISSN 0018-9464.
Available at: <http://ieeexplore.ieee.org/lpdocs/epic03/wrapper.htm?arnumber=4033136>
- [38] Danielsson, O., Eriksson, M. and Leijon, M.: Study of a longitudinal flux permanent magnet linear generator for wave energy converters. *Int. J. Energy Res.*, vol. 30, pp. 1130–1145, 2006. ISSN 0363907X.
Available at: <http://doi.wiley.com/10.1002/er.1209>
- [39] Wang, J., Wang, W., Atallah, K. and Howe, D.: Comparative studies of linear permanent magnet motor topologies for active vehicle suspension. In: *2008 IEEE Veh. Power Propuls. Conf. VPPC 2008*. 2008. ISBN 9781424418497.
- [40] Boldea, I.: *Linear Electric Machines, Drives, and MAGLEVs Handbook*. CRC Press, Taylor and Francis Group, 2013.
- [41] Wang, J., Howe, D. and Lin, Z.: Comparative studies on linear motor topologies for reciprocating vapor compressors. In: *Proc. IEEE Int. Electr. Mach. Drives Conf. IEMDC 2007*, vol. 1, pp. 364–369. 2007. ISBN 1424407435.
- [42] Chen, X., Zhu, Z. and Howe, D.: Modeling and Analysis of a Tubular Oscillating Permanent-Magnet Actuator. *IEEE Trans. Ind. Appl.*, vol. 45, 2009. ISSN 0093-9994.
- [43] Vermaak, R. and Kamper, M.: Construction and control of an air-cored permanent magnet linear generator for direct drive wave energy converters. In: *Electr. Mach. Drives ...*, Section III, pp. 1076–1081. Department of Electrical and Electronic Engineering, University of Stellenbosch, South Africa, Ieee, 2011. ISBN 9781457700613.
Available at: http://ieeexplore.ieee.org/xpls/abs/_all.jsp?arnumber=5994750

- [44] Vermaak, R. and Kamper, M.M.J.: Design Aspects of a Novel Topology Air-Cored Permanent Magnet Linear Generator for Direct Drive Wave Energy Converters. *IEEE Trans. Ind. Electron.*, vol. 59, no. 5, pp. 2104–2115, may 2012. ISSN 0278-0046.
Available at: <http://ieeexplore.ieee.org/lpdocs/epic03/wrapper.htm?arnumber=5955119>[http://ieeexplore.ieee.org/xpls/abs_{_}all.jsp?arnumber=5955119](http://ieeexplore.ieee.org/xpls/abs/_all.jsp?arnumber=5955119)
- [45] Gysen, B.L.J., Lomonova, E.A., Paulides, J.J.H. and Vandenput, A.J.A.: Analytical and Numerical Techniques for Solving Laplace and Poisson Equations in a Tubular Permanent-Magnet Actuator :. *IEEE Trans. Magn.*, vol. 44, no. 7, pp. 1751–1760, 2008. ISSN 00189464.
- [46] Ibrahim, T., Wang, J. and Howe, D.: Analysis and experimental verification of a single-phase, quasi-Halbach magnetized tubular permanent magnet motor with non-ferromagnetic support tube. *IEEE Trans. Magn.*, vol. 44, no. 11, pp. 4361–4364, 2008. ISSN 00189464.
- [47] Zhu, Z.Q., Chen, X., Howe, D. and Iwasaki, S.: Electromagnetic modeling of a novel linear oscillating actuator. *IEEE Trans. Magn.*, vol. 44, no.11, pp. 3855–3858, 2008. ISSN 00189464.
- [48] Bianchi, N., Bolognani, S., Dalla Corte, D. and Tonel, F.: Tubular Linear Permanent Magnet Motors : An Overall Comparison. *IEEE Trans. Ind. Appl.*, vol. 39, no. 2, pp. 466–475, 2003.
- [49] Yan, L., Zhang, L., Jiao, Z., Hu, H., Chen, C.Y. and Chen, I.M.: Armature reaction field and inductance of coreless moving-coil tubular linear machine. *IEEE Trans. Ind. Electron.*, vol. 61, no. 12, pp. 6956–6965, 2014. ISSN 02780046.
- [50] Strauss, J.M.: *Direct Piston Displacement Control of*. Ph.D. thesis, Stellenbosch University, 2013.
- [51] Xu, Z. and Chang, S.: Improved moving coil electric machine for internal combustion linear generator. *IEEE Trans. Energy Convers.*, vol. 25, no. 2, pp. 281–286, 2010. ISSN 08858969.
- [52] Gysen, B.L.J., Meessen, K.J., Paulides, J.J.H. and Lomonova, E.A.: General Formulation of the Electromagnetic Field Distribution in Machines and Devices Using Fourier Analysis. *Magn. IEEE Trans.*, vol. 46, pp. 39–52, 2010. ISSN 0018-9464.
Available at: <http://ieeexplore.ieee.org/stamp/stamp.jsp?tp={&}arnumber=5357513>
- [53] Wang, J., Howe, D. and Jewell, G.W.: Fringing in Tubular Permanent-Magnet Machines : Part I . Magnetic Field Distribution , Flux Linkage , and Thrust Force. *IEEE Trans. Magn*, vol. 39, no. 6, pp. 3507–3516, 2003.

- [54] Wang, J., Lin, Z. and Howe, D.: Analysis of a short-stroke , single-phase , quasi-Halbach magnetised tubular permanent magnet motor for linear compressor applications. *IET Electr. Power Appl.*, vol. 2, no. January, pp. 193–200, 2008.
- [55] Bianchi, N., Bolognani, S. and Tonel, F.: Design Criteria of a Tubular Linear IPM Motor. *IEEE Trans. Ind. Electron.*, vol. 3, pp. 1–7, 2001.
- [56] Polinder, H., Sloopweg, J.G., Compter, J. and Hoeijmakers, M.: Modelling a linear PM motor including magnetic saturation. 2002.
- [57] Wang, J., Member, S., Howe, D. and Lin, Z.: Design Optimization of Short-Stroke Single-Phase Tubular Permanent-Magnet Motor for Refrigeration Applications. *IEEE Trans. Ind. Electron.*, vol. 57, no. 1, pp. 327–334, 2010.
- [58] Gysen, B.L.J., Lomonova, E.A., Paulides, J.J.H. and Vandenput, A.J.A.: Analytical and numerical techniques for solving laplace and poisson equations in a tubular permanent magnet actuator: Part II. Schwarz-Christoffel mapping. *IEEE Trans. Magn.*, vol. 44, no. 7, pp. 1761–1767, 2008. ISSN 00189464.
- [59] O’Connell, T.C. and Krein, P.T.: A Schwarz-Christoffel-based analytical method for electric machine field analysis. *IEEE Trans. Energy Convers.*, vol. 24, no. 3, pp. 565–577, 2009. ISSN 08858969.
- [60] Krop, D.C., Lomonova, E.A. and Vandenput, A.J.: Application of schwarz-christoffel mapping to permanent-magnet linear motor analysis. *IEEE Trans. Magn.*, vol. 44, no. 3, pp. 352–359, 2008. ISSN 00189464.
- [61] Zarko, D., Ban, D. and Lipo, T.A.: Analytical solution for electromagnetic torque in surface permanent-Magnet motors using conformal mapping. *IEEE Trans. Magn.*, vol. 45, no. 7, pp. 2943–2954, 2009. ISSN 00189464.
- [62] Wang, J., Jewel, G.W. and Howe, D.: A general framework for the analysis and design of tubular linear permanent magnet machines. *IEEE Trans. Magn.*, vol. 35, no. 3, pp. 1986–2000, may 1999. ISSN 00189464.
Available at: <http://ieeexplore.ieee.org/lpdocs/epic03/wrapper.htm?arnumber=764898>
- [63] Wang, J., Howe, D. and Lin, Z.: Comparative study of winding configurations of short-stroke , single phase tubular permanent magnet motor for refrigeration applications. *Ind. Appl. Conf. 2007. 42nd IAS Annu. Meet. Conf. Rec. 2007 IEEE*, pp. 311–318, 2007.
- [64] Ouagued, S., Amara, Y. and Barakat, G.: Cogging Force Analysis of Linear Permanent Magnet Machines Using a Hybrid Analytical Model. *IEEE Trans. Magn.*, vol. 52, no. 7, 2016.

- [65] Amara, Y. and Barakat, G.: Analytical modeling of magnetic field in surface mounted permanent-magnet tubular linear machines. *IEEE Trans. Magn.*, vol. 46, pp. 3870–3884, 2010. ISSN 00189464.
- [66] Amara, Y., Barakat, G. and Reghem, P.: Armature Reaction Magnetic Field of Tubular Linear Surface-Inset Permanent-Magnet Machines. *IEEE Trans. Magn.*, vol. 47, no. 4, pp. 805–811, 2011.
- [67] Tiegna, H., Amara, Y. and Barakat, G.: Overview of analytical models of permanent magnet electrical machines for analysis and design purposes. *Math. Comput. Simul.*, vol. 90, pp. 162–177, 2013. ISSN 03784754.
Available at: <http://dx.doi.org/10.1016/j.matcom.2012.12.002>
- [68] Yan, L., Chen, I.-m. and Lim, C.K.: Magnetic Field Modeling of Linear Machines with. *fluid power mechatronics, IEEE*, pp. 1–6, 2011.
- [69] Wang, J.W.J. and Howe, D.: Design optimization of radially magnetized, iron-cored, tubular permanent-magnet machines and drive systems. *IEEE Trans. Magn.*, vol. 40, no. 5, pp. 3262–3277, 2004. ISSN 0018-9464.
Available at: <http://ieeexplore.ieee.org/stamp/stamp.jsp?arnumber=1333136>
- [70] Kumar, P. and Bauer, P.: Improved analytical model of a permanent-magnet brushless DC motor. *IEEE Trans. Magn.*, vol. 44, no. 10, pp. 2299–2309, 2008. ISSN 00189464.
- [71] Randewijk, P.J. and Kamper, M.J.: Analytical analysis of a Radial Flux Air-cored Permanent Magnet machine with a double-sided rotor and non-overlapping double-layer windings. In: *2012 XXth Int. Conf. Electr. Mach.*, pp. 1178–1184. 2012. ISBN 978-1-4673-0142-8.
Available at: <http://ieeexplore.ieee.org/xpl/articleDetails.jsp?tp={&}arnumber=6350025{&}contentType=Conference+Publications{&}searchField=Search{ }All{&}queryText=randewijk>
- [72] Tsai, N.-C. and Chiang, C.-W.: Design and analysis of magnetically-drive actuator applied for linear compressor. *Mechatronics*, vol. 20, no. 5, pp. 596–603, 2010. ISSN 09574158.
Available at: <http://linkinghub.elsevier.com/retrieve/pii/S0957415810001030>
- [73] Stratton, J.A.: *Electromagnetic Theory*. John Wiley and Sons Ltd, 1995. ISBN 9780470131534.
Available at: <http://scitation.aip.org/content/aip/magazine/physicstoday/article/48/1/10.1063/1.2807887>
- [74] Binns, K. and Lawrenson, P.: *Analysis and Computation of Electric and Magnetic Field Problems*. 2nd edn. Pergamon Press Ltd, Oxford, New York, 1973. ISBN 0-08-016638-5.
- [75] Furlani, E.P.: *Permanent Magnet and Electromechanical Devices*. Academic Press, 2001. ISBN 0122699513.

- [76] Korenev, B.G.: *Bessel Functions and Their Applications.pdf*. Taylor and Francis, 2002.
- [77] Abramowitz, M. and Stegun, I.A.: *Handbook of Mathematical Functions with Formulas, Graphs, and Mathematical Tables*. Ninth edn. National Bureau of Standards, Washington D.C, 1970. ISBN 0486612724.
Available at: <http://www.ncbi.nlm.nih.gov/pubmed/22230940>
- [78] Bowman, F.: *Introduction to Bessel Functions*. Longmans, Green and Co., 1938.
- [79] Hayt, W.H.J. and Buck, J.A.: *Engineering Electromagnetics*. Seventh edn. McGraw-Hill, Singapore, 2006. ISBN 007-124449-2.
- [80] Bargallo, R.: *Finite Elements for Electrical Engineering*. Polytechnic University of Catalonia, Spain, 2006. ISBN 0521253217.
- [81] Gysen, B.L.J., Meessen, K.J., Paulides, J.J.H. and Lomonova, E.A.: General Formulation of the Electromagnetic Field Distribution in Machines. *IEEE Trans. Magn*, vol. 46, no. 1, pp. 39–52, 2010.
- [82] Xia, B., Jin, M.J., Shen, J.X. and Zhang, A.G.: Design and analysis of an air-cored axial flux permanent magnet generator for small wind power application. *2010 IEEE Int. Conf. Sustain. Energy Technol.*, pp. 1–5, 2010.
- [83] Vermaak, R. and Kamper, M.: Novel permanent magnet linear generator topology for wave energy conversion. . . . *Drives (PEMD 2010), 5th IET . . .*, 2010.
Available at: http://ieeexplore.ieee.org/xpls/abs/_all.jsp?arnumber=5523800
- [84] Zhu, Z.Q., Howe, D. and Mitchell, J.: Magnetic Field Analysis and Inductances of Brushless DC Machines with Surface-Mounted Magnets and Non-overlapping Stator Windings. *IEEE Trans. Magn.*, vol. 31, no. 3, pp. 0–3, 1995. ISSN 0018-9464.
- [85] Wang, J. and Howe, D.: Tubular modular permanent-magnet machines equipped with quasi-Halbach magnetized magnets - Part II: Armature reaction and design optimization. *IEEE Trans. Magn.*, vol. 41, no. 9, pp. 2479–2489, 2005. ISSN 00189464.
- [86] Wang, J., Howe, D. and Amara, Y.: Armature reaction field and inductances of tubular modular permanent magnet machines. *J. Appl. Phys.*, vol. 97, no. 10, pp. 1–4, 2005. ISSN 00218979.
- [87] Chembe, D.K. and Strauss, J.M.: ARMATURE REACTION MAGNETIC FIELD PREDICTION FOR A MOVING-COIL TUBULAR PERMANENT MAGNET LINEAR. In: *25th South. African Univ. Power Eng. Conf. (SAUPEC 2017)*, pp. 309–314. Southern African Universities Power Engineering Conference (SAUPEC) and the South African Institute of Electrical Engineers (SAIEE), 2017.
- [88] Wang, J., Howe, D. and Jewell, G.W.: Fringing in Tubular Permanent-Magnet Machines : Part II. Cogging force and its minimization. *IEEE Trans. Magn.*, vol. 39, no. 6, pp. 3517–3522, 2003.

- [89] Tiegna, H., Bellara, A., Amara, Y. and Barakat, G.: Analytical modeling of the open-circuit magnetic field in axial flux permanent-magnet machines with semi-closed slots. *IEEE Trans. Magn.*, vol. 48, no. 3, pp. 1212–1226, 2012. ISSN 00189464.
- [90] Lucas, C. and Tootoonchian, F.: Multi-Objective Design Optimization of a Linear Brushless Permanent Magnet Motor Using Particle Swarm Optimization (PSO). *Iran. J. Electr. Electron. Eng.*, vol. 6, no. 3, pp. 183–189, 2010.
- [91] Lubin, T., Mezani, S. and Rezzoug, A.: Analytical computation of the magnetic field distribution in a magnetic gear. *IEEE Trans. Magn.*, vol. 46, no. 7, pp. 2611–2621, 2010. ISSN 00189464.
- [92] Lubin, T., Mezani, S. and Rezzoug, A.: 2-D exact analytical model for surface-mounted permanent-magnet motors with semi-closed slots. *IEEE Trans. Magn.*, vol. 47, no. 2 PART 2, pp. 479–492, 2011. ISSN 00189464.
- [93] Barakat, G. and Amara, Y.: Analytical Modeling of Flat and Tubular Linear PM Machines with Surface-Mounted Magnets and Semi-Closed Slots. *IEEJ J. Ind. Appl.*, vol. 1, no. 2, pp. 78–88, 2012.
- [94] Gieras, J.: *Permanent Magnet Motor Technology Design and Applications*. Taylor and Francis Group, 2010. ISBN 9781420064407. [arXiv:1011.1669v3](https://arxiv.org/abs/1011.1669v3).
- [95] Kim, J., Joo, S., Hahn, S., Hong, J., Kang, D. and Koo, D.: Static characteristics of linear BLDC motor using equivalent magnetic circuit and finite element method. *IEEE Trans. Magn.*, vol. 40, 2004. ISSN 0018-9464.
- [96] Li, L., Tang, Y., Ma, M. and Pan, D.: Analysis and Optimization of Air-Core Permanent Magnet Linear Synchronous Motors with Overlapping Concentrated Windings for Ultra-precision Applications. *J. Int. Conf. Electr. Mach. Syst.*, vol. 2, no. 1, pp. 16–22, 2013.
- [97] Selcuk, A.H. and Kurum, H.: Investigation of end effects in linear induction motors by using the finite-element method. *IEEE Trans. Magn.*, vol. 44, no. 7, pp. 1791–1795, 2008. ISSN 00189464.
- [98] Vermaak, R.: *Development of a Novel Air-Cored Permanent Magnet Linear Generator for Direct Drive Ocean Wave Energy Converters*. Ph.D. thesis, Stellenbosch, 2013.
- [99] Wang, J.W.J., Wang, W.W.W., Atallah, K. and Howe, D.: Design Considerations for Tubular Flux-Switching Permanent Magnet Machines. *IEEE Trans. Magn.*, vol. 44, 2008. ISSN 0018-9464.
- [100] Gerber, S.: *A Finite Element Based Optimisation Tool for Electrical Machines*. Ph.D. thesis, Stellenbosch University, mar 2011.
Available at: <http://scholar.sun.ac.za/handle/10019.1/6635><http://ir1.sun.ac.za/handle/10019.1/6635>